# Navigating the Storm

## New Approaches to Tropical Cyclone Risk Analyses and Their Implications for Coastal Flooding Predictions

Nederhoff, C.M.

**DOI**
10.4233/uuid:88aa9fc1-1d69-4697-9a20-38d788c66da8

**Publication date**
2024

**Document Version**
Final published version

**Citation (APA)**
Nederhoff, C. M. (2024). *Navigating the Storm: New Approaches to Tropical Cyclone Risk Analyses and Their Implications for Coastal Flooding Predictions*. [Dissertation (TU Delft), Delft University of Technology]. IHE Delft Institute for Water Education. https://doi.org/10.4233/uuid:88aa9fc1-1d69-4697-9a20-38d788c66da8

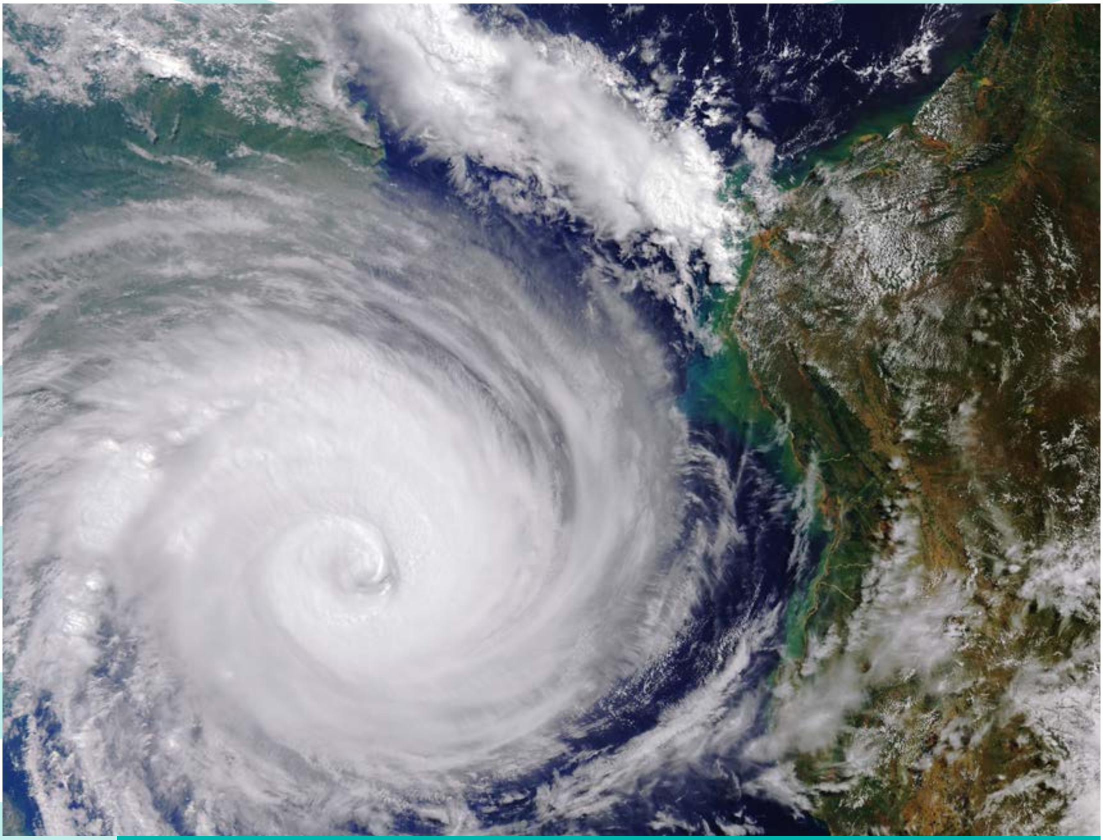

# **Navigating the Storm**
## New Approaches to Tropical Cyclone Risk Analyses and Their Implications for Coastal Flooding Predictions

C.M. (Kees) Nederhoff

# NAVIGATING THE STORM

## NEW APPROACHES TO TROPICAL CYCLONE RISK ANALYSES AND THEIR IMPLICATIONS FOR COASTAL FLOODING PREDICTIONS

# NAVIGATING THE STORM

## NEW APPROACHES TO TROPICAL CYCLONE RISK ANALYSES AND THEIR IMPLICATIONS FOR COASTAL FLOODING PREDICTIONS

**Dissertation**

for the purpose of obtaining the degree of doctor
at Delft University of Technology
by the authority of the Rector Magnificus prof.dr.ir. T.H.J.J. van der Hagen,
chair of the Board for Doctorates
and
in fulfillment of the requirement of the Rector of IHE Delft
Institute for Water Education, prof.dr. E.J. Moors,
to be defended publicly on
on Thursday, 20 June 2024 at 15:00 o'clock
in Delft, the Netherlands

by

**Cornelis Mattheus NEDERHOFF**

Master of Science in Hydraulic Engineering, Delft University of Technology
born in Werkendam, the Netherlands

This dissertation has been approved by the (co)promotor.

Composition of the doctoral committee:

| | |
|---|---|
| Rector Magnificus TU Delft | chairperson |
| Rector IHE Delft | vice-chairperson |
| Prof.dr.ir. J.A. Roelvink | IHE Delft / Delft University of Technology, promotor |
| Dr. J.A.A. Álvarez Antolínez | Delft University of Technology, copromotor |
| Dr. A.R. van Dongeren | IHE Delft / Deltares, copromotor |

*Independent members:*

| | |
|---|---|
| Prof.dr. R.A. Luettich | The University of North Carolina, USA |
| Prof.dr. F.J. Mendez | University of Cantabria, Spain |
| Dr. M.I. Vousdoukas | University of the Aegean, Greece |
| Prof.dr.ir. A.J.H.M. Reniers | Delft University of Technology |

*Reserve member:*

| | |
|---|---|
| Prof.dr.ir. I.I. Popescu | IHE Delft / Delft University of Technology |

Dr. J. (Jay) Veeramony has been a key contributor to the preparation of this dissertation.

*This research was conducted under the auspices of the Graduate School for Socio-Economic and Natural Sciences of the Environment (SENSE)*

Published by IHE Delft Institute for Water Education
www.un-ihe.org
ISBN 978-90-73445-61-1

Printed by: Veenman+
Cover: Cyclone Idai heading towards Mozambique and Zimbabwe in 2019

# CONTENTS

# SUMMARY

Tropical cyclones, often referred to as hurricanes in the Atlantic and Northeast Pacific or typhoons in the Northwest Pacific, are powerful storm systems characterized by strong rotating winds, heavy rainfall, and low atmospheric pressure. Cyclones typically form over warm tropical waters, fueled by the heat and moisture from these waters, and are one of the most significant drivers of coastal flooding in tropical and subtropical regions. There are about 50 cyclones annually worldwide reaching hurricane strength (maximum sustained winds >33 m/s). The flooding that these cyclones induce occurs due to storm surges combined with heavy rainfall and other relevant drivers. These floods jeopardize surrounding communities and natural ecosystems. Moreover, risks are only heightened due to climate change and increased human activities. However, it remains challenging to accurately predict coastal flooding under the influence of tropical cyclones due to their complex spatial features, limited record length, and uncertainties in forecasting.

This dissertation aims to determine the extent to which improved tropical cyclone descriptions of wind geometry and their pathways can enhance the reliability of forecasts and the accuracy of risk analysis for coastal flood assessments. In this thesis, we address both operational and strategic flood risk analyses. Both types play a vital role in understanding and reducing potential environmental threats. Operational risk analysis is associated with short-term forecasting (several days before and after a cyclone event), while strategic risk analysis focuses on long-term climate variability assessments on the scale of decades. Both perspectives are critical for comprehensive climate risk management, as they offer different scales and time frames for preparedness and prevention.

A key component for both operational and strategic flood risk analyses is the ability to accurately represent tropical cyclone conditions in computational methods. By analyzing historical best-track data, we derived empirical stochastic relationships for two tropical cyclone geometry parameters which are measures of the size of the storms: the radius

of maximum winds and the radius of gale-force winds. The relationships improved the estimates of tropical cyclone geometry parameters by up to 25%. Larger improvements were found for cyclones not impacting the United States since most of the existing relationships are derived from basins adjacent to the United States. These parameters (either based on observations or on derived relationships) were needed to accurately compute the spatial distribution of surface winds with the well-known parametric Holland wind model. Accurate estimates of tropical cyclone winds are crucial for coastal flood evaluations.

Strategic risk analyses are often hindered by an insufficient number of historical tracks for a reliable analysis of flood hazards and risk. We introduce a methodology that uses the empirical track model based on Markov chains and can simulate thousands of computer-generated pathways that hypothetical storms might follow (synthetic tracks). The open-source Tropical Cyclone Wind Statistical Estimation Tool (TCWiSE) handles track initialization, evolution, and termination based on historical information. Validation showed accurate skill compared to historical best-track data and good agreement for observed extreme wind speeds. Strategic risk analyses benefit from the improved estimate of extreme tropical cyclone conditions.

Subsequently, the data-driven methods were combined with physics-based modeling to quantify coastal flooding for strategic risk analysis focused on the Southeast Atlantic Coastal Zone of the United States. In particular, we compared cyclone-induced flooding relative to non-cyclonic-induced (or extratropical) flooding to place them in perspective. Non-cyclonic events such as extratropical cyclones were mainly responsible for frequent flooding events. For example, we found that for the current sea level, extratropical cyclones contributed to half of the flooded area. Tropical cyclones drove the majority of the infrequent, but more severe, flood hazards. For example, for the 100-year event, tropical cyclones contributed 96% of the flooded area and likely affected 30 times the number of people. However, at higher sea levels, the flood risk exclusively driven by tropical cyclones diminished as areas were flooded regardless of the physical driver. This analysis underscored the significance of both event types and highlights the need for future research to consider both flooding factors.

Operational risk assessments are crucial for protecting lives and minimizing economic impacts days before a storm. We introduced a methodology that uses uncertainties in track, forward speed, and wind speed/intensity and can simulate thousands of ensem-

ble members. The open-source Tropical Cyclone Forecasting Framework (TC-FF) handles all major relevant physical drivers, including tide, surge, and rainfall, and considers cyclone uncertainties through Gaussian error distributions and autoregressive techniques. A comparison of TC-FF and operational ensembles revealed differences of <10%, suggesting that TC-FF can be employed as an alternative, especially in data-scarce environments. A case study of Cyclone Idai in Mozambique stressed the need to include a sufficiently large number of ensemble members (200 members for 3 days of lead time) for reliable forecasting of tropical cyclone flood hazards.

This thesis provides new insights into tropical cyclones with descriptions of wind geometry, pathways, statistical properties, and their role in compound flooding. In addressing future research directions, the importance of enhanced data collection, particularly from satellites, is crucial for validating models and understanding storm characteristics. While efficient computational methods used in this dissertation have been foundational in assessing coastal flood risk, there is an urgent need to incorporate overlooked processes, harness the potential of data assimilation, and explore even more efficient methods. Concurrently, the rise of Deep Learning offers promising opportunities for faster flood assessment which is paramount to capturing tropical cyclone variability.

# SAMENVATTING

Tropische cyclonen, vaak aangeduid als orkanen of tyfonen, zijn krachtige stormsystemen die worden gekenmerkt door sterke roterende winden, hevige regenval en lage atmosferische druk. Orkanen vormen zich boven warme tropische wateren en zijn een van de meest belangrijkste veroorzakers van kustoverstromingen. Deze overstromingen brengen mensen en natuurlijke ecosystemen in gevaar. Klimaatverandering en toegenomen menselijke activiteit langs de kust maken deze stormen mogelijk nog gevaarlijker. Het blijft echter een uitdaging om kustoverstromingen onder de invloed van tropische cyclonen nauwkeurig te berekenen vanwege hun complexe ruimtelijke kenmerken, beperkte gegevens en onzekerheden in de voorspelling.

Dit proefschrift beoogt te bepalen in welke mate verbeterde beschrijvingen van tropische cyclonen de betrouwbaarheid en de nauwkeurigheid voor kustoverstromingen kunnen verbeteren. In dit proefschrift richten we ons zowel op operationele als strategische risicoanalyses. Beide typen spelen een cruciale rol. Operationele risicoanalyse is geassocieerd met kortetermijnvoorspellingen (enkele dagen voor een cycloon aan land komt), terwijl strategische risicoanalyse zich richt op de langetermijnbeoordeling van het klimaat. Beide perspectieven zijn essentieel voor een grondig begrip van klimaatrisico's, omdat ze verschillende tijdskaders bieden voor voorbereiding en preventie.

Een kernonderdeel voor zowel operationele als strategische risicoanalyses is een nauwkeurige weergave van de condities rondom tropische cyclonen. Op basis van historische gegevens van tropische cyclonen zijn empirische stochastische relaties afgeleid die de cycloongeometrie beschreven: de straal van maximale winden en de straal van stormkracht winden. Deze relaties verbeterden de schattingen van de geometrische parameters van tropische cyclonen met 25%. Grotere verbeteringen werden specifiek gevonden voor niet-Amerikaanse cyclonen aangezien de meeste bestaande relaties zijn afgeleid voor Amerikaanse oceaanbekkens. Cycloongeometrie (gebaseerd op waarnemingen of de afgeleide relaties) waren nodig om cycloonwinden nauwkeurig te berekenen met een parametrisch windmodel. Nauwkeurige inschattingen van tropische cycloon winden zijn cruciaal voor de evaluatie van kustoverstromingen.

Strategische risicoanalyses worden vaak gehinderd door een onvoldoende aantal historische cyclonen voor een betrouwbare analyse van de kans op overstroming. We introduceren een methodologie die duizenden plausibele maar hypothetische stormen (synthetische cyclonen) kan generen op basis van historische informatie. De open-source Tropical Cyclone Wind Statistical Estimation Tool (TCWiSE) behandelt de initialisatie, evolutie en beëindiging van synthetische cyclonen. Bij de validatie bleken synthetische cyclonen en historische stormen goed overeen te komen. Strategische risicoanalyses profiteren van de verbeterde inschatting van de kans op extreme tropische cycloneconditiес.

Vervolgens werden de datagedreven methoden gecombineerd met op fysica gebaseerde modellering om kustoverstromingen te kwantificeren voor een strategische risicoanalyse gericht op de zuidoostelijke Atlantische kustzone van de Verenigde Staten. We hebben cyclone-geïnduceerde overstromingen vergeleken met niet-cyclone (reguliere stormen) geïnduceerde overstromingen om ze in perspectief te plaatsen. Voor dit gebied waren reguliere stormen voornamelijk verantwoordelijk voor de meer frequente overstroming. Zo vonden we dat bij het huidige zeeniveau reguliere stormen verantwoordelijk waren voor de helft van jaarlijks overstroomde gebied. Tropische cyclonen veroorzaakten de meerderheid van de zeldzame maar ernstigere overstroming. Voor de 100 jaar storm droegen tropische cyclonen 96% bij aan het overstroomde gebied en werden 30 keer zoveel mensen getroffen door cyclonen dan niet-cyclonen. Bij hogere zeeniveaus verminderde het overstromingsrisico gedreven door alleen tropische cyclonen aangezien gebieden overstroomden ongeacht het type storm. Deze analyse benadrukte het belang van beide soorten stormen en de noodzaak om in toekomstig onderzoek beide mee te nemen.

Operationele risicoanalyses zijn cruciaal voor het beschermen van levens en het minimaliseren van economische schade dagen voor een storm aan land komt. We introduceerden een methodologie die gebruikmaakt van onzekerheden in het cycloonpad, voorwaartse snelheid en windsnelheid/intensiteit en die duizenden cyclonen kan simuleren rondom de hoofdvoorspelling (’ensembles’). Het open-source Tropical Cyclone Forecasting Framework (TC-FF) neemt alle belangrijke fysica mee en houdt rekening met onzekerheden van de cycloonvoorspelling door gebruik te maken van Gaussische foutdistributies en autoregressieve technieken. Een vergelijking van TC-FF en operationele ensembles onthulde verschillen van <10%, wat suggereert dat TC-FF kan worden gebruikt als een alternatief. Een casus van Cycloon Idai in Mozambique benadrukte de noodzaak om een voldoende groot aantal ensembles mee te nemen (bijvoorbeeld 200 ensembles 3 dagen voor de storm aan land komt) voor het betrouwbaar voorspellen van overstroming als het gevolg van de cycloon.

Dit proefschrift biedt nieuwe inzichten in de parametrische beschrijving en statistische eigenschappen van tropische cyclonen en hun rol in overstromingen. Voor toekomstig onderzoek is een verbeterde gegevensverzameling, met name via satellieten, cruciaal voor het valideren van modellen en het begrijpen van stormkenmerken. Er is ook een dringende behoefte om missende fysica en processen mee te nemen in de berekening. Daarnaast is het van belang om het potentieel van gegevensassimilatie en (nog) efficiëntere methoden te verkennen. De opkomst van Deep Learning is ook een veelbelovende mogelijkheid voor snellere overstromingsberekeningen.

# 1

# INTRODUCTION

## 1.1. THE IMPACT OF COASTAL FLOOD HAZARDS

Flooding can have catastrophic impacts on communities, often resulting in fatalities and causing substantial economic damage. Globally, over half a billion individuals live in the coastal zones that lie below 10 meters in elevation relative to mean sea level (MSL). This number is expected to rise above 1 billion by 2050 due to urbanization and migration trends (Merkens et al., 2016). Increased economic activities, such as tourism and infrastructure growth, further amplify the exposure of these coastal areas. Disastrous hurricanes like Katrina (2005), Harvey (2017), and Ian (2022) caused a financial loss of more than $400 billion[1] emphasizing the vulnerability of coastal areas (NOAA, 2023).

Elevated sea levels during high tides can, in conjunction with surges from storm systems, lead to extensive flooding of low-lying coastal areas. Flooding can be further intensified when these phenomena coincide with substantial rainfall or high waves. This interplay of physical processes, ranging from marine (tide, surge, waves), fluvial (riverine flow), and pluvial (rainfall and infiltration) components, is referred to as compound flooding (Wahl et al., 2015) and can increase the severity of coastal flooding.

---

[1] Values throughout this dissertation are adjusted to 2022 values and in USD Dollars.

Climate change will accelerate hazards and impacts from coastal storms, resulting in increased flooding frequencies due to sea level rise (SLR; Easterling et al., 2000), changes in storm frequencies (Vitousek et al., 2017b), and increased and prolonged precipitation (Trenberth et al., 2003). The socioeconomic impacts of increased flooding can be immense. Wing et al., 2018 estimated that in the entire continental United States (CONUS), 40 million people might be exposed to 100-year flooding, causing damages of approximately $1200 billion – numbers that could quadruple by 2100.

## 1.2. METHODS FOR ASSESSING COASTAL FLOODING

Computing coastal flooding is critical as it helps to predict and assess the impact of rising sea levels and extreme weather events on coastal areas. Understanding coastal flood hazards through observations is fundamental for a comprehensive grasp of the present climate. However, the future remains uncertain, and computational methods are therefore essential in quantifying, visualizing, and preparing for unseen challenges. Several methods can be used for this purpose. The most straightforward and widely used method is an estimation of flooding with a bathtub approach. This approach assumes that any part of the land located below the extreme (offshore) water level is inundated, while a hydrological connection restriction is often applied (e.g., Muis et al., 2016). Typically, bathtub approaches overestimate the flooded area as storm water levels vary in time during the event, which means that a smaller volume than expected will inundate the land. On the other hand, this approach ignores flooding due to rainfall and river drivers. Recent events (e.g., Hurricane Florence in 2018) serve as a stark reminder of the importance of compound flooding. Such events have made it evident that traditional computing methods are often insufficient, underscoring the need for more physics-based modeling approaches to assess coastal flooding.

A variety of modeling systems exist that allow for physics-based modeling of flood hazards. For example, the Coastal Storm Modeling System (CoSMoS; Barnard et al., 2019) makes detailed storm-induced flooding predictions. These modeling systems, including CoSMoS, use modeling trains of large-scale Delft3D-based hydrodynamic (Kernkamp et al., 2011) and wave models (Booij et al., 1999) in combination with local computationally expensive XBeach (Roelvink et al., 2018) models for wave runup. A new development is the application of the lower-fidelity models. The idea is to reduce the complexity of physics in combination with simplified numerics to allow for much faster physics-based hazard modeling. A reduced computational expense also allows for more computations. An example of this approach is the SFINCS model (Super-Fast INundation of CoastS; Leijnse et al., 2021) which was developed for large-scale coastal compound flood assessments.

The advanced capability to assess flood hazards is pivotal for operational and strategic risk analyses, serving as the foundation for evaluating potential environmental risks. Operational risk analysis, typically associated with short-term forecasting (several days), provides immediate preparedness and response for imminent disasters, ensuring the safety and protection of people and property (Roy and Kovordányi, 2012). Conversely, strategic risk analysis focuses on long-term climate variability assessments, delivering insights into hazards and their socio-economic and environmental impacts, thus facilitating informed policy decisions and adaptation strategies (e.g., Bloemendaal et al., 2020). Though distinctly different, both perspectives are critical for comprehensive climate risk management, as they offer different scales and time frames for prevention, preparedness, response, and recovery.

## 1.3. INSIGHTS INTO TROPICAL CYCLONES

Tropical cyclones (TCs) are one of the most significant drivers of coastal flooding (Peduzzi et al., 2012) and have been responsible for many extreme flood events in tropical and subtropical areas. TCs, also known as hurricanes in the Atlantic and Northeast Pacific or typhoons in the Northwest Pacific, are powerful storm systems characterized by strong, rotating winds, heavy rainfall, and low atmospheric pressure. Cyclone-induced flooding occurs as the cyclone's strong winds push a large volume of seawater toward the shore, a phenomenon known as storm surge. This surge, combined with heavy rainfall, leads to extensive flooding in coastal and adjacent inland areas. Cyclones typically form over warm tropical waters and affect a large portion of the globe, including Australia, East Asia, Southeast Asia, South Asia, East Africa, the Caribbean, and the United States. (Figure 1.1; Knapp et al., 2010). Their formation is fueled by the heat and moisture from these waters, which intensifies their energy and sustains their power over time. Predicting coastal flooding accurately in the presence of TCs continues to be a challenge due to their complex spatial characteristics, the limited duration of historical records, the lack of accuracy in the knowledge of field conditions such as bathymetry, and the inherent uncertainties in forecasting. Globally, there are about 50 cyclones annually reaching a strength >64 kt (or >33 m/s, Saffir–Simpson hurricane wind scale, SSHWS, of 1 or higher, Klotzbach et al., 2022) of which 25 reach category 4 and 5.

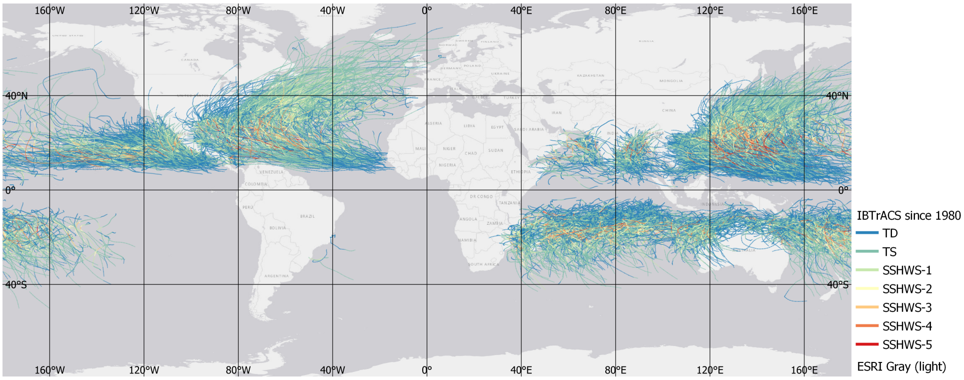

Figure 1.1: Global distribution of tropical cyclone tracks provided by IBTrACS (Knapp et al., 2010). Only tracks after 1980 were included.

### 1.3.1. STRATEGIC ANALYSIS OF TROPICAL CYCLONE RISKS

The TC track record varies from 50 years worldwide (from the 1970s) to more than 150 years in the Gulf of Mexico. This data is crucial for conducting strategic risk analyses centering on evaluations of long-term climate variability. Termed as best-track data (BTD), this information includes the coordinates of the TC, related intensity measures such as wind speed or pressure drop, and geometric details, including the radius of maximum winds (RMW) and the radius of gale-force winds (ΔAR35). The reliability of the BTD has been increasing over the years especially compared to older data. Therefore, depending on the area of interest, the accuracy and number of events vary greatly. Also, in specific regions, the frequency of TC landfall is very low, limiting the sample size of observed activity. When using only a handful of observed TCs in recent history, model estimates for extreme wind speeds and overland flooding for rare return frequencies will be affected since a few individual storms will strongly affect the determined extremes and their probability. Sampling errors in the BTD undermine the accuracy of analysis and can result in over- and underestimations of hazards in strategic risk analysis. Emulation can be employed through the generation of synthetic TC tracks, thereby augmenting the data set with plausible cyclone scenarios (see e.g., Vickery and Twisdale, 1995).

In coastal engineering, Global Circulation Models (GCMs) are commonly used as forcing conditions for computational methods to assess coastal flooding. GCMs simulate key climate components (atmosphere, land surface, ocean, and sea ice) and their interactions. Reanalysis products (e.g., ERA5; Hersbach et al., 2020) enhance the strength of GCMs by integrating model data based on physical laws with observations. These models are vital for predicting and understanding flooding due to their capability to simulate intricate interactions between climate components, thus allowing the quantification of climate change. Although model accuracy and resolution have increased substantially, these are often insufficient to resolve TCs (e.g., Murakami and Sugi, 2010), resulting in an underestimation of the TC intensity, and thus GCMs are often unable to assess TC-induced coastal flood hazards.

Alternatively, the spatial distribution of TC surface winds can also be estimated using parametric wind profiles based on track information. Several (horizontal) parametric wind profiles (e.g., Fujita, 1952, Chavas et al., 2015) exist in the literature, with the original Holland wind profile (Holland, 1980) being the most widely used due to its relative simplicity. However, without calibration, parametric wind profiles are often unable to accurately reproduce the spatial distribution of winds in TCs (e.g., Willoughby and Rahn, 2004). In strategic analysis, the accuracy of TC is paramount and refers to how close the model's predictions are to the actual observed outcomes. A mismatch potentially leads to an under- or overestimation of wind speeds and associated coastal hazards.

### 1.3.2. OPERATIONAL ANALYSIS OF TROPICAL CYCLONE RISKS

Accurate and on-time TC forecasts are crucial for saving human lives and reducing the economic costs of TCs. Forecasting agencies such as the National Hurricane Center (NHC) have significantly improved operational meteorological risk analyses, credited to gains made in numerical weather prediction models (e.g., McAdie and Lawrence, 2000, Cangialosi et al., 2020). However, despite these advancements, operational forecast errors in landfall location, timing and intensity persist. Therefore, it is vital to account for these inherent uncertainties in TC forecasts for informed preparedness decision-making which requires a reliable method (Lamers et al., 2023). Here, the reliability of the method refers to the consistency or dependability of the forecast probabilities over time. Reliability in this context does not ensure the accuracy of a single (deterministic) forecast ensemble member, but refers to the long-term performance and trustworthiness of the probabilistic forecasts.

The National Hurricane Center (NHC) dynamically models the meteorological conditions, which yields the official (deterministic) forecast. Moreover, it produces a probabilistic forecast based on a set of 1,000 ensemble members using the DeMaria et al., 2009 method. Each ensemble member has its intensity forecast which is computed by randomly sampling from the distributions database with track and intensity errors of the last five years. While this methodology gives valuable information on the probability of wind hazards, it has not been developed to forecast TC-induced coastal flooding. Probabilistic modeling systems for TC-induced coastal flooding for operational risk analyses are starting to be developed for the US and Japan. In particular for the US, P-Surge (e.g., Taylor and Glahn, 2008, Gonzalez and Taylor, 2018) uses data from the NHC to create synthetic storms but does not account for several marine and inland relevant processes (e.g. tides, waves, rainfall, infiltration). The Japan Meteorological Agency (JMA) does deploy a more complete physics model but only accounts for a limited number of ensemble members (see Hasegawa et al., 2015 for more details).

## 1.4. RESEARCH AIM AND RESEARCH QUESTIONS

Coastal flooding poses significant societal and ecological risks and is an area of growing concern due to climate change and increased anthropogenic activities along coastlines. The challenge lies in accurately and reliably predicting coastal flooding, especially when considering the influence of tropical cyclones (TCs).

**Aim of the dissertation**

**Determine the extent to which improved tropical cyclone descriptions of geometry, tracks, and statistical uncertainty can enhance the reliability of forecasts and the accuracy of risk analyses for coastal flood assessments**

This aim is pursued with the following research questions that form the core of this dissertation:

1. How to accurately describe TC geometry and winds with parametric relationships for any oceanic basin in the world?
2. How to reliably include TCs in coastal flood risk assessments in environments with limited observed activity?
3. How important is the contribution of TCs in coastal flood risk assessments?
4. How to reliably account for TC uncertainty in operational coastal risk analysis?

While *accurate* and *reliable* are terms often used interchangeably, they have different meanings. Accurate refers to how close a computed value is to the true (observed) value. For example, a single deterministic computation is compared to observed measurements of wind speeds or water levels, and the model accuracy is determined by how closely it matches the observations. On the other hand, reliability pertains to consistency with which the predicted probabilities match the long-term observed frequencies. For example, if a compound flood model predicts a 70% chance of flooding in a particular area, and it actually floods on 70 out of 100 days with that forecast, then the model is considered reliable.

The first question is assessed with the derivation of new relationships to estimate TC geometry for each oceanic basin with parametric and stochastic relationships, which improves our ability to describe time and spatially varying TC wind fields. The second question focuses on a new method to artificially generate paths that TCs might follow (synthetic tracks), based on historical data to aid strategic risk assessments. The third question is addressed in a case study form with the development of a new modeling framework that efficiently combines synthetic TC tracks and extratropical events to assess and project compound flood hazards across large regions. The fourth question focuses on a novel forecasting workflow that addresses the uncertainties and relevant physical drivers of TC-induced compound flooding for operational risk analysis.

## 1.5. APPROACH AND STRUCTURE OF THE DISSERTATION

The four research questions are addressed in Chapters 2 to 5, respectively. Various methods were combined to answer the research questions: decades of data were analyzed, computational code was developed for strategic and operational risk analysis and flooding was modeled with physics-based assessments. The focus is on the description of TC geometry and wind fields (Chapter 2), strategic risk analysis (Chapters 3 and 4), and operational risk analysis (Chapter 5). Each chapter was published independently in the open literature as peer-reviewed articles. The structure of the papers was maintained for consistency. Figure 1.2 provides a visual representation of this dissertation.

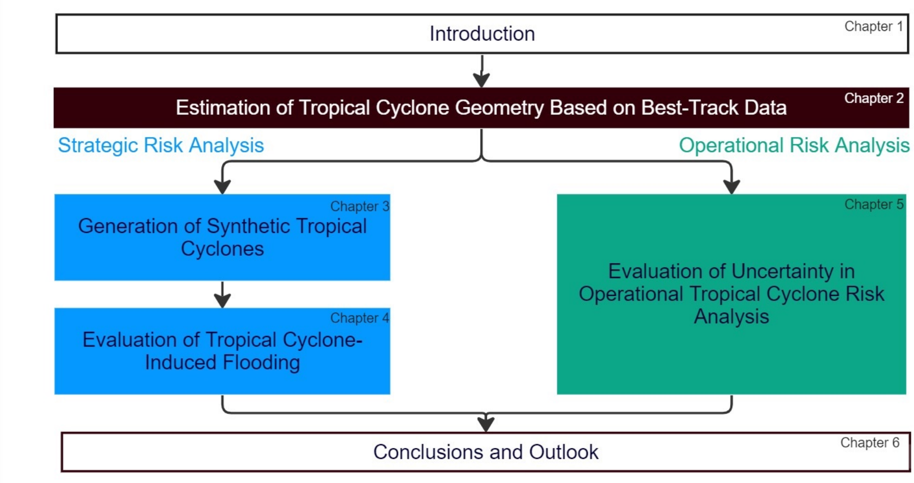

Figure 1.2: Structure and content of this PhD thesis. White boxes indicate generic chapters. Black is used for the improved description of tropical cyclones and forms the basis for follow-up risk analysis. The blue chapters are focused on strategic risk analysis and the green chapters on operational risk analysis. The respective chapters are indicated at the top right corner of the boxes.

In Chapter 2, empirical stochastic relationships are derived to describe two important parameters affecting the TC geometry: the radius of maximum winds (RMW) and the radius of gale-force winds (ΔAR35). These relationships are formulated using historical BTD for all oceanic basins. These relationships make it possible to estimate these variables when they are unknown and result in improved parametric wind fields that can be used when the spatial distribution of TC surface winds is unknown.

In Chapter 3, a new method for the generation of synthetic TC tracks based on (historical) data is proposed. The method has been implemented in the highly flexible open-source Tropical Cyclone Wind Statistical Estimation Tool (TCWiSE). The tool can be used to determine the wind extremes, and the output can be used for the reliable and accurate assessment of coastal flood hazards. Synthetic tracks are a valuable source of information for strategic risk analysis to overcome sampling errors.

In Chapter 4, a large-scale strategic risk analysis for a case study of the subtropical Southeast Atlantic Coast of the United States is performed. An unprecedentedly long and high-resolution data set was created by leveraging the computational speed of the lower-fidelity model SFINCS. Different flood hazards such as tropical and extratropical cyclones (ETCs, or migratory cyclones/storms of middle and high latitudes) are considered. This data set allows for a detailed breakdown of relevant drivers of flooding and results in an improved understanding of the role of tropical cyclones and extratropical events in the compound flood hazard, impact, and risk in the area.

In Chapter 5, a new method for operational risk analysis for coastal flood hazards is proposed. The method, called the Tropical Cyclone Forecasting Framework (TC-FF), allows for the consideration of uncertainties in forecasts of compound flooding induced by tropical cyclones. The open-source method accounts for all major relevant physical drivers, including tide, surge, and rainfall, uses the computationally efficient SFINCS model, and considers TC uncertainties in track, forward speed, and wind speed/intensity through Gaussian error distributions and autoregressive techniques similar to DeMaria et al., 2009.

Finally, Chapter 6 reevaluates the research questions introduced in Chapter 1, aligning them with the research objective. It concludes with insights, a forward-looking perspective, and suggestions for subsequent studies.

# 2

# ESTIMATION OF TROPICAL CYCLONE GEOMETRY BASED ON BEST-TRACK DATA

*Computational methods for assessing coastal flooding require an estimate of tropical cyclone winds. However, the spatial distribution of surface winds, crucial for coastal flood evaluations, is typically undefined. While parametric wind profiles serve to fulfill this need, they require accurate estimates of tropical cyclone geometry - a frequently unavailable parameter. In this chapter, best-track data are used to derive empirical stochastic relationships that can be used when geometry parameters are unknown. The focus of this chapter is on the ability to produce accurate tropical cyclone wind speeds for both strategic and operational risk analysis within coastal flood assessments.*

---

This chapter is a revised version of **Nederhoff**, **K.**, Giardino, A., van Ormondt, M., & Vatvani, D. (2019). Estimates of tropical cyclone geometry parameters based on best-track data. *Natural Hazards and Earth System Sciences*, *19*(11), 2359–2370. https://doi.org/10.5194/nhess-19-2359-2019.

**Abstract** Parametric wind profiles are commonly applied in a number of engineering applications for the generation of tropical cyclone (TC) wind and pressure fields. Nevertheless, existing formulations for computing wind fields often lack the required accuracy when the TC geometry is not known. This may affect the accuracy of the computed impacts generated by these winds. In this paper, empirical stochastic relationships are derived to describe two important parameters affecting the TC geometry: the radius of maximum winds (RMW) and the radius of gale-force winds ($\Delta$AR35). These relationships are formulated using best-track data (BTD) for all seven ocean basins (Atlantic; S, NW, and NE Pacific; and N, SW, and SE Indian oceans). This makes it possible to (a) estimate RMW and $\Delta$AR35 when these properties are not known and (b) generate improved parametric wind fields for all oceanic basins. Validation results show how the proposed relationships allow the TC geometry to be represented with higher accuracy than when using relationships available from the literature. Outer wind speeds can be reproduced well by the commonly used Holland wind profile when calibrated using information either from best-track data or from the proposed relationships. The scripts to compute the TC geometry and the outer wind speed are freely available.

## 2.1. INTRODUCTION

Tropical cyclones (TCs) are among the most destructive natural hazards worldwide. TCs can cause hazardous weather conditions including extreme rainfall and wind speeds, leading to coastal hazards, such as extreme storm surge levels and wave conditions. The impact of TCs is different in developed and developing countries. Generally, the worst effects in the developed world are direct economic losses. In the United States (U.S.) alone, the mean annual damage due to TCs was estimated by Willoughby, 2012 as $11.0 billion (based on the year 2015). In the developing world, TCs conflict with immense social costs in terms of destruction and mortality. For example, between 1960-2004 more than half a million inhabitants of Bangladesh died as a consequence of TCs, primarily due to storm surge. Additionally, TCs can also have devastating effects on nature, geomorphology, agriculture, and freshwater supply. Thus, due to the extensive costs in lives, property, and other damages, the ability to effectively model these storms is essential.

Numerical models can be applied to quantify the effects of TCs (Giardino et al., 2018b). In hindcasting studies, this is generally done by using surface winds derived by data assimilation techniques (e.g. HRD Real-time Hurricane Wind Analysis System or H*WIND; e.g., Powell et al., 1998). However, in multi-hazard risk assessments, the spatial distribution of surface winds is generally not known. Therefore, wind fields based on best track data (BTD) or synthetic tracks, are generated using parametric wind profiles. Several (horizontal) parametric wind profiles (e.g., Fujita, 1952, Willoughby et al., 2006, Chavas et al., 2015) exist in the literature, with the original Holland wind profile (Holland, 1980; hereafter H80) being the most widely used due to its relative simplicity. However, without calibration, parametric wind profiles are often unable to accurately reproduce the spatial distribution of winds in TCs (e.g., Willoughby et al., 2006). This potentially leads to an under- or overestimation of wind speeds and associated coastal hazards. Calibration of TC formulations is possible by applying additional relationships, supported by the use of suitable data. In particular, information on the wind radii of cyclones can constrain the decay of wind speeds away from the eye wall and can be included in the most recent version of the Holland wind profile formulation (Holland et al., 2010; hereafter H10).

The radius of maximum winds (RMW), which describes the distance from the center to the strongest axially symmetric wind in the core of the cyclone, is one of the most important parameters to define a parametric wind profile. Moreover, the RMW plays an important role in the assessment of hazards induced by TCs since the storm surge level increases as a function of the RMW (Loder et al., 2009). Several relationships exist in literature to estimate the RMW (e.g., Vickery and Wadhera, 2008, Knaff et al., 2015). However, these relationships are derived either for the Atlantic and/or Eastern Pacific Ocean (i.e. U.S. coast) and are therefore not necessarily valid for other ocean basins. Each ocean basin has its own climatological properties and, for example, there seems to be an observational relationship between (mean) storm size, in terms of precipitation area (Lin et al., 2015) or wind speeds (Chavas et al., 2016) and the relative sea surface temperature (SST). The reason that most relationships are derived for the U.S. coast is because of the high-quality data availability (i.e. aircraft reconnaissance data). Relationships that estimate wind radii at different wind speeds are scarcer. Knaff et al., 2007 explicitly describe the TC surface winds using a modified Rankine vortex, which makes it also possible to compute different wind radii corresponding to different wind speeds (i.e. 34, 50, 64, 100 knots). However, these results are derived from BTD of the Atlantic, Northeast Pacific, and Northwest Pacific Oceans.

In the last decades, a large amount of higher-quality data has become available which can be used to improve and validate the relationships and parametric wind profiles found in the literature. In addition to the RMW, the wind radii of 35 (or 34), 50, 65 (or 64), and 100 knots (hereafter referred to as R35, R50, R65, R100) for the four geographical quadrants around the cyclone are currently recorded (see also left panel of Figure 2.1). There are numerous sources that can provide information on the spatial distribution of surface winds ranging from in-situ observations (e.g. surface reports and buoy observations) to scatterometry (e.g., QuikSCAT, see Chavas and Vigh, 2014). Some methods are more reliable than others, but a posteriori it is not clear which sources were used for individual wind radii estimates in the best-track data (BTD). However, the currently operationally available satellite-based wind radii estimates are characterized by higher accuracy than in the past (Sampson et al., 2017).

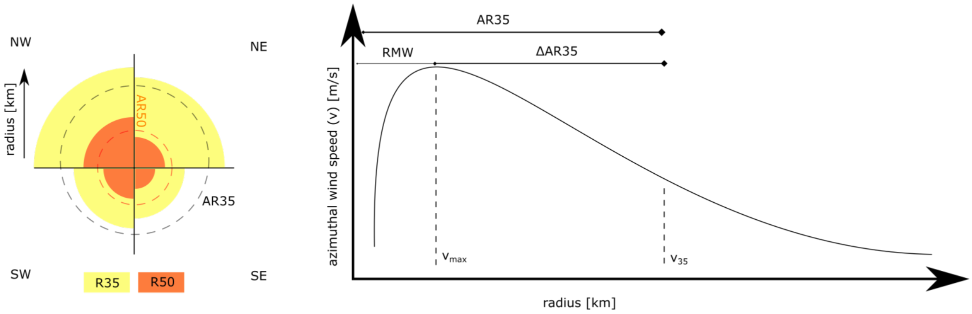

Figure 2.1: Sketch of the terminology used in this dissertation. Left panel difference in wind radii from different quadrants (NW, NE, SE, SW). Right panel difference in RMW, AR35 and ΔAR35

In this chapter, new relationships are proposed to estimate the median RMW and radius of gale-force winds (ΔAR35) for each ocean basin. In addition, the standard deviation of the TC geometry is described explicitly, making it possible to treat the TC geometry stochastically with a certain probability distribution. This means that TC geometry is a random variable whose possible values are an ensemble of different outcomes. This is useful when TC size is not known and the probability of a relatively large and/or small TC and consequent risks need to be assessed (e.g. in a Monte Carlo analysis with synthetic tracks). Moreover, the paper demonstrates how the proposed relationships lead to improved error statistics compared to those found in the literature. On top of that, validation with QSCAT-R shows that outer wind speeds can be well reproduced by a parametric wind profile while using the newly developed relationships or observed values for RMW and wind radii.

This Chapter is outlined as follows: Section 2.2 describes the data used for the study. The new relationships describing the radius of maximum winds and the radius of gale-force winds are derived in Section 2.3 and then validated in Section 2.3. Finally, Section 2.4 and 2.5 discuss and summarize the main conclusions of the study.

## 2.2. DATA UTILIZED FOR DERIVATION

### BEST TRACK DATA (BTD)

Two data sources were used to describe the RMW and R35: data from the North Atlantic and Northeast and North-Central Pacific data sets from the National Hurricane Center (NHC) and the data set from the Joint Typhoon Warning Center (JTWC). The second data set includes data from different ocean basins (the Northwest Pacific Ocean, the South Pacific Ocean, and the Indian Ocean). Note that the estimation of wind radii is rather subjective and strongly dependent on data availability as well as different climatology and analysis methods (e.g. aircraft observations versus the Dvorak method). In this chapter, all the available data were used and potential shortcomings in the data are disregarded in order to fit new empirical stochastic relationships with the largest possible data set and for every ocean basin separately. This approach, with its advantages and disadvantages, is discussed in Section 2.4. Some of the historical records do not contain values for either the RMW or R35 and therefore these records are discarded. Although these BTD are used as ground truth, the errors in the best-track wind radii are estimated to be as high as 10%–40% (e.g., Knaff and Sampson, 2015). The accuracy of a single record depends on the quality and quantity of the available observational data. For example, if in situ observations were available in proximity to the TC or if a complete scatterometer passed over the TC, the accuracy may increase. However, information on the accuracy is not available per single data entry.

The archives from the NHC and JTWC contain six-hourly storm positions and maximum intensity estimates of tropical and subtropical systems. For this analysis, all data points with a wind speed of 20 m/s or higher were included in the study, since the focus is on tropical storms. Moreover, it is expected that parametric wind profiles cannot capture subtropical systems. Also, data points with an RMW larger than 100 kilometers (km) were excluded from the analysis because, generally, those points refer to tropical depressions, with large spatial coverage, which are outside the scope of this study. Moreover, the averaged value of R35 ($\overline{R35}$ over the four quadrants, similarly to Carrasco et al., 2014) was used. Only data entries with an estimate of R35 for all four quadrants were used. Therefore, all data entries have both an estimate for RMW and R35. On top of that, using all the six-hourly storm positions and maximum intensity estimates in the calibration and validation assumes statistical independence. Lastly, the data used are not continuous but are highly discretized. In particular, wind speed intensities vary in 5 knots increments and wind radii have steps of 5 nm.

In this chapter, TC geometry variables RMW and R35 were treated as stochastic variables. This means that, although physically not realistic, RMW could assume larger values than R35. In order to overcome this, a new variable was defined: the average difference in radius of 35 knots (ΔAR35; similar to Xu and Wang, 2015), or radius of gale-force winds, describing the difference between the RMW and the average radius of 35 knots (AR35), see Equation 2.1. In practical applications, one would first retrieve the RMW based on data or estimate the RMW based on an empirical relationship. Secondly, the R35 would be calculated by adding up the RMW with the ΔAR35 (see also right panel of Figure 2.1). An additional advantage of introducing this new variable is that ΔAR35 contains considerably less scatter.

$$\Delta AR35 = AR35 - RMW \tag{2.1}$$

## QSCAT-R

The QuikSCAT-based QSCAT-R database (Chavas and Vigh, 2014), with data for the period 1999–2008, was used to validate the computed outer (azimuthal) winds using H10 wind profile and the new proposed empirical relationship. The data set, developed by researchers at the NASA Jet Propulsion Laboratory (JPL), is derived from the latest version of the QuikSCAT near-surface ocean wind vector database. It includes 690 unique TC profiles and it is optimized specifically for tropical cyclones with higher wind speeds. QuikSCAT measurements are accurate in all weather conditions for winds up to 40 m/s (Stiles et al., 2013), while their precision decreases for the inner wind speeds in the TC core (Hoffman and Leidner, 2005). Therefore, QSCAT-R data were only used to validate the outer wind speeds, and not the inner wind speeds or TC core. The tropical cyclone data set carries a 1-2 m/s positive bias and a 3 m/s mean absolute error, which is not further discussed or taken into account in the analysis.

### OCEAN BASINS

According to the WMO (World Meteorological Organization), areas of TC formation were divided into seven basins (Figure 2.2 - panel A). These include the North Atlantic Ocean (NAO), the Northwest Pacific Ocean (NWPO), the Northeast Pacific Ocean (NEPO), the South Pacific Ocean (SPO), the Southwest Indian Ocean (SWIO), the Southeast Indian Ocean (SWEI) and the North Indian Ocean (NIO). Other ocean basins (e.g. the South Atlantic Ocean) were not included in this study since weather systems in these areas rarely form a TC.

### DATA CONVERSION

Data were converted to International System of Units (SI) units (wind speeds in m/s from knots with a conversion of 1 knots = 0.514 m/s and wind radii in kilometers (km) from nautical mile with a conversion of 1 nm = 1.852 km). Throughout this chapter, a maximum cyclone sustained wind $v_{max}$ has been determined at a 10-m elevation over the open sea and a 1-minute average. The reason for this averaging is to be consistent with the JTWC and NHC which also reports the maximum sustained surface winds in terms of 1-minute mean wind speed. Other nations, however, report maximum sustained surface winds averaged over different time intervals, which in some cases is 10 minutes. Also, numerical models often require 10-minute averaged winds. For the conversion of 1-minute to 10-minute averaged wind speed, a conversion factor equal to 0.93 can be used, based on WMO guidelines (Harper et al., 2010). However, in this study, conversions between 1-minute and 10-minute wind speeds were not needed.

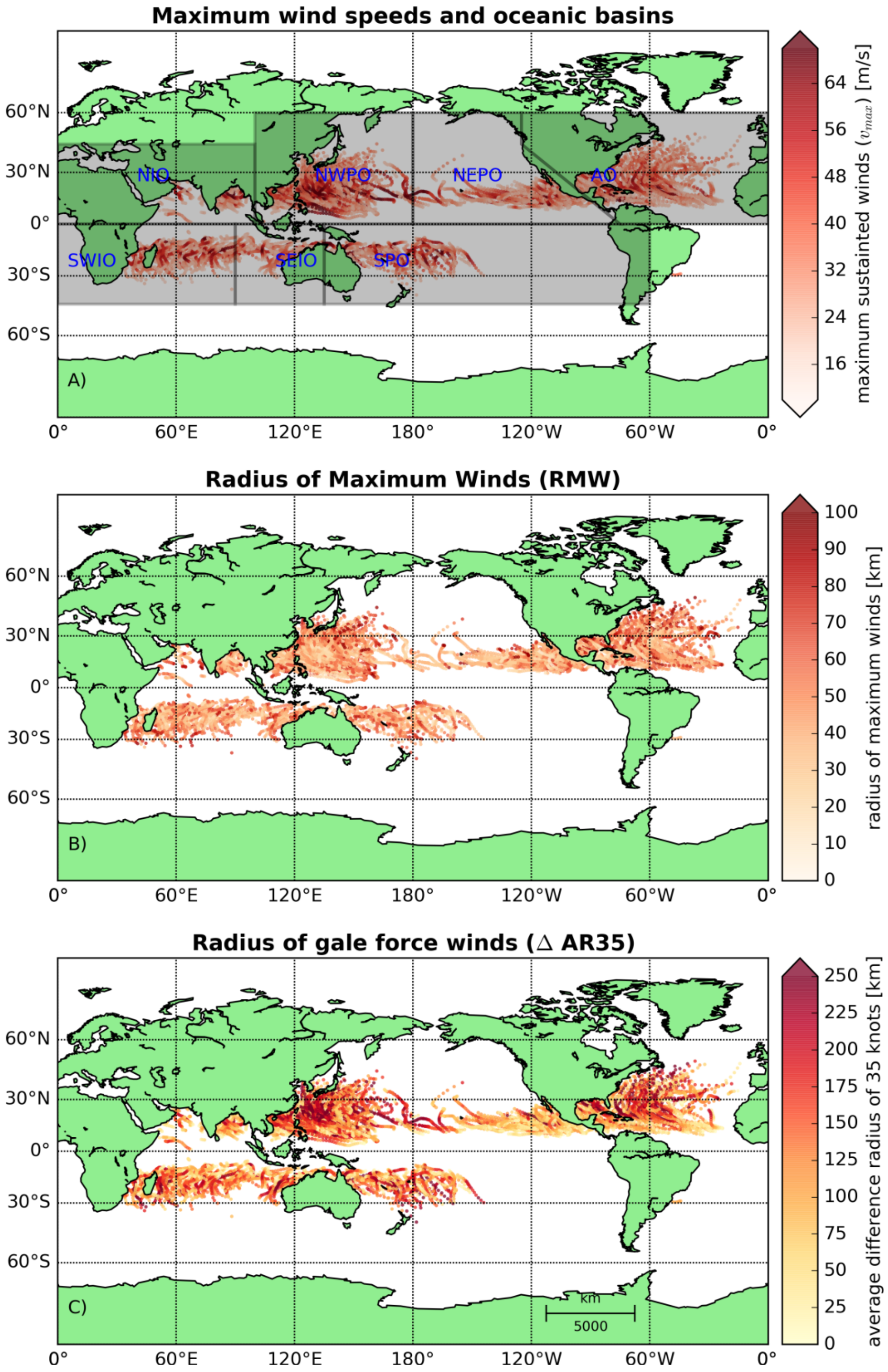

Maximum wind speeds and oceanic basins

Radius of Maximum Winds (RMW)

Radius of gale force winds (△ AR35)

Figure 2.2: Observed maximum sustained wind speeds and definition of the different ocean basins (a). The observed radius of maximum winds (b) and observed radius of gale-force winds (c) for all the BTD

## 2.3. RESULTS

### 2.3.1. DERIVATION OF NEW EMPIRICAL RELATIONSHIPS FOR WIND RADII

In this subsection, empirical relationships to estimate the radius of maximum winds (RMW; see Figure 2.2 - panel B) and the radius of gale-force winds (ΔAR35; see Figure 2.2 - panel C) were derived based on BTD from the calibration period (2000-2014).

RADIUS OF MAXIMUM WINDS (RMW) The Vickery and Wadhera, 2008 relationship, derived for all major hurricanes ($\Delta p_c$ > 30 hPa or $v_{max}$ >35 m/s) in the Gulf of Mexico and Atlantic Ocean (hereafter VW08), is one of the several relationships in literature providing an estimate of the RMW. VW08, derived based on H*WIND data, relates RMW to pressure drop in the eye and latitude. While we acknowledge the existence of several other relationships to estimate the RMW, VW08 was used due to its relative simplicity. Figure 3.3 compares RMW data from the BTD during the calibration period with results from VW08 in the form of a scatter plot with the maximum sustained wind speed ($v_{max}$) indicated by color intensity. The data shows a large amount of scatter, both for lower and higher RMW values. However, there is a clear pattern visible that larger maximum sustained wind speeds result in a smaller RMW. This is in line with other observations (e.g., Willoughby et al., 2006 or based upon idealized Sawyer Eliassen models (e.g., Schubert and Hack, 1982; Willoughby et al., 1982) that TC eyewalls generally contract during intensification. There is also a tendency in the data set for TCs at higher latitudes to have larger eye diameters (e.g., Knaff et al., 2015; not shown here). The large negative bias of 17 km, computed as a difference between observed and computed RMW is noteworthy, indicating that VW08 often underestimates the RMW, especially for lower maximum sustained wind speeds.

Given the large spread in the data, as also shown in Figure 3.3, it was decided to treat RMW as a stochastic variable. Instead of directly deriving an empirical equation that relates RMW to $v_{max}$ using a least-square fitting procedure as typically done in similar studies, the following approach was used. At first, parameters of a probability density function (PDF) that fits the variation of RMW for a range of $v_{max}$ and latitude values were fitted. Then empirical equations were derived that relate these parameters to $v_{max}$ and latitude. The benefit of this approach is that it can produce an estimate of the most probable value for RMW (i.e. mode) or median/mean as well as its variance (e.g. 90% prediction interval, PI).

First, the RMW for each TC category was fitted to various parent distributions. In particular, the following fitting parent distributions were tested by visual comparison and by applying the Kolmogorov-Smirnov test: normal, lognormal, Gumbel, Rayleigh, and gamma. The lognormal distribution was found to provide the best fit with the measured data, and therefore further used to describe the distribution of RMW. This is also consistent with the distribution used for describing ΔAR35 and findings in the literature (e.g. Dean et al., 2009). Secondly, the chosen parent distribution was used to fit the BTD in order to derive the shape ($\sigma$) and location parameter ($\mu$) of the lognormal distribution, dependent on latitude and wind speed. In particular, the BTD from the calibration period was divided based on a moving window with a bin of 10 m/s in wind speed and 10 degrees in latitude (0-10, 1-11, 2-12, etc.). A shape parameter was used with an exponential decay function, and fitting coefficients constant per each ocean basin. This resulted in Equation 2.2 for the $\mu$ parameter which, for a log-normal distribution, corresponds to the median value:

$$\mu_{RMW} = A_2 e^{v_{max}/B_2}(1 + C_2|\theta|) + D_2 \tag{2.2}$$

where $\mu RMW$ represents the location parameter of the lognormal distribution for RMW, $v_{max}$ is the maximum (1-minute averaged) wind speeds, $\theta$ is the latitude in degrees, and A2, B2, C2, and D2 are fitting coefficients.

As observed in the literature (e.g. Knaff et al., 2015), the median RMW ($\mu RMW$) in Equation 2.2 depends on $v_{max}$ (i.e. higher wind speeds result in lower RMW) and latitude (i.e. higher latitude result in higher RMW). The addition of storm duration or the use of the axisymmetric component of the wind speed only as input parameters resulted in very limited skill improvement in the estimation of RMW; therefore these variables were discarded. This procedure was applied to the combined JTWC and NHC BTD from the calibration period at all basins, and then for each individual ocean basin. Table 2.1 contains the shape and location values for the fitting parameters to be used in Equation 2.2.

A scatter plot describing the RMW derived from BTD as a function of the maximum wind speed and for (an arbitrarily chosen) latitude of 10 degrees and computed according to Equation 2.2, is shown in Figure 2.4. The green line shows the median RMW based on the BTD, whereas the solid blue line represents the mean RMW obtained from Equation 2.2. The black lines indicate the 5 and 95 percent exceedance values computed based on BTD. Finally, the 90% prediction interval is shown using the filled red color. The figure shows how the variance in RMW decreases (both in the data and in the empirical relationship) as a function of $v_{max}$, indicating that faster-rotating cyclones are characterized by less noise. The new empirical equation for RMW is evaluated in Section 2.3.2.

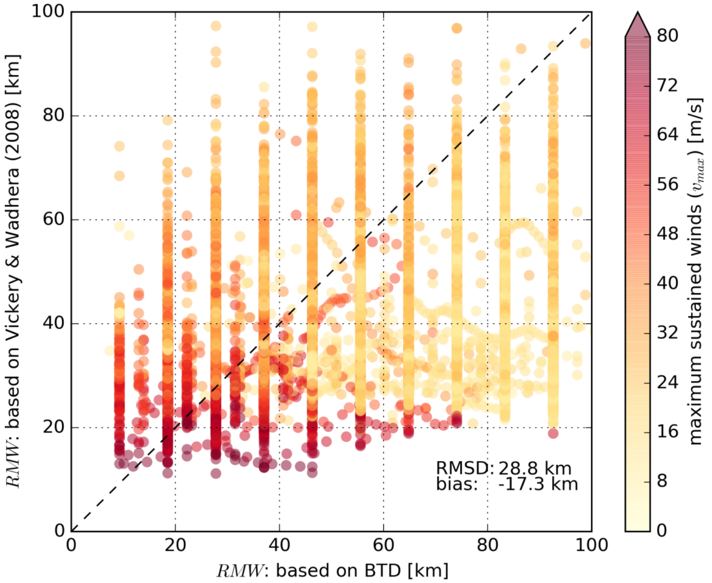

Figure 2.3: Scatter plot describing BTD RMW (x-axis) versus computed RMW based on VW08 (y-axis). Data points are colored-coded based on the maximum sustained wind speeds in the BTD. The dashed line represents a perfect fit between BTD and computed data based on VW08.

RADIUS OF GALE-FORCE WINDS ($\Delta$AR35) By applying a parametric wind profile, it is possible to derive the $\Delta$AR35. Here, the H10 wind profile was applied, in which the $B$ parameter was computed based on H80 (Equation 2.3), and in which information on the wind radii of cyclones was used to constrain the decay of wind speeds away from the eye wall (Equation 2.4). When no additional information on the wind radii

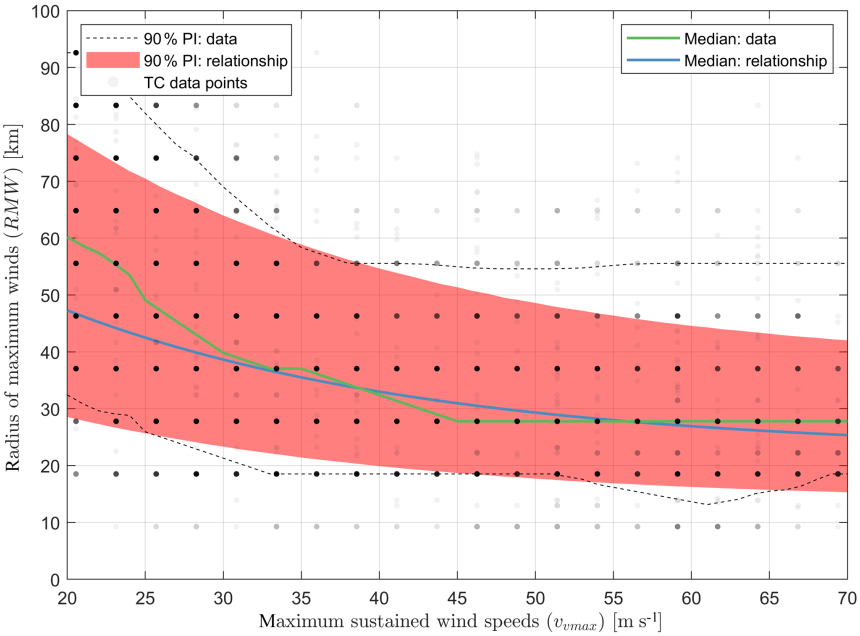

Figure 2.4: Scatter plot describing RMW (BTD and computed; y-axis) as a function of the maximum sustained wind speeds (x-axis; and the latitude; not shown). The blue line is the median of the proposed relationship derived for all basins at an arbitrarily chosen latitude of 10 degrees. The green line is the median of the BTD. The red area shows the 90% prediction interval (PI) based on the proposed relationship for all basins. The 5% and 95% exceedance values from the BTD are presented as black dashed lines. The gray dots are observation points in which more frequent observations are shown as darker points and less frequent observations as lighter points

Table 2.1: Fitting coefficients for the lognormal RMW as described in Equation 2.2

|  | Shape | Location ($\mu$) |  |  |  |  |
|---|---|---|---|---|---|---|
| Basin | ($\sigma$) | A2 | B2 | C2 | D2 | Count |
| NIO | 0.307 | 132.4 | 14.6 | −0.003 | 20.4 | 480 |
| SWIO | 0.338 | 229.2 | 9.5 | 0.004 | 28.4 | 1889 |
| SEIO | 0.343 | 85.3 | 30.7 | 0.002 | 5.8 | 832 |
| SPO | 0.364 | 127.8 | 11.8 | 0.016 | 25.5 | 1118 |
| NWPO | 0.359 | 153.7 | 11.5 | 0.007 | 28.9 | 4836 |
| NEPO | 0.311 | 261.5 | 7.0 | 0.026 | 29.2 | 2570 |
| AO | 0.395 | 19.1 | 24.1 | 0.106 | 23.2 | 3075 |
| All | 0.370 | 44.8 | 23.4 | 0.030 | 22.4 | 14800 |

is provided, H10 reduces to the original H80 wind profile, which is often unable to accurately reproduce the spatial distribution of winds in TCs (e.g., Willoughby and Rahn, 2004).

$$B = \frac{v_{\max}^2 \rho_a e}{100(\Delta p_c)} \tag{2.3}$$

$$x = 0.5 + \frac{x_n - 0.5}{r_n - \mathrm{RMW}} \tag{2.4}$$

Here, $B$ represents the Holland pressure profile parameter, $\rho_a$ is the air density (assumed constant at $1.15\,\mathrm{kg\,m^{-3}}$), $e$ is the base of natural logarithms, $\Delta p_c$ is the pressure drop in the core of the TC in hectopascals, $x$ is the exponent used to compute the wind profile in H80–H10 and $x_n$ represents the adjusted exponent to fit the peripheral observations at radius $r_n$.

Knaff et al., 2007 relationships (hereafter CLIPER, climatology, and persistence models), derived for the NAO, NWPO and NEPO, are among the few in literature providing an estimate of the TC surface winds. Knaff et al., 2007 fitted a modified Rankine vortex on the BTD of NHC and JTWC, which also makes it possible to retrieve the ΔAR35. Figure 2.5 compares ΔAR35 from the BTD, derived from the calibration period, with results from CLIPER, in which $v_{\max}$ is indicated by the color intensity in the scatter plot.

In order to improve the estimate of the ΔAR35, generic relations were derived as part of this study based on BTD from the calibration period from all ocean basins, as well as data from each individual basin separately. The method followed is similar to the one applied to estimate RMW. First, a representative parent distribution of the data was sought, secondly, the parameters of the PDF were determined, and thirdly the parameters of the PDF were fitted for a range of $v_{\max}$ and latitude values. The same parent distributions were tested and the lognormal distribution was again chosen as the most representative, which aligns with Chavas et al., 2016.

Similarly to RMW, the BTD from the calibration period was divided based on a moving window with a bin width of $10\,\mathrm{m\,s^{-1}}$ for wind speed (0–10, 1–11, 2–12,

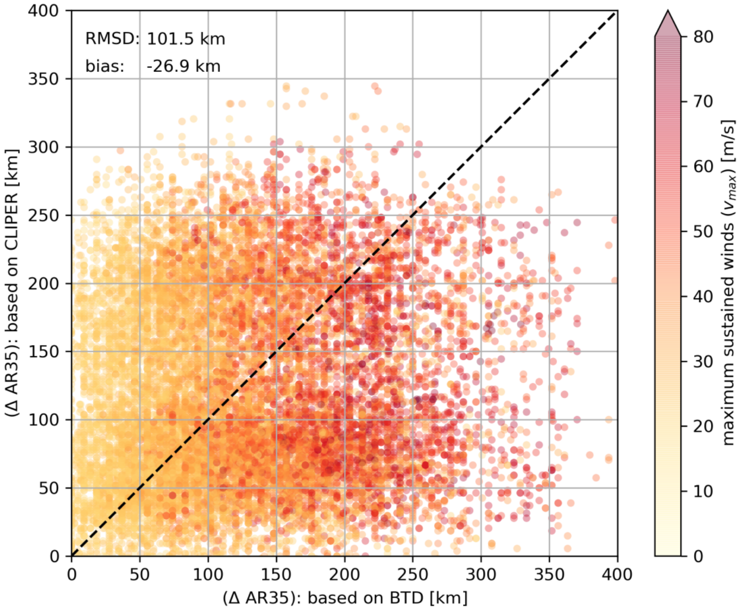

Figure 2.5: Scatter plot describing BTD ΔAR35 ($x$ axis) versus computed ΔAR35 based on CLIPER ($y$ axis). Data points are colored-coded based on the maximum sustained wind speeds in the BTD. The dashed line represents a perfect fit between the BTD and the computed data based on CLIPER.

etc.) and 10° for latitude. This led to Equations Equations 2.5 and 2.6 in which exponential functions, dependent on the wind speed per oceanic basin, were used to describe the location parameter and the shape parameter. Additionally, the analysis of the data showed that ΔAR35 is dependent on the latitude, with TCs generally increasing in size at higher latitudes. Adding additional parameters (e.g. storm duration or intensity change of the wind speed) resulted in very limited skill improvement for the estimate of ΔAR35. This procedure was applied to both the combined JTWC and NHC BTD from the calibration period of all basins and for each individual ocean basin. Table 2.2 contains the values for the fitting parameters for the ΔAR35 of Equations 2.5 and 2.6.

$$\sigma_{\Delta AR35} = A_3 + e^{v_{\max}\cdot B_3} \cdot (1 + C_3|\theta|) \tag{2.5}$$

$$\mu_{\Delta AR35} = A_4 \cdot (v_{\max} - 18)^{B_4} \cdot (1 + C_4|\theta|) \tag{2.6}$$

Here, $\mu_{\Delta AR35}$ and $\sigma_{\Delta AR35}$ represent, respectively, the location and shape parameter of the lognormal distribution for ΔAR35, and $A_3$, $A_4$, $B_3$, $B_4$, $C_3$, and $C_4$ are fitting coefficients.

Table 2.2: Fitting coefficients for the lognormal ΔAR35 as described in Equations 2.5 and 2.6.

| | Shape ($\sigma$) | | | Location ($\mu$) | | | |
|---|---|---|---|---|---|---|---|
| Basin | $A_3$ | $B_3$ | $C_3$ | $A_4$ | $B_4$ | $C_4$ | Count |
| NIO | 0.1215 | −0.0522 | 0.0329 | 30.93 | 0.531 | −0.012 | 480 |
| SWIO | 0.1312 | −0.0444 | 0.0023 | 30.21 | 0.415 | 0.022 | 1889 |
| SEIO | 0.1223 | −0.0454 | 0.0133 | 26.59 | 0.426 | 0.029 | 832 |
| SPO | 0.1205 | −0.0350 | −0.0052 | 23.88 | 0.431 | 0.038 | 1118 |
| NWPO | 0.1561 | −0.0417 | 0.0050 | 33.27 | 0.429 | 0.017 | 4836 |
| NEPO | −0.2513 | −0.0091 | −0.0051 | 18.11 | 0.486 | 0.030 | 2570 |

A scatter plot describing the $\Delta AR35$ derived from BTD as a function of the $v_{\max}$ and latitude and computed according to Equations 2.5 and 2.6 is shown in Figure 2.6. The green line shows the median $\Delta AR35$ based on the BTD, whereas the solid blue line represents the mean $\Delta AR35$ obtained from Equations 2.5 and 2.6. The black lines indicate the 5% and 95% exceedance values computed based on BTD. Finally, the 90% prediction interval is shown using a filled red color. The figure shows how the median $\Delta AR35$ increases as a function of $v_{\max}$ while the variance stays fairly constant. The new empirical equation for $\Delta AR35$ is evaluated in the next section.

### 2.3.2. VALIDATION OF WIND RADII AND COMPUTED AZIMUTHAL WIND SPEEDS

In this subsection, empirical relationships to estimate the RMW and ΔAR35 were validated based on BTD from the validation period (2015–2017). Moreover, the outer wind profile based on the Holland wind profile, in combination with observed wind radii, was further validated using the QSCAT-R database.

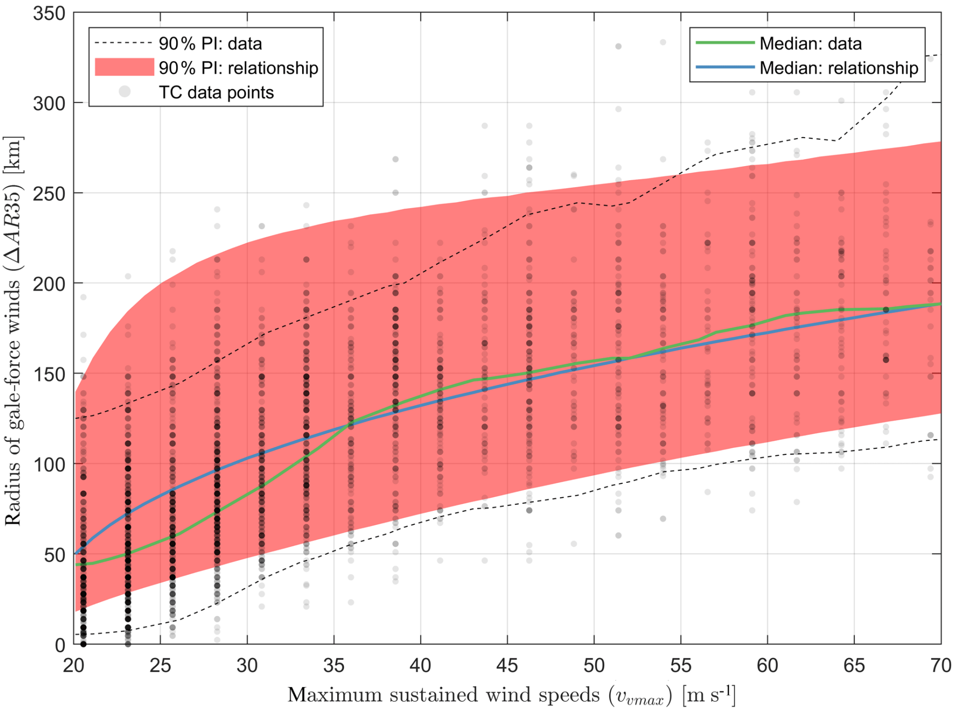

Figure 2.6: Scatter plot describing $\Delta AR35$ (BTD and computed, $y$ axis) as a function of the maximum sustained wind speeds ($x$ axis; and the latitude; not shown). The blue line is the median of the proposed relationship derived for all basins at an arbitrarily chosen latitude of 10°. The green line is the median of the BTD. The red area shows the 90% prediction interval based on the proposed relationship for the standard deviation. The 5% and 95% exceedance values from the BTD are presented as black solid lines. The gray dots are observation points in which more frequent observations are shown as darker points and less frequent observations as lighter points.

WIND RADII A subset of the BTD (from 2015 to 2017) was used to validate the wind radii. Error statistics are summarized in Table 2.3. The values indicate that, for all basins combined, the RMSD between the BTD and the proposed relations for the RMW is 17% lower than compared to VW08 (RMSD of 18 km compared to 21 km). In the NEPO basin, VW08 performs relatively better than in other basins. When comparing the performance of the proposed relations and VW08, it is important to note that the relation of VW08 was derived for storms with central pressures lower than 980 hPa, thereby explicitly focusing on the most severe TCs. When the data were filtered to include only data points with a pressure drop $\Delta p_c$ larger than 30 hPa, the RMSD decreased and differences became much smaller (0%–10% decrease in RMSD). Moreover, the bias also decreases.

Table 2.3: Root-mean-square difference (RMSE; first number), bias (second number), and scatter index (SCI; third number) for RMW in kilometers for the validation period for both the proposed relationships as for VW08. Statistics are presented for all data points, as well for data points with a pressure drop ($\Delta p_c$) larger than 30 hPa.

| Basin | Proposed | | VW08 | |
|---|---|---|---|---|
| | all | $\Delta p_c > 30$ | all | $\Delta p_c > 30$ |
| NIO | 20.9/-14.2/0.39 | 25.3/-17.7/0.47 | 14.0/-4.5/0.43 | 14.1/-2.5/0.43 |
| SWIO | 16.8/-7.0/0.35 | 20.0/-8.6/0.41 | 10.4/-0.2/0.34 | 9.8/0.3/0.32 |
| SEIO | 17.9/-10.7/0.35 | 24.0/-14.0/0.47 | 9.6/-1.6/0.35 | 10.9/4.9/0.40 |
| SPO | 18.1/-9.1/0.37 | 22.1/-10.1/0.46 | 12.9/-3.0/0.39 | 12.7/1.5/0.39 |
| NWPO | 17.2/-6.4/0.36 | 22.4/-5.5/0.46 | 12.1/-0.3/0.37 | 14.7/4.6/0.45 |
| NEPO | 16.9/-8.4/0.38 | 17.5/-6.7/0.39 | 13.1/-4.8/0.39 | 11.6/-1.2/0.34 |
| AO | 21.0/-8.7/0.41 | 21.5/-0.8/0.42 | 17.2/-4.1/0.43 | 18.2/8.1/0.45 |
| All | 18.0 /-7.1/0.37 | 21.0/-6.5/0.44 | 13.1/-1.6/0.39 | 14.2/3.3/0.42 |

Table 2.4 shows the error statistics related to the estimation of $\Delta$AR35. In particular, the RMSD between the proposed relations and the BTD for all basins combined is 25% lower compared to CLIPER (RMSD of 74 km compared to 94 km) and there is a negative bias ranging between 9 and 37 km. Remarkably, the deviations of the $\Delta$AR35 based on BTD in the NIO and SEIO from CLIPER are significantly smaller compared to the differences for the AO for which CLIPER was derived. When the H10 wind profile is applied without additional information to compute the decay of wind speeds away from the eye wall (H80), the $\Delta$AR35 is strongly overestimated (overall bias of 177 km).

Table 2.4: Root-mean-square difference (RMSE; first number), bias (second number), and scatter index (SCI; third number) for $\Delta$AR35 in kilometers for the validation period for the proposed relationships, CLIPER (Knaff et al., 2015 and the H80 wind profile.

| Basin | Proposed | CLIPER | H80 | Count |
|---|---|---|---|---|
| NIO | 48.0/−17.5/0.43 | 51.0/+3.3/0.45 | 275.2/221.9/2.45 | 146 |
| SWIO | 68.9/−31.4/0.43 | 123.1/−95.3/0.76 | 248.4/190.9/1.54 | 365 |
| SEIO | 37.2/−9.0/0.33 | 69.0/−58.3/0.61 | 238.8/187.7/2.12 | 107 |
| SPO | 59.6/−16.3/0.41 | 104/−74.7/0.71 | 267.2/214.1/1.83 | 424 |
| NWPO | 83.8/−37.3/0.44 | 95.0/−25.6/0.50 | 294.2/198.8/1.55 | 1389 |
| NEPO | 47.4/−10.3/0.40 | 86.4/+68.7/0.73 | 125.4/59.3/1.06 | 1031 |
| AO | 90.0/−16.3/0.49 | 116.8/+7.1/0.64 | 552.7/252.4.1/3.02 | 424 |
| All | 74.1/−37.3/0.45 | 94.2/−13.9/0.58 | 316.8/177.0/1.94 | 1389 |

**OUTER WIND SPEEDS** The QSCAT-R database was used to validate the computed (outer) azimuthal wind speeds while using the H10 wind profile in combination with several sources to constrain the decay of wind speeds. QuikSCAT includes 690 unique tropical cyclones and is known to provide reliable results for outer wind speeds of lower intensity. Figure 2.6 displays the error profile, representing the difference between modeled wind speed and measured data based on QuikSCAT, as a function of the normalized radius. This means that for all validated TCs the radius on the *x* axis is divided by the RMW. A horizontal line equal to zero indicates no difference between modeled and measured wind speed data, while the solid-colored lines represent the median difference. The filled area indicates the interquartile range (IQR).

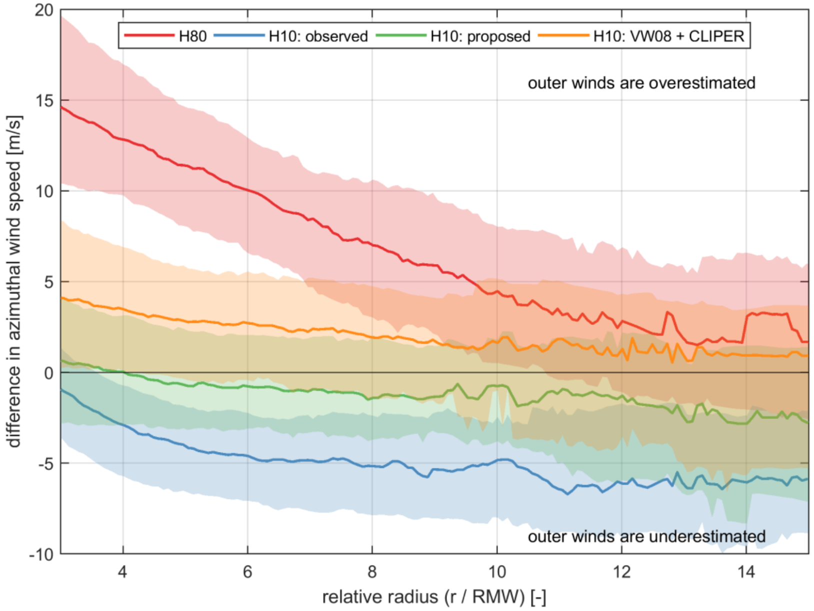

Figure 2.7: Wind speed error (observed QSCAT-R minus modeled) profiles for different models as a function of relative TC radius ($r/\mathrm{RMW}$). A value equal to zero on the *y* axis indicates a perfect match between model and observations. Interquartile ranges are shown with shaded colors and the solid line represents the median. Note: for the proposed relationships the most probable value for RMW and AR35 was used (i.e., mode).

The figure shows that in combination with the H10 wind profile, the proposed relationships result in the smallest difference with respect to the measured wind speeds (green line). However, applying the H10 wind profile with observed values for the wind radii (i.e., based on BTD values) results in an underestimation of the modeled outer winds (blue line). On the other hand, applying the H10 wind profile, without additional information on the gale-force winds (H80), results in a strong overestimation of the outer winds (red line). Similarly, a combination of other existing relationships for RMW (VW08) and ΔAR35 (CLIPER) results in an overestimation of the outer winds but to a lesser degree (orange line).

The same information is also shown in Table 2.5, where the root-mean-square differences and bias between modeled wind speeds and measurements are summarized. Using the proposed relationship with the H10 wind profile results in the lowest RMSD and smallest bias.

Table 2.5: Root-mean-square difference (RMSD) and bias (m/s) between modeled and measured azimuthally averaged wind speeds based on QSCAT-R data. The data analyzed in the table refer to all TCs with wind speeds between 40 and 5 m/s and a normalized radius between 3 and 16. Statistics are shown for median values (50%) and the IQR range (25%–75%). With "H10: observed" the authors refer to the Holland et al., 2010 wind profile in combination with the RMW and AR35 from the BTD.

| Wind profiles | RMSD | | | Bias | | |
|---|---|---|---|---|---|---|
| | median (50%) | low (25%) | high (75%) | median (50%) | low (25%) | high (75%) |
| H80 | 11.24 | 8.32 | 14.57 | 10.98 | 7.89 | 14.34 |
| H10: observed (BTD) | 5.46 | 3.85 | 7.04 | -4.67 | -6.32 | -2.6 |
| H10: VW08 + CLIPER | 3.60 | 2.06 | 5.76 | 1.64 | -1.27 | 4.16 |
| H10: proposed | 2.86 | 1.71 | 4.51 | -1.04 | -3.3 | 1.39 |

## 2.4. DISCUSSION

For clarity, discussion points have been grouped under three main topics, which are as follows.

### DATA

In this study, all available BTD from NHC and JTWC were used and combined into one data set. This approach was followed to create the largest sample size possible, in order to derive empirical (stochastic) relationships valid for each ocean basin, various latitudes, different TC geometries and strengths. This approach is limited by the debatable assumption that each 6-hourly data point is statistically independent. Moreover, errors in the BTD can be quite significant, so previous studies (e.g., Holland, 2008) selected a specific subset of the BTD in order to ensure the quality of the data and remove potential inconsistencies. However, the advantage of including all data entries is that the derived relationships are more widely applicable (i.e., larger parameter space). Moreover, as they are based on larger data sets, it is possible to treat TC geometry variables using a stochastic rather than a deterministic approach.

## METHODOLOGY

In order to derive the new empirical relationship for RMW and ΔAR35, the maximum sustained wind speed and latitude were used. Although other authors used additional parameters to describe the TC geometry (e.g. pressure drop, storm duration, rapid intensification), limited predictive skill improvement was found by incorporating those additional parameters. This makes the derived relationships relatively simple for practical applications. Moreover, lognormal statistical distributions in combination with exponential functions were used to fit all available data and derive those relationships. For our application, exponentially shaped functions resulted in the best fit compared to the available data. The choice of lognormal statistical distributions was based on a comparison of the different cumulative distribution functions (CDFs) derived using different distributions and the Kolmogorov–Smirnov test and supported by findings from literature (e.g., Dean et al., 2009; Chavas et al., 2016. However, different statistical distributions and functions are available in the literature to fit and describe TC geometry data. The strength of using statistical distributions to derive these relationships is that TC geometry is treated stochastically, therefore providing not only mean and median values but also prediction intervals. This is especially of importance when the TC geometry is not known (e.g. for older BTD and/or Monte Carlo analysis with synthetic tracks) with numerical models. Another possibility would be the derivation of wind speed probability estimates. A possibility to further improve these relationships would be to use machine learning techniques such as Bayesian neural networks to estimate TC geometry parameters when enough data are available (via either additional observations or surrogate data derived by numerical models).

## DIFFERENCES IN MEASURED AND MODELED OUTER WIND PROFILES

QuikSCAT data were used to validate the (outer) azimuthal wind speeds derived using the new empirical relationships in combination with the H10 wind profile. The analysis has shown how the proposed relationships in combination with the H10 wind profile result in the lowest RMSD and smallest bias for the outer winds, compared to other existing relationships (see Figure 2.6). This gives confidence that parametric wind models can be used to compute the outer wind speeds. This is of particular importance for the estimation of coastal hazards (i.e., storm surge and wave heights).

However, differences were also found for individual TCs, where the Holland wind profile in combination with the empirical relationships derived in this paper did not result in a good reproduction of the outer wind speeds. As an example, panel A of Figure 2.8 shows computed and measured wind speeds for TC Vaianu (2006), which was characterized by an extremely large radius of gale-force wind (R35 equal to 292 km ≈ 10% probability of exceedance). Measured values are shown in Figure 2.8 by the black circles. When applying the proposed relationships to compute the most probable values of the wind radii (red line), an R35 value equal to 162 km is obtained, resulting in an overall underestimation of the measured outer wind speeds. Also, when using the observed wind radii information (blue line), TC outer winds are not well reproduced, which shows that even with the correct wind radii value, parametric wind models can have the wrong shape. This approach is also limited when measured wind speeds cannot be represented by an exponential decay, as is assumed by the Holland wind profile. For example, TCs characterized by two wind maxima cannot be reproduced by an exponential decay of wind speed (Figure 2.8 - panel B). However, the Holland wind profile is widely used due to its relative simplicity and does, most of the time (80% of the TCs are reproduced with an RMSE of less than 5 $m\ s^{-1}$), reproduce the decay of wind speed fairly well as shown in the evaluation of 690 unique TCs in Figure 2.6).

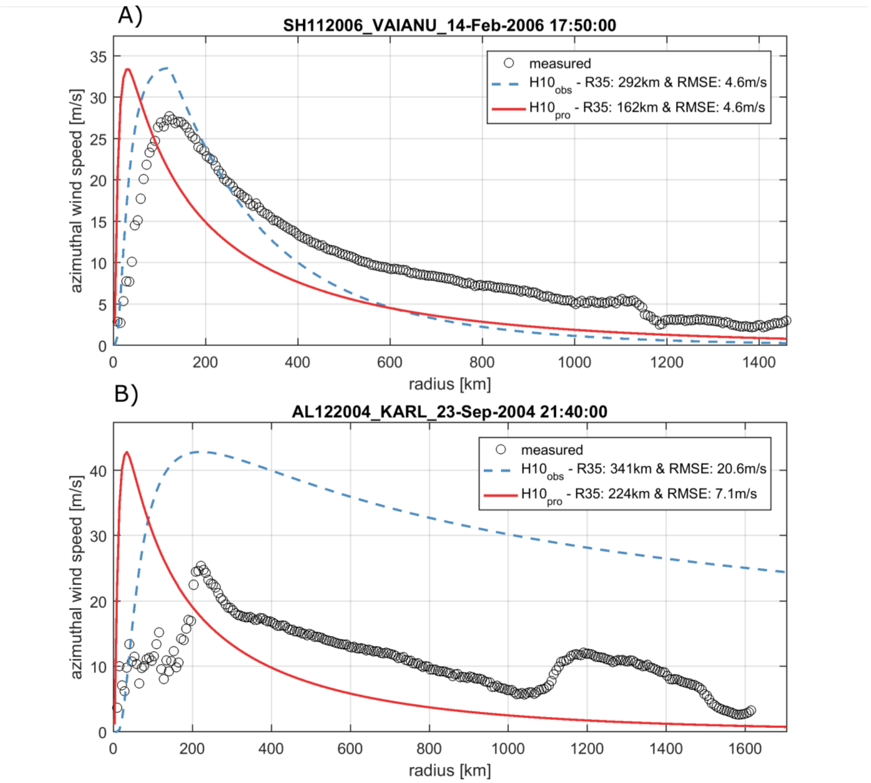

Figure 2.8: Radial wind profiles for measured wind speeds (black circles), computed wind speeds based on relationships for wind radii (red lines) and computed based on observed wind radii for tropical cyclones Vaianu (14 February 2006) (a) and Karl (23 September 2004) (b). Measured data are based on QSCAT-R data, while computed values are based on the H10 wind profile calibrated with the relationships proposed in this paper (red line) or observed data (blue line). Panels (a) and (b) are examples indicating when a difference between measured wind speeds and TC size can be encountered.

## 2.5. CONCLUSION

In this chapter, new empirical relationships are derived that estimate tropical cyclone (TC) geometry with simple and generic equations and with higher accuracy with respect to other well-known empirical relationships available from the literature. Those new relationships are valid for any ocean basin (Atlantic; S, NW, and NE Pacific; N, SE, and SW Indian oceans). Moreover, the new relationships include a stochastic description for both the radius of maximum winds (RMW) and the radius of gale-force winds (ΔAR35). This allows the quantification of the prediction interval around the median estimates, making the estimation more useful.

According to the derived relationships, the RMW is described as a function of the maximum sustained wind speeds and latitude. The radius of gale-force winds is estimated using a newly introduced ΔAR35 parameter (average difference between a radius of 35 knots and a radius of maximum wind) and is also dependent on the maximum sustained winds and latitude. Both parameters are fit through simple exponential functions. Compared to best-track data, the proposed relationships improve the estimation of RMW and ΔAR35 by reducing the root-mean-square difference (RMSD) up to 25%. Larger improvements were found in particular for non-US TCs since most of the existing relationships are based on data from the Atlantic Ocean, northeastern Pacific Ocean, and/or northwestern Pacific Ocean.

The new relationships, in combination with the Holland wind profile, were validated using a subset of the BTD and (outer) azimuthal wind speeds from the QSCAT-R database. The results showed that (outer) azimuthal wind speeds of the TC can be reproduced with the H10 wind profile when using either the BTD (“observed”) for RMW and ΔAR35 or the relationships derived in this paper. When no additional information on wind radii was used to calibrate the H10 wind profile, which is generally done when the radius of gale-force wind is not known, surface wind speeds were overestimated.

The derived empirical relationships can be used in a variety of applications. For example, a better estimate of TC pressure and surface wind speeds for Monte Carlo analysis with synthetic tracks for risk assessments with numerical models can result in a more accurate description of wave and surge conditions resulting from the TC. As a result, this can lead to a better quantification of coastal hazards, and consequent risks and damages. Similarly, an improved assessment of those hazards can help the design of appropriate adaptation measures. Other fields of application may vary from improved design parameters for offshore structures to navigation. The application of the new empirical relationships is presented in Nederhoff et al., 2021a.

# 3

# GENERATION OF SYNTHETIC TROPICAL CYCLONES FOR STRATEGIC RISK ANALYSIS

*The results of Chapter 2 revealed that empirical stochastic relationships make it possible to estimate tropical cyclone geometry when this is not known. These parameters are paramount to generating accurate parametric wind fields for strategic and operational risk analysis. Nonetheless, strategic risk analysis is often hindered by an insufficient amount of historical tracks for a reliable analysis. In this chapter, we introduce a methodology that focuses on computer-generated pathways that hypothetical storms might follow. These synthetic tropical cyclone tracks are created based on analyzing data and patterns from historical real-world cyclone tracks. The focus of this chapter is to introduce and validate a new methodology called the Tropical Cyclone Wind Statistical Estimation Tool (TCWiSE) that can be used for strategic risk analysis.*

---

This chapter is a revised version of **Nederhoff**, **K.**, Hoek, J., Leijnse, T., van Ormondt, M., Caires, S., & Giardino, A. (2020). Simulating Synthetic Tropical Cyclone Tracks for Statistically Reliable Wind and Pressure Estimations. *Natural Hazards and Earth System Sciences Discussions, 2020,* 1–30.

**Abstract** The design of coastal protection measures and the quantification of coastal risks at locations affected by tropical cyclones (TCs) are often based solely on the analysis of historical cyclone tracks. Due to data scarcity and the random nature of TCs, the assumption that a hypothetical TC could hit a neighboring area with equal likelihood to past events can potentially lead to over- and/or underestimations of extremes and associated risks. The simulation of numerous synthetic TC tracks based on (historical) data can overcome this limitation. In this paper, a new method for the generation of synthetic TC tracks is proposed. The method has been implemented in the highly flexible open-source Tropical Cyclone Wind Statistical Estimation Tool (TCWiSE). TCWiSE uses an empirical track model based on Markov chains and can simulate thousands of synthetic TC tracks and wind fields in any oceanic basin based on any (historical) data source. Moreover, the tool can be used to determine the wind extremes, and the output can be used for the reliable assessment of coastal hazards. Validation results for the Gulf of Mexico show that TC patterns and extreme wind speeds are well reproduced by TCWiSE.

## 3.1. INTRODUCTION

Tropical cyclones (TCs) are among the most destructive natural disasters worldwide. TCs can cause hazardous weather conditions including extreme rainfall and wind speeds, leading to coastal hazards such as extreme storm surge levels and wave conditions. In assessing the impacts of these hazards and consequent risks, the spatial distribution of surface winds is needed. Past observed best-track data (BTD) can be used to reliably reproduce spatially varying wind conditions during individual TCs using parametric models (e.g., Nederhoff et al., 2019) and consequent hazards (e.g., Giardino et al., 2018b). For TCs, one often refers either to the first-order hazards due to the TC (e.g. maximum wind speed) or to second-order effects (e.g. storm surge levels and wave heights). This is required, for example, to define design conditions for coastal protection measures or to quantify coastal risks. Extreme value theory is concerned with the distribution of rare events, rather than usual occurrences.

A wide range of such statistical methods exist, all of which rely on the use of numerous observational points to derive reliable extreme values. When the data set covers the return period of the event, the extreme value estimation can be based directly on historical values (i.e., non-parametric). However, for the estimation of extremes associated with longer return periods, one must resort to fitting a statistical distribution to the data (i.e., parametric). The simplest technique is to fit either a Gumbel distribution with two parameters (location and scale) under certain assumptions or a generalized extreme value (GEV) to a time series of annual maxima (e.g., Coles, 2001). Other methods make better use of the available data, for example, via a peaks-over-threshold (POT) approach to identify all extremes within a year and to fit the generalized Pareto distribution (GPD) to them (Caires, 2016).

Worldwide the length of TC track records varies from approximately 50 years (from the 1970s onward) to more than 150 years in the Gulf of Mexico (GoM), with arguably increasing accuracy for more recent observations compared to very old data. Thus, depending on the region, the number (and accuracy) of events recorded in the direct vicinity of a location varies significantly. Furthermore, in certain regions, the frequency of occurrence is also very low, making the sample size of historical events very limited. Only using a handful of observed TCs in recent history has severe limitations when estimating extreme wind, storm surge, and wave conditions for rare (e.g. 1000-year) return periods, since individual storms will start to affect the derived extremes. In particular, biases (both over- and underestimations) will emerge due to sampling errors.

To overcome this data scarcity problem, one potential approach is to generate synthetic TC tracks, which increase the amount of data by introducing cyclones that could potentially occur. Two different types of models are available for the generation of synthetic tropical cyclones: the simple track model (STM) and the empirical track model (ETM). STM (e.g., Vickery and Twisdale, 1995) was the first method developed to generate synthetic cyclones. The basic idea is that specific observed TC characteristics (e.g. wind speed, central pressure deficit, the radius of maximum winds (RMW), heading (the direction in which the TC is propagating in degrees), translation speed, coast-crossing position) are obtained and used to construct probability density functions. Next, these characteristics are sampled from their distributions using Monte Carlo simulations and passed along a track that does not vary, ensuring that TC characteristics are kept constant along the track. The downside of this method is that it is very site-specific as all parameters are gathered for a single area or coastline. ETM is, in principle, the evolution of STM (e.g., Vickery et al., 2000). It uses the same technique of gathering the statistics and then sampling them, utilizing Monte Carlo simulations. Instead of sampling all parameters once, the variables can change in their characteristics every time step along the track.

In the recent literature, several synthetic TC databases and/or methods have been published. Vickery et al., 2000 used statistical properties of historical tracks and intensities to generate a large number of synthetic storms in the North Atlantic (NA) basin. Six-hour changes in TC properties were modeled as linear functions of previous values of those quantities as well as position and sea surface temperature. James and Mason, 2005 applied a similar, yet slightly simpler and less data-intensive, approach since the focus was on synthetic TCs affecting the Queensland coast of northeastern Australia, where fewer data were available compared to the NA basin. Arthur, 2019 used a fairly similar approach to James and Mason, 2005 but instead focused on the entire continent of Australia, included the fitting of extreme value distributions, and made the code open-source. Vickery et al., 2009 added a second step in the TC generation by including thermodynamic and atmospheric environmental variables such as sea surface temperature, tropopause temperature, and vertical wind shear. Emanuel et al., 2006 also used the ETM; however, for the generation of the synthetic tracks they applied Markov chains (e.g., Brzeźniak and Zastawniak, 2000) with kernel density estimates (KDEs) conditioned on a prior state, time, and position, instead of using a linear function. Bloemendaal et al., 2020 developed a synthetic TC database on a global scale following the principles outlined in James and Mason, 2005. Other approaches (e.g., Lee et al., 2018) are less data-intensive but more environmentally forced.

While there are numerous methods and tools available to generate synthetic TCs, most of them were developed with a very specific focus in mind and therefore may not be suitable to use for other areas in the world or different utilizations. Moreover, none of these methods are yet available open-source for review by other peers, and all these methods are focused purely on the generation of the track itself. For example, for coastal engineering or risk-based applications, the possibility to easily link the track to other processes (e.g., generation of wind profiles, rainfall, hazard modeling) could offer a wide range of opportunities for different utilizations.

In this chapter, a new method for the generation of synthetic cyclone tracks and wind fields is described. The method has been implemented in a new tool to compute synthetic TC tracks, based on the ETM method, for any oceanic basin in the world. This new tool, named TCWiSE (Tropical Cyclone Wind Statistical Estimation Tool), has been made publicly free and open-source via https://www.deltares.nl/en/software/tcwise/. The tool is set up as a Markov model where (historical) meteorological data serve as a source to compute synthetic tracks. Additionally, TCWiSE can create meteorological forcings for further use in different hazard models (e.g. surface wind fields, TC-induced rainfall), including the possibility of assessing current and future climate variability.

TCWiSE has been developed in an attempt to give users flexibility in their choices. For example, while a comprehensive historical TC database is already included in IBTrACS (International Best Track Archive for Climate Stewardship; Knapp et al., 2010), the tool offers the option to choose from different sources within this data set. Additionally, variables like the resolution of KDEs and internal parameters can be optimized if desired. Also, it is possible to choose among several wind profiles to create temporally and spatially varying wind fields. This approach makes it feasible to calibrate parameters in TCWiSE that arguably vary from case study to case study. TCWiSE has been successfully applied in several studies prior to this publication (e.g., Deltares, 2017; Hoek, 2017; Bader, 2019). In general, the whole tool is data-driven, but, due to the usage of Markov chains and KDEs, variability within the data set can also be explored (i.e., combinations of statistically plausible parameters that have not occurred historically).

This Chapter is outlined as follows: Section 3.2 describes the method and code structure of TCWiSE. Section 3.3 presents a validation case study for the GoM. Finally, Sections 3.4 and 3.5 discuss and summarize the main conclusions of the study.

## 3.2. TROPICAL CYCLONE WIND STATISTICAL ESTIMATION TOOL (TCWISE)

### INTRODUCTION

TCWiSE comprises a Monte Carlo method for synthetic TC generation and involves four main components: track initiation, track evolution, wind field construction, and determination of extreme surface wind speeds. Based on the average number of TCs per year, their monthly distribution, and the distribution of the genesis location, timestamps, and synthetic genesis locations are generated. Subsequently, an ETM is used to determine the changes in track and intensity at certain time intervals (i.e., 3-hourly by default). The ETM is a Markov model where the values of the next time step solely depend on that of the previous time step, similar to the methods developed by, for example, Vickery et al., 2000 and Emanuel et al., 2006. The main variables it keeps track of are location (latitude and longitude), time, maximum sustained wind speeds ($v_{\text{max}}$), forward speed ($c$) and heading ($\theta$) of the synthetic TC track. After the TC tracks have been generated, the temporally and spatially varying surface wind fields are constructed using the updated Holland wind profile (Holland et al., 2010) with calibrations based on Nederhoff et al., 2019. Finally, the generated data of wind fields are used to estimate TC wind extremes. The main outputs of the tool are the synthetic tracks, the wind fields per TC, and the wind extremes. The output wind fields can be used further to derive extremes of associated second-order effects, such as storm surges and waves. The tool is written in MATLAB and leverages the Parallel Computing Toolbox to allow the utilization of multi-core processors on computer clusters.

## FLOWCHART

A compact flowchart of the method which is used to generate the synthetic tracks is shown in Figure 3.1. The steps of this process are as follows:

1. *Define settings.* The user specifies the data source, the area of interest, the number of years that are to be simulated, and a number of numerical parameters. In particular, the included IBTrACS dataset contains data from several meteorological agencies from which the user can choose. Also, the users can define settings such as the kernel size. The user can also define bulk climate variability parameters such as changes in TC frequency and intensity due to climate change.
2. *Construct statistics of original data.* TCWiSE processes the (historical) data and computes the probability of genesis and termination per location on the map. Moreover, it computes change functions for the three variables of which the tool keeps track. In particular, KDE of the conditionally dependent changes

in maximum sustained wind speeds (intensity $v_{\max}$), forward speed ($c$), and heading ($\theta$) as a function of the location and the variable itself are determined and saved for later usage. This information will be used within the Markov chains during the simulation of synthetic tracks.

3. *Compute cyclone genesis.* The tool computes the number of storms to be generated by taking the average number of storms observed per year within the oceanic basin of interest. The monthly distribution (i.e., seasonality) is also taken into account by first using a Poisson distribution for the number of TCs per each year, after which the monthly distribution is taken into account by giving each track a unique timestamp within the number of years to be simulated based on a KDE of historical data. For every track, its genesis location is determined, and each TC track gets an associated initial $v_{\max}$, $c$, and $\theta$ associated with the genesis location.
4. *Compute new location and intensity.* For every track, TCWiSE samples in 3-hourly intervals change to the three sampled parameters ($v_{\max}$, $c$, and $\theta$) until the termination of the track. KDE is used to randomly sample changes to these parameters as a function of location and the parameter itself. The tool uses the maximum sustained wind speeds as the intensity parameter. Heading and forward speed are the location parameters. All these three parameters are sampled at a use-definable time step (3-hourly by default).
5. *Compute landward decay.* It is possible to include an additional decrease in intensity on land via relationships developed by Kaplan and DeMaria, 1995. Implicitly, part of the decrease of intensity on land is already accounted for via the KDE of $v_{\max}$. However, due to search windows, some of this effect is smoothed out.
6. *Terminate track.* After each interval of 3 hours, the tool checks if the tracks should be terminated. The termination criteria are defined in three different ways: probability, wind speed criteria, and sea surface temperature (SST).
7. *Validate track.* To make sure realistic TC tracks are generated, the tool checks if the synthetic track that is terminated has reached a wind speed of at least 17 m/s (default threshold definition TC, but user-definable) during its lifetime (approximate TC category 1 based on the Saffir–Simpson hurricane wind scale (SSHWS)). This prevents the generation of extratropical storms that never reach TC status.
8. *Finalize tracks.* TCWiSE continues with this loop until the last synthetic TC track has been generated. This is reached once the total number of synthetic

tracks has been created.

9. *Create temporally and spatially varying surface wind field maps.* The tool creates meteorological forcing conditions, i.e., the surface wind fields per time step per TC, for subsequent analysis and the application within numerical models, currently only Delft3D4 and Delft3D-FM are supported including flow and wave (Lesser et al., 2004, Kernkamp et al., 2011).
10. *Create wind swaths*: TCWiSE creates maximum surface wind speeds for each TC by taking the maximum over all the timestamps of the TC. The maximum surface wind speeds of a single TC are also called wind swaths or wind extremes. Via non-parametric and parametric estimates probabilities or return periods can also be given to wind swaths. In particular, output wind speeds are in units of meters per second and by default 10 min averaged, though this is user-definable. Note that different meteorological agencies use different wind speed averaging periods. Harper et al., 2010 recommend for at-sea conditions a conversion factor of 1.05 going from 10 min to 1 min averaged wind speeds.

A more detailed description of the track initialization, track and intensity evolution, termination, climate variability, and wind fields is described in the paragraphs below.

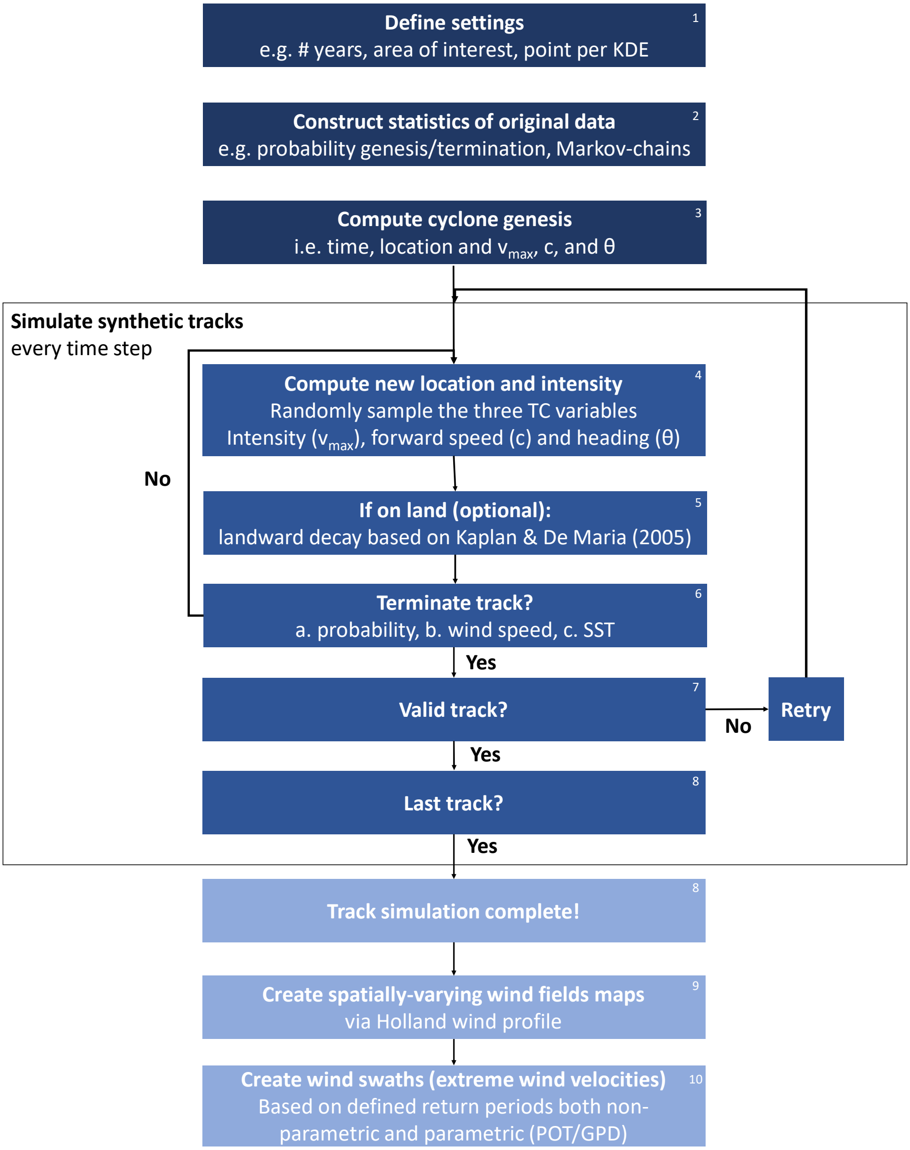

Figure 3.1: Flowchart of the track modeling procedure. Dark blue colors are pre-processing steps, blue colors are the computational core of TCWiSE, and light blue post-processing steps. KDE stands for kernel density estimation, SST stands for sea surface temperature and POT/GPD is the acronym of peak over threshold and generalized Pareto distribution.

### TRACK INITIALIZATION

The track initialization is done through random sampling of the genesis locations for each track from a spatially varying probability constructed based on (historical) input data. Only the spatial occurrence of the genesis locations is sampled, as no temporal variability of genesis locations or other input parameters are included in the genesis. The spatially varying probability used to sample the genesis locations is constructed by first drawing a rectangular grid of a user-definable size (default: $1^\circ \times 1^\circ$) around all historical events under consideration. For each grid point, all genesis locations within a certain distance (user-definable; default: 200 km) are counted and normalized with the total number of counted genesis points to obtain the genesis density at each grid point.

### TRACK EVOLUTION

After the generation of the genesis location and parameters, the evolution of the track and intensity is modeled during its lifetime in (by default) 3-hour intervals. The propagation is modeled by sampling the change in the heading ($\Delta\theta$), forward speed ($\Delta c$), and intensity ($\Delta v_{\max}$) for each time step.

**SEARCH RANGE** The KDE is constructed for each grid point based on input data within a specific search range. This search range is defined by a rectangular box of a user-definable size (default: $1^\circ \times 1^\circ$) around the point of interest. The minimum number of data points required within the search range is 250 (default, user-definable). If less than the specified amount of points is located within the search range, the search range is increased until the required number of data points is found or until the maximum is reached (user-definable; default: $5^\circ \times 5^\circ$).

The change in intensity evolution and track propagation, which includes the heading and forward speed, are all treated similarly. Changes are sampled from the pre-processed KDEs that are conditionally dependent on the previous time step. Historical occurrences are smoothed since a KDE from raw histograms is used (Wand and Jones, 1994). This smoothing overcomes possible discrete signals. By default, the heading is divided into 17 equally large bins and partly overlapping bins of 45°, forward speed is divided into 17 overlapping bins of 2.5 knots, and wind speed is divided into 37 overlapping bins of 5 knots. This ensures that the full parameter range for TCs is covered. For each variable, the search range (i.e., the range for which values are included in the bin) is twice the window size (i.e., the difference per each subsequent bin) to ensure a smooth transition between different bins. All these settings are user-definable. Data points that are on land can be excluded from the computation of the intensity evolution.

No additional parameters are defined for the track evolution. Effects such as intensification, the Coriolis effect, wind shear, and beta drift (Holland, 1983) are not explicitly defined nor controlled for. The conditionally dependent KDE of change per variable per location drives the complete track evolution.

EFFECT OF LAND When a TC makes landfall, TCs weaken due to, among other factors, a lack of heat sources (Tuleya, 1994). This effect should be part of the conditionally dependent KDE, but due to the possibly large search ranges per location (and thus blending of on-land and on-water conditions) the effect of land can be underestimated (and the intensity on water underestimated). Therefore, the user can exclude data points on land. When this is chosen, one should use additional formulations to reduce intensity when the synthetic TC is on land. Among other relationships available in the literature, Kaplan and DeMaria, 1995 created a simple empirical model for computing cyclone wind decay after landfall. In TCWiSE, a similar method can be used to compute the decay of wind speed after landfall. Following the relationships of Kaplan and DeMaria, 1995, wind speed decreases exponentially based on how long a TC is on land. The specific amount of decay as a function of time is, again, user-definable.

TRACK TERMINATION During each interval of 3 hours, the tool checks if the tracks should be terminated. The termination criteria are defined in three different ways:

1. when the wind speed is lower than a user-definable low value (default 10 knots)
2. when the synthetic TC is over a user-definable low water temperature (default 10 degrees Celsius)
3. the probability of termination based on (historical) input data.

When different methods of termination are used, the termination of a synthetic TC is thus not completely similar to the historical probability of termination. Hence, termination within TCWiSE can also be triggered by low wind speeds (due to the fact the TC is on land) and/or too-low SST.

CLIMATE VARIABILITY Projected effects of climate change on the frequency and intensity of TCs can also be taken into account via the heuristic implementation of a factor on both the frequency and intensity. These factors can be defined using expert assessment of TC climate predictions (e.g., Knutson et al., 2015), allowing, for instance, the assessment of changes in TC coastal hazards in the next century. The effect of climate variability on possible shifts of the TC tracks or regional changes of parameters are not included yet but could be included by modifying the (historical) KDEs or using global climate models as an input source for TCWiSE.

### TEMPORALLY AND SPATIALLY VARYING SURFACE WIND FIELD

After the generation of the track (time, location, and intensity), temporally and spatially varying wind fields are computed based on the parametric model of Holland et al., 2010 via the Wind Enhanced Scheme (WES; Deltares, 2018). The relationships of Nederhoff et al., 2019 are used either to compute the most probable TC geometry (RMW and radius of gale-force winds, also known as the radius of 35 knots or R35) or to take geometry into account as a stochastic variable. The user has the choice between generic relationships and calibrations for different basins. This ensures reliable azimuthal wind speeds. TC asymmetry is considered based on Schwerdt et al., 1979 and assumes a constant inflow angle of 22° (Zhang and Uhlhorn, 2012). More details on the implementation of the Holland parametric wind model are provided in Deltares, 2018.

### WIND SWATHS

After the generation of the wind fields, wind swaths for different return periods are generated. Both non-parametric and parametric extremes based on a fitted POT/GPD for different return periods are computed. TCWiSE utilizes the POT method combined GPD (Caires, 2016) for extreme value analysis. In particular, the choice of the threshold for the POT and the fitting of the coefficients are automatically performed. Parametric estimates of extremes are preferred when statistical uncertainties need to be quantified or when fewer observations are available on which to base the non-parametric estimates.

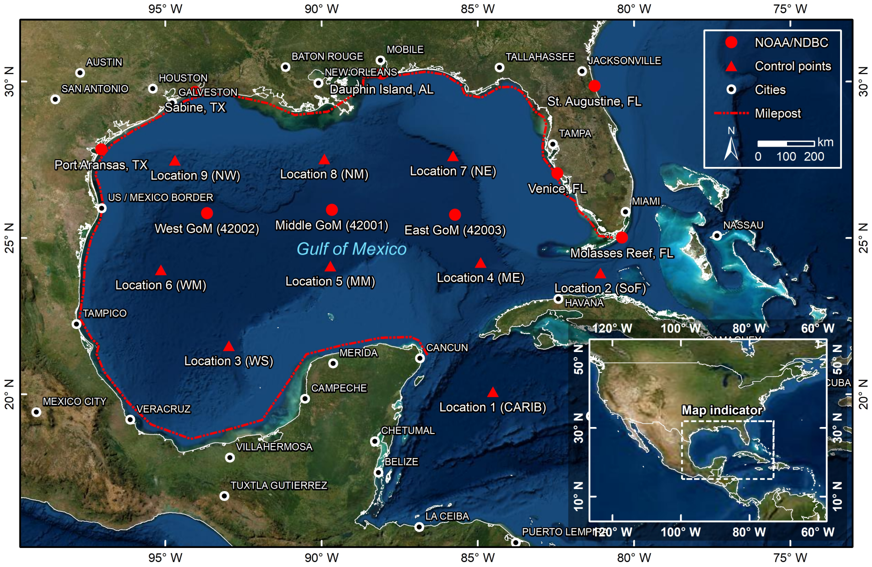

Figure 3.2: Area of interest of the Gulf of Mexico, including the locations of the nine control points in the GoM (red triangles), NOAA/NDBC measurement location (red dots), cities (white circles), and milepost (red dashed line). ©Esri, DigitalGlobe, GeoEye, Earthstar Geographics, CNES/Airbus DS, USDA, USGS, AeroGRID, IGN and the GIS User Community

## 3.3. RESULTS

### 3.3.1. STATISTICAL DATA AND TESTS USED FOR VALIDATION

BACKGROUND The United States (US) is one of the countries most affected by TCs over the years. In particular, the US Gulf Coast has suffered severely from hurricanes in the past, which have caused a significant number of casualties and a significant amount of damage. Among the most notorious, TCs Andrew in 1992, Katrina in 2005, and Harvey in 2012 devastated US territory. In the severe hurricane season of 2017 alone, Harvey, Irma, and Maria resulted in more than $ 250 billion in damage in the US (NOAA, 2018)

In this subsection, a validation of generation, occurrence, propagation, and termination of synthetic TC is carried out, by comparing with historical tracks for the entire NA basin. A more detailed comparison between historical BTD from the IBTrACS database and simulated synthetic tracks by TCWiSE is performed for nine control points in the GoM. Subsequently, extreme wind speed estimates from TCWiSE and from historical data are compared along the coastline and also validated against the literature. Figure 3.2 presents the area of interest for the validation case study, including relevant locations for this analysis.

DATA The NA basin data from the IBTrACS database are used within the TCWiSE algorithm to compute 10.000 years of synthetic TCs. Only historical data observed from 1886 up to 2019 are considered. The cutoff year of 1886 is chosen because of the increase in accuracy of the observation of the maximum wind speeds. This yields 955 historical TCs and 71.320 synthetic TCs for the entire NA basin.

Measured winds from a total of nine National Data Buoy Center (NDBC, https://www.ndbc.noaa.gov, last access: 22 December 2019) buoys across the GoM have been used in this study to validate the TCWiSE-computed extreme wind speeds. Computed and observed wind speeds are all converted if needed to 10 m height and 10 min averaged (see, e.g., Harper et al., 2010). This is generally the height and the averaging period needed for hydrodynamic models (in wave modeling this is typically the 1 hr average wind speed). Only observations from buoys with at least 20 years of data have been used to validate modeled wind speeds. Furthermore, only observations within a 200 km radius of an active TC (based on IBTrACS) are considered. This prevents the inclusion of peak wind speeds due to extratropical storms instead of TCs in the validation.

Moreover, TCWiSE-computed extreme values are compared to values found in the literature. For example, Vickery et al., 2009 present simulated TC-induced wind speeds across the US coastline for return periods of 50 up to 2000 years. Following the methodology of Neumann, 1991, along the US coastline, NOAA (National Oceanic and Atmospheric Administration) presents hurricane return periods for both hurricanes (>64 knots) and major hurricanes (>96 knots) within 50 nautical miles (92.6 km) based on the track information. TCWiSE-computed return periods are compared to NOAA's reported values (https://www.nhc.noaa.gov/climo/, last access: 1 February 2019).

STATISTICAL TEST FOR TC VALIDATION A variety of tests are available for statistical comparison between computed and historical cyclone parameters. The tests are used to prove the hypothesis that the historical values come from the same statistical population as the simulated values. For each parameter, such as forward speed, a goodness of fit for the historical cumulative distribution function (CDF) can be performed and compared to the CDF from the synthetic tracks. Strictly, this would require that different data sets are employed for model fitting and for model testing so that distributional parameters of the model used to generate the large-sample CDF are not estimated from the historical sample. However, in this paper, we utilized all available observational data to include as much climate variability in the synthetic tracks as possible.

Several tests exist (e.g. Kolmogorov–Smirnov, Cramér–von Mises, Anderson–Darling, Kuiper, Watson) to test the null hypothesis that the samples x and y come from the same (continuous) distribution (Stephens, 1974). In addition, a more pragmatic approach is available which consists of simply computing the mean absolute error (MAE) on the historical and computed CDFs. In this paper, we present a combination of different statistics to test if the synthetic tracks have similar statistical properties to the BTD. In particular, normalized mean absolute error (nMAE; MAE divided by variance of BTD), root-mean-square error (RMSE), and bias are presented. Additionally, the CDFs of several TCs physical properties are compared for the historical and synthetic tracks. Finally, the Kirchhofer, 1974 method is used for quantifying similarities and differences in spatial patterns (e.g. TC genesis, evolution).

### 3.3.2. VALIDATION OF TROPICAL CYCLONE PARAMETERS

In the following subsection, the modeled results of TCWiSE are compared to historical BTD. Validation follows the life of a TC first with a visual and qualitative validation of the generation being presented. Subsequently, the track occurrence, evolution, and CDFs of the three main parameters of TCWiSE are compared quantitatively to historical data. Lastly, a visual and qualitative validation of the termination is presented.

GENERATION Historical and simulated genesis probability for the entire NA basin is shown in Figure 3.3. Cyclone genesis is taken as the first point which the BTD identifies as such, which means it is the point from where meteorological institutes started tracking the storm. As shown in Figure 3.3 panel A, the simulated and the historical genesis match well visually. A hot spot of TC genesis is illustrated on the west coast of the African continent. Additionally, two hot spots are visible east of the Caribbean Sea and in the western part of the Caribbean. Within the GoM some areas also show cyclone genesis. Genesis in these specific basins is related to increases in oceanic heat content (Emanuel, 2005). The spatial patterns of genesis are almost identical while being slightly smoothed out in the simulated synthetic tracks (Figure 3.3 - panel B). This visual assessment was quantified and confirmed by using the Kirchhofer metric score, which provided a value equal to 0.967 (a value of 1.0 represents a perfect match). In particular, grid cells that are zero (either in the historical or synthetic data set) are not taken into account in the analysis. This gives confidence that TCWiSE can reproduce the genesis patterns observed in the historical BTD.

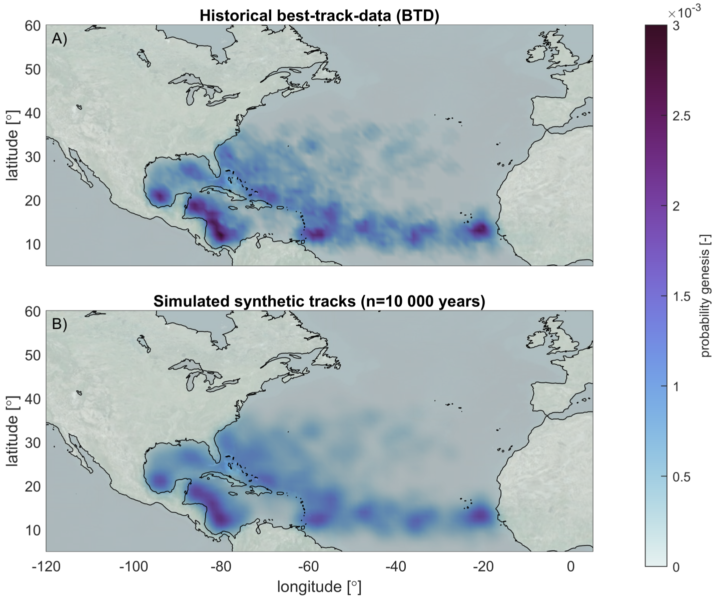

Figure 3.3: Genesis probability of historical BTD (a) and simulated TCs with TCWiSE (b) for the NA basin. Occurrence is based on TCs within 200 km per grid cell for historical TCs from 1886–2019 and 10.000 years of simulated events. ©Microsoft Bing Maps.

TRACK OCCURRENCE, EVOLUTION, AND CDFS Sea surface temperature also plays a role in the track occurrence and evolution of TCs, providing the necessary energy for their development and strengthening. This is particularly evident in the warm waters of the Caribbean Sea and the Gulf of Mexico, where conditions are optimal for TC intensification. Additionally, wind shear is a significant factor (Hibbert et al., 2023). While low wind shear in these regions supports cyclone strengthening, as systems move northward or are steered into the mid-latitudes, they frequently encounter cooler ocean waters and increased wind shear. This transition often leads to a decrease in intensity. Moreover, these northward-moving systems can be caught up in the mid-latitude westerlies, influencing their path and potentially leading to extratropical transition (Evans et al., 2017).

Historical and simulated TC intensity tracks are shown in Figure 3.4. All individual tracks are plotted with a color code derived from the intensity of the eye of the storm (i.e., maximum sustained wind speed). Tracks with higher intensity are plotted on top of those with lower intensity. The figure shows that TCs are generated around latitudes of ±10–20° (see also Figure 3.3). Some of the TCs increase in intensity while moving towards the northwest, making landfall in the US, in Central America, in the northern countries of South America, and across the Caribbean. Others turn back in an eastward direction and propagate towards Europe. Intensities are generally larger in the Caribbean and GoM, while TCs that propagate northward decrease in intensity. Similar patterns can be observed in the simulated synthetic TCs (Figure 3.4 - panel B). However, higher intensities can be observed for individual simulated synthetic tracks due to the larger number of years of data that are presented (10,000 years of simulated tracks vs. 134 years for the historical tracks) and thus a larger likelihood of having a more intense TC. Moreover, it does seem that synthetic TC tracks have a less clear southwest–northeast orientation in heading on the North Atlantic Ocean.

The average yearly occurrence of historical and synthetic TCs is presented in Figure 3.5. A high occurrence of TCs in the GoM, in the Caribbean, and along the east coast of the US is observed for both historical and simulated tracks. The simulated occurrence is quite similar but, as expected, more smoothened for the synthetic tracks. The Kirchhofer metric score for occurrence confirms the matching of the patterns with a high score of 0.926. This gives confidence that TCWiSE produces synthetic TCs with a similar occurrence rate to what has been historically observed.

The generation of synthetic TCs includes three distinct parameters that can be compared between the historical and synthetic tracks, namely forward speed ($c$),

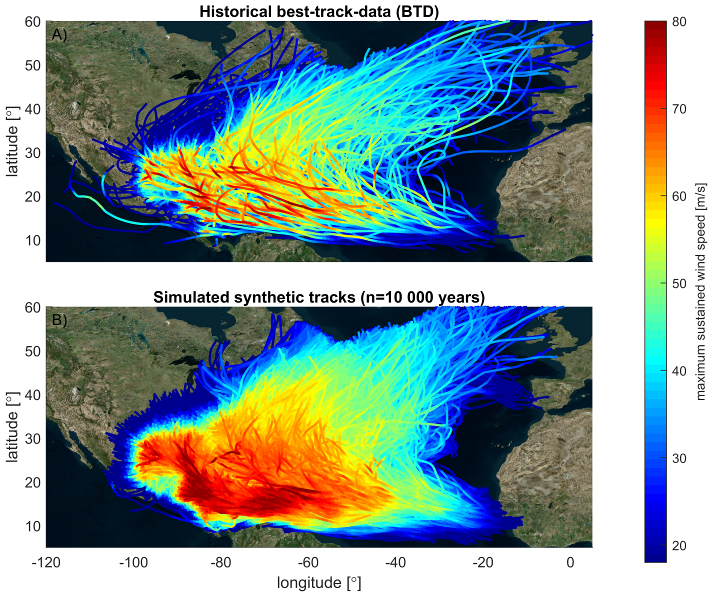

Figure 3.4: Overview of historical tropical cyclone tracks in the IBTrACS database for the period 1886–2019. (b) 10.000 years of simulated tracks with TCWiSE. Colors indicate the maximum intensity of the eye. Note that the maximum intensity is the maximum wind speed at the core of the TC, which is different from the temporally and spatially varying wind field and/or spatially varying wind swaths. In particular, further away from the TC eye, gale-force winds can still be present due to the TC. ©Microsoft Bing Maps.

heading ($\theta$), and maximum sustained wind speeds ($v_{\max}$). The CDFs are presented for these parameters in Figures 3.6, 3.7, 3.8 for the nine locations as shown on the map in Figure 3.2. Visually the CDFs of the synthetic data appear to match those of the historical data rather well. nMAEs of the forward speed (Figure 3.6) vary between 0.02–0.20 with an average RMSE of around 0.43 m/s and with a bias of +0.31 m/s. Location 3 (WS) and location 9 (NW) have a larger error due to the positive bias. Statistical errors in the headings (Figure 3.7) are generally small too. Locations 2 and 9 have larger nMAE than the other control locations (possibly due to the effect of land), while locations 7 and 8 have the lowest errors. The nMAE of maximum sustained wind speed (Figure 3.8) varies between 0.00–0.04 with, on average, a RMSE of around 3.62 m/s and with a bias of -3.10 m/s. These error statistics do reveal a general tendency for larger deviations closer to land but give confidence in the synthetic generation and propagation of the TC.

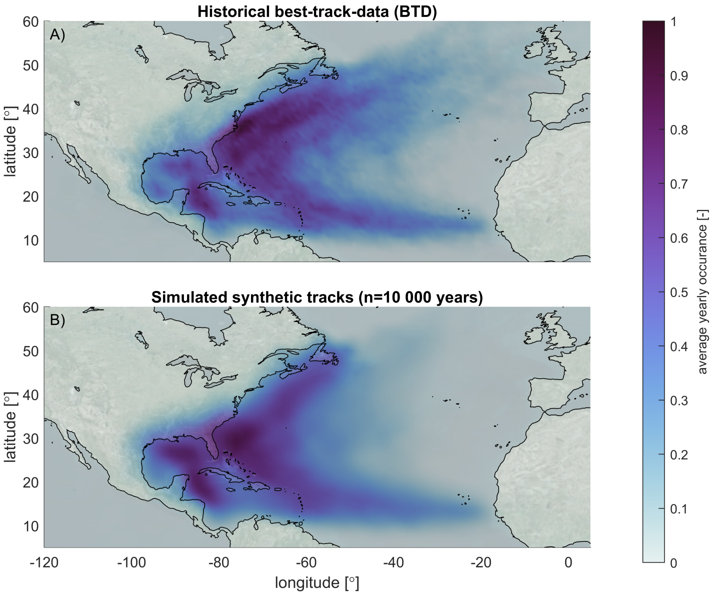

Figure 3.5: Average occurrence of historical BTD **(a)** and simulated TCs with TCWiSE **(b)** for the NA basin. Occurrence is based on TCs within 200 km per grid cell for historical TCs from 1886–2019 and 10,000 years of simulated events. ©Microsoft Bing Maps.

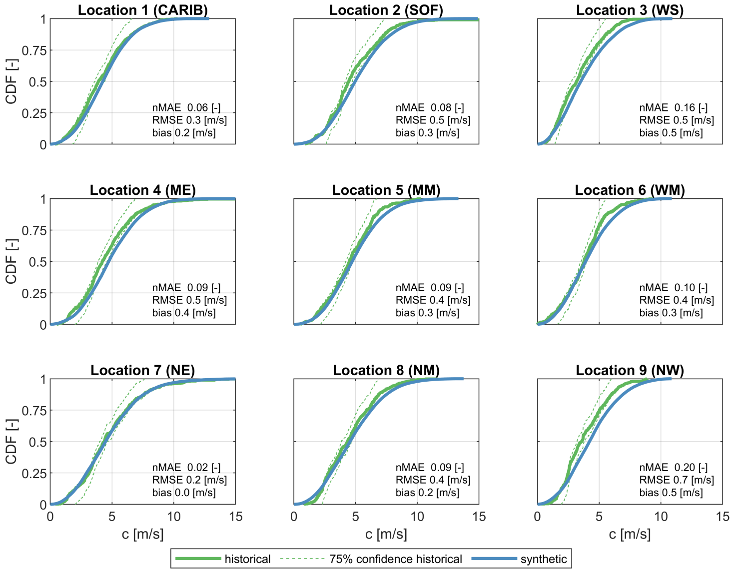

Figure 3.6: CDFs of forward speed ($c$ [m $s^{-1}$]) of historical (green line) and synthetic (blue line) TCs at nine locations within the NA basin, as shown on the map in Figure 3.6. The 75% confidence interval (dashed green line) of historical data is also shown. Historic data are based on data available between 1886 and 2019, while synthetic data are derived from 10,000 years of simulated events with TCWiSE. Data points within 200 km from the control location are included in the analysis for both the historical and synthetic data.

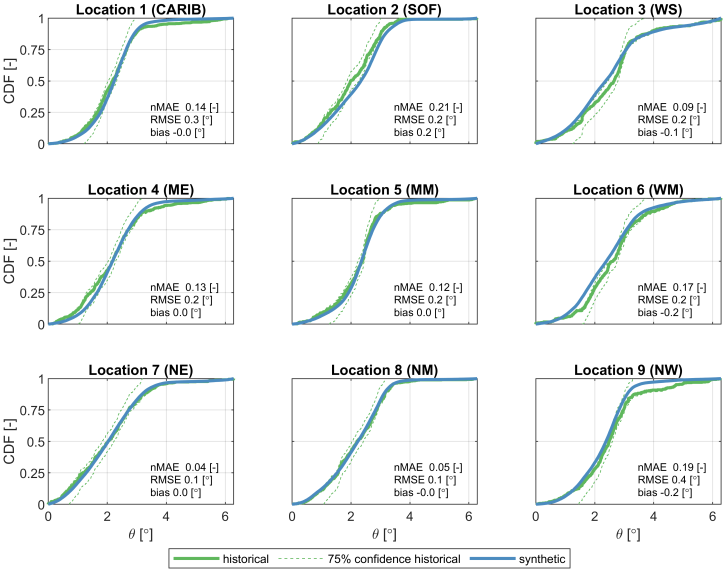

Figure 3.7: CDFs of heading of historical (green line) and synthetic (blue line) TCs at 9 locations within the NA basin

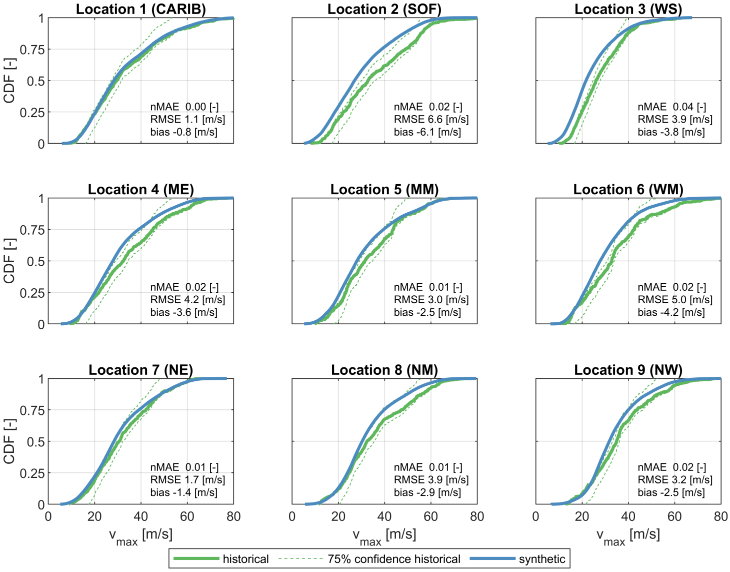

Figure 3.8: CDFs of maximum sustained wind speed ($v_{\max}$ [m s$^{-1}$]) of historical (green line) and synthetic (blue line) TCs at nine locations within the NA basin

TRACK TERMINATION Historical and simulated termination probability is shown in Figure 3.9. In TCWiSE, cyclone termination is defined as the last point of TC that is obtained from the BTD. The figure shows that historically there is a large probability of termination at the east coast of Canada (i.e., Nova Scotia and the island of Newfoundland) (see, e.g., Elsner et al., 1999) and the east coast of Mexico. In some cases, TCs terminate after landfall in the US or while propagating on the Atlantic Ocean. TCs terminate for various reasons primarily due to changes in environmental conditions that are no longer conducive to sustaining their structure and intensity (e.g., land interaction, cold water, increased wind shear). Visually, the historical and simulated termination do not align as well. The reasons for deviations are that termination can be triggered by several different physical processes and is thus not so closely related to the input data. In particular, in TCWiSE, synthetic TCs can terminate due to a low ocean temperature or low wind speed on land. Hence, the differences in this comparison can be explained due to the schematization of the physical processes which lead to a different TC termination in TCWiSE than based on the historical probability alone. Also, errors from the previous steps in the TC life cycle (i.e., genesis location, propagation) will be compounded in the track termination. The comparison between historical and simulated termination probability was quantified by using the Kirchhofer metric score for termination, which provided a value of 0.622 (compared to 0.967 for genesis and 0.926 for occurrence).

### 3.3.3. VALIDATION OF TROPICAL CYCLONE WIND SPEEDS

OBSERVED EXTREME WIND SPEEDS Figure 3.10 presents the non-parametric 10-year return value estimates of TC wind speed for the GoM based on synthetic TCs. Cooler colors depict lower TC wind speeds, and warmer colors have higher wind speeds. The circles indicate the non-parametric estimates based on buoy observations for the same return period; given that the observations cover about 40 years, they are the fourth-highest ever recorded value. The figure shows how the general patterns of higher wind speeds in the central GoM and lower values near land, as shown by the data, are reproduced correctly by TCWiSE. The model-computed values are biased high (i.e., overestimation) for stations near land. This is most likely due to land-related processes not being fully accounted for in TCWiSE. Also, the data scarcity (sub-sampling) affects the estimates from the observations.

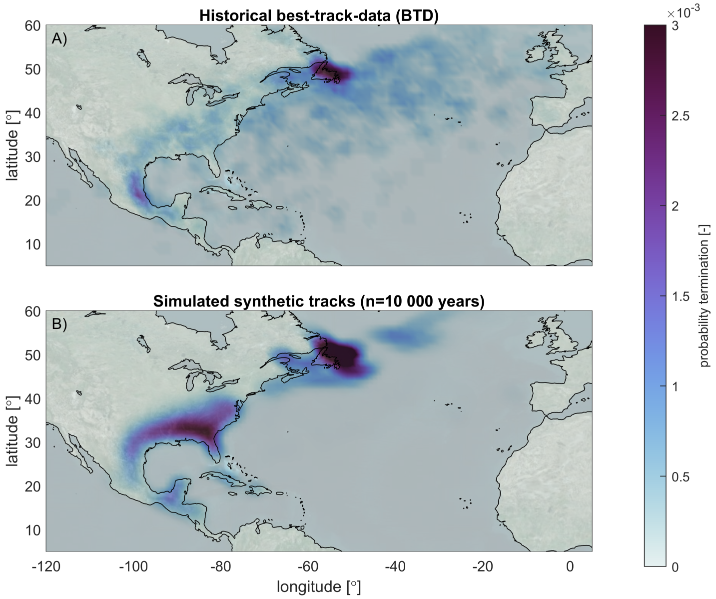

Figure 3.9: Termination probability of historical BTD **(a)** and simulated TCs with TCWiSE **(b)** for the NA basin. Occurrence is based on TCs within 200 km per grid cell for historical TCs from 1886-2019 and 10,000 years of simulated events. ©Microsoft Bing Maps.

Figure 3.11 presents a comparison between observed and TCWiSE-computed TC extreme wind speeds, for different return periods, at nine locations throughout the GoM, both based on 134 years of historical and 10,000 years of synthetic tracks. As could already be seen in Figure 3.10, there is some scatter between observed, historical, and synthetic TC wind speeds. For example, the peak in the observed wind speed, in particular, that of larger return periods, in the east GoM (Figure 3.11a) and middle GoM (Figure 3.10 - panel b) are underestimated by both the historical and synthetic TCs. These are respectively peaks corresponding to Hurricane Rita (2005) and Hurricane Kate (1985). Based on the observation record of 40 years, the non-parametric return period estimate is 40 years, whereas TCWiSE indicates that the return period associated with those events is higher. The cause of the large difference between observed wind speeds and values derived from historical and synthetic TCs wind speed for the west GoM (Figure 3.11 - panel c) is unclear. On the other hand, wind speed extremes at Venice, FL (Figure 3.11 - panel e), and Port Aransas, TX (Figure 3.11 - panel i), seem to be overestimated by the historical and synthetic TCs, which could be related to unresolved land-related processes.

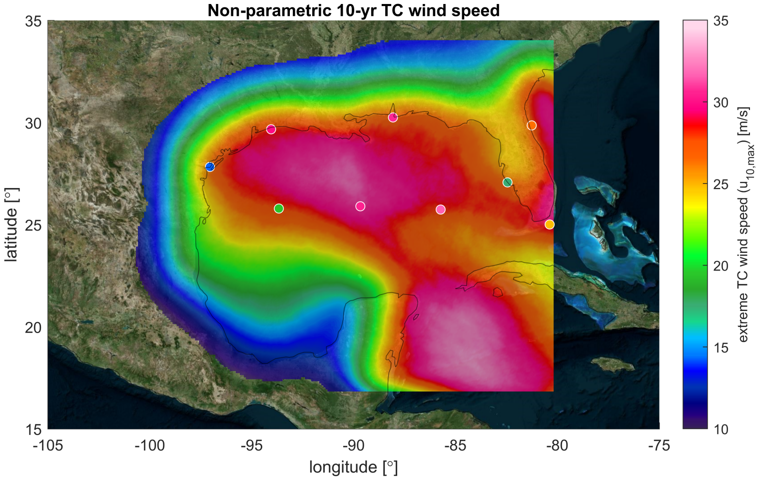

Figure 3.10: Model estimates for a non-parametric empirical estimate of 10-year TC wind speed return values based on extreme wind speeds based on 10,000 years of TCWiSE computations. The white circles indicate observed TC wind speed extremes based on NDBC wave buoys and NOAA data. All wind speeds are in meters per second, 10 min averaged, and determined at a 10 m height. ©Microsoft Bing Maps.

## MODELED EXTREME WIND SPEEDS

Figure 3.12 presents the 1000-year parametric TC wind speed for the GoM, estimated by fitting a GPD to the POT of the generated data. The figure shows a spatial pattern similar to that of the 10-year non-parametric TC wind speeds (Figure 3.10). The highest values are found in the Caribbean Sea and central GoM. Lower values can be found in northwest Florida and in the southwest of the GoM. This is in line with the literature (e.g., Neumann, 1991). Computed occurrence rates are also in line with NOAA values for both hurricanes ($> 64$ knots) and major hurricanes ($> 96$ knots) within 50 nautical miles (92.6 km). Occurrence rates for major hurricanes ($> 96$ knots) are the highest for South Florida and Louisiana, with a respective return period of 17–20 years. TCWiSE estimates are 19–22 years.

Figure 3.13 presents the estimated TC wind speed return value swaths versus coastal milepost which starts at Cancún, Mexico and goes across the GoM in a clockwise

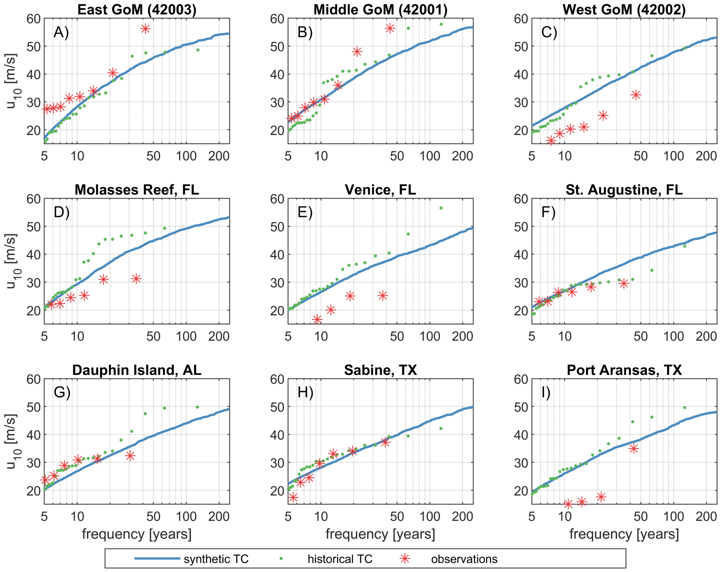

Figure 3.11: Observed and TCWiSE-computed TC extreme wind speeds for different return periods. Red stars are observed events from NDBC and NOAA wave buoys. Green dots are historical TCs based on BTD and the Holland wind profile, and blue line are synthetic modeled events based on synthetic tracks and the Holland wind profile. All wind speeds are in meters per second, 10 min averaged and determined at a 10 m height.

orientation. Several return periods are depicted in different colors. Moreover, TC wind speed is presented both averaged over 10 min in units of meters per second and averaged over 1 min in units of knots. The SSHWS is included as well. TCWiSE simulation indicates for a return period of 10 years TC wind speed of around 30 m/s (close to SSHWS-1) near Cancún and large stretches of the US coastline. For a return period of 1000 years, this increases to values around 60 m/s (around SSHSS-4). Generally, values near Villahermosa are the lowest for all of the GoM. Vickery et al., 2009 reported maximum gust TC wind speeds with a return period of 100 years that vary between 33-57 m/s. TCWiSE indicates values on the same order of magnitude but with less spatial variability.

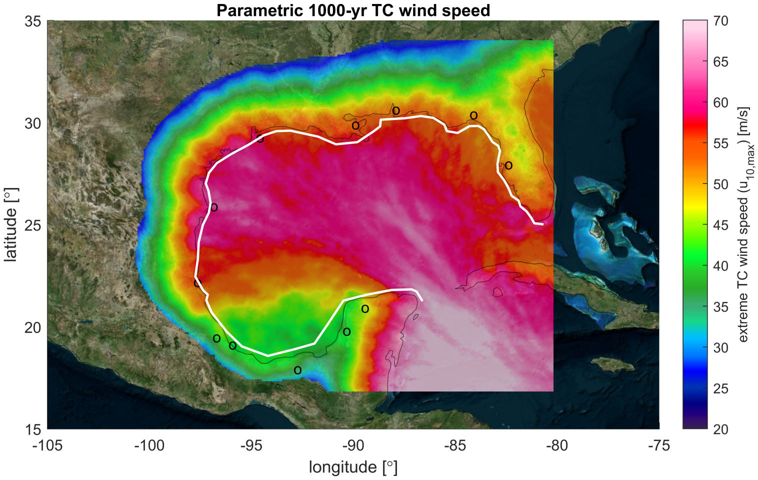

Figure 3.12: Model estimates for the parametric empirical estimate of 1000-year TC wind speed return values based on extreme wind speeds based on 10,000 years of TCWiSE computations. All wind speeds are in meters per second, 10 min averaged and determined at a 10 m height. Black dots are the location of cities as plotted in Figure 3.10 and 3.13. Microsoft Bing Maps.

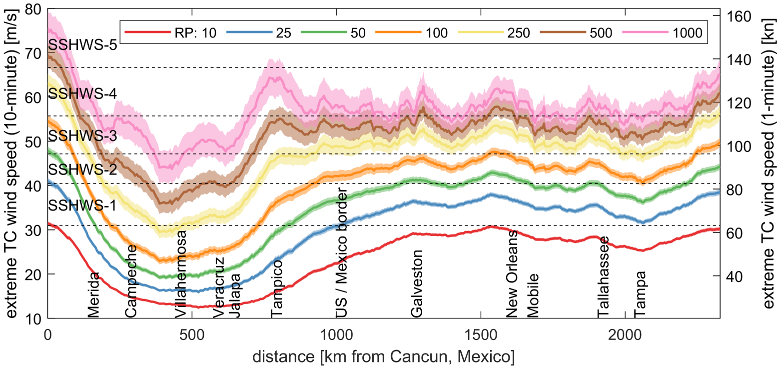

Figure 3.13: TCWiSE 10-, 25-, 50-, 100-, 250-, 500- and 1000-year return value estimates of wind speed. All wind speeds are in meters per second, 10 min averaged and determined at a 10 m height (left axis) or 1 min averaged in knots (right axis). Cities on the *x* axis are also depicted in Figure 3.12 as black circles. Milepost is presented in the same figure as a white line. Shading shows the 5–95% confidence interval. SSHWS value indicates the corresponding Saffir-Simpson hurricane wind scale.

## 3.4. DISCUSSION

For clarity, discussion points have been grouped under three main topics: the TCWiSE tool, validation study, and computational performance.

THE TCWISE TOOL The philosophy that guided the development of TCWiSE is to release an open-source tool, giving modelers full control over the track generation, propagation, and termination. However, this makes TCWiSE also more sensitive to input errors compared to pre-generated global synthetic TC data products (e.g., Bloemendaal et al., 2020). However, the strength of this approach is 2-fold. First of all, this allows the user of TCWiSE to rigorously calibrate and validate assumptions within the code for the user's own case study site. Secondly, the flexible MATLAB coding language allows easy adjustments of the tool and implementation of additional processes. For example, stochastic rainfall was recently added to the original code by Bader, 2019.

TCWiSE is an almost completely data-driven tool to simulate synthetic TCs. As such, output values are highly dependent on the (historical) input data and not the physical processes describing the genesis, propagation, and termination of these TCs. This limits the possibility of synthetic TCs computed by TCWiSE that are physically credible but statistically unlikely. Moreover, this assumes stationarity of the historical record. If cyclone characteristics are expected to behave identically to the last decades, this method has been proven accurate for the determination of extremes. However, climate change is expected to influence the frequency and intensity of future TCs (e.g., Knutson et al., 2010). This can already be accounted for by a heuristic factor to adjust both the frequency and intensity of the TC (or other variations implemented by the user) to reflect changes due to climate change. Other ways to account for this – such as by adjusting the KDE, applying data-driven probabilities of TC genesis as a function of SST, and/or further use of data sets derived by global climate models – are currently being investigated.

The effect of land on intensity can be taken into account either directly via the conditionally dependent KDE or landward decay based on Kaplan and DeMaria, 1995. The latter is beneficial since TC information on land contaminates the KDE of intensity. In particular, due to the applied search range methodology, information from decreasing winds on land starts to affect winds on the water. The downside of this method is that this does introduce an additional calibration coefficient for the user and larger deviations in the termination. Moreover, TCWiSE does not include a boundary layer model, which means that the physical wind response to variable surface drag and terrain height is not included. In particular, the at-sea TC wind will extend inland before the TC center crosses the coast and the decay turns on. Done et al., 2020 have shown, however, that the output of parametric wind models can be used to simulate the near-surface wind swaths of landfalling TCs, accounting for terrain effects such as coastal hills and abrupt changes in surface roughness due to coastlines and forested or urban areas.

In TCWiSE, track termination can be either be purely based on historical track termination or via additional formulations based on user-definable cut-off wind speed and/or SST. While these additional formulations were of importance to get the track evolution (and thus associated coastal hazards) simulated correctly, they do result in deviations of simulated track termination compared to historical data. However, arguably, track termination is not of importance for the simulation of coastal hazards, and therefore this is deemed an acceptable trade-off for the more reproductive skill in the track evolution.

TCWiSE does not take into account errors in the wind fields or the associated impact on the confidence interval for the computed return periods for wind speeds. Nederhoff et al., 2019 demonstrated that the Holland wind profile in combination with reliable estimates of the TC geometry (i.e., the radius of maximum wind and gale-force winds) to calibrate the wind profile wind has a median root-mean-square difference of 2.9 m/s. Other approaches (e.g., Vickery et al., 2009) do include error estimates in their estimates of the extreme winds. Vickery et al., 2009 conclude that uncertainty in the estimated 100-year return period wind speed varies by around 6%, which corresponds to about $\pm 3-5\,\mathrm{m\ s^{-1}}$.

VALIDATION STUDY Validation results across the NA basin and in particular the GoM have shown that TCWiSE can reproduce the main patterns seen in the BTD, wind observations, and literature. This can be done despite the lack of a physical description of the climate dynamics given that TCWiSE is a purely data-driven tool and does not include specific processes to steer TC propagation.

A comparison of similarities in spatial patterns between synthetic tracks and historic tracks, evaluated using the Kirchhofer metric score, shows that TCWiSE can correctly reproduce genesis and TC occurrence, while differences were found for the TC termination. These differences can be attributed to TC termination, which can get triggered by several criteria in TCWiSE. Hence, it is not just related to the historical probability of termination. At the same time, this has a relatively minor effect on the track evolution and consequently coastal hazards.

The comparison of CDFs of forward speed, heading, and maximum sustained wind speed of historical and synthetic tracks shows a good agreement for the different stations in general. While differences between observed and modeled CDFs are apparent, results of the goodness-of-fit tests are generally acceptable (Figure 3.6-3.8), with a mean nMAE of 0.08. More classical statistical tests such as Kolmogorov–Smirnov were not presented here and often reject the null hypothesis that the observed and modeled data are from the same distribution. This is related to the methodology of providing inputs to the Markov chains. While this method resulted in reliable probability distributions, it also smoothed out some local spatial patterns and therefore resulted in differences at the nine control locations. Arguably, local patterns in the BTD (features $< 500\,\text{km}$) could well be subject to a sampling error and not necessarily a feature of the TC climate we aim to reproduce.

All BTD, since 1866, have been included as a basis for the generation of synthetic tracks. Especially for pre-satellite records, errors in the BTD can be quite significant, so previous studies (e.g., Holland, 2008) selected a specific subset of the BTD to ensure the quality of the data and remove potential inconsistencies. However, the advantage of including all data entries is that the derived TC climate is more widely defined (i.e., larger parameter space). Another drawback is that employing the same dataset for both training and validation diminishes the reliability of the model's performance assessment on new, unseen data.

COMPUTATIONAL PERFORMANCES To provide the reader with a rough estimate of the computation performance of the tool, TCWiSE simulations for the NA and in particular GoM were performed on a 16-core Windows machine. The simulation of 10,000 years of synthetic tracks took several hours. The generation of temporally and spatially varying wind fields, wind swaths, and matching extreme value analysis took another ±15 d.

## 3.5. CONCLUSION

A new methodology and highly flexible open-source tool have been developed with which synthetic Tropical Cyclones (TCs) can be generated and used for subsequent analysis of (coastal) hazards. In particular, TCWiSE handles track initialization, evolution, and termination based on historical TC information. Subsequently, the tool creates a temporally and spatially varying wind field based on the Holland wind profile calibrated for TC geometry. Lastly, TCWiSE computes non-parametric and parametric wind swaths for user-definable return periods.

The validation study for the NA and in particular the GoM showed reliable skill in terms of track initialization and evolution compared to the historical Best Track Data (BTD). A more detailed assessment of the goodness of fit at nine control locations showed that normalized errors are generally smaller than 10%. Extreme wind speeds show agreement for more frequent return periods, with possible deviation for the most extreme cases. This is the result of biases associated with the scarcity of observed data.

TCWiSE can be useful in a variety of applications. Improved estimates of extreme TC conditions can lead to a better quantification of coastal hazards (e.g. extreme storm surge levels and waves) and consequent risks and damages resulting from these hazards. Similarly, an improved assessment of those hazards can help guide the design of appropriate adaptation measures. Other fields of application may vary from improved design parameters for offshore structures to navigation. In all these types of applications, the flexibility of TCWiSE to tailor the synthetic TC generation to user-specific needs and questions makes the tool very well-suited for coastal engineers. The application of the tool for determining coastal hazards will be presented as part of a separate paper (Leijnse et al., 2022).

# 4

# EVALUATION OF TROPICAL CYCLONE-INDUCED FLOODING IN THE SOUTHEAST ATLANTIC COASTAL ZONE OF THE UNITED STATES FOR STRATEGIC RISK ANALYSIS

*In Chapter 3 we introduced a methodology for performing strategic risk analysis. This chapter employs such a methodology to quantify coastal flooding and is set up as a case study focused on the Southeast Atlantic Coastal Zone of the United States. We compare cyclone-induced relative to non-cyclone-induced flooding to place them in perspective. This comparative analysis is crucial, as the contribution to flood risk from these distinct weather phenomena is often not well understood and can be significant. In particular, these events each possess their unique characteristics and movement patterns, influencing the duration, intensity, and spatial dispersion of flooding, and consequently, their associated hazards and impacts.*

---

This chapter is a revised version of **Nederhoff**, **K.**, Leijnse, T. W. B., Parker, K., Thomas, J., O'Neill, A., van Ormondt, M., McCall, R., Erikson, L., Barnard, P. L., Foxgrover, A., Klessens, W., Nadal-Caraballo, N. C., & Massey, T. C. (2024b). Tropical or extratropical cyclones: what drives the compound flood hazard, impact, and risk for the United States Southeast Atlantic coast? *Natural Hazards*. https://doi.org/10.1007/s11069-024-06552-x

**Abstract** Subtropical coastlines are impacted by both tropical and extratropical cyclones. While both may lead to substantial damage to coastal communities, it is difficult to determine the contribution of tropical cyclones in coastal flooding relative to that of extratropical cyclones. We conduct a large-scale flood hazard and impact assessment across the subtropical Southeast Atlantic Coast of the United States, from Virginia to Florida, including different flood hazards. The physics-based hydrodynamic modeling skillfully reproduces coastal water levels based on a comprehensive validation of tides, almost two hundred historical storms, and an in-depth hindcast of Hurricane Florence. We show that yearly flood impacts are two times as likely to be driven by extratropical than tropical cyclones. On the other hand, tropical cyclones are thirty times more likely to affect people during rarer 100-year events than extratropical cyclones and contribute to more than half of the regional flood risk. With increasing sea levels, more area will be flooded, regardless if that flooding is driven by tropical or extratropical cyclones. Most of the absolute flood risk is contained in the greater Miami metropolitan area. However, several less populous counties have the highest relative risks. The results of this study provide critical information for understanding the source and frequency of compound flooding across the Southeast Atlantic Coast of the United States.

## 4.1. INTRODUCTION

A large and growing share of the world's population lives in coastal regions and is vulnerable to extreme events, such as tropical cyclones. Merkens et al., 2016 estimated that 680 million people live in the low-lying coastal zone worldwide and that this amount could reach more than one billion by 2050. The high concentration of people in coastal areas has resulted in many economic benefits, including improved transportation, industrial and urban development, revenue from tourism, food production, and many more. However, this also concentrates exposure to natural hazards in the coastal zone. Moreover, humans are not the only species in the coastal regions that can be affected by extreme events. Beaches, dunes, and tidal wetlands are diverse ecosystems in the coastal zone that are sensitive to climate change and extreme events. For example, Dewald and Pike, 2014 showed that hurricanes affect 97% of the sea turtle nesting beaches in the Northwestern Atlantic and Northeastern Pacific Oceans.

Sea-level rise (SLR) increases coastal flooding (e.g., Vitousek et al., 2017b; Taherkhani et al., 2020; Sweet et al., 2022). Coastal flooding is driven by many complex factors, including changes in sea level, storms, and high tides (king tides), or a combination of the three. Storms, both tropical cyclones (TCs) and extratropical cyclones (ETCs), can result in storm surge, high waves, and rainfall that can contribute to or result in flooding. Moreover, the intensity, duration, and occurrence of these storm impacts are expected to change in the coming decades due to climate change. For example, as a consequence of warmer waters and a warmer, more humid atmosphere, Knutson et al., 2015 showed that global average TC intensity, rainfall rates, and occurrence of very intense TCs are projected to increase. In addition, global climate models (GCMs) show a projected poleward shift in midlatitude ETC tracks, with varying changes in the strength of storms across the globe (Chang et al., 2012).

In recent years, more focus has been given to coastal compound flooding, caused by the co-occurrence of high tides, coastal storm surges, waves, precipitation, and/or river discharge (Wahl et al., 2015). Storm events, such as Hurricane Florence (2018), have highlighted the importance of compound events and the need to include all relevant drivers of flooding to assess local and regional coastal flood risk. Hurricane Florence resulted in large amounts of rainfall in North and South Carolina. For example, locally, Swansboro and Elizabethtown, N.C., recorded close to 90 cm of rain (Callaghan, 2020). Rainfall together with other drivers resulted in a large compound flood zone in the low-lying coastal zone where ocean, precipitation, and river discharge were all of importance (Ye et al., 2021). However, a priori, the relative contribution of each physical driver to the flooding is often unknown. Whereas flooding hazards from each physical process may be realized, quantifying hazards due to the combination of two or more processes is difficult due to a large number of possible combinations and non-linear physical interactions (e.g., Huang et al., 2021). One solution is to apply multivariate extreme value theory, which requires dynamic downscaling of many events to define the critical region where flooding occurs. Ideally, all possible combinations need to be simulated by either the use of extensive computational resources or computationally efficient methods. Computationally efficient methods can be achieved by an acceleration of the direct simulations, developing a series of event reduction techniques, or by a combination of the two, for example, through hybrid downscaling (Bakker et al., 2022).

In addition to the general challenges of modeling compound flooding (Santiago-

Collazo et al., 2019), estimating return periods (RPs) of TC-included flooding remains a significant obstacle. This challenge is related to two factors. First, TCs are poorly resolved in many synoptic-scale and global climate datasets used for meteorological forcing due to coarse spatial and temporal resolution, causing an underestimation in TC intensity (Roberts et al., 2020) and, consequently, storm surge and wave conditions (Murakami and Sugi, 2010). Second, the limited record length of available meteorological forcing data, in combination with the low probability of TCs, means the number of TCs is too small to estimate RPs robustly (e.g., Lin and Emanuel, 2016; Leijnse et al., 2022). In flood risk assessment, it is possible to overcome some of these limitations via synthetic emulation of TC tracks (e.g., Vickery et al., 2000; Bloemendaal et al., 2020; Nederhoff et al., 2021a) or other statistical techniques such as the joint probability method (JPM; Resio and Irish, 2015; Nadal-Caraballo et al., 2022. Still, these approaches suffer from parameterizations of key physics (e.g., land-sea interactions or seawater temperature) and are based on datasets with limited temporal length. Alternatives could be the pseudo-global warming approach (Jyoteeshkumar Reddy et al., 2021) or the full dynamical approach (Mori and Takemi, 2016), this last only available to a few nationwide research centers with very high computing capacity (Mori et al., 2021).

In recent years, the scientific community has increasingly focused on (TC-induced) compound events. In all these efforts, coupling procedures between marine (tide and surge) and inland processes (rainfall and riverine discharge) are paramount to capture the complex physical interactions. For example, at the local-watershed scale, Bilskie and Hagen, 2018 showed local impacts on water levels in the flood transition zone when considering different techniques for combining marine and inland flooding. Gori et al., 2020 simulated all the physical iterations of multiple flood drivers for many synthetic TC events to produce probabilistic hazard maps, including a breakdown of rainfall versus surge-dominated flood zones. Bates et al., 2021 took this one step further and provided the first integrated and high-resolution view of the U.S. fluvial, coastal, and pluvial flood hazard, as a single layer, driven by both TC and ETC events. However, that study did not provide an estimate of the contribution of TCs to compound flooding. Booth et al., 2016 provided a breakdown between TCs and ETCs for the U.S. mid-Atlantic and Northeast Coasts based on observational data and showed that TCs typically dominate the most extreme events (e.g., 100-year event) while more common events (e.g., yearly) driven by ETCs are equally important. However, no study has yet estimated the relative contribution of TCs and ETCs to compound flooding using an integrated physics-based model that encapsulates inland and coastal processes across thousands of kilometers. The contributions of TC and ETC to compound flooding matter because the weather phenomena have different characteristics and patterns of movement, which affect the time scale, intensity, and spatial distribution of the flooding and, consequently, hazards and impacts.

In this chapter, we introduce, validate, and apply a workflow for analyzing and predicting compound flooding hazards, impacts, and risks for both tropical and extratropical cyclones. This approach is applied on large spatial scales and for dozens of realizations in the future climate and for seven SLR scenarios. This work is part of a broader project led by the U.S. Geological Survey (USGS) to map future coastal flooding and erosion hazards across the Southeast United States due to SLR and storms in a changing climate (Barnard et al., 2023a, Barnard et al., 2023b, Parker et al., 2023). This work focuses on the overland coastal flooding component of the study. The novelty of this manuscript is investigating the contribution of TC and ETC events to flood hazards and how this will change with SLR. The paper is structured as follows. First, we describe the regional domain in this study (Section 4.2). Second, the materials and methods applied in this workflow are described (Section 4.3). Third, the results are presented, which a) focus on the validation of tide, historical conditions, and Hurricane Florence, and b) on the application of the model to assess flood hazards and impacts on the future climate and SLR scenarios (Section 4.4). Lastly, we present our discussion and conclusions sections.

## 4.2. CHARACTERIZATION OF THE SOUTHEAST ATLANTIC COASTAL ZONE

The Southeast Atlantic Coast includes vast stretches of coastal and inland low-lying areas, the southern reach of the Appalachian Mountains, several high-growth metropolitan areas (e.g., Miami, Jacksonville, Savannah, Charleston, Wilmington, and Norfolk), and large rural expanses. This study focuses on the coastal zone of the Southeast Atlantic Coast, ranging from Biscayne Bay, Florida in the south up to the mouth of the Chesapeake Bay in the north (gray counties shown in Figure 4.1 panel A). The coastal zone is manually defined here as the area between the present-day shoreline and about the 10 m elevation contour relative to NAVD88. This Low Elevation Coastal Zone (McGranahan et al., 2007) typically extends about 100 km inland in this region.

The Southeast Atlantic Coast is rapidly urbanizing. For example, the Southeast Atlantic Coast contains many of the fastest-growing metropolitan areas in the country, including several of the top 20 fastest-growing urban regions in 2020 (United States Census Bureau, 2020). This shift is on top of existing sizeable urban city centers such as the greater Miami area (Miami-Dade, Broward, and Palm Beach counties). These trends toward a more urbanized Southeast are expected to persist, creating new vulnerabilities by increasing population exposure to areas in the flood hazard zone (e.g., 100-year flood map).

Flood hazards are expected to increase significantly in the future due to rising global sea levels (Vitousek et al., 2017b, Taherkhani et al., 2020; Sweet et al., 2022). The average global mean sea level (GMSL) has risen about 21-24 cm from 1880 to 2021 and are 97 mm above 1993 levels (NOAA, 2022). Moreover, its rise has been accelerating since 1990 (Dangendorf et al., 2017, Sweet et al., 2022). Moreover, GMSL rise is projected to continue to accelerate due, for example, to the increased mass loss of the Antarctic ice sheet (Le Bars et al., 2017). Recent downscaled projections for the Southeast Atlantic Coast by Sweet et al., 2022 suggested rates and an increase in local sea levels, relative to the 2000 range, of 0.3-0.5 m for 2050, 0.5-1.6 m for 2100, and 0.7-2.7 m for 2150. This will significantly alter flooding frequency in many already vulnerable communities.

Many cities across the Southeast Atlantic Coast are starting to plan for the impacts rising waters are likely to have on their infrastructure. For example, flood events in Charleston, S.C., have been increasing and are projected to increase substantially more in the future with sea-level rise; the city has prepared a Sea-Level Rise Strategy Plan (The City of Charleston, 2015). The city is also planning to undertake subsequential steps to further protect the city and its inhabitants from nuisance flooding.

Besides high tide events, which will be exacerbated due to SLR, the Southeast Atlantic Coast is regularly impacted by extreme weather events. TCs can bring strong winds, heavy rainfall, and high surges and waves in the summer and fall. Some of these TCs, such as Hurricane Andrew (1992), were extremely powerful and devastated communities in the Southeast Atlantic Coast. ETC events can also trigger a large amount of flooding due to wind and precipitation and subsequent storm surges and high waves. For example, during October 2015, a significant rainfall nor'easter caused historic flash flooding across North and South Carolina, resulting in \$2.5 billion in damages (NCEI; NOAA National Centers for Environmental Information, 2022) Hurricane Florence in 2018 resulted in \$24 billion in wind and water damage (NHC, 2019).

## 4.3. RESEARCH METHODOLOGY AND MATERIALS

### OVERVIEW

The modeling approach is based broadly on the Coastal Storm Modeling System (CoSMoS: Barnard et al., 2014, Barnard et al., 2019, Erikson et al., 2018, O'Neill et al., 2018), initially developed for the West Coast of the United States, but with significant modifications and updates to address the need to capture and resolve TCs as well as pluvial contributions to flooding. Figure 4.2 shows a conceptual framework as applied in this study. The numerical computation of overland flooding is based on the open-source hazard model SFINCS (Super-Fast INundation of CoastS; Leijnse et al., 2021). Five computational domains were created for the study region (Figure 4.1) based on topo-bathymetry, soil type, and land cover data across the region. Boundary conditions for water levels, discharges, and atmospheric conditions for tens of thousands of emulated extratropic and tropical storms were provided. First, we simulated a validation period and compared results to validation data to determine model skill (Section 4.4.1). Secondly, storms for the climate projection period were simulated for different sea level rise scenarios. Results per storm were used in an extreme value analysis to determine their frequency and downscaled at higher spatial resolution. High-resolution water depth maps were used as input for the open-source impact model Delft-FIAT (Flood Impact Assessment Tool) to determine impacts and risks. Compound flood hazards and impacts are described in Section 4.4.2. The latter includes a breakdown of the contribution of TC versus ETCs. In subsequent subsections, input data and individual methodological and model components are described, followed by detailed explanations of the numerical methods and computational framework.

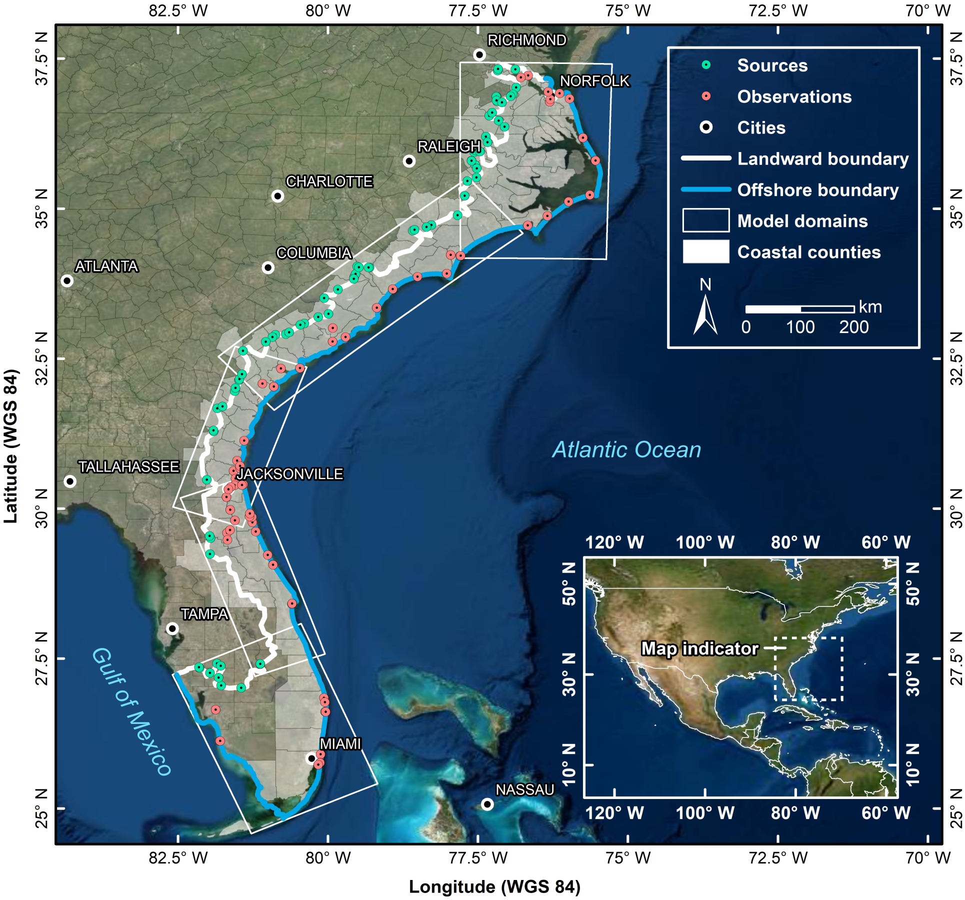

Figure 4.1: The study area (shown in gray) consists of the coastal counties in the United States Southeast Atlantic Coast states of Florida, Georgia, South Carolina, North Carolina, and parts of Virginia. Also, shown are the SFINCS (Super-Fast Inundation of CoastS) flood model domains (white outlines), offshore boundary (blue line), sources (green dots), and observation points (red dots). Model domains typically reach about 100 km inland to about 10 m above NAVD88 (the landward boundary of the model in white). Several major city names are presented to orient the reader. ©Esri, DigitalGlobe, GeoEye, i-cubed, USDA FSA, USGS, AEX, Getmapping, Aerogrid, IGN, IGP, swisstopo, and the GIS User Community.

## INPUT DATA

TOPO-BATHYMETRY, SOIL TYPE, LAND COVER Before generating the overland flood models, elevation datasets were extracted along the entirety of the Southeast Atlantic Coast from the area's Coastal National Elevation Database (CoNED) topographic model (Danielson et al., 2016; Tyler et al., 2022), Continuously Updated Digital

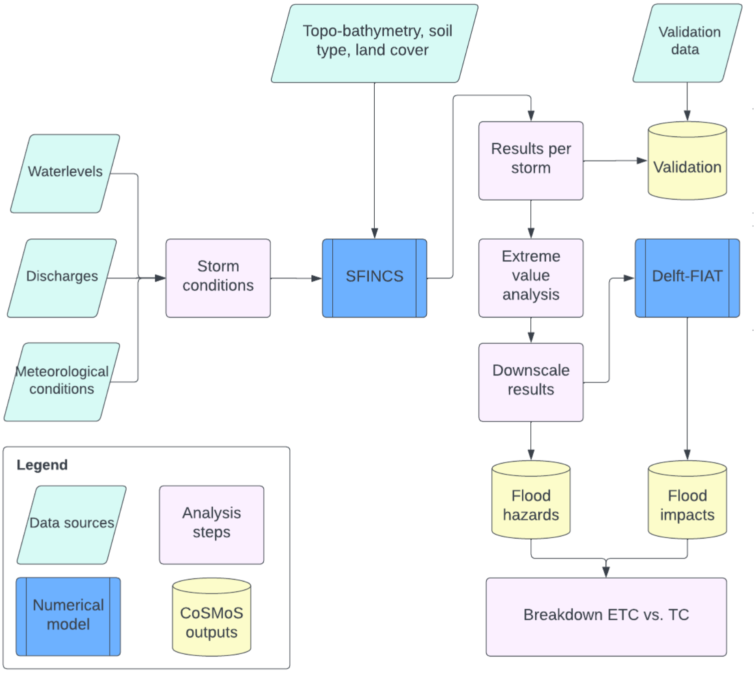

Figure 4.2: Conceptual workflow of the CoSMoS framework. Green data boxes are data sources, purple terminator boxes are analysis steps, predefined blue processes are numerical models SFINCS (hazard model) and Delft-FIAT (impact model), and yellow database symbols are the eventual outputs used as results.

Elevation Model (CUDEM; CIRES, 2014), and Coastal Relief Model (NOAA National Geophysical Data Center, 2001). Topo-bathymetric data were applied in the order listed to cover the entire area and fill data gaps. The model landward extent was manually determined to allow for minimal inflow boundary locations and typically reaches +10m elevation relative to NAVD88. The seaward extent was set to around NAVD88 –10 m. This depth suffices for overland flood modeling purposes. Maximum dune elevations along the coast were derived from CoNED and cross-checked with Doran et al., 2017 to include coastal flood defenses in the overland flooding models.

Information from the National Land Cover Database (Homer et al., 2020) was converted to roughness values using Manning's coefficients and approaches as described by Nederhoff et al., 2021b to define a spatially varying roughness map across each SFINCS model (see Table 4.2). Friction in open water was set to a typical coastal value of 0.020 and was thus not used for calibration purposes.

Data from the U.S. General Soil Map (STATSGO2; United States Department of Agriculture, 2020) provided the input for the Curve Number infiltration method used in the overland flooding models. STATSGO2 is an inventory developed by the U.S. Department of Agriculture and includes soil characteristics information across the Continental U.S. The hydrologic soil group (HSG) information and hydraulic conductivity (Ks) from the surface layer were used for this study. In particular, HSG information was combined with a landcover map to estimate the curve numbers according to United States Department of Agriculture, 1986.

BOUNDARY CONDITIONS: WATER LEVELS, DISCHARGES, AND METEOROLOGICAL CONDITIONS Water level time series were applied at the offshore boundary of the SFINCS models. These time series were derived from a linear superposition of the Global Tide and Surge Model (GTSM; Muis et al., 2016) outputs and wave setup; wave setup was computed with a parameterized empirical formula (Stockdon et al., 2006) and waves from the ERA5 reanalysis (Hersbach et al., 2020) and projection time-periods (Erikson et al., 2022). Statistical corrections were applied to improve modeled water level components. In particular, a correction on the tidal components, seasonality, and non-tidal residual was performed to improve the skill of the boundary conditions. For more information on this correction, one is referred to Parker et al., 2023. For the TC simulations, water levels from the coupled numerical hydrodynamic and wave model setup (ADCIRC+STWAVE), which includes tide, wind-driven surge, and wave-driven setup, were used.

Discharges for 74 rivers flowing into the study domain were derived from the NOAA National Water Model (NWM) CONUS Retrospective Dataset (NOAA, 2021). This river discharge reanalysis dataset was used directly for the hindcast (validation) period. River discharge for the projection period was derived using a relationship between NWM discharge and historical precipitation and applying this relationship to estimate future discharge rates. In particular, the upstream watershed location of each river was identified from the network of river-reach IDs used by the NWM (Liu et al., 2018). For each watershed, cumulative precipitation was computed and the best correlation using a linear fit with a variable time lag between cumulative daily precipitation and discharge was found. This linear fit was then applied to the projected precipitation, yielding projected future discharge for each of the streams. The projected future discharge was bias-corrected, based on the historical NWM discharge using empirical quantile matching (Li et al., 2010). A baseflow, as calculated from NWM using a digital filter method from the HydRun toolbox (Tang and Carey, 2017), was also applied in the TC simulations. Baseflow was included to get an estimate of discharge-driven compound flooding during TCs.

All the model domains were forced with the same meteorological conditions (wind, sea-level pressure, and rainfall). The meteorological conditions used for the hindcast (validation) period (1980–2018) were based on ERA5 (Hersbach et al., 2020) for wind and pressure. For the same period, the North American Land Data Assimilation System (NLDAS; Chang et al., 2012 was used for rainfall. For the projection period (2020–2050), conditions were applied from the Coupled Model Intercomparison Project - Phase 6 (CMIP6). In particular, an ensemble of three CMIP6 models was used from the High-Resolution Model Intercomparison Project (HighResMIP) based on the SSP5-8.5 greenhouse gas concentration scenario: CMCC-CM2-VHR4 (Scoccimarro et al., 2017), GFDL-CMC4C192 (Guo et al., 2018), and HadGEM3 (Roberts, 2019). These models were chosen because of their increased atmospheric and ocean resolution as fine as 25-50 km, which is expected to better resolve coastal storm events that are not adequately resolved with the native resolution of most GCMs (Roberts et al., 2020). The chosen CMIP6 models, at the time of this study, had data from 2020–2050. All 31 years of data of all three models were used for this study. No bias corrections were performed on the projection period meteorological conditions (wind, pressure, and rainfall data fields from CMIP6). Implications of the lack of bias correction for CMIP6 are described in the discussion section.

Multi-decadal-scale hindcast, reanalysis, and General Circulation Models, such as ERA5 and CMIP6-HighResMIP, allow for an analysis of the long-term evolution of the climate and how it affects global processes. However, model resolutions are often insufficient to fully resolve TCs and have a limited temporal length (see introduction). The U.S. Army Corps of Engineers (USACE) Coastal Hazards System (CHS; Nadal-Caraballo et al., 2020) synthetic TC dataset was applied to overcome these limitations. The CHS (https://chs.erdc.dren.mil) is primarily a probabilistic analysis and machine learning framework based on the Joint Probability Method (JPM). It also encompasses high-resolution numerical simulation of thousands of synthetic TCs under current and future climates. For more information on the CHS and the JPM method, refer to Nadal-Caraballo et al., 2022. In the present study, the probabilities of the CHS synthetic TCs were updated to reflect climate change in which more intense hurricanes are likely to be observed more frequently in the study area from northern Florida northward. This change is related to higher sea surface temperatures. For information on how this was done, one is referred to Appendix 4.6. Rainfall for TCs was based on the Interagency Performance Evaluation Task Force Rainfall Analysis (IPET, 2006) method. The IPET method relates pressure deficit to rainfall which decreases exponentially as a function of the TC radius. Within the eye of the storm, rainfall rates are constant. No asymmetry and/or rainfall bands are included in this method.

For the historical periods, we assumed that ERA5-NLDAS had sufficient resolution to resolve TC activity for validation purposes (Dullaart et al., 2020). On the other hand, for the projection period, we assumed TC events were missing in CMIP6 and only ETCs were included (Han et al., 2022).

EXPOSURE AND VULNERABILITY DATA Impact computations for computed flood maps were performed with HydroMT-FIAT, an open-source python wrapper (Eilander and Boisgontier, 2022) for the Delft-FIAT flood impact and risk model. Delft-FIAT (Flood Impact Assessment Tool) is a flexible open-source toolset for building and running flood impact models which are based on the unit-loss method (de Bruijn, 2005). Inputs for FIAT are a hazard layer (water depth), exposure layer (object map with population), and vulnerability (depth-damage curves).

The exposure layer used in Delft-FIAT was based on a method that combines the Global Urban Footprint (GUF; Esch et al., 2017) for the presence of buildings and the Global Human Settlement Layer (GHSL; Florczyk et al., 2019) for population density. In other words, the GHSL estimates the number of people in certain areas, which are distributed over the building footprints provided by GUF. The result is a method that can produce an exposure layer for any place on the globe. In this chapter, we calibrated the population per county using the 2020 Census, which resulted in a total population size of 18,828,520 for the area of interest. Vulnerability curves are based on Huizinga et al., 2017. Flood impact is defined here as the population affected via the vulnerability curve. Flood risk is defined as the product of the probability of a flood event and potential adverse consequences for humans (Kron, 2005).

### VALIDATION DATA

A comprehensive set of validation data was used to assess model skill. First, all observed 6-minute interval water levels from all long-term National Oceanic and Atmospheric Administration (NOAA) water level stations (CO-OPS - NOAA Tides and Currents, 2022) between 1980 and 2018 for the area of interest were collected and processed into continuous time series. In total, 24 NOAA stations were included in the validation (see Figure 4.1, Figure 4.17, or Figure 4.18 for their locations).

The observed water levels were used to determine tidal constituents using UTide (Codiga, 2011) for each NOAA gauge. In addition, the XTide database (retrieved via Delft Dashboard; van Ormondt et al., 2020) was also used to identify 68 locations with observed tidal amplitude and phases for model validation. See Figure 4.17 for the location of both the NOAA and XTide stations.

Special attention was given to validating Hurricane Florence (2018), which made landfall near Wilmington, N.C. For this singular event, an additional 156 pressure gauges and 396 high water marks (HWM) made available by the U.S. Geological Survey (USGS) were also used to validate the model (U.S. Geological Survey, 2021; see Figure 4.4 for their locations).

### NUMERICAL METHOD: OVERLAND FLOODING WITH SFINCS

OVERVIEW SFINCS (Leijnse et al., 2021) was successfully applied to simulate compound flooding, including dynamic hydraulic processes such as tidal propagation, rainfall, and river runoff while maintaining computational efficiency (e.g., Sebastian et al., 2021) and was therefore chosen to predict overland flooding for this study. The physics model dynamically computes water propagation throughout the domain with a computational time step of several seconds (varies per simulation). High-resolution topo-bathymetry and land roughness were included in the native 1x1 meter resolution utilizing subgrid lookup tables (Leijnse et al., 2020). The continuity and momentum computations were performed on a coarse 200x200 meter resolution grid to save computational expense. Sub-grid bathymetry features were included to account for maximum dune height based on the DEM to control overflow during storm conditions. Leijnse et al., 2020 showed water level computations for

Hurricane Irma (2017) were still accurate when including subgrid features based on the high-resolution elevation data. The SFINCS model was not calibrated but instead applied with default parameters throughout this study. Advection was deactivated to save computational time but was not found to influence the results (typical in non-wave-driven flooding applications; Leijnse et al., 2021).

Derived overland maximum flood levels were subsequently downscaled to 10x10 meter resolution water depths using the nearest neighbor interpolation for the water level in combination with a box filter of 3 neighboring grid cells. The five computational SFINCS domains overlap to overcome any possible boundary effects. Results from overlapping model domains were merged by taking the average water level.

The water levels (described by the tide, non-tidal residual; NTR, and wave setup components) were imposed at the offshore boundary (see Figure 4.1 for the location). Hence, we apply SFINCS not just as an overland flood model but also to propagate water levels through the domain, solving the same governing equations describing overland flooding as well as being responsible for tidal propagation (Leijnse et al., 2021). In particular, the model accounts for various factors influencing propagation, such as bathymetry (water depth), bottom friction, Coriolis force, wind stress, and external boundary conditions. Water levels were imposed approximately every 500 meters along-shore at the ocean boundary. Incoming short and infragravity waves were not accounted for (except through statistical downscaling of wave setup from offshore wave conditions) since dynamically downscaling this was computationally prohibitive (increasing computation times about 1000-fold). Implications of the model setup are described in the discussion section. River discharges are accounted for as a vertical point source, linked to the closest grid cell center, and at each time step mass according to the discharge time series is added.

CURVE NUMBER METHOD Infiltration was computed at every computational time step with the newly implemented Curve Number method in SFINCS. This method is based on the SCS (Soil Conservation Service, currently known as Natural Resource Conservation Service) Curve Number method for evaluating the volume of rainfall resulting in direct surface runoff. SCS was first developed in 1954 and is described in most hydrology handbooks and textbooks (e.g., Bedient et al., 2013). This method was added to SFINCS to take advantage of most practicing engineers' familiarity with this method and the availability of tabulated curve numbers for a wide range of land use and soil groups. The Curve Number method is a combined loss method that estimates the net loss due to interception, depression storage, and infiltration to predict the total rainfall excess from a rainfall event.

The Curve Number model uses the following equation to relate total event runoff Q to total event precipitation P.

$$Q = \frac{(P - I_a \cdot S_{\max})^2}{P + (1 - I_a) S_{\max}} \tag{4.1}$$

$$S_{\max} = \left( \frac{100}{CN} - 10 \right) \times 0.0254 \tag{4.2}$$

in which Ia is the initial abstraction percentage (default 20%), CN is the Curve Number, and S is the retention after runoff begins. Note that here we directly convert the original curve number in inches to meters via the computation of Smax. Since SFINCS is a continuous model, the Curve Number computation is done at a time-step level (order of seconds). It computes the infiltration rate by subtracting the total precipitation with runoff and dividing by the time step (forward differences).

The moisture storage capacity of the soil can be depleted during wet periods and replenished during dry periods. To model this behavior with the Curve Number method, whether it rains or not, we implemented the effective storage capacity (Se), which is tracked during the simulation. During rainfall, the capacity is slowly filled (Equations 4.1 and 4.2). During a period with no precipitation, the effective moisture storage capacity is assumed to be replenished at a rate proportional to Smax. Here, we related the recovery constant to the soil saturation akin the approach used in the Storm Water Management Model (SWMM; U.S. US Environmental Protection Agency (US EPA), 2019). In particular, the continuous recovery kr is estimated with the following equation $k_r = \sqrt{K_s}/75$, in which Ks is the hydraulic conductivity in inch/hr and kr is the recovery in the percentage of Smax per hour. At the start of new simulations, the cumulative variables are reset to 0, and Se is set equal to 50% of Smax. Implications of the 50% saturation assumption are described in the discussion section.

The Curve Number infiltration methodology goes hand-in-hand with precipitation. In particular, we first compute the gross rainfall rate per grid cell. Second, we compute the infiltration rate with the methodology outlined in this paragraph. Lastly, we compute the effective rainfall rate by subtracting the infiltration rate from the gross rainfall. The effective rainfall is accounted for by adding the net water volume at each grid cell and each time step as part of the continuity updating step in SFINCS.

## COMPUTATIONAL FRAMEWORK

STORM SELECTION Two slightly different approaches were followed to define the storms. The first one is used to define storms to be run in the validation period. The second one is used for the climate projection period.

First, using all the observed water level data between 1980 and 2018 retrieved from all NOAA tide gauges within the region, the observed linear sea level trend was removed from each individual gauge. In particular, for stations with at least 10 years of data, we determined the linear trend and corrected this trend so all observations are applicable to the current MSL. Next, unique observed storm peaks were detected via the peak-over-threshold method by finding, on average, three maximum water levels yearly per gauge (39 years x 3 peaks = 117 peaks for most gauges). The threshold was detected automatically on a gauge-by-gauge basis and set at a relatively low value of three. This ensures the inclusion of all significant events over decadal time periods, while keeping computational constraints in mind of not being able to model all events. A minimum of seven days between peak events at each gauge was imposed to guarantee independence between the storms. This resulted in a total of 198 historical storms, used here for validation purposes. In regard to duration, each validation storm is simulated for at least seven days around the middle of the peak when the storm is characterized by a single peak, and for longer in case of containing multiple peaks. In this case, the minimum and maximum peak date defines the duration of the storm and, consequently, the simulation time. In regard to the hydrograph characterization of the storm, the simulation starts at low water of NAVD88 – 0.5 m to avoid low-lying flooding areas since SFINCS initializes water levels across the domain based on the starting water level.

Second, for the 31 years of climate projection record, particular storms per CMIP6 model, were selected based on three independent criteria. In a similar fashion as for the observed data, for each offshore water level boundary point, we detect water level peaks in which the threshold is set to identify, on average, three extreme water level events yearly. A similar method was used for discharge and rainfall. The peaks were identified for all 74 discharge points and for the total rainfall per SFINCS domain, combined, and run similarly to the validation runs. Common peaks were found as a result of these methods; however, only the unique storms were combined per SFINCS domain, resulting in 263 to 347 events per domain per CMIP6 model. This method was chosen to reduce computational expense since, in this way, we simulated around 20% of the total record and could run simulations in parallel. The main difference between both periods is that fluvial and pluvial data were included as criteria for selecting storms in the climate projection period. However, for the validation period the available validation data were limited to tide gauges and therefore, only these data were used to define storms.

For the TC simulations, a total of 1059 tracks were included. Each track had a probability, location of landfall, heading, forward speed, and intensity based on the synthetic dataset from Nadal-Caraballo et al., 2020. Specific TCs were neglected if a track resulted in less than 20 cm of storm surge everywhere in each domain. The number of neglected tracks varies per domain (799 to 933 from the total of 1059 were included).

EXTREME VALUE ANALYSIS Flood hazards per numerical (SFINCS) grid cell were determined using empirical estimates of exceedance probabilities, without regressing return period estimates using any extreme value parametric distribution. In this way, the full set of potential candidates for compound flooding is simulated without making any a priori inference on the underlying processes beyond compound flooding. The maximum computed water level, maximum depth-averaged flow velocity, and wet duration per event and per grid cell were stored. Each storm is ranked on maximum water level, gives the same frequency resulting in an estimate of the probability of m/(n+1) in which m is the ranking and n is the number of years, here 31 (i.e., Weibull plotting position; Weibull, 1939). TC probability per simulation is derived from the CHS JPM-based input dataset, and the probability is estimated by integrating the discrete storm probability weights over the range of predicted water levels. Per sorted event, the associated maximum depth-averaged flow velocity and wet duration are provided to inform possible conditions during these events.

To combine ETC and TC runs, we first determined the extreme value distribution for high water per grid cell for ETC and TC runs separately. For the three CMIP6 models, we determined the extreme value distribution per model and used the ensemble mean as the estimate for ETC. Afterward, the extremes were combined by taking the inverse of the sum of the TC and ETC yearly exceedance frequency. We follow Dullaart et al., 2021 and for a given high water, we calculated its return period as follows:

$$RP(x) = \frac{1}{\frac{1}{RP_{ETC}(x)} + \frac{1}{RP_{TC}(x)}} \tag{4.3}$$

where RP is the return period in x years of high water. $RP_{TC}$ and $RP_{ETC}$ refer to the return period of the TC and ETC water level at the same value of water level. Examples of the probability of high water levels by ETC, TC, and jointly for six stations throughout the domain can be found in the Appendix (Figure 4.15). No storm conditions were based on a simulation with a spring-neap tidal cycle of 30 days. During this stimulation, a baseflow from rivers was included but the effects of waves and rainfall were excluded. No-storm simulations were included to provide an estimate of nuisance flooding.

### SIMULATION PERIODS AND COMPUTATIONAL EXPENSE

Flood predictions were made for two time periods: historical (1980-2018) and future projections (2020-2050).

For validation of the model skill, historical conditions were simulated for 1980–2018. First tidal conditions were simulated and compared to NOAA and XTide stations across the U.S. Southeast. This simulation is based on a 365-day-long simulation without meteorological conditions and baseflow discharge rates for the year 2016. Secondly, 198 historical storms were simulated to assess model skill in reproducing extreme water levels. Thirdly, an in-depth analysis of Hurricane Florence (2018) was performed.

Flood hazard, impact, and risk computations were performed for 2020–2050 using CMIP6 ETC storm events outlined above and TCs from the USACE-CHS framework. Additionally, all ETC and TC model simulations were repeated for seven SLR scenarios: 0-, 0.25-, 0.50-, 1.00-, 1.50-, 2.00- and 3.00-meter compared to the year 2005. These scenarios cover the range of plausible sea level projections for the U.S. Southeast through 2100, as reported by Sweet et al., 2022.

Model simulations were performed on the Deltares Netherlands Linux-based High-Performance Computing platform using 54 Intel Xeon CPU E3-1276 v3. On average, a 7-day simulation (typical duration for an individual event) took about 41 minutes on a single core. Running all 80,000 events (all TCs + ETCs for seven SLR scenarios) took 31 days.

### MODEL SKILL

To quantify the skill of the model to reproduce water levels, several accuracy metrics were calculated: model bias, mean-absolute-error (MAE; Equation 4.4), root-mean-square-error (RMSE; Equation 4.5) and unbiased RMSE (uRMSE; RMSE with bias removed from the predicted value)

$$\mathrm{MAE} = \frac{1}{N}\sum \left| y_i - x_i \right| \tag{4.4}$$

$$\mathrm{RMSE} = \sqrt{\frac{1}{N}\sum (y_i - x_i)^2} \tag{4.5}$$

where N is the number of data points, yi is the i-th predicted (modeled) value, x is the i-th measurement.

## 4.4. RESULTS

### 4.4.1. MODELING SYSTEM VALIDATION

TIDAL VALIDATION Model skill in reproducing tidal amplitudes and phases is assessed at 24 NOAA stations and 56 XTide stations across the area of interest and presented in

Figure 4.17 and Table 4.3 in the Appendix. The model framework can reproduce tide with a median MAE of 8.3 cm and a median RMSE for high water of 9.9 cm (median computed over the different stations). Across the region, MAE is typically lower than 20 cm (80% of the stations). The most significant model error is shown at Savannah, GA, (MAE of 32 cm). The model error generally increases farther away from the ocean boundary in narrow estuaries and harbors. The model-computed tidal amplitude at these locations is typically underestimated compared to observations. We hypothesize that the underestimation of tidal amplitudes has to do with the a) SFINCS model resolution and b) high roughness values from land that may be mapped to the channel in some locations due to the coarse resolution of the land cover map.

STORM VALIDATION ACROSS THE REGION Four examples of time series of modeled and observed water levels are presented in Figure 4.3 for large historical hurricanes for stations from north to south: Irene (2009), Hugo (1989), Matthew (2006) and Wilma (2008). Observed and modeled water levels and tides are shown. Tides are based on astronomical components only. The tidal component of the water levels visually match well the observations before the hurricane arrival, except for Money Point, VA. (8639348). At this station, there is an underestimation of the tidal amplitude, and the tide arrives too late (i.e., overestimating phase). The lower skill for tidal modeling at 8639348 can also be seen in Table 4.3. The peak water levels are particularly skillful. Computed NTR is also found to match well with the observations since the median MAE increased from 8.3 cm for tide only to 11.9 cm for the water level signal over all storms.

The accuracy of the proposed model framework is presented in Table 4.1 and Figure 4.18. Model skill is good, with a median MAE between 8 and 20 cm (25-75 percentile). However, biases per station do exist. For example, Duck, N.C. (8651370), has a median bias of +25 cm, while I-295 Buckman Bridge, FL (8720357) has a median bias of -19.2 cm. We hypothesize that Duck's overestimation is driven by the inclusion of an open-coast wave setup, which is not measured at the NOAA station (see Parker et al., 2023). On the other hand, the underestimation at the I-295 bridge, being situated inland along the St. John's River, might be driven by an underestimation of pluvial/fluvial processes or by underestimation of tide.

Table 4.1: Overview of skill scores (mean-absolute-error; MAE, unbiased root-mean-square error; uRMSE and bias) for 24 NOAA observations across 198 events from 1980-2018. The number of storms simulated is listed as ’n’. Skill scores are in cm and computed as the median over the storm events (first value) and the standard deviation is presented as the (second value).

| **IDcode** | **Name** | **n** | **MAE [cm]** | **uRMSE [cm]** | **bias [cm]** |
|---|---|---|---|---|---|
| 8638610 | Sewells Point | 84 | 11.7 ± 4.4 | 10.6 ± 1.6 | -8.0 ± 8.4 |
| 8639348 | Money Point | 52 | 22.2 ± 3.5 | 20.2 ± 2.7 | -15.0 ± 6.9 |
| 8651370 | Duck | 84 | 29.0 ± 10.9 | 22.5 ± 5.1 | 25.2 ± 13.5 |
| 8652587 | Oregon Inlet Marina | 60 | 14.7 ± 5.7 | 9.6 ± 3.5 | -13.8 ± 7.2 |
| 8656483 | Beaufort | 84 | 9.7 ± 3.1 | 9.4 ± 2.8 | -2.5 ± 7.3 |
| 8658120 | Wilmington | 68 | 23.9 ± 4.4 | 26.3 ± 3.7 | -3.0 ± 13.6 |
| 8658163 | Wrightsville Beach | 45 | 17.7 ± 8.3 | 12.8 ± 4.7 | 16.2 ± 9.7 |
| 8661070 | Springmaid Pier | 68 | 14.5 ± 6.6 | 13.8 ± 4.1 | 11.3 ± 9.5 |
| 8662245 | Oyster Landing | 25 | 10.5 ± 2.8 | 11.2 ± 2.2 | -0.5 ± 6.4 |
| 8665530 | Charleston | 69 | 12.1 ± 4.2 | 11.0 ± 2.8 | -8.5 ± 8.4 |
| 8667633 | Clarendon Plantation | 16 | 41.4 ± 7.8 | 47.1 ± 8.3 | -11.9 ± 7.0 |
| 8670870 | Fort Pulaski | 86 | 14.4 ± 3.3 | 14.9 ± 3.0 | -3.1 ± 8.4 |
| 8720030 | Fernandina Beach | 50 | 10.2 ±4.8 | 10.2 ± 4.1 | -1.4 ± 9.1 |
| 8720145 | Edwards Creek | 7 | 14.6 ± 1.9 | 14.2 ± 1.9 | -4.9 ± 8.5 |
| 8720218 | Mayport | 34 | 8.6 ± 4.2 | 9.0 ± 3.3 | -0.8 ± 8.5 |
| 8720357 | I-295 Buckman Bridge | 30 | 17.6 ± 7.1 | 7.0 ± 2.7 | -19.2 ± 12.4 |
| 8721147 | Ponce De Leon Inlet | 7 | 6.6 ± 2.5 | 6.2 ± 1.5 | 4.4 ± 3.6 |
| 8721604 | Trident Pier | 29 | 10.5 ± 3.4 | 11.0 ± 1.6 | 2.7 ± 8.1 |
| 8722548 | Palm Beach | 7 | 11.6 ± 4.2 | 12.2 ± 5.5 | 4.8 ± 7.6 |
| 8722588 | Port of West Palm Beach | 7 | 10.3 ± 6.3 | 13.3 ± 6.9 | 10.3 ± 7.9 |
| 8722669 | Lake Worth ICW | 7 | 12.4 ± 5.2 | 11.1 ± 4.7 | 12.4 ± 6.8 |
| 8723214 | Virginia Key | 39 | 8.8 ± 4.7 | 7.8 ± 2.9 | 4.3 ± 8.8 |
| 8725110 | Naples | 57 | 8.8 ± 3.5 | 8.6 ± 3.1 | -1.9 ± 8.0 |
| 8725520 | Fort Myers | 59 | 8.2 ± 4.3 | 7.7 ± 2.7 | -3.2 ± 8.0 |
|  | Median |  | 11.9 | 11.1 | -1.6 |

HURRICANE FLORENCE In this subsection, the SFINCS model setup is validated for Hurricane Florence (2018). The spatial extent of this detailed validation covers about 500 km alongshore and centered around Wilmington, N.C., where Florence made landfall, and includes all data available within the cross-shore extent of the SFINCS domains (in the order of 100 km). Figure 4.4 panel A shows the orientation compared to the rest of the study area including the track of Florence. Merged model results for SFINCS domains 4 and 5 were used in this section. Figure 4.4 panel B presents the stations used for the in-depth validation of Florence, a combination of permanent NOAA gauges and USGS deployed rapid deployment gauges and high water marks (HWMs; U.S. Geological Survey, 2021). The validation focuses first on

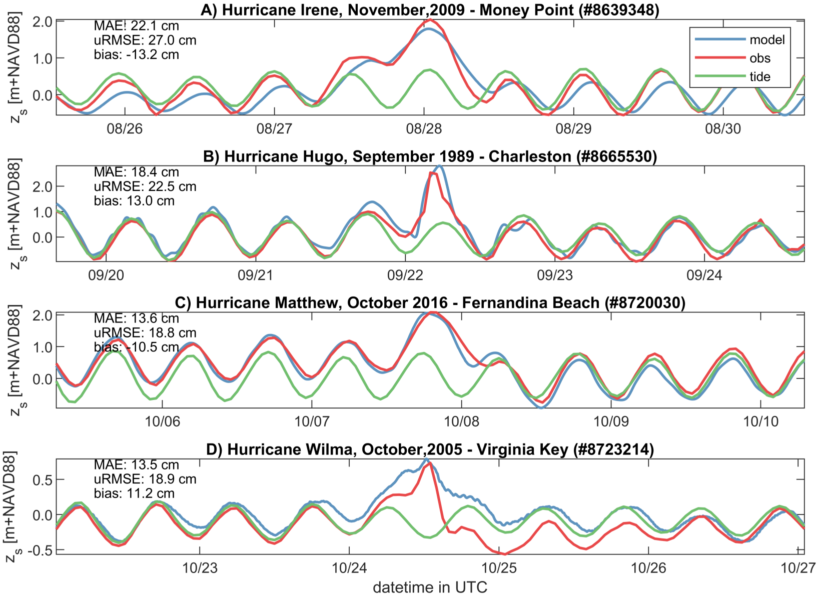

Figure 4.3: Time series of observed (red), computed (blue), and tidal (green) still water level for four events across the area of inter-est. Panel A depicts Hurricane Irene (2009) in time series at Money Point, Virginia. Panel B shows Hurricane Hugo (1989) at Charleston, South Carolina, C Hurricane Matthew (2016) at Fernandina Beach, Florida, and D depicts Hurricane Wilma (2005) at Virginia Key, Florida. Stations are listed from north to south. Skill scores are presented in the top left corner.

reproducing six time series in the area, after which the HWMs are discussed. These time series are randomly chosen across a range of stations to show coastal, riverine, and mixed locations with various degrees of model skill

The time series of the water levels for six gauges around the landfall of Hurricane Florence are shown in Figure 4.5. The first gauge shows Oyster Landing, N.C. (8662245). At this station, the model reproduces the tide well (as shown in previous sections). Oyster Landing is located southwest of the location of landfall, which explains the decrease in water levels (setdown) caused by offshore directed wind after landfall of the TC. The second gauge, USGS SCHOR14330, located in a local creek and about 1 km from the shoreline, mainly shows the impact of rainfall runoff, albeit slightly influenced by tides. The model can reproduce both signals. Gauges 3, 4, and 6 show a similar pattern of tidal oscillation with a slight increase in mean water level

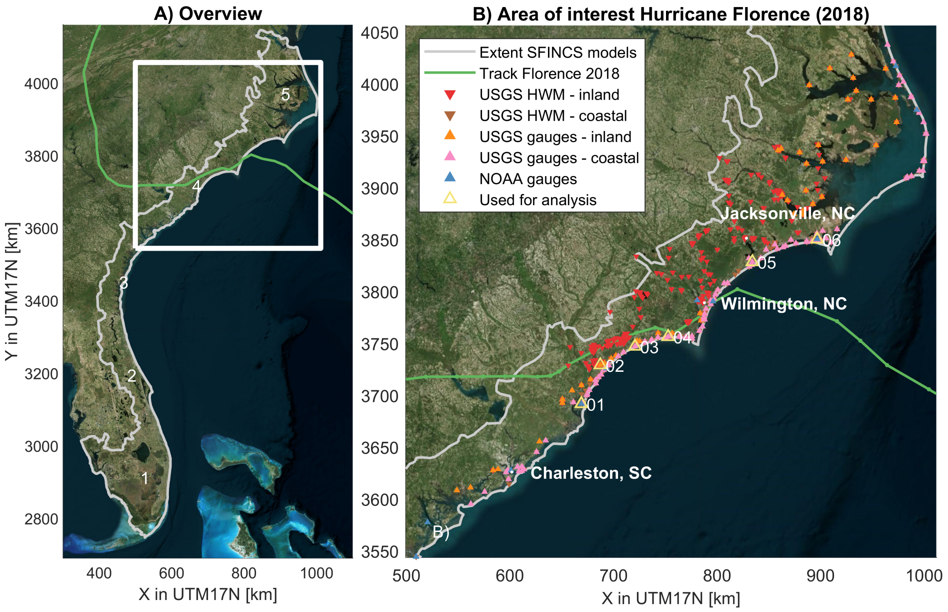

Figure 4.4: Observational data and model extent for the detailed validation of Hurricane Florence (2018). Panel A: overview figure for the entire study area showing the five different SFINCS (Super-Fast INundation of CoastS) domains, the track of Hurricane Florence (green) and the area of interest Panel B: USGS stations used for the validation of Hurricane Florence model re-sults. USGS gauges have been divided into coastal (pink) and inland (orange) locations based on the classification given when the data were released. Gauges and high water marks (HWM) are marked, respectively, with upward-pointing and downward-pointing triangles. The best track is based on International Best Track Archive for Climate Stewardship (IBTrACS; Knapp et al., 2010).The coordinate system of this figure is WGS 84 / UTM 17 N (EPSG 32617). ©Microsoft Bing Maps.

with the hurricane's landfall. These temporarily placed gauges were only partially inundated, so they only provided a signal to compare the model with at higher water levels. Gauge 5 was in a salt marsh near the town of Sneads Berry, N.C., close to the New River estuary. The observations show a tidally influenced riverine behavior where the water level rises due to rainfall until several days after landfall, after which time the water level slowly falls again. The model underestimates the peak of the water level, possibly due to the underestimation of the TC precipitation boundary condition. Moreover, the model drains too quickly compared to observations, which could be caused by hydrological processes such as infiltration via the Curve Number method or underestimation with friction.

High water marks are compared to modeled water depth and water level in Figure 4.6. A clear flooding pattern of the hinterland is both computed and observed (Figure 4.5 - panel A). The model underestimates the HWM (4.5 - panel B). Based on the division between coastal and riverine points, the under-estimation is already present in the coastal points (30 cm); however, the bias reaches 91 cm for the riverine points. These biases affect the model skill, resulting in a MAE for all the points of 69 cm. A similar result is shown for the linear regression fit (green line), which has an offset that gets worse with higher water levels. It is hypothesized that this underestimation is driven by a difference in modeled (input) and actual precipitation (modeled max 70 cm versus more than 90 cm observed) and river discharge. This situation would explain why the time-series model skill is higher than HWM skill.

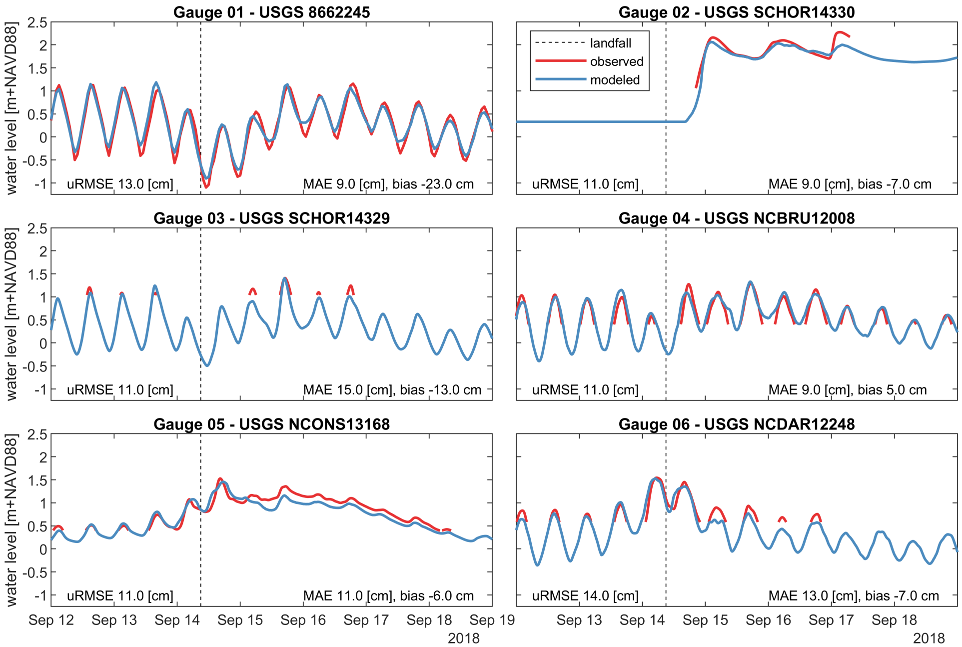

Figure 4.5: Water level time series as observed (red) and modeled (blue) during Hurricane Florence (2018). Dashed black line is mo-ment of landfall. The location of the six gauges is shown on the map in Figure 4.4 and stations are listed from west to east.

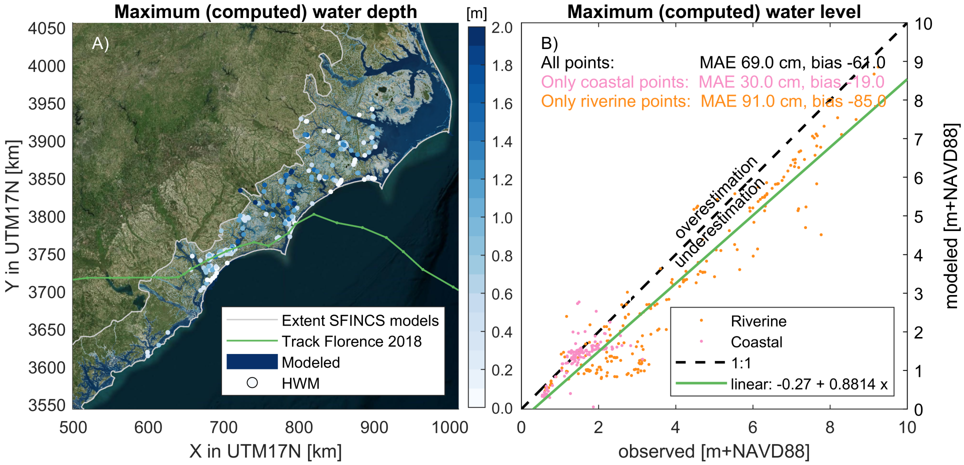

Figure 4.6: Validation of the maximum water depth and level for Hurricane Florence (2018). Panel A: maximum water depth with high water marks (HWMs; circles) compared to spatial color for model. Panel B: maximum water level for the same HWMs. Different colors represent either coastal (pink) or riverine (orange) points. 'Linear' is a least-squares linear fit on all the data points and shows tendency for underestimation of the modeled HWM (negative bias) that increases with water level. Note the increasing dealignment between the green line and dashed black line. Model estimates of extreme water levels have substantial scatter and bias which increases with water level. The latter explains the higher error for riverine versus coastal points. The coordinate system of this figure is WGS 84 / UTM 17 N (EPSG 32617). ©Microsoft Bing Maps.

## 4.4.2. STRATEGIC ANALYSIS OF FLOODING

FLOOD HAZARDS While flood hazards are calculated on a high detail level (tens of meters) for over 1000 km of coastline, for clarity only a limited region around Charleston, S.C. are presented, as an example of the output (Figure 4.7). Panels A and B show the water level (A) and Panel B the water depth, both (A and B) for a return period of 50 years and the SLR scenario of 100 cm. Panel C presents the range of flooding for progressively larger events for the SLR scenario of 100 cm with colors indicating a flooded grid cell and associated lowest return frequency. Finally, panel D presents the progressing effects of sea level for a 50-yr storm. The color represents which SLR scenario, given a 50-year event (2% chance per year), results in flooding. Data for all return periods and SLR scenarios can be accessed via Barnard et al., 2023a and Barnard et al., 2023b.

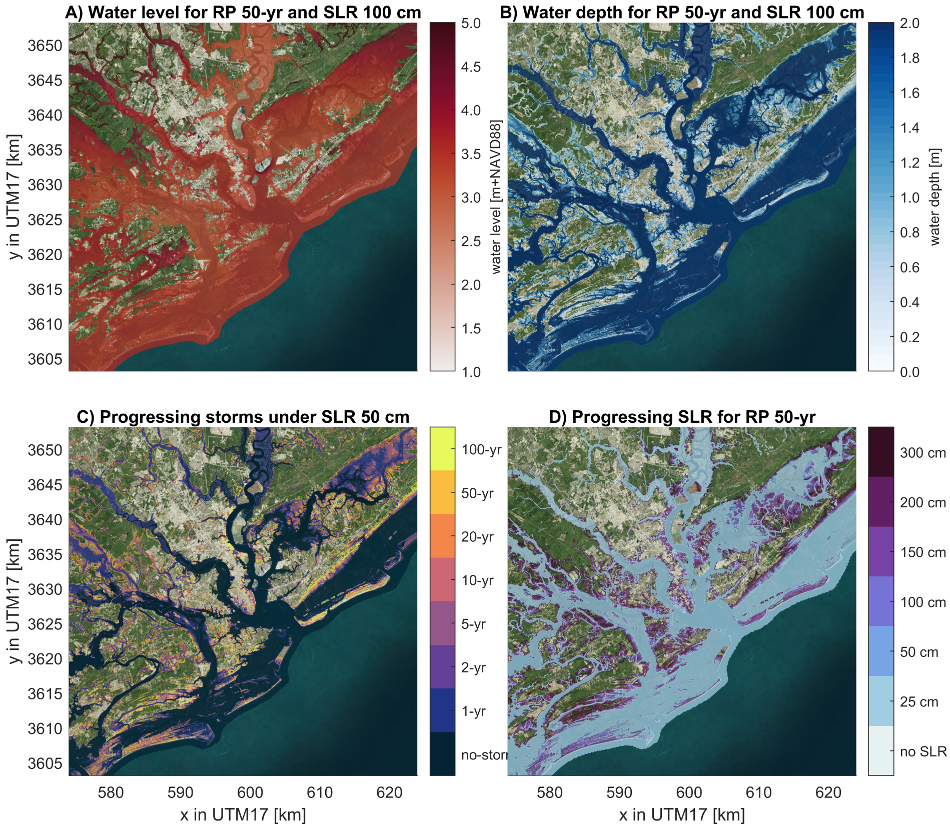

Figure 4.7: Example output for Charleston, S.C.. Panel A: Water level for a 50-year return period storm in combination with a 100 cm SLR. Panel B: Water depth 50-year return period storm in combination with a. Panel C: progressing flood extent for different storm frequencies for a SLR scenario of 100 cm. Panel D: Progressing flood extent for different SLR scenarios for a 50-year return period. The progressing flood extent (C and D) shows with which lowest storm frequency or sea level rise scenario the area gets flooded. The coordinate system of this figure is WGS 84 / UTM 17 N (EPSG 32617). ©Microsoft Bing Maps.

A regional analysis of flood-hazard area (minimum threshold water depth of 10 cm) over the entire U.S. Southeast is shown in Figure 4.8. Only grid cells with a bed level above NAVD88 + 1 m are considered, to exclude low-lying flooding of natural systems. The area of interest is defined as the Low Elevation Coastal Zone above NAVD88 +1 m. Flood hazards can occur during no-storm conditions (i.e., flooding during regular tides together with SLR, consider here as nuisance flooding, shown in panel A) or storm conditions with a specific return period (panel B). A relatively small area currently gets flooded under regular (non-storm) conditions, representing

2,000 km2 or 1% of the area of interest. This flood hazard area increases significantly with SLR. The increases with SLR are initially small but increase at more than a linear rate. For example, an increase of the mean sea level from the current level to 50 cm increases the non-storm flood hazard by 560 km2 (+26%). The same mean sea level increase from 100 to 150 cm results in an increase of flooded area by >4,200 km2 (+750% increase). In other words, increasing sea level inundates disproportionally more and more area. Storm hazards increase with return period and rising sea level (Figure 4.7 - panel B). Yearly storm events without SLR (SLR of 0 m) flood around 13,000 km2 or 6.2% of the study area and are projected to increase to 8.0 and 11.7% for 100 and 200 cm of SLR, respectively. The 100-year flood event, without SLR, floods almost 4.5 times as much area compared to the annual event. Moreover, Figure panel B of4.8 shows a well-described phenomenon in the scientific literature (e.g., Vitousek et al., 2017b), where, for instance, a 20-year flood hazard at current sea level will, with 200 cm SLR, be the new 3-year event (i.e., decreased return period).

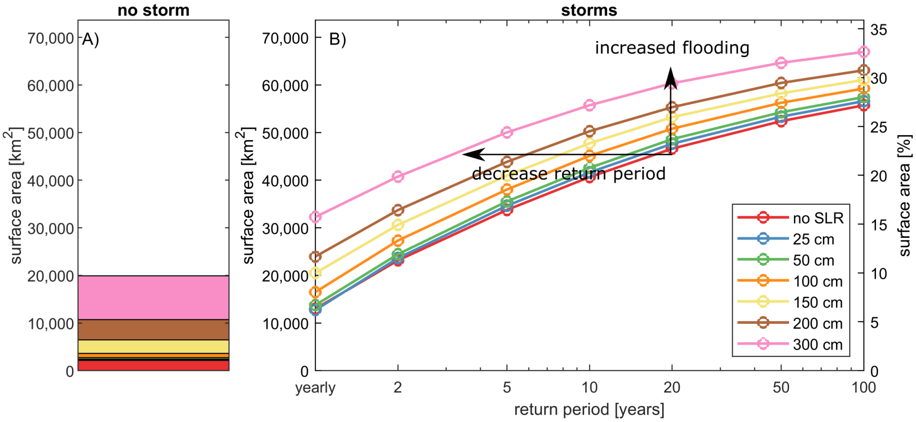

Figure 4.8: Flood hazard for the no storm (daily; tide-only) condition (left panel A) and storms (right panel B). Color depicts different sea level scenarios of current sea level (red), 25 cm (blue), 50 cm (green), 100 cm (orange), 150 cm (yellow), 200 cm (brown) and 300 cm (pink). Note that A and B share the same y-axes. For absolute numbers use the left y-axis and for a relative of the total the right y-axis. Hazards increase with increasing SLR scenarios, which means that the same area is flooded with lower return periods and that the same storm return period gets more severe. The relative increase in surface area is larger for lower return periods than for higher return periods and increase more than linear for higher SLR scenarios.

Analyzing the entire area of interest together allows for the quantification of flood impact in number of people affected for both non-storm (i.e., nuisance flooding; 4.9

- panel A) and storm conditions (Figure 4.9 - panel B). Model results indicate that on average 150,000 people are currently affected yearly by compound flooding in the coastal zone. People are impacted as a function of the hazard (water depth), exposure (where people are located), and vulnerability (depth-damage curve; see also Section 4.3). This increase grows to 2,210,000 for a 100-year event (1% chance). That is an increase from 1 to 14% of the total population of the area of interest. A 100-year flood impact today will be a yearly impact with a 200 cm SLR. Moreover, the 20-year impact increased from 1.4 to 3.3 million people for 150 cm of SLR. This is an increase of 132% and is substantially higher than the increase in flood hazard for the same return period and SLR scenario (14%). Also, the number of people expected to be negatively affected by non-storm conditions (i.e., nuisance flooding) is likely to increase to almost 3 million for 300 cm of SLR.

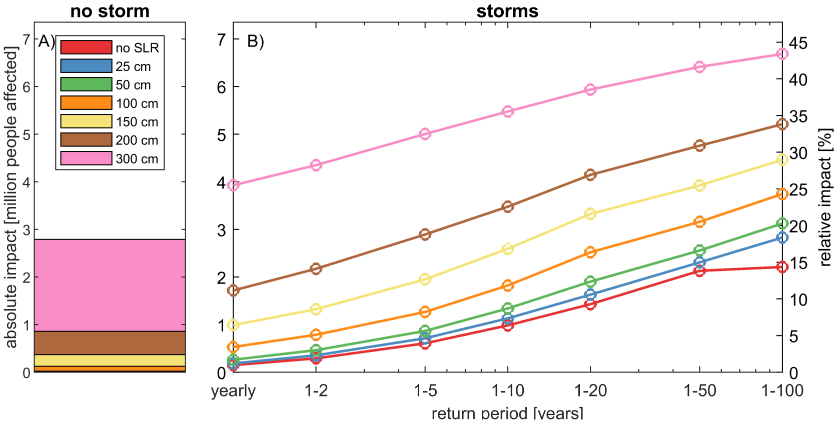

Figure 4.9: Flood impact in terms of people affected for the no storm condition (left panel A) and storms (right panel B). Note that A and B share the same y-axes. For absolute numbers use the left y-axis and for a relative of the total the right y-axis. Color depicts different sea level scenarios of current sea level (red), 25 cm (blue), 50 cm (green), 100 cm (orange), 150 cm (yellow), 200 cm (brown) and 300 cm (pink). Impacts increase with increasing SLR scenarios and have a large relative increase compared to hazards (Figure 4.8).

Flood impacts per return period can be integrated over frequency to provide an estimate of annual risk. This process, which will be referenced throughout the rest of the paper as (absolute) flood risk, is used in generating the results shown in Figure 4.10 through 4.12. The non-storm scenario is not included in the flood risk estimate. In particular, we integrated the affected people per storm frequency and compute the Expected Annual Affected People (EAAP; Giardino et al., 2018b). Figure 4.10 presents the EAAP as a function of SLR for the 14 most populous counties in the area of interest. The most considerable contribution of the total compound flood risk is for the three southeast Florida counties of Miami-Dade, Broward, and Palm Beach Counties (i.e., greater Miami metropolitan area), which comprise 62-72% of the total EAAP.

Similar to flood hazards, there is a stronger than linear increase of impact of flood risk as a function of SLR. The first 50 cm SLR results in an increase in EAAP from 480,000 to 700,000 people. That is an increase of 220,000 people (+45%). SLR scenarios of 100, 150, and 200 cm result in increases of 360,000, 530,000 and 840,000 EAAP (+119, +240, and +413% or fourfold increase).

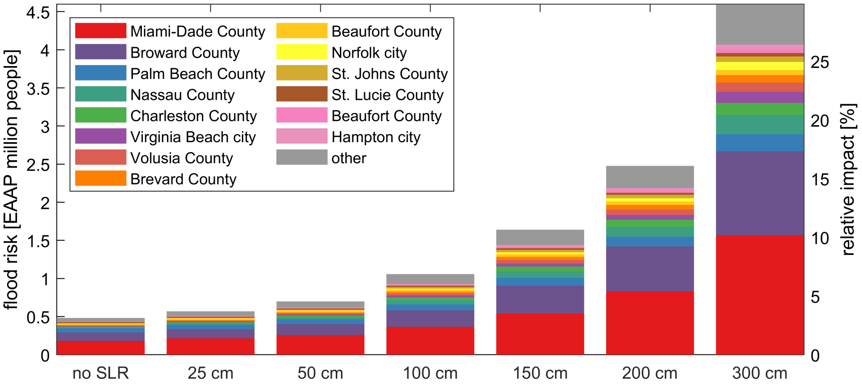

Figure 4.10: Flood risk in Expected Annual Affected People (EAAP) as a function of sea-level-rise (SLR) for absolute numbers (left y-axis) and percentage of total (right y-axis). Color depicts the top affected 14 counties, including the 15th color for all the other counties (gray). EAAP increases strongly with SLR, and the Florida's Miami-Dade, Broward, and Palm Beach Counties account in absolute as relative terms for the largest EAAP.

Absolute flood risk or EAAP strongly follows exposure; thus, densely populated areas generally have the most significant flood risk in this analysis. Relative flood risk can be computed by dividing the EAAP by the county's total population (Figure 4.11). Vulnerable counties such as Miami-Dade and Broward Counties are both populous and have a high relative flood risk. However, a county like Poquoson in Virginia does not show up in the previous (absolute) analysis but does in terms of relative risk because a high percentage of the population would be exposed to flooding (Figure 4.11). In a situation without SLR, these communities can be negatively affected during rare but severe storms (e.g., 100-year events). For the example of Poquoson County, with 1.6-meter of SLR, what is currently a 100-year flood impact event will become the new yearly event with dire consequences regarding relative flood risk.

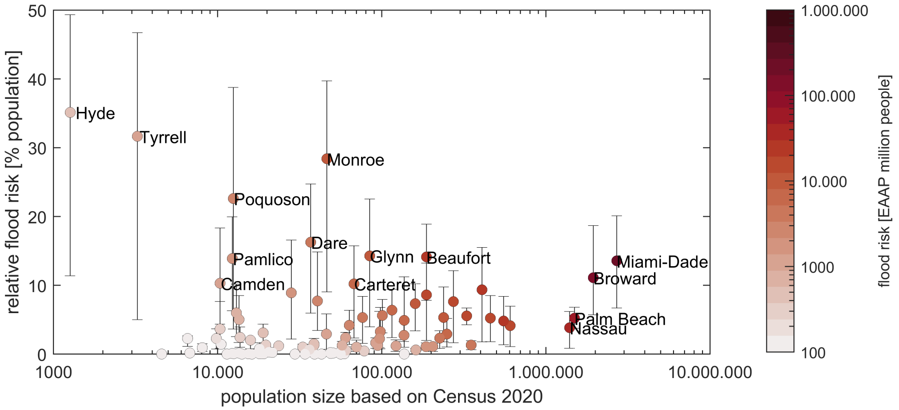

Figure 4.11: Relative flood risk as a function of population size for a SLR projection of 1 m color-coded in Expected Annual Affected People (EAAP). The bar shows the change from the current sea level to 1 meter (lower value) and the increase from 1 to 2 meter. Several smaller, less populous counties have the highest relative risk of the area.

Relative flood risk provides a framework to identify when significant proportions of counties will start to face negative consequences because of SLR. Figure 4.12 shows the relative flood risk per county for the different SLR scenarios analyzed (25 cm SLR results are not shown, for conciseness of the figure). Higher sea levels result in more relative risk. In particular, only one county (Hyde County) has a relative compound flood risk greater than 10% for the current sea level. This value is expected to increase to 12 counties for a SLR of 100 cm and 41 for 300 cm for a total of 94 counties analyzed. Similarly, no county has a 20% or higher flood risk for the current sea level (see also Figure 4.11). With 100 cm of SLR, four counties (Poquoson, Tyrrell, Monroe, Hyde) will have this level of relative flood risk, and this increases to 29 counties with 300 cm of SLR. Note a low risk does not mean that a county cannot be impacted by floods. It means there is a lower likelihood that a large percentage of the county's population is negatively impacted by flooding.

TROPICAL VERSUS EXTRATROPICAL The relative portion of TCs, ETCs, or either physical driver can be determined by the differences between the combined results and the TC- or ETC-only results for flood hazards (Figure 4.13 - panel A; flooded area), flood impact (Figure 4.13 - panel B; impacted people), and flood risk (Figure 4.13 - panel C; EAAP). For example, the combined flood hazard zone of the whole

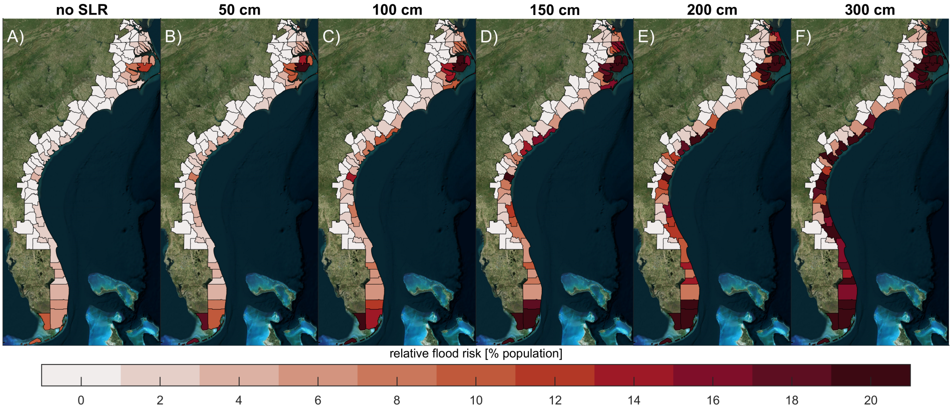

Figure 4.12: Color-coded relative flood risk per county as a function of sea-level-rise (SLR). Different panels (A-F) represent different SLR scenarios (no SLR to 300 cm). 25 cm SLR results are not shown, for conciseness of the Figure. Relative flood risk is projected to increase with SLR. The coordinate system of this figure is WGS 84 / UTM 17 N (EPSG 32617). ©Microsoft Bing Maps.

area with 100 cm of SLR and an annual return period event is 16,489 km2. Only considering TCs results in a hazard area of 7,360 km2 and ETCs alone gives 9,201 km2. Combining the TC-only and ETC-only areas gives an area larger than the combined flood hazard zone by 72 km2, indicating the portion of the combined flood hazard zone that can be flooded by either driver (0.4%). Of the combined flood hazard zone, the portion that is due to ETCs-only is thus 55.4% (9,129 km2), and the portion due to TCs only is 44.2% (7,288 km2). Therefore, we estimate that ETCs dominate the annual flood hazards compared to TCs (division is 55.6% ETC and 44.4% TCs). The division between TCs and ETCs are computed by dividing the area flooded uniquely by ETCs compared to the total area that is uniquely flooded by ETC and TCs.

Flood hazards (Figure 4.13 - panel A), regardless of the driver, increase considerably as a function of the return period from 16,500 km2 for annual return period (8% area) to about 60,000 km2 (29% area) for the 100-year event. For higher return periods, TCs drive an increasingly larger share of the division. For example, a 2-year event (50% annual probability) is 47.2% driven uniquely by TCs versus 24.5% uniquely by ETC and 28.3% by either driver. This percentage of uniquely flooded areas results in a breakdown of 66% for TCs and 34% for ETCs. This breakdown increases to 96% for TCs and 4% for ETCs for the 100-year event (1% annual probability). The increasing dominance of the third category, either physical driver (Figure 4.13 – blue colors), is due to the binary nature of flood hazards (i.e., wet or dry). In other words, low-lying areas will get flooded for the most extreme events regardless if the driving force is a TC or ETC. The analysis only reveals if areas get flooded uniquely by TCs or ETCs. We apply the ratio to establish the division between ETC and TC. For a visual impression of this analysis, see in the Appendix a detailed breakdown for Charleston, S.C., flooding with annual frequency, 10-year, 100-year (Figure 4.16).

A similar trend emerges for the flood impacts (Figure 4.13 - panel B). For an SLR scenario of 100 cm, it is estimated that 530,500 people (3.4%) are negatively affected annually by flooding. This impact increases to almost 3,743,000 people (or 24.3% of the population) for the 100-year event. The annual impact is about 22.7% uniquely driven by TCs, 42.8% by ETCs, and 34.5% by either driver. In other words, ETCs result in almost twice the amount of negative impact with a yearly frequency based on the division estimate (division TC/ETC 35-65%). However, for the 100-year event, 58.3% is driven by TCs versus 2.0% by ETCs and 39.8% by either driver (i.e., 30x more TC-driven impact). The lack of a linear correlation between hazards and impacts is noteworthy.

Regarding flood risk (Figure 4.13 - panel C), TCs generally dominate over ETCs. For the current sea level, 52.2% of the flood risk is uniquely related to TCs. In comparison, 24.1% is related to ETCs and 23.7% to either driver. In other words, TC-induced flood risk is about twice that of ETCs based on the division TC/ETC. This distribution of risk decreases to 17.3% TCs, 14.0% ETCs, and 68.7% for either driver for the 300 cm SLR scenario. Higher SLR scenarios result in more and more flood risk regardless of the ETCs or TCs. Moreover, the contribution of TCs to compound flood risk decreases from 70 to 55% from no SLR to 300 cm (or 30% and 45% ETCs).

## 4.5. DISCUSSION

The validation shows that the presented workflow and the developed five SFINCS domains can skillfully reproduce tidal (median MAE 8.3 cm; Figure 4.17) and coastal extreme water levels (median MAE 11.9 cm; Figure 4.18). It is hypothesized that this model skill has been achieved by 1) nesting the overland flow domains

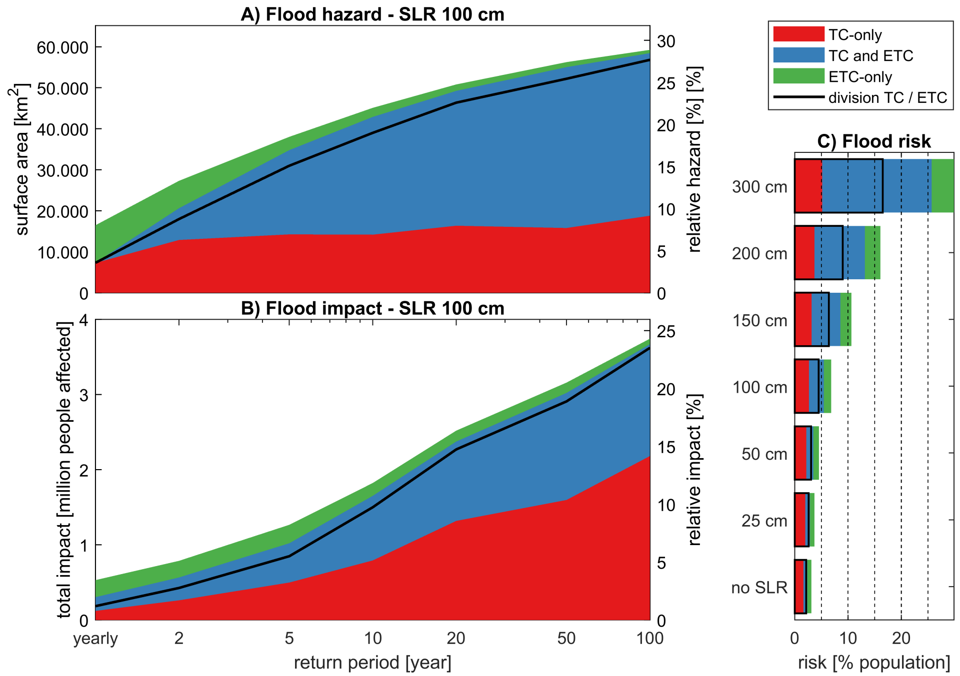

Figure 4.13: The division TC/ETC (black line) and contribution of TC-only (red) versus ETC-only (green) or either (blue) for compound flooding. Panel A. Flood hazard as a function of return period for SLR scenario of 100 cm. Panel B. Flood impact as a func-tion of return period for SLR scenario of 100 cm. Panel C. Flood risk in EAAP for different SLR scenarios. The contribution of TCs increase with return period for both hazards and impacts but decreases for flood risk as function of SLR.

into large-scale hydrodynamic and wave models that provide statistically corrected boundary conditions and 2) including relevant bathymetry features. Computational efficiency was prioritized to allow for the deterministic computation of flood hazards and impacts of thousands of events. Limited computational resources did constrain the utilized approach to a relatively coarse model resolution of 200x200 meters in combination with subgrid lookup tables that resolve fine-scale flood features at the resolution of the 1-m Digital Elevation Model. Similar to other approaches (e.g., Volp et al., 2013; Sehili et al., 2014), the subgrid approach substantially reduced computational cost without significant accuracy loss. The underestimation of tides at several stations is likely driven by incorrect friction, as derived from the landcover map, and not a limitation in the subgrid method itself. The accuracy of the boundary conditions could also play a role (see Parker et al., 2023). Moreover, as part of sensitivity testing, it was found that model skill versus computational cost seems optimal at a model resolution of 200x200 meters. More refined model simulations did minimally increase model skill but with a considerable increase in computational cost. The near-continuous computations allowed for the usage of empirical extreme value statistics on a cell-by-cell basis. This method eliminated the need to fit statistical distributions that could potentially yield incorrect results when limited data points are presented. The latter mainly occurs for overland compound flooding, where only several (rare) storms result in flooding.

The version of SFINCS applied in this manuscript does not include a stationary wave solver, infra-gravity waves, sediment transport, or morphology. Wave setup was used at the offshore boundary based on the empirical formula of Stockdon et al., 2006 and presented in Parker et al., 2023. Still, the accuracy of this correction was not able to be assessed. A more in-depth validation at a case study site with good observational data might provide insight. The lack of infragravity waves, sediment transport, and morphological change is a limitation since breaches and overtopping are commonly reported during extreme events (e.g., during Hurricane Florence; Biesecker and Kastanis, 2018 or more recently during Ian and Nicole in the 2022 season). This restriction would, most likely, result in underestimating the computed flood hazards and impacts. Moreover, in this chapter, we have assessed flood hazards and impacts given SLR scenarios but without taking into account morphological and societal changes such as population dynamics and construction of flood risk management features. The natural system will respond given changes in climate (Antolínez et al., 2018), for example, shorelines are projected to undergo a large recession (e.g., Bruun, 1954; Ranasinghe et al., 2012). Moreover, the U.S. Southeast is projected to continue its economic growth (Hauer, 2019), but any local mitigation and adaptation measures taken will be beholden to the question of how flood hazards and risks develop in the future. These changes are not considered in this chapter. Moreover, no validation of the impact computation was performed. Lastly, Lockwood et al., 2022 showed that sea level rise and changes in the meteorological conditions correlate; however, in this chapter, they were assumed independent to allow for the computation of several sea level rise scenarios under one future projected climate.

Hydrological processes were resolved in this chapter by 1) applying the NWM for riverine inflow into the SFINCS domains and 2) computing rainfall run-off by including rainfall and estimating infiltration with the Curve Number method. Validation for Hurricane Florence did show clear observed and modeled inland flooding, including raised water levels in the analyzed time series of observations and models due to precipitation and riverine flow (Figure 4.6). However, the error in reproducing the HWM with an MAE of 63 cm is much higher than the other errors presented in this chapter, but they are in the same order as other Hurricane Florence validations (e.g., Ye et al., 2021 reported an average MAE of 73 cm). In addition, dynamic processes such as groundwater and (managed) urban drainage systems are not included, which could substantially influence results locally. For example, South Florida is known for its permeable karst substrate in combination with regulated channels, which affects the risk of flooding (Czajkowski et al., 2018; Sukop et al., 2018). Moreover, it is unclear how the assumption of 50% saturation in the Curve Number at the start of each simulation has influenced the results. Sensitivity testing showed that the soil saturation assumption influences results for milder more-frequent storms. Nonetheless, the impact of more substantial events, such as Hurricane Florence, was restricted due to the considerable overall precipitation relative to the infiltration capacity (see for example sensitivity testing in Appendix 4.6). Moreover, the 50% saturation value was held constant for the sea level rise scenarios, although one might expect increased soil saturation through changes in precipitation patterns and rising temperatures associated with a warming climate. Continuous, deterministic, simulations could overcome this limitation but were deemed computationally too expensive for this large-scale study. Besides these limitations, the SFINCS-based estimate of flood hazards and impacts across the region provides valuable information to coastal managers and policymakers on an unprecedented scale and resolution. In particular, we hypothesize that reported hazards, impacts, and risk values can provide relative insights due to the physics-based derivation despite model shortcomings.

The simulation and detailed analysis of both TCs and ETCs allowed quantifying the contribution of tropical and extratropical events. Similar to Dullaart et al., 2021, this paper also found that it is vital to include TCs, especially for infrequent events. Here, we estimate a dominance in TC risk across the study area to be around 55-68%, which is in the same order of magnitude as Dullaart et al., 2021, who provided estimates for storm surge across the globe or Booth et al., 2016 who provided its estimate based observational water level data. A limitation of our study is the record length of 31 years for ETCs and, therefore, implicitly assuming dominance of TCs for higher return periods. However, in this study, we do see that TCs dominate the signal earlier in the frequency range for the Southeast Atlantic Coast. For other areas (e.g., West Coast or New England states), this dominance of TCs is most likely not the case, and another method needs to be explored.

In this study, we directly applied an ensemble of three high-resolution CMIP6 models to determine ETC-driven flooding for the projected climate. This was done because historical high-resolution CMIP6 data were not available at the time of this study, which would have allowed for bias correlation or an assessment of percent change between the historical and future periods. However, GCMs are known to have biases, which propagate and can thus influence the simulations (e.g., Xu et al., 2021). On the other hand, high-resolution CMIP6 models (in the order of 25 km) are starting to be sufficient to resolve the relevant meteorological features for large-scale flood assessments (e.g., Roberts et al., 2020). For example, a recent study by Muis et al., 2023 showed a positive bias of 10% in computed storm surge levels corresponding to a 10-year return period between a HighResMIP ensemble and ERA5 reanalysis along the eastern North Atlantic U.S. coast which gives confidence these products start to resolve relevant features flood assessments. Moreover, taking an ensemble, as was done in this study, is expected to perform better than individual members (Tebaldi and Knutti, 2007), and preserves event consistency among meteorological forcings for projected storm events (wind, pressure, and rain). We do acknowledge the limitation of bias and are exploring the possibility of incorporating historical and projected scenarios based on the same CMIP6 models to overcome possible biases in meteorological forcing. Other methods include working with historical climate forcing such as the ERA5 reanalysis to overcome these potential biases. Additionally, the CMIP6 projections utilized in this study are based solely on the SSP5-8.5 scenario, which represents the upper limit of potential outcomes and is deemed improbable in light of current emission trends.

## 4.6. CONCLUSION

Using well-calibrated numerical models, it is shown that predicting both tropical and extratropical cyclones is vital for accurately assessing coastal hazards and impacts. Extratropical cyclones are mainly responsible for frequent flooding events. In particular, we find that for the current sea level, extratropical cyclones contribute to half of the flooded area. However, these events affect almost twice the amount of people compared to tropical cyclones with a yearly frequency. However, tropical cyclones drive the majority of the infrequent flood hazards. For example, for the 100-year event, tropical cyclones contribute  96% of the flooded area and likely affect 30 times the number of people. Moreover, we find that tropical cyclones contribute to more than half of the total coastal compound flood risk. The relative importance of tropical cyclones to compound flood risk does decrease with sea level rise.

The relative impact of flood hazards from annual storm events is limited to 6.3% of low-lying areas of U.S. Southeast Atlantic coast at the current sea level. In comparison, 100-year events flood 27.2% of the considered area. With sea-level rise (SLR), flooding increases significantly. In particular, annual hazards increased from 6.3% today to 8.0 and 11.7% with 100 and 200 cm, respectively, of sea level rise. This change makes rare events more severe and decreases the return period for current extreme events. For example, a 100-year flood impact today will be a yearly impact with a 200 cm SLR. Also, flood impacts are projected to have a larger relative increase compared to flood hazards for the same return period and SLR scenario. Flood risk is expected to grow non-linearly from roughly 3.1% (0.5 million people) today to 6.9 and 16.1% (1.1 and 2.6 million people) for 100 and 200 cm, respectively, of sea level rise. Impacts are mainly driven by exposure in the most populous counties in the area (Miami-Dade, Broward, and Palm Beach County together comprise 62-70% of the total risk in the area). However, several smaller, less populous counties have the highest relative risk of the study area compared to the high absolute flood risk for the populated southeast Florida region. This implies that relative risk (people affected divided by the total population in the county) could prove a valuable metric for policy decisions.

While our methodology is targeted at coastal flooding, precipitation and hydrology are included to capture coastal compound flooding. In particular, the model framework developed in this study can skillfully reproduce coastal water levels. Model errors in these areas are driven by errors in tide (median mean-absolute-error, MAE, 8.3 cm) and storms (median MAE 11.9 cm). As demonstrated in the validation of Hurricane Florence, the model error increased farther inland due to less well-resolved hydrological processes such as rainfall, infiltration, and riverine flow.

## APPENDICES ASSOCIATED WITH THIS CHAPTER

### UPDATING SYNTHETIC TROPICAL CYCLONE PROBABILITIES TO REFLECT CLIMATE CHANGE

We conducted a comparative analysis of tropical cyclone (TC) characteristics in a CMIP6 multi-model ensemble for historical (1980-2014) and future (2016-2050) periods to assess the need for modifying probabilities in the USACE CHS synthetic TC dataset. For the TC comparisons between the historical and future model ensembles, we examined TC storm parameters (frequency, location, heading, forward speed, radius of maximum winds, and intensity based on central sea level pressure deficit) at a 600 km radius around USACE shoreline locations. In particular, we utilized eight atmosphere-ocean coupled CMIP6 models and the tracks of TCs using the TRACKS method (Roberts, 2019). Our analysis revealed a change in the sea level pressure deficit for the most intense storms within our region. The other TC parameters did not change. The strongest 2% of storms in the 8-model ensemble showed increased storm strength from northern Florida north-ward, indicating more frequent intense TCs in this area. These alterations were incorporated into the USACE CHS synthetic TC dataset, leading to recalculated probabilities that reflect this intensification.

### SENSITIVITY TESTS FOR SATURATION PERCENTAGE

In this study, we assessed the sensitivity of the Curve Number method to the assumption of 50% saturation focused on the computed flood extents for Hurricane Florence (Section 4.1.3). A series of tests were conducted using saturation percentages that varied from 0% (indicative of full saturation, yielding a Se value of 0) to 100% (representing complete insaturation, leading to a Se value of Smax) in 25% increments. Throughout the study, we applied a 50% value (see Section 3.4.2). The sensitivity analysis of this parameter for Hurricane Florence revealed a maximum variation in flood extent ranging from +2.6% to -0.3% (Figure 4.15 - panel B). Notably, the most pronounced disparities were observed in the range of 0 to 50% saturation, indicating the fully saturated spectrum of the parameter. Furthermore, these differences were predominantly evident further inland and further away from the hurricane's landfall (Figure 4.15 - panel A). We hypothesize that such variations can be attributed to the substantial cumulative rainfall concentrated within the storm's eye, which surpasses infiltration capacity irrespective of the initial saturation percentage. Additionally, further inland, the primary flooding source tends to be rainfall-induced, in contrast to coastal areas where tidal surges pre-dominantly contribute to flooding events.

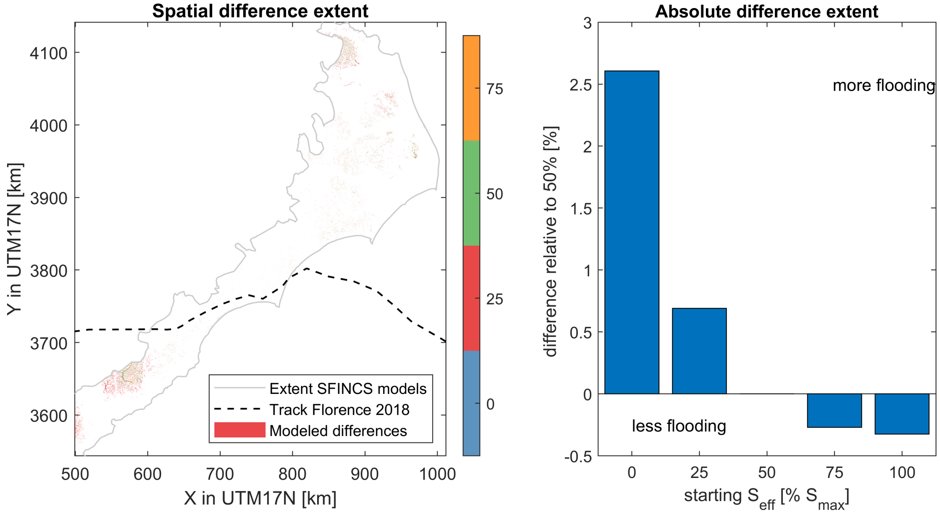

Figure 4.14: Sensitivity testing on the saturation percentages on the flood extent computed for Hurricane Florence (2018). Panel A: overview figure for spatial difference in flood extent (colors), domains (gay) and the track of Hurricane Florence (black dashed). Panel B: Difference in relative flood extent area relative to a 50% saturation percentage. The best track is based on International Best Track Archive for Climate Stewardship (IBTrACS; Knapp et al., 2010).The coordinate system of this figure is WGS 84 / UTM 17 N (EPSG 32617).

## ADDITIONAL FIGURES AND TABLES

Table 4.2: Lookup table for conversion of National Land Cover Database Land to roughness values using Manning's coefficients

| **NLCD class** | **Description** | **Manning n** |
|---|---|---|
| 11 | Open water | 0.020 |
| 21 | Developed, Open Space | 0.070 |
| 22 | Developed, Low Intensity | 0.100 |
| 23 | Developed, Medium Intensity | 0.120 |
| 24 | Developed, High Intensity | 0.140 |
| 31 | Barren land | 0.070 |
| 41 | Deciduous Forest | 0.120 |
| 42 | Evergreen Forest | 0.150 |
| 43 | Evergreen Forest | 0.120 |
| 52 | Evergreen Forest | 0.050 |
| 71 | Grassland/Herbaceous | 0.034 |
| 81 | Sedge/Herbaceous | 0.030 |
| 82 | Cultivated Crops | 0.035 |
| 90 | Woody Wetlands | 0.100 |
| 95 | Emergent Herbaceous Wetlands | 0.035 |
|  | Other | 0.020 |

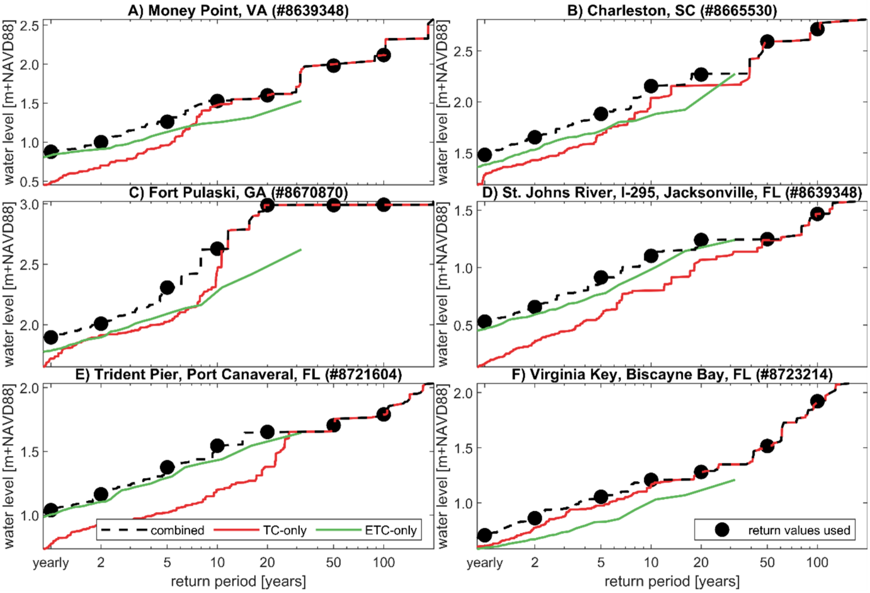

Figure 4.15: Extreme water level return levels and periods for TC-only simulation (red), EC-only (green) and the combined results (black dashed lines). The return values presented throughout this study are the yearly, 2-year, 5-year, 10-year, 20-year, 50-year and 100-year estimates and are shown as black dots. The dominance of ETC versus TC varies per station and return period.

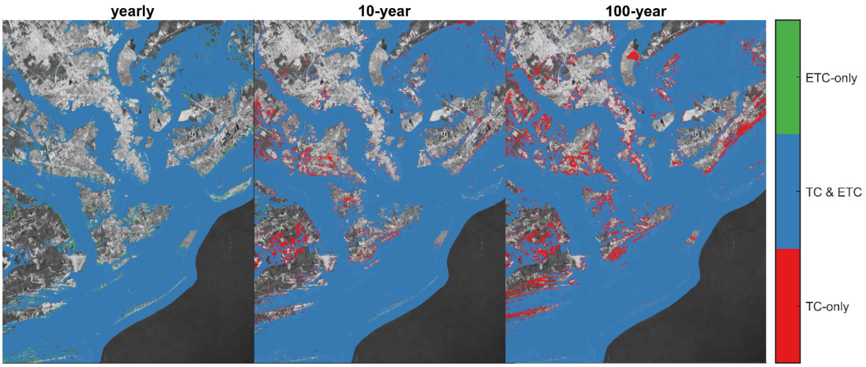

Figure 4.16: Breakdown of flooding for Charleston, South Carolina, for annual, 10-year and 100-year flooding. Color-coded is the source of the flooding. Most of the grid cells are flooded by both TC & ETC (either driver; blue color). Flooding with a yearly frequency is driven more by ETC-only drivers (green) while 100-year events are driven more by TC-only (red).

Table 4.3: Overview of tidal skill scores for 68 stations (part 1)

| Short name | MAE [cm] | uRMSE [cm] | bias [cm] | RMSE HW [cm] |
|---|---|---|---|---|
| **8638610** | 6.6 | 7.5 | -0.4 | 3.3 |
| **8639348** | 19.4 | 22.3 | -0.5 | 25 |
| **8651370** | 12.8 | 14.7 | -0.1 | 21 |
| **8652587** | 26.2 | 30.2 | 0.2 | 29.8 |
| **8656483** | 6.5 | 7.5 | -0.6 | 11.5 |
| **8658120** | 26.9 | 30.5 | 0.7 | 35.5 |
| **8658163** | 4.6 | 5.6 | -0.1 | 6 |
| **8661070** | 4 | 4.8 | 0 | 7.6 |
| **8662245** | 9.8 | 11.7 | -1.5 | 14.6 |
| **8665530** | 4.5 | 5.3 | -0.9 | 9.3 |
| **8667633** | 28.9 | 32.8 | -5 | 26.1 |
| **8670870** | 8.3 | 9.8 | 0.1 | 14.3 |
| **8720030** | 4.4 | 5.5 | -0.8 | 10.6 |
| **8720059** | 21.6 | 24.4 | 0.1 | 34.2 |
| **8720145** | 16.6 | 19.3 | -0.5 | 23.6 |
| **8720218** | 3.6 | 4.3 | 0.1 | 6.2 |
| **8720357** | 5.2 | 6.3 | 0.1 | 8.2 |
| **8721147** | 9.2 | 10.9 | -1.2 | 9.1 |
| **8721604** | 20.7 | 24.8 | -1.9 | 25.5 |
| **8722548** | 5 | 6.1 | 0.6 | 4.4 |
| **8722588** | 1.6 | 1.9 | -0.1 | 2.6 |
| **8722669** | 12.5 | 14.5 | 5 | 8.5 |
| **8723214** | 6.1 | 7.1 | 0.3 | 4.4 |
| **8725110** | 4.2 | 5.1 | 0.1 | 4.4 |
| **8725520** | 2.2 | 3.1 | 0.1 | 2.6 |
| **Bear Cut** | 6.2 | 7.2 | 0.3 | 4.2 |
| **Bings Landing** | 16.9 | 20.2 | -0.6 | 19.5 |
| **Buffalo** | 8.1 | 9.5 | -0.2 | 13.2 |
| **Canaveral** | 24.2 | 29.2 | -1.6 | 32.1 |
| **Capers** | 25.5 | 29.1 | -2.1 | 35.1 |
| **Chesapeake** | 3 | 3.6 | -0.2 | 2.3 |
| **Cooper** | 26.7 | 30.2 | 0.5 | 37.6 |
| **CoreSound** | 20 | 23.1 | 0.7 | 22.3 |
| **Crescent** | 25 | 28.9 | -3.8 | 32.3 |

Table 4.4: Overview of tidal skill scores for 68 stations (part 2)

| | | | | |
|---|---|---|---|---|
| **Dame Point** | 11.7 | 13.4 | 0.1 | 16.6 |
| **Daytona** | 4.5 | 5.4 | 0.1 | 7.3 |
| **Fernandina** | 6.4 | 7.7 | -0.9 | 13.1 |
| **Hatteras** | 19.8 | 23 | -0.4 | 29.2 |
| **Haulover** | 6.2 | 7.5 | 0 | 8.6 |
| **Jacksonville** | 9.2 | 10.6 | 0.7 | 12.9 |
| **Kingsbay** | 12.2 | 14.3 | -1.2 | 20.6 |
| **Kingsmill** | 13.2 | 15 | -0.1 | 14.7 |
| **LakeWorth** | 3.9 | 4.7 | 0.2 | 6.1 |
| **Matanzas** | 17.1 | 20.4 | 0.4 | 21.8 |
| **Mayport** | 4.1 | 4.9 | 0 | 6.9 |
| **MiamiBeach** | 8.3 | 9.8 | 0.1 | 10.6 |
| **MiamiHarbor** | 12.6 | 15.1 | -0.1 | 15.2 |
| **NavalStation** | 2 | 2.5 | 0 | 2.6 |
| **Ocracoke** | 25.3 | 29.3 | 0.5 | 29.3 |
| **Oregon** | 8.3 | 9.9 | -0.9 | 9 |
| **Palatka** | 8.3 | 9.8 | 0.1 | 13.3 |
| **Ponce** | 10.1 | 12.2 | -1 | 10.5 |
| **Portsmouth** | 11.4 | 13.1 | -0.7 | 12.4 |
| **RacyPoint** | 7.2 | 8.4 | -0.1 | 11.1 |
| **RedBay** | 5.5 | 6.6 | -0.1 | 8.7 |
| **Rudee** | 8.2 | 9.6 | 0.2 | 9.9 |
| **Savannah** | 32.2 | 36.3 | -2.5 | 48.7 |
| **Scotland** | 11.5 | 13 | 0.1 | 11.1 |
| **Southport** | 6.5 | 7.5 | -0.3 | 10.2 |
| **StAugustine** | 4.3 | 5 | -0.1 | 6.6 |
| **StHelena** | 7.7 | 9.1 | -2.3 | 15.9 |
| **StJohns** | 10.1 | 11.6 | 0.4 | 15.6 |
| **StMarys** | 8 | 9.7 | -1 | 13.4 |
| **StSimons** | 15 | 18.2 | -0.3 | 18.2 |
| **Sunset** | 4.7 | 5.8 | 0 | 7.2 |
| **Vilano** | 22.5 | 26.2 | -0.2 | 25 |
| **Welaka** | 3.9 | 5.6 | -0.6 | 7.1 |
| **Wrightsville** | 25.2 | 30.4 | -1.4 | 29.4 |
| **Median** | 8.3 | 9.9 | -0.1 | 12.7 |

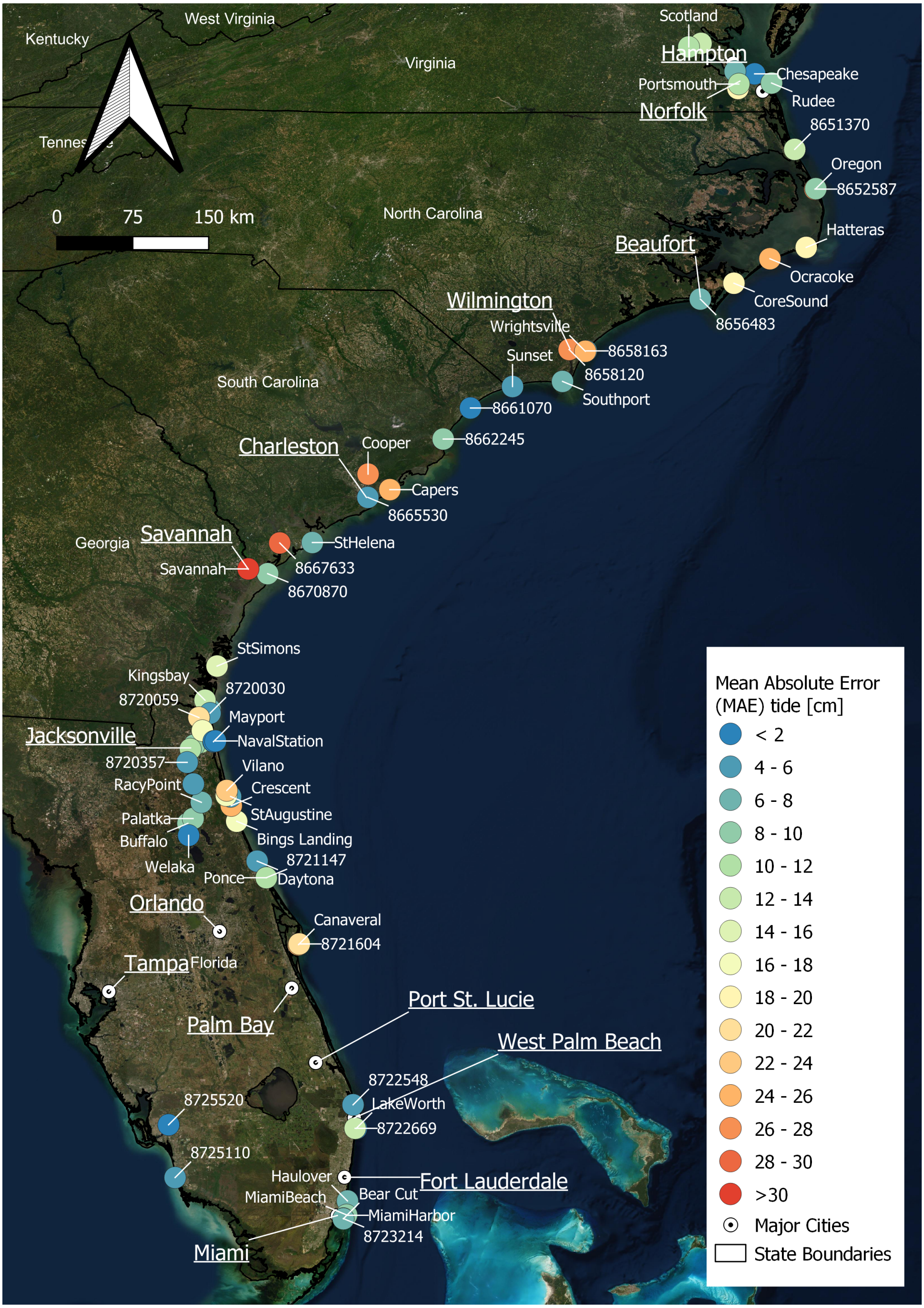

Figure 4.17: Overview of the Mean Absolute Error (MAE) of tidal water levels at 24 NOAA stations (depicted with station ID) and 68 XTide stations (shown with names) across the study area. For more detailed information on the model skill is provided in Table 4.3. Several major city names are presented to orient the reader. ©Esri, DigitalGlobe, GeoEye, i-cubed, USDA FSA, USGS, AEX, Getmapping, Aerogrid, IGN, IGP, swisstopo, and the GIS User Community.

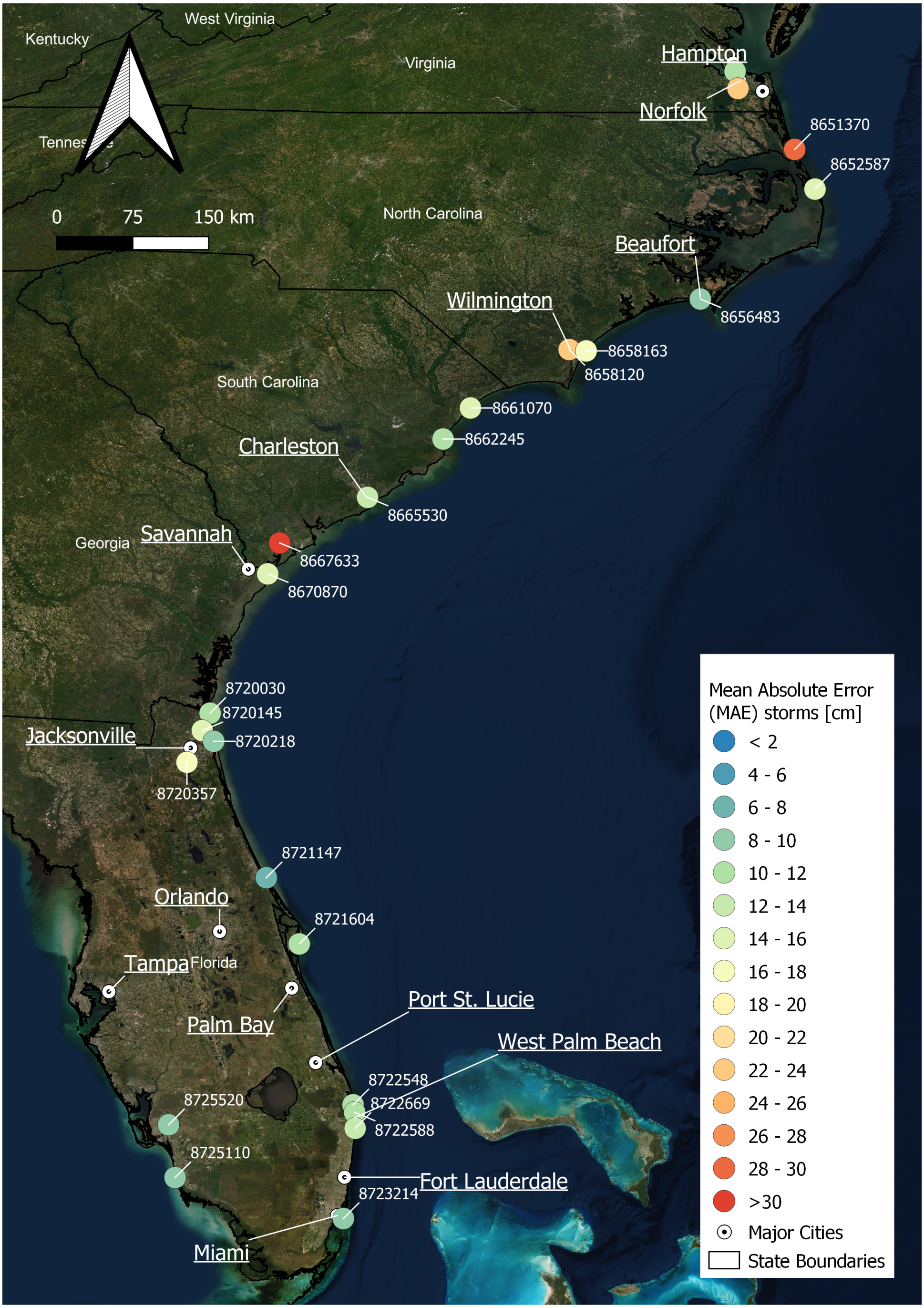

Figure 4.18: Overview of the median Mean Absolute Error (MAE) of storm water levels at 24 NOAA stations (depicted with station ID) across the study area. For more detailed information on model skill, refer to Table 4.1. Several major city names are presented to orient the reader. ©Esri, DigitalGlobe, GeoEye, i-cubed, USDA FSA, USGS, AEX, Getmapping, Aerogrid, IGN, IGP, swisstopo, and the GIS User Community.

# 5

# EVALUATION OF UNCERTAINTY IN OPERATIONAL TROPICAL CYCLONE RISK ANALYSIS

*Whereas the prior two chapters focused on strategic risk analysis, this chapter shifts the focus to operational risk analysis related to tropical cyclones. Accurate tropical cyclone forecasts are crucial for safeguarding lives and minimizing economic impacts. However, the methodologies used by the National Hurricane Center do not yet address predictions for coastal flooding. In this chapter, we introduce a methodology that focuses on creating operational and probabilistic forecasts of compound flooding induced by tropical cyclones. The ensemble members are created based on a forecasted track and take into consideration uncertainties in track, forward speed, and wind speed. The focus of this chapter is to introduce and apply a new methodology called the Tropical Cyclone Forecasting Framework (TC-FF) that can be used for operational risk analysis.*

---

This chapter is a revised version of **Nederhoff, K.**, Van Ormondt, M., Veeramony, J., Van Dongeren, A., Antolínez, J. A. Á., Leijnse, T., & Roelvink, D. (2024c). Accounting for Uncertainties in Forecasting Tropical Cyclone-Induced Compound Flooding. *Geoscientific Model Development*, *17*(4), 1789–1811. https://doi.org/10.5194/gmd-17-1789-2024

**Abstract** Tropical cyclone impacts can have devastating effects on the population, infrastructure, and on natural habitats. However, predicting these impacts is difficult due to the inherent uncertainties in the storm track and intensity. In addition, due to computational constraints, both the relevant ocean physics and the uncertainties in meteorological forcing are only partly accounted for. This paper presents a new method, called the Tropical Cyclone Forecasting Framework (TC-FF), to probabilistically forecast compound flooding induced by tropical cyclones, considering uncertainties in track, forward speed, and wind speed/intensity. The open-source method accounts for all major relevant physical drivers, including tide, surge, and rainfall, and considers TC uncertainties through Gaussian error distributions and autoregressive techniques. The tool creates temporally and spatially varying wind fields to force a computationally efficient compound flood model, allowing for the computation of probabilistic wind and flood hazard maps for any oceanic basin in the world, as it does not require detailed information on the distribution of historical errors. A comparison of TC-FF and JTWC operational ensembles, both based on DeMaria et al., 2009, revealed minor differences of <10%, suggesting that TC-FF can be employed as an alternative, for example, in data-scarce environments. The method was applied to Cyclone Idai in Mozambique. The underlying physical model showed reliable skill in terms of tidal propagation, reproducing the storm surge generation during landfall and flooding near the city of Beira (success index of 0.59). The method was successfully applied to forecast the impact of Idai with different lead times. The case study analyzed needed at least 200 ensemble members to get reliable water levels and flood results three days before landfall (<1% flood probability error and <20 cm sampling errors). Results showed the sensitivity of forecasting, especially with increasing lead times, highlighting the importance of accounting for cyclone variability in decision-making and risk management.

## 5.1. INTRODUCTION

Tropical cyclone (TC) induced compound flooding, which occurs when storm surge, heavy rainfall, high tide, and river discharge coincide, can have devastating impacts on coastal communities (Wahl et al., 2015). This type of flooding is particularly concerning as it can result in higher water levels and increased inland flooding, leading to damage and loss of life (e.g., Resio and Irish, 2015). The increased frequency and severity of compound flooding events are expected to worsen due to climate change included sea level rise (e.g., Easterling et al., 2000, changes in extreme storm surges and wave climates (e.g., Lin et al., 2012; Mori and Shimura, 2023), increased and prolonged precipitation (e.g., Trenberth et al., 2003) as well as ongoing coastal development and population growth (e.g. Neumann et al., 2015). Mitigation and preparedness strategies require a sound toolbox for assessing TC-induced compound flooding on coastal communities that enhance short to long-term decision-making.

Operational and strategic risk analyses are instrumental in analyzing and mitigating potential environmental risks. Operational risk analysis, typically associated with short-term forecasting (order of several days), provides immediate response and preparedness for imminent disasters, ensuring the safety and protection of people and property (Roy and Kovordányi, 2012). Conversely, strategic risk analysis focuses on long-term climate variability assessments, delivering insights into hazards and their socio-economic and environmental impacts, thus facilitating informed policy decisions and adaptation strategies (e.g., Nederhoff et al., 2021a). Though distinctly different, both perspectives are critical for comprehensive climate risk management, as they offer different scales and timeframes for prevention, preparedness, response, and recovery.

Forecasting agencies such as the National Hurricane Center (NHC) have significantly improved operational meteorological risk analysis, credited to gains made in numerical weather prediction models (McAdie and Lawrence, 2000, Cangialosi et al., 2020). Despite advancements, operational forecast errors remain significant enough to necessitate considering the inherent uncertainties in these forecasts for informed preparedness decision-making (Lamers et al., 2023). A common probabilistic approach is to represent the resulting uncertainty in track prediction by a cone envelope as a graphical representation that illustrates the possible track variation of the TC center (National Hurricane Center, 2023). The shape of the cone can be derived from the historical error data of the forecast and typically represents a 66.7% probability that the track will be within the cone (i.e., 33.3% chance the track falls outside the cone). The cone increases in size with lead time as the errors in the prediction accumulate. While the cone gives valuable insight into the potential range of TC variability of the core, it can be easily misinterpreted as the corresponding impacted area, which can be substantially larger. Quantification of the uncertainty in track prediction can be computed with several methods. For example, DeMaria et al., 2009 introduced a Monte Carlo method to generate 1,000 realizations by randomly sampling from historical error distribution functions from the past 5 years for both the track and intensity. DeMaria et al., 2013 improved their method so that the track uncertainty is estimated on a case-by-case basis using the Goerss predicted consensus error (GPCE; Goerss, 2007), where the uncertainty is estimated based on the spread of a dynamical model ensemble instead of historical averages. Other methods exist and for example Chen et al., 2023 introduced a deep-learning ensemble approach for predicting tropical cyclone rapid intensification. However, these methods were all derived to provide insight, before landfall, into the uncertainty of the wind speeds and not designed to force hydrodynamic or wave models and can thus result in too erratic forcing conditions.

Early Warning Systems (EWS) for coastal compound flooding are sensitive to uncertainties in the TC, including nonlinear interactions between the TC size, forward speed, location of landfall, tides, rainfall, and infiltration. However, often EWS for coastal flooding use physics-based and, due to computational constraints, deterministic approaches in which the best track is used to force a hydrological and hydrodynamic model that computes the storm surge and the complex interactions between coastal, fluvial, and pluvial processes. For example, the Global Storm Surge Information System (GLOSSIS) is based on Delft3D Flexible Mesh (Kernkamp et al., 2011) and run operationally 4 times daily to produce 10-day water level and storm-surge forecasts for the entire globe. GLOSSIS is typically forced with NOAA's GFS forcing although there is also functionality in place to use hurricane tracks. Another example is the Coastal Emergency Risks Assessment (CERA) based on ADCIRC (Luettich et al., 1992). CERA is an effort providing operational advisory services related to impending hurricanes in the United States only and uses the NHC official advisory every 6 hours. Neither GLOSSIS nor CERA accounts for uncertainties in the meteorological forcing.

Several examples of probabilistic coastal flood methods do capture uncertainty in forcing. For example, the Global Flood Awareness System (GloFAS; Alfieri et al., 2013) is a modeling chain run by the European Centre for Medium-Range Weather Forecasts (ECMWF) based on the LISFLOOD hydrological model forced by 51 ensemble members. While GloFAS is an excellent resource for communities worldwide, it operates at a large scale with a relatively coarse resolution of 0.1

degrees (order of 10 km), is thus not designed explicitly for TCs that require high spatial resolutions (Roberts et al., 2020, and neither account for relevant coastal processes such as tides. Higher resolution and the inclusion of coastal processes can be found in several regional applications. For example, the Stevens Flood Advisory System (SFAS; Ayyad et al., 2022) is an ensemble-based probabilistic forecasting of tide, surge, and riverine flow across the US Mid-Atlantic and Northeast coastline and runs for 96 different atmospheric forcing datasets. Other examples include forecasting systems from the UK Met Office (Flowerdew et al., 2010) and the Royal Netherlands Meteorological Institute (de Vries, 2009). All these systems rely on coarser numerical forecasting products, focus on mid-latitude regions, and are thus not explicitly designed to forecasts hazards related to TCs.

Probabilistic modeling systems for TC-induced coastal flooding for operational risk analyses in the US and Japan include P-Surge (Taylor and Glahn, 2008 Gonzalez and Taylor, 2018), which uses data from the NHC to create a set of synthetic storms by perturbing the storm's position, size, and intensity based on past errors of the advisories. Subsequently, the Sea, Lake, Overland, Surge from Hurricanes model (SLOSH; Jelesnianski et al., 1992) is run and forecasts storm surge in real-time when a hurricane is threatening. However, SLOSH does not account for several relevant (coastal) processes (e.g., tides, waves, rainfall, infiltration) and thus lack their interactions. The Japan Meteorological Agency (JMA) does use a dynamic tide and storm surge model (Nakagawa, 2009) but only accounts for a limited number of 11 ensemble members (Hasegawa et al., 2015). Moreover, both methods are created with a specific region in mind and are not easily transferable to other locations.

Besides probabilistic physics-based techniques, statistical machine-learning techniques (e.g., Lecacheux et al., 2021 or Nguyen and Chen, 2020) are becoming increasingly popular in reducing the computational expense of forecasting compound flooding. However, these machine learning downscaling methods lack nonlinear interactions between relevant coastal processes driving compound flooding. Hybrid methods focus on reducing the number of tracks simulated and proved capable of accurately representing a larger set of scenarios (Bakker et al., 2022).

As introduced by Suh et al., 2015, the constraints in real-time forecasting for operational risk analysis are around both 'accuracy' and 'promptness'. In other words, the time constraints associated with forecasting dictate that some modeling systems use a purely deterministic approach or a limited number of ensemble members to perform more detailed compound flooding predictions and thus simplify the meteorological uncertainty (e.g., GLOSSIS, CERA, JMA). On the other hand, probabilistic approaches for meteorology with a large number of ensemble members use simplified hydrodynamics or have an insufficient resolution for TCs and thus do not account for the processes needed to forecast TC-induced coastal compound flooding (e.g., GloFAS, SFAS, NHC). In summary, the current shortcomings of existing methodologies include the absence of high-resolution models specifically tailored for analyzing coastal compound flooding. Additionally, there is a notable deficiency in probabilistic assessments of tropical cyclone flooding that incorporate the uncertainties inherent in forecasting cyclone tracks. Moreover, there is a need for a universally applicable methodology that can be seamlessly adapted to various case studies globally.

To address the limitations listed, we propose a method to generate probabilistic wind and compound flood hazard maps by using, for the first time, ensembling techniques via statistical emulation of TCs combined with physics-driven modeling for coastal compound flooding. The workflow emulates the TC evolution using an autoregressive technique in combination with reported mean errors in track and intensity, similar to DeMaria et al., 2009 but without the need for historical error distribution functions. Next, this emulator produces an ensemble of several (herein thousands) TC members. Then, for each ensemble member, a time- and spatially-varying wind field is generated and used to force a computationally efficient compound flood model SFINCS (Leijnse et al., 2021). The output consists of probabilistic wind and flood hazard maps that can be forecast on time with limited computational resources anywhere in the world. This paper refers to the TC forecasting framework as the Tropical Cyclone Forecasting Framework, TC-FF.

The paper is structured as follows. Section 5.2 introduces the Monte Carlo forecasting methodology. Section 5.3 describes the case study site and historical event of interest. The materials and methods used in this paper are described in Section 5.4. Validation in terms of tides and storms and application of the forecasting methodology are presented in Section 5.5. Finally, Sections 5.6 and 5.7 discuss and summarize the main conclusions of the study.

## 5.2. TROPICAL CYCLONE FORECASTING FRAMEWORK (TC-FF)

In this paper, we introduce the probabilistic Tropical Cyclone Forecasting Framework, TC-FF, to compute TC-induced compound flooding for operational risk analysis. Our approach integrates a TC emulator using a Monte Carlo-based ensemble sampling generation with an autoregressive technique, which is a simplified adaptation of DeMaria et al., 2009. The ensemble members are generated around the forecasted official track, considering the average historical errors in intensity, cross-track, and along-track. We deem these variables as the primary source of track uncertainty (e.g. Fossell et al., 2017). Other variables (e.g. information on wind radii) can be (stochastically) correlated to them. The ensemble members are provided as input for the fast compound flood model called SFINCS. Additionally, TC-FF considers tidal movements, storm surge, precipitation, and infiltration. The outcomes are consolidated into a unified probability product. By choice, each member has an equal likelihood of occurrence. The Python code for this method is accessible on GitHub via the following link: https://github.com/Deltares-research/cht_cyclones or one is referred to Zenodo (Nederhoff and van Ormondt, 2023)

### TC-FF FLOWCHART

A compact flowchart of TC-FF used to generate the ensemble member is shown in 5.1. The steps of this process are as follows:

1. *Define settings*: The user specifies the data source, period, time step of the ensemble generation, and the number of ensemble members requested.
2. *Input best track*: The code either determines the best track based on gridded time and spatial-varying wind and pressure fields (e.g., COAMPS-TC; Doyle et al., 2014 or reads in the forecasted track by one of the forecasting centers (e.g., NHC or other agencies).
3. *Error matrices for along-track, cross-track, and intensity*: The tool first computes random realizations based on the along-track, cross-track, and intensity standard deviations imposed for the time steps requested. The imposed mean absolute error is scaled with the timestep to overcome any time step dependency.

4. *Generate ensemble members*: Following the approach of DeMaria et al., 2009, a Monte Carlo method generates numerous ensemble members based on error matrices of the previous step in combination with an autoregressive technique for the along-track, cross-track, and intensity error.
5. *Generate wind, pressure, and rain fields*: Generate meteorological forcing conditions, i.e., the surface wind and pressure fields per time step per ensemble member, based on parametric methods (e.g., Holland et al., 2010 for subsequent analysis and application within numerical models. Rainfall can be included as well via intensity relationships.
6. *Simulation and post-processing*: In this study, the compound flood model SFINCS is applied, but in principle, other hydrodynamic models can also be applied, albeit typically at a higher computational expense. Data from the different ensembles are combined into several probabilistic outputs ranging from the probability of gale-force winds (wind speed > 35 knots or >18 m/s), compound flooding (water depth> 15 cm) to quantile estimates (e.g., 1% exceedance water level).

In the subsequent paragraphs, we describe in more detail the pre-processing, the computation of the ensemble members (track and intensity variations), and the determination of time- and spatially-varying wind fields.

## PRE-PROCESSING AND INPUT DATA

The pre-processing of TC-FF comprises three components.

First, one specifies the period they would like to simulate, including the total time period over which wind fields need to be generated and the time period over which the ensembles need to be generated. In addition, a timestep for ensemble generation (default 3 hours) needs to be specified. At this stage, one also specifies the mean absolute error and auto-regression coefficients for the along-track, cross-track, and intensity. When these values are unknown, calibration needs to be performed to determine them by comparing them with the reported errors of the forecast center (see calibration in Section 5.5.2. At this stage, one also specifies the number of ensemble members requested. The influence of the number of ensemble members is discussed in Section 5.5.3.

Second, since TC-FF creates random realizations around the best track, an input track is needed. Depending on the application, TC-FF reads a forecast bulletin that generates the track or determines the best track from the output of a high-resolution regional meteorological model. The determination of a track from a meteorological model is based on an algorithm that finds the minimum pressure in an area of interest. It takes in grid values, u and v wind components, pressure, minimum distance for clustering, and returns lists of x and y coordinates of cyclone eyes, the maximum wind speed plus pressure around each eye.

Third, before the generation of the ensemble members, TC-FF creates random errors with a normal distribution based on the provided average errors. Matrices are two-dimensional, with one dimension being the number of time stamps and the other the number of ensemble members. The imposed mean absolute error is scaled with the timestep to overcome any time step dependency and converted into a standard deviation.

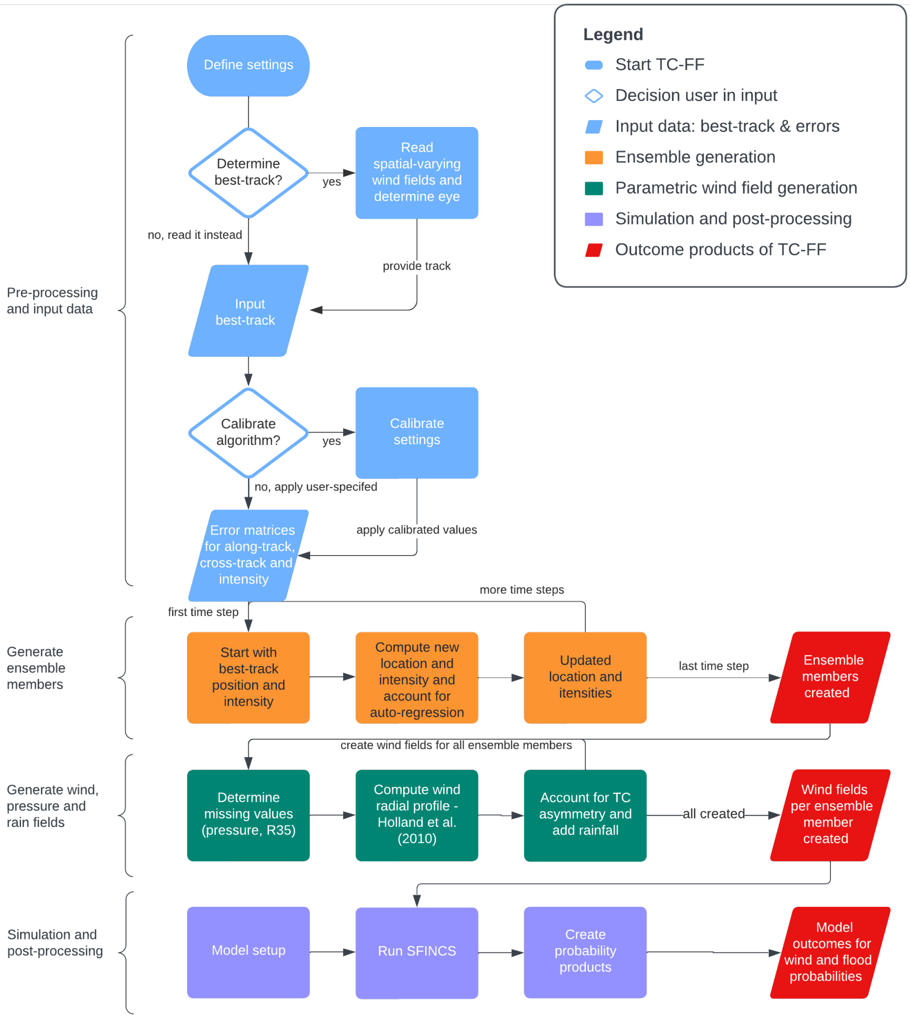

Figure 5.1: Flowchart of the Tropical Cyclone Forecasting Framework (TC-FF). Pre-processing stages are represented in light blue, the computational core of ensemble generation is denoted in orange, the parametric wind field generation is portrayed in green, the hydrodynamic simulation and analysis of winds are marked in purple and outcomes in red.

## ENSEMBLE MEMBERS

TRACK REALIZATIONS AND CALIBRATION An important component in TC-FF is the generation of track realizations (or ensemble members) from the official track forecast. The official positions are interpolated with a spline function to include values at all requested times. Our approach for the track realization largely follows DeMaria et al., 2009. We decompose the track error into the along-track (AT) and cross-track (CT) components and account for the track error serial correlation via autoregressive regression (Equations 5.2 and 5.2).

$$AT_t = a_t AT_{t-i} + B_{rnd} \tag{5.1}$$

$$CT_t = c_t CT_{t-i} + D_{rnd} \tag{5.2}$$

in which ATt and CTt are the AT and CT error at time steps t, at and ct are constants, ATt-3 and CTt-3 are errors of the previous time step (typically i=3 hours), and B and D are random numbers that are normal (Gaussian) distributed, scaled with the mean absolute error but are limited to +/- $2\sigma$.

Unlike DeMaria et al., 2009, we do not access the probability distributions of historical errors. Instead, we calibrate the parameters (at, ct, and mean absolute errors for B and D) based on the reported historical errors from the agency responsible for the issued forecast (see Section 5.5.2. This is a simpler methodology and requires substantially less data (which is also typically not accessible outside the forecast centers). These historical errors are routinely reported by the forecast centers (e.g., see Section 5.4 for information on the data sources used in this paper). Note that errors in our implementation (neither the error nor the auto-regressive coefficient) vary with lead time. We calibrate a constant mean absolute error in combination with a single auto-regression coefficient (see Section 5.5.2 for calibration and for the influence of simplifications). Moreover, the mean absolute error is converted into a standard deviation using a fixed relationship assuming a normal distribution of the error and scaled with the applied time step to allow the user flexibility in the applied time step.

The determination of the ensemble members is subsequently based on the sum of the forecast and random error components. In other words, we add the along-track and cross-track error to forecasted along- and cross-track. An example of the first 20 ensemble members is presented in Figure 5.2 panel B. Using this procedure, 10,000 ensembles are generated for each forecast case within this study; however, it is possible to use fewer ensemble members to reduce the computational cost but at larger statistical uncertainty (see Section 5.5.3 for trade-offs).

**INTENSITY REALIZATIONS AND CALIBRATION** Similar to the track realization, the maximum wind speed (intensity) at a specific interval is determined using a random sampling approach. The starting point is the official forecast of intensity that is interpolated to include values at all requested times, and a random error component (VEt) is added.

$$VE_t = e_t VT_{t-3} + F_{rnd} \tag{5.3}$$

in which VEt at time steps t, et is a constant, VEt-3 are errors of the previous time step (typically 3 hours) and F is random numbers that are normally distributed, scaled with the mean absolute error and is limited to +/- $2\sigma$.

The inland wind decay model adjusts the maximum intensity as a function of the distance inland, is directly based on DeMaria et al., 2009 and is computed with Equation 5.4. If the intensity of any inland ensemble member exceeds this predetermined value at any forecast time, the intensity is adjusted to match this value. Subsequently, the intensity errors are recalculated based on the adjusted intensity. Additionally, if the intensity of an inland ensemble member falls <7.7 m/s (15 knots) at any point in time, the TC intensity is reset to zero for all subsequent periods to overcome any unrealistic reintensifying TCs. All these criteria follow DeMaria et al., 2009.

$$V_i = 20 + 120e^{0.0035D} \tag{5.4}$$

in which the maximum wind speed (Vi) in knots and the distance to land (D) in kilometers (with negative values indicating inland cyclones) are given, the intensity of an inland cyclone can be determined.

The intensity implementation differs from DeMaria et al., 2009 in the following ways. We remove the dependency that the error scales with wind intensity and bias correction. Again, the determination of the ensemble members is based on the sum of the forecasted and random components computed with Gaussian mean absolute errors and an auto-regressive constant over lead time. Similar to the track realization, intensity errors are scaled with the time step to overcome any time step dependency. The influence of the simplifications and the difference compared to NOAA operational code based on the original DeMaria et al., 2009 and DeMaria et al., 2013 implementation are discussed in Section 5.5.2.

PARAMETRIC WIND FIELDS After the determination of the ensemble members, the time and spatial varying wind fields are constructed and written in a polar coordinate system. Several (horizontal) parametric wind profiles have been presented in the literature (e.g., Fujita, 1952; Chavas et al., 2015), with the original Holland wind profile (Holland, 1980) being the most widely used due to its relative simplicity. Several codes have been developed for storm surge models to provide time and spatial wind and pressure fields (e.g., Hu et al., 2012 for ADCIRC). Deltares, 2018 has developed the Wind Enhance Scheme (WES) to generate TC wind and pressure field around the specified location of a tropical cyclone center and given a number of TC parameters. In its current implementation, information on wind radii (radius of gale-force winds) can be considered in the Holland et al., 2010 formulation using information either from best track-data or from the proposed relationships of Nederhoff et al., 2019, which increases the accuracy of the method. Furthermore, the asymmetry of the wind field in a TC is also implemented, as delineated by Schwerdt et al., 1979. Winds throughout this study are converted from 1-minute to 10-minute using a conversion factor equal to 0.93 (Harper et al., 2010. Additionally, tropical cyclone-induced precipitation can be incorporated using empirical relationships such as IPET, 2006.

### SFINCS SIMULATION AND POST-PROCESSING

After the determination of the wind fields for all the requested ensemble members, TC-FF runs a hydrodynamic model. In this study, we apply the compound flood model SFINCS (Leijnse et al., 2021), which lends itself well to a large number of simulations in a reasonable amount of time due to its reduced complexity. SFINCS reads the tidal boundary conditions and wind, pressure, and rainfall conditions from the wind fields. Once all the ensemble member simulations have finished, probability products regarding wind and flood hazards are created. These products are created by sorting the results for each grid cell and providing estimates for either specific intervals (e.g. wind speeds > 35 knots or water depth> 15 cm) or quantile estimates (e.g., 1% exceedance water level). Only track uncertainty is considered in these estimates.

## 5.3. INSIGHTS FROM CYCLONE IDAI: A CASE STUDY

The TC forecasting framework is applied to a historical event that took place in Mozambique's Sofala province: Cyclone Idai, in March 2019. Mozambique is a country located in southeastern Africa (Figure 5.2). The country has a diverse population of over 31 million people, of which 2 million live in the Sofala province in central Mozambique. Sofala is primarily rural, with small communities along the Pungwe and Buzi river deltas (Emerton et al., 2020). Beira is the province's largest city, home to over 500,000 people, and an important port linking the hinterland to the Indian Ocean. The city is prone to flooding, particularly during the rainy season, which generally extends from October to April or May. This period coincides with the cyclone season, as cyclones often bring intense rainfall to the region. The vulnerability of Beira to flooding is exacerbated by factors such as climate change, rapid urbanization, and limited infrastructure.

Cyclone Idai was an example of a compound flood event that affected large parts of the coastal delta of Sofala (Eilander et al., 2022). The storm began as a tropical depression in the Mozambique Channel, causing extensive flooding after its first landfall in early March. It later intensified as it moved back over the sea, developing into a tropical cyclone with 10-minute sustained wind speeds of 165 km/h. Idai made landfall near the port city of Beira, bringing powerful winds, resulting storm surge, and heavy rains that caused widespread flooding and destruction. Large areas were flooded, first around the coast and a few days later, more inland in the Buzi and Pungwe floodplains. The total rainfall across the five days from March 13-18 ranged from 250–660 mm (NASA GPM, 2019). Over 112,000 houses were destroyed, and an estimated 1.85 million people were affected (UN OCHA, 2019.

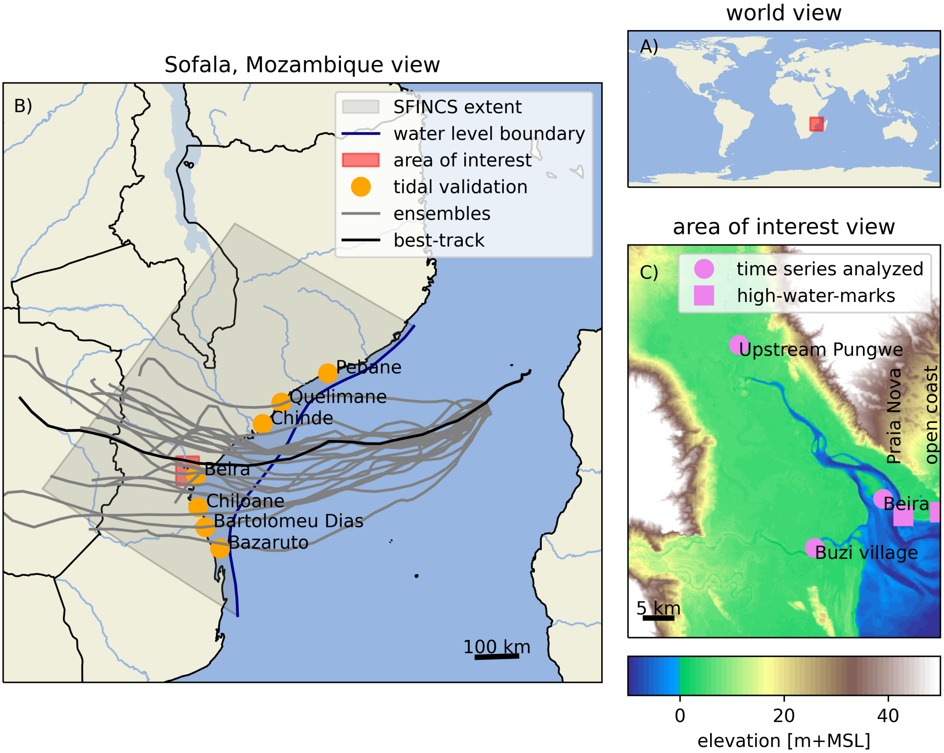

Figure 5.2: View of the study site: (A) Mozambique's Sofala Province is situated in the southeastern region of Africa in the Southern Hemisphere. (B) Geographical and hydrodynamic representation of the study area. The SFINCS model extent, highlighted in Panel B, encompasses a portion of the Sofala region, forced offshore with a water level boundary, and is validated at seven tidal stations (indicated by orange circles; see Section 8.1). The best track is represented by a solid dark line, with the first 20 ensemble members 5 days before landfall demonstrated as gray lines. (C) The area of interest is the Pungwe estuary, situated near the city of Beira. Model validation also takes place at two high-water-marks close to the city (signified by a purple box), with model outcomes depicted at three diverse locations across the estuary (marked by circles).

## 5.4. RESEARCH METHODOLOGY AND MATERIALS

### MATERIALS

ELEVATION DATASETS Several topographic and bathymetric datasets were collected and combined to develop a merged DEM. Data includes field survey data points collected during three campaigns in November-December 2020 across Beira, locally-collected LiDAR with a resolution of 2 meter, bathymetric charts, MERIT (Yamazaki et al., 2017; 90 meter) and GEBCO19 (IHO and BODC, 2003; 450 meter). Careful consideration was given to prioritize specific datasets in space to ensure the most detailed, recent, and accurate datasets were used in a given area. For example, survey and LiDAR data is bare earth and prioritized over the usage of MERIT and GEBCO19. The merged DEM was produced on medium-resolution (50 m) regional DEM, and a fine-resolution (5 m) local DEM in Beira. For more information on merging the data, one is referred to Deltares, 2021.

FORCING CONDITIONS Tidal boundary conditions were based on harmonic constituents provided by TPXO 8.0 (Egbert and Erofeeva, 2002), and tidal amplitudes and phases for all available 13 components were applied. The best track data (BTD) by the Joint Typhoon Warning Center (JTWC) is used throughout this study for meteorological forcing conditions (Joint Typhoon Warning Center, 2022). Reported error statistics by the JTWC for the 5-year average from 2016-2020 were used to inform the ensemble generation (Joint Typhoon Warning Center, 2021). Ensemble members from TC-FF were compared to 1,000 members produced with the code from NOAA, NHC, and JTWC based DeMaria et al., 2009 and DeMaria et al., 2013 that is used operationally (Buck Sampson, personal communication; June 5, 2023).

VALIDATION DATA Observed tidal coefficients near the city of Beira were used for the calibration and validation of the model (van Ormondt et al., 2020; see Figure 5.2 for locations). The validation of the event Cyclone Idai (2019) consisted of comparing both, observed and modeled flood extent in deltas of the Pungwe and Buzi rivers and high-water marks in the city of Beira. The observed flood extent was derived from Sentinel-1 synthetic aperture radar data (Eilander et al., 2022); and two observed high water marks (Deltares, 2021) were used, one at Praia Nova, in the western side of the city, and another one at the open coast beach in the southeast (see Figure 5.2 for locations). Correspondingly, values of modeled flood extent and high water marks were output at the same locations.

## METHODS

AREA SCHEMATIZATION For this study, we employed the Super-Fast INundation of CoastS (SFINCS) model, which solves the simplified equations of mass and momentum for overland flow in two dimensions (Leijnse et al., 2021). The goal was to create one continuous compound flood area model that computes tidal propagation, storm surge, pluvial and fluvial flooding.

The area schematization builds upon Eilander et al., 2022 but varied in three ways. First, we extended the model alongshore and in deeper water to alleviate the need to nest in a large-scale regional coastal circulation model and generate tidal propagation and storm surge within the domain. The model was extended 500 km alongshore from Beira to ensure that a cyclone hitting Beira is fully resolved within the domain. Moreover, the model was extended into 1000-meter water depth where wind shear has a negligible impact on the storm surge. Using a quadtree implementation (e.g., Liang et al., 2008), we applied a variable model resolution ranging from 8000 to 500 meters. A quadtree is a technique in which the refinement from one level to another is based on the original cell but divided into 4 smaller cells with 2 times smaller grid size and allows extending the model setup into deeper water without having time step restrictions in deeper water based on the explicit numerical scheme of SFINCS. Second, high-resolution topo-bathymetry and land roughness were included in the native resolution utilizing subgrid lookup tables (Leijnse et al., 2020). However, the hydrodynamic computations were performed on a coarser resolution to save computational time. Up to 10 meter DEM information was included in the 500 meter grid cells (i.e., factor 50 refinement). Lastly, subgrid bathymetry features were included to account for maximum dune height based on the DEM to control overflow during storm conditions around Beira. For both the subgrid lookup tables and features, the elevation datasets from Deltares, 2021 on 5-meter resolution were used (see Section 5.4 for more information). For the lookup tables, we linearly interpolated the high-resolution DEM onto the subgrid. For the subgrid features, the lines element had a resolution of 500 meters and per vertices the highest point in a radius of 500 meter was used.

A spatially-varying roughness and infiltration was used based on land elevation. All points above mean sea level (MSL) have a high Manning friction coefficient of 0.06 s/m1/3, and an infiltration rate of 1.9 mm/hr (typical values from HSGs Group C; United States Department of Agriculture, 2009), and all other points have lower friction of 0.02 to represent water and do not have any infiltration. The SFINCS model was forced with tidal boundary conditions and time- and spatially varying winds, pressure, and rainfall fields. At the offshore boundary, tidal water levels were imposed and inverted barometer effect accounted for. We refer to Appendix 5.7 for calibration of the tides, in which we show that the area model reproduces tides with a median MAE of 21 cm. Wind and pressure fields were created with the Holland wind profile (Holland et al., 2010) based on the BTD (see Section 5.2 for details). Rainfall for TCs was based on the Interagency Performance Evaluation Task Force Rainfall Analysis (IPET, 2006 method. Comparison with the reported rainfall total revealed a significant underestimation of cumulative rainfall during Idai based on IPET. Based on the magnitude of the underestimation, rainfall estimates by IPET were tripled, resulting in a cumulative rainfall in the area of interest of 495 mm for the best track, which is in a similar order of magnitude as observed (see Section 5.3). For fluvial processes, rather than using data sources like river discharge measurements or a hydrological model, our model only relies on a rain-on-grid with infiltration methodology to simulate surface runoff and its subsequent accumulation, thus providing an first-order estimate of fluvial flooding.

SIMULATIONS PERIODS The validation of the area schematization focused on two time periods. First, 3 spring-neap cycles (January 13, 2022, until February 26, 2022) were used for the tidal calibration and validation in the area of interest (see Appendix 5.7). Second, Idai was hindcasted forced with the JTWC BTD and compared to observational data for flood extent and high-water levels (Section 5.5.1). After validation of the area schematization, the new forecasting methodology introduced in Section 5.2 was applied. Various lead times ranging from 1 to 5 days before the second landfall for 10,000 ensemble members were computed (Section 5.5.3).

Model runs were performed on the Deltares Netherlands Linux-based High-Performance Computing platform using 10 Intel Xeon CPU E3-1276 v3. The simulations were run on CPU with openMP enabled to utilize the 4 cores per Xeon processor. On average, a 7-day Idai simulation took about 4 minutes on a single processor. Running all 50,000 events took 15 days using all 10 processors.

**MODEL SKILL** Several accuracy metrics were calculated throughout this study: model bias, mean-absolute-error (MAE; Equation 5.5), root-mean-square-error (RMSE; Equation 5.6), unbiased RMSE (uRMSE; RMSE with bias removed from the predicted value). These error metrics are used for comparison in water levels, wind speed and track errors.

$$MAE = \frac{1}{N}\sum\left(\left|y_i - x_i\right|\right) \tag{5.5}$$

$$RMSE = \sqrt{\frac{1}{N}\sum\left(y_i - x_i\right)^2} \tag{5.6}$$

where N is the number of data points, yi is the i-th prediction (modeled) value, xi is the i-th measurement.

Moreover, skill is quantified by binary flood metrics (Wing et al., 2017). The model output (M) is converted to one of two states: wet (1) or dry (0), using a commonly used threshold of 15 cm (e.g., Wing et al., 2017) and compared to the Sentinel benchmark data (B). The Critical Success Index (C; Equation 5.7) accounts for both overprediction and underprediction and can range from 0 (no match between modeled and benchmark data) to 1 (perfect match between modeled and benchmark data).

$$C = \frac{M_1 B_1}{M_1 B_1 + \ M_0 B_{1+} \ \ M_1 B_0} \tag{5.7}$$

For the comparison of cumulative distribution functions (CDF) of cross-track, along-track and intensity, we also applied the Continuous Ranked Probability Score (CRPS; Matheson and Winkler, 1976). CRPS measures how good forecasts are in matching observed outcomes; where CRPS = 0, the forecast is wholly accurate, and CRPS = 1, the forecast is wholly inaccurate.

$$CRPS\,(F, x) = \int_{-\infty}^{\infty} \left[F\left(y\right) - F_0(y)\right]^2 dy \tag{5.8}$$

where F(y) is the CDF is associated with an empirical probabilistic reference and prediction.

ANALYSIS METHOD The analysis of forecasting results was undertaken using several methods. Initially, extreme wind speeds and water levels were assessed by charting them as time-series data, inclusive of quantile estimates such as the 95% confidence interval (CI). Following this, the maximum values registered during the simulation were organized into cumulative distribution functions (CDFs). This process offered insights into their exceedance probability. Finally, the mean probability of flooding was computed. The method to derive this value entailed counting the instances where computational cells registered a minimum of 15 cm of water. Only cells positioned above mean sea level (MSL) were incorporated into the area estimates.

## 5.5. RESULTS

This section is organized into three parts, each addressing a crucial aspect of our study on Cyclone Idai's compound flooding. First, we assess the model's accuracy in simulating tidal, storm surge, and combined pluvial and fluvial impacts (Section 5.5.1). Next, calibration of TC-FF to average errors for the along-track, cross-track, and intensity for the Southern Hemisphere and validation of TC-FF for Idai specifically to the implementation from NOAA, NHC and JTWC that are used operationally is presented (Section 5.5.2). Lastly, we delve into forecasting uncertainties and their effects on flood predictions, using ensemble simulations with various lead times (Section 5.5.3).

### 5.5.1. VERIFICATION OF NUMERICAL MODELING

Computed water levels near Beira show the strong tidal modulation and the wind-induced storm surge during the landfall of the cyclone (Figure 5.3 – panel A; blue line for water level and vertical line for moment of landfall). Based on the difference between the predicted astronomic tide and the total modeled water level, we estimate a storm surge of >3.5m due to the 45 m/s wind speeds (Figure 5.3 – panel B). The storm surge at Beira is driven by wind setup as well as pluvial and fluvial drivers. Deeper in the estuary, in the Pungwe flood plains, water levels peaked several days after landfall due to intense upstream rainfall and subsequent runoff. Water levels near Buzi Village seem to be a combined result of first marine and second riverine-driven water levels.

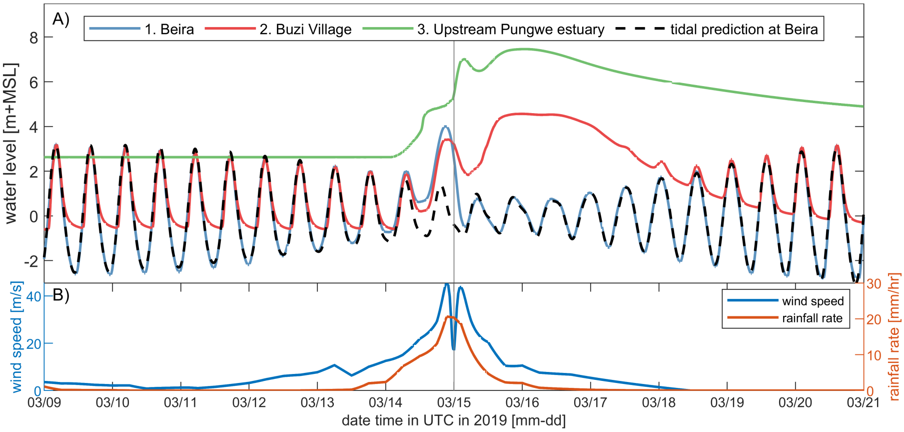

Figure 5.3: Time series of water levels, wind speed, and precipitation within the study area. (A) Computed water levels at various locations (blue for Beira, red for Buzi village, and green for upstream in the Pungwe estuary (see Figure 5.2 - panel C for their location) and the black dashed line representing the astronomical prediction at Beira. (B) Simulated wind speed (blue) and rainfall rate (red) over the same period. Idai made landfall on March 15, and its powerful winds and rainfall resulted in marine flooding at Beira and riverine-driven flooding upstream in the estuary. The vertical line represents the moment of landfall.

Validation of the SFINCS model for the observed extent (blue colors in Figure 5.4 - panel A) gives confidence in the ability to simulate the compound flooding (Figure 5.4). The model can reproduce the Sentinel-1 derived extent with a Critical Success Index of 0.59. This skill score is comparable to previous work by Eilander et al., 2022, albeit somewhat lower. Based on the differences between the modeled and satellite-derived extent, it becomes apparent that the model underestimates the flooding around the Buzi River (false negative; orange colors in Figure 5.4B around 660-7800 km). We hypothesize this is due to the lack of river inflow related to an underestimation of rainfall further upstream and/or overestimation of infiltration due to soil saturation which is not considered. Moreover, the comparison with satellite-derived flood extent indicates an overestimation of the flooding at Beira (false positive; red colors in Figure 5.4). Here, we suspect that the benchmark data might be off, and the coastal flooding already receded before the Sentinel data recorded the extent. The observed high-water marks near Beira ranged from 3.6 m within the estuary to 2.9 m+MSL at the open coast and are reproduced by SFINCS with respectively 3.8 and 3 m+MSL. This difference suggests a positive bias of the model results at the coast of 10-20 cm, similar to the tidal validation (see Appendix 5.7), which revealed a median MAE of 21 cm.

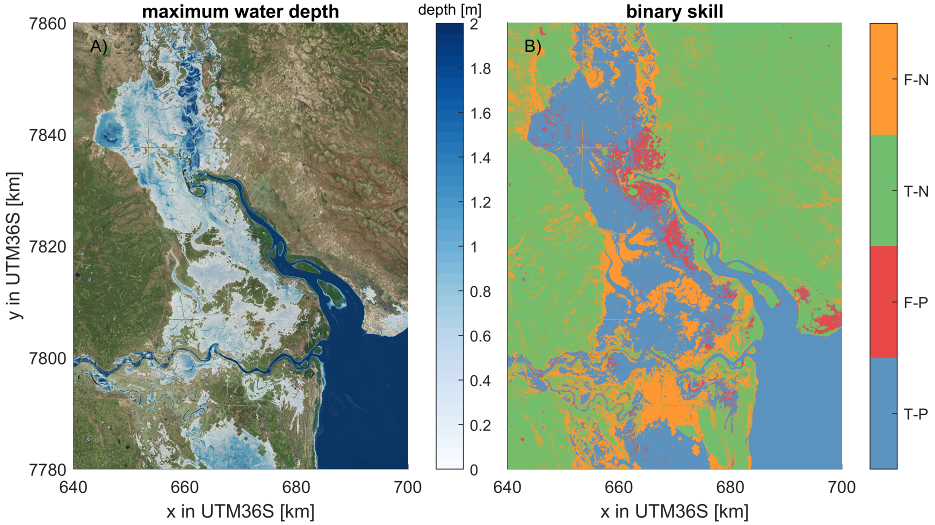

Figure 5.4: Maximum computed water depth (Panel A) and binary skill of flood extents for Idai (Panel B). Water depths are downscaled from the model resolution to the 10x10 meter resolution of the topo-bathymetry. The binary skill evaluation (Panel B) assists in determining the model's accuracy and dependability, and the Sentinel-1 radar data is used as a reference to determine skill. A true-positive (T-P) outcome denotes a correct flood prediction by the model compared to Sentinel-1 derived extent, whereas a false-positive (F-P) occurs when the model forecasts a non-existent flood. In contrast, a false-negative (F-N) indicates where the model overlooks an actual flood, and a true-negative (T-N) result occurs when the model accurately predicts the lack of a flood event. The model produces large-scale flooding, which is largely also observed in the data, but local differences of over- and underestimation exist. The coordinate system of this figure is WGS 84 / UTM 36 S (EPSG 32736). ©Microsoft.

### 5.5.2. CALIBRATION AND IMPACT OF SIMPLIFICATIONS

This study used JTWC-reported errors for the along-track, cross-track, and intensity for the Southern Hemisphere to calibrate our methodology (Joint Typhoon Warning Center, 2021). For other case studies, for example, based on different forecasting agencies or in other ocean basics), these reported errors can be used instead. Calibration is performed by minimizing the square-root difference between computed and reported mean absolute values for various lead times using the Nelder-Mead method. This effort resulted in mean absolute errors for B and D of 68.5 and 55.3 km and autoregression coefficients $a_t$, $c_t$, of 1.214 and 1.181 (Figure 5.5 - panels A and B) for the along-track and cross-track. Moreover, we calibrated the mean absolute error and regression coefficients for the intensity, which resulted in mean absolute errors for F of 9.28 m/s and autoregression coefficient $e_t$ of 0.624 (Figure 5.5 - panel C).

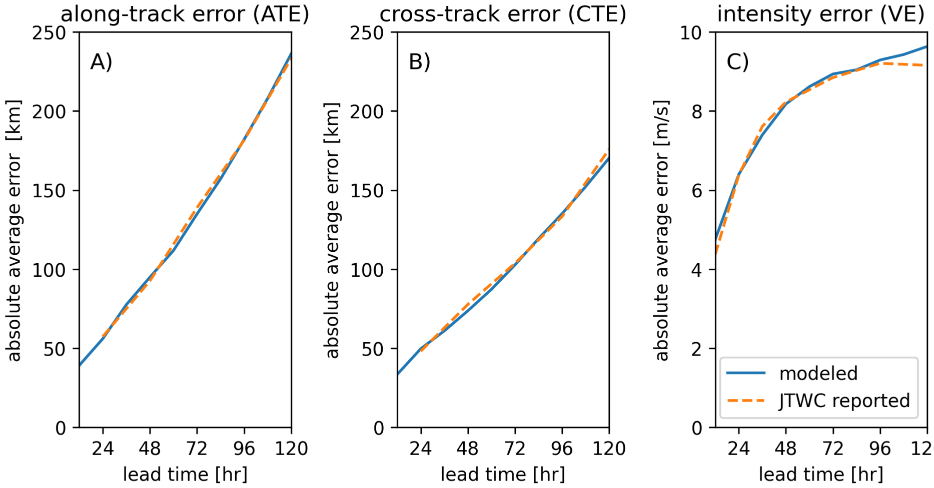

Figure 5.5: Comparison of calibration results for the probabilistic forecasting method TC-FF (solid blue line) and the Joint Typhoon Warning Center (JTWC) reported error statistics based on the 5-year average (2016-2020) in the Southern Hemisphere (dashed orange line). Panel A represents the along-track error, Panel B demonstrates the cross-track error, and Panel C exhibits the wind speed or intensity error. Modeled errors are based on 1,000 ensemble members. Modeled absolute average errors are similar to JTWC.

Errors produced by TC-FF are compared to the implementation from NOAA, NHC and JTWC that are used operationally. Minor differences between the TC-FF and full implementation based on DeMaria et al., 2009 and DeMaria et al., 2013 exist and are attributed to the simplifications used in the error distribution (including the lack of GPCE). The distribution in along-track, cross-track, and intensity error is typically in the same order (Figure 5.6), which is confirmed by a median CPRS over various lead times from 0 to 120 hours of 0.07, 0.05, 0.10 and median MAE of 37 km, 21 km, and 7 m/s of for respectively the along-track, cross-track, and intensity. At the same time, TC-FF has by design no bias corrections in terms of cross-track, along-track and intensity errors, whereas the operational system does, leading to the positive median along-track error in red compared to the blue line in Figure 5.6A and a median bias of -16 km. Besides the median estimates, the interquartile range (25-75%) and 95% CI match relatively well for the along-track and cross-track errors. Larger differences are found for the intensity error. In general, the wind intensity error looks visually erratic and doesn't start at zero for no lead time, which is the result of the inland wind decay model. Both JTWC and TC-FF have a negative bias due to the effect of land, but TC-FF does have a median bias of +6.7 m/s compared to JTWC, suggesting that TC-FF overestimates. However, more substantial differences are found for the interquartile range and 95% CI. These findings for the along-track, cross-track, and intensity are supported by a more detailed analysis of the CDF for the different parameters as a function of lead time (Figure 5.12, Figure 5.13, Figure 5.14). For the along-track and cross-track, we observe an increase in the MAE and uRMSE as a function of lead time but a decrease in the CPRS. The increasingly larger error distribution influences this pattern. Moreover, TC-FF produces Gaussian-distributed errors while the JTWC error distribution differs since it is based on historical error distribution and adjusted based on the GPCE. Similar to Figure 5.6, larger differences are found for the intensity error, which is influenced by the bias correction that increases with lead times.

### 5.5.3. FORECASTING INSIGHTS FROM CYCLONE IDAI

This section presents the application of forecasting Idai using the TC-FF.

UNCERTAINTY THREE DAYS BEFORE LANDFALL The TC-FF method with 10,000 ensemble members is applied to the case of Cyclone Idai. The results reveal that accounting for the uncertainty of the TC track and intensity of eye three days before landfall results in considerable uncertainty regarding wind speeds and water levels near Beira (Figure 5.7) or the region (Figure 5.8). In particular, the wind speeds show a 95% CI of about 7-40 m/s at the moment of landfall (Figure 5.7 - panel A) versus 45 m/s or a Saffir-Simpson Hurricane Wind Scale (SSHWS) of 2 of the best track. Moreover, TC category 1 wind speeds could occur as early as March 14 at 07:30 UTC or as late as March 15 at 11:10 UTC. This spread of possible maximum wind speeds at Beira results from the large uncertainties in intensity and a difference in landfall location and time. Based on the same model simulations, the empirical cumulative distribution function (CDF) of the maximum wind speed at Beira ranges from 8.8 to 59.2 with a median wind speed of 25.5 m/s, while the best track has a

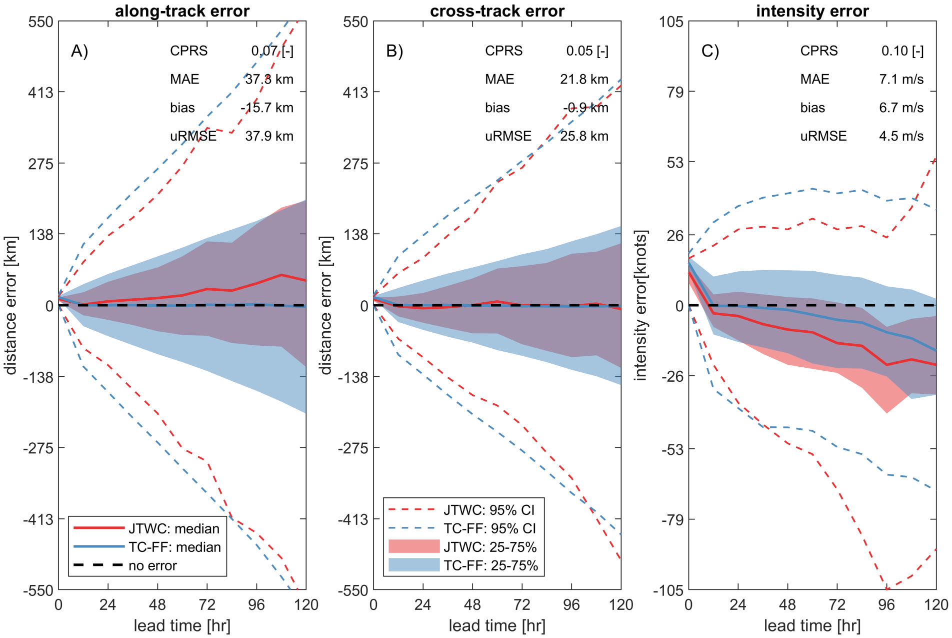

Figure 5.6: Comparison of validation results for the probabilistic forecasting method TC-FF (blue line) and the Joint Typhoon Warning Center (JTWC) operational product (red line). Panel A represents the along-track error, Panel B demonstrates the cross-track error, and Panel C exhibits the wind speed or intensity error. Errors computed for both the TC-FF and JTWC are based on 1,000 ensemble members. Solid lines are median estimates, shaded areas the interquantile range (25-75% CI) and dashed line the 95% CI. TC-FF and JTWC produce broadly similar error distributions for different lead times.

5.9% exceedance probability (Figure 5.7 - panel B). Consequently, water levels vary greatly (Figure 5.7 - panel C). For example, ensemble members can exhibit a sizeable wind-driven setup due to TC wind blowing from offshore into the estuary, pushing water up in the estuary and at Beira. For landfall locations west of the estuary, the wind blows offshore, resulting in a large set-down. Note that Beira is in the Southern Hemisphere, and due to the Coriolis effect, TCs spin clockwise. The highest water levels occur when high tide and wind-driven setup coincide, which explains the three peaks in the 95% CI water level given the semi-diurnal tide and the highest possible wind speed for 1.5 days (Figure 5.7 - panel C). The maximum water levels are dominated by the tide except in the situation of cyclone impact (see the CDF in Figure 5.7 - panel D and the minimum value of 3.5m+MSL around 90%, which is influenced by the tide and time window over which it is determined). The specific track of Idai resulted in relatively extreme conditions compared to other possible combinations (both for winds and water levels). A similar pattern can be observed in the spatial maps shown in Figure 5.8. The average probability of flooding in the area is 26%, with higher probabilities of flooding found in the lower-lying portions of the estuary (note we are excluding points below MSL; Figure 5.8 - panel A). The 1% exceedance flood depth threshold shows a large extent and is quite similar to the computed extent due to Idai (see Figure 5.4 - panel A for comparison with Figure 5.8 - panel B). The main difference is that there is more flooding near the city of Beira and somewhat less near Buzi Village. The match between the 1% exceedance flood depth and the best track with Idai suggests that the event was relatively severe and implies that even though many other potential scenarios could have unfolded, they likely would not have resulted in the same extensive flooding caused by Idai.

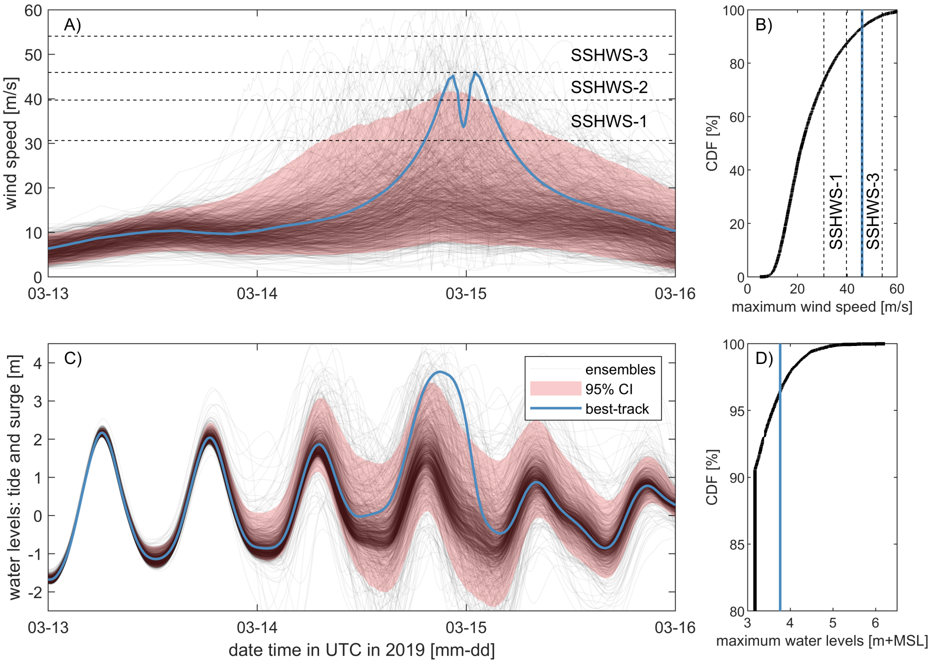

Figure 5.7: Multi-panel Analysis of wind and water Levels three days before landfall: (A) time series of wind speeds, (B) maximum wind speeds, (C) time series of water levels near Beira, and (D) maximum water levels. Data is derived from 10,000 ensemble members (black transparent line; every 10th plotted) with red shading representing the 95% CI. The best track (blue line) and the Saffir-Simpson Hurricane Wind Scale are included for comparison (panels A and B only). There is substantial uncertainty in wind speeds and water levels near Beira three days prior to landfall.

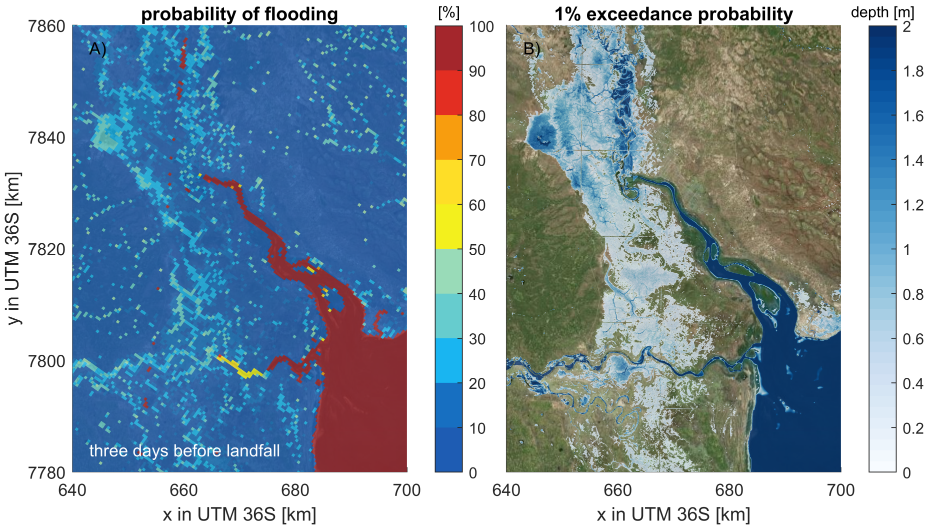

Figure 5.8: Probabilistic flood analysis for Cyclone Idai three days before landfall: (A) Spatial distribution of flooding probability; (B) Corresponding 1% exceedance water depth estimates, highlighting areas at most significant hazard. Results in panel A are determined from 10,000 ensemble members on the original 500-meter model resolution, while water depth in panel B is downscaled to the original 10x10-meter bathymetry resolution. Higher probabilities of flooding are found in the lower-lying portions of the estuary. The coordinate system of this figure is WGS 84 / UTM 36 S (EPSG 32736). ©Microsoft.

INFLUENCE OF SAMPLING SIZE As described by Cashwell and Everett, 1959 and DeMaria et al., 2009, the precision of Monte Carlo techniques is proportional to the number of ensemble members (N). The convergence rate typically shows a slower progression than 1/N, constituting a limitation intrinsic to all Monte Carlo methods. To investigate the convergence rate and the error induced by employing a finite number of ensemble members, the Idai forecasting case three days prior to landfall is used, analogous to the preceding section, albeit with a variable number of ensemble members. Additionally, bootstrapping is employed to approximate convergence rates and the accompanying uncertainty.

The estimation of the 95% exceedance maximum water levels in proximity to Beira exhibits convergence with the number of ensemble members, albeit with considerable deviations compared to a fully converged solution with 10,000 members when implementing a low number of ensemble members (Figure 5.9 - panel A). For instance, employing merely 50 ensemble members results in an interquartile range (25-75%) of -0.28 to +0.10 m. Increasing the number of ensemble members reduces this sampling uncertainty to a range of -0.09 to +0.06 m for 200 ensemble members.

Similarly, the standard deviation for several quantiles of maximum water level estimates at Beira reduces with more ensemble members. It exhibits a similar pattern from higher to lower quantiles (Figure 5.9 - panel B). In essence, estimating rare events necessitates executing more ensemble members to attain comparable convergence. This study found that the 95% exceedance maximum water level at Beira when utilizing 200 ensemble members has a standard deviation of 21 cm (blue line Figure 5.9 - panel B). This level of convergence seems acceptable since it is in a similar order as the skill of the hydrodynamic model (see Section 5.5.1).

The probability of error in flood potential is expressed as a function of N on a log-log plot (Figure 5.9 - panel C). Compared to a fully converged solution with 10,000 members, for N=200, the mean error constitutes 0.95%, and the maximum error amounts to 1.53%. Note that this estimate is without considering the model error. In the log-log diagram, the errors exhibit near-linear correlations with N and could serve as a basis for determining the number of ensemble members needed for a specified confidence level. For instance, to achieve a maximum error of 1% in flood probability, it would be necessary to utilize 500 ensemble members.

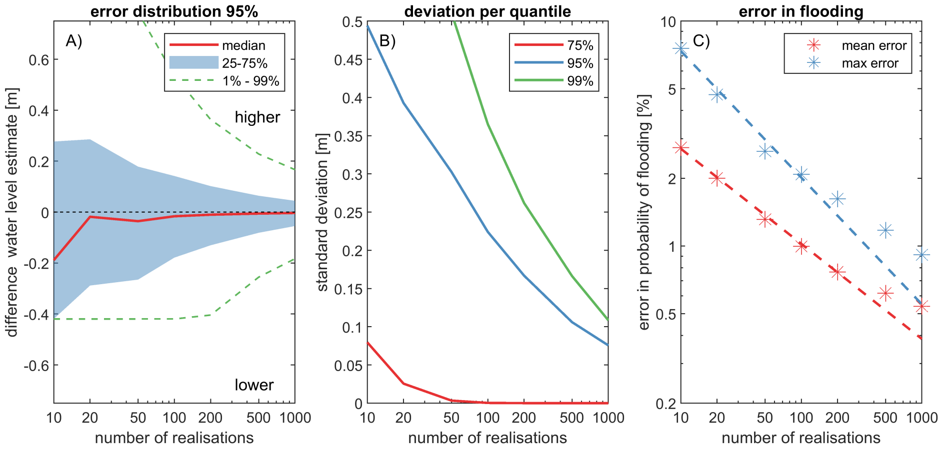

Figure 5.9: Sampling size effects on flood estimation accuracy. (A) Quantiles of sampling error for the 5% exceedance water level. (B). Standard deviation of 75%, 95%, and 99% quantiles, illustrating the uncertainty in estimation. (C) Comparison of maximum and average error in flood probability predictions. All panels were generated using 10,000 ensemble members and a 1000-bootstrap resampling approach. Using more ensemble members reduces the sampling uncertainty.

IMPORTANCE OF LEAD TIME Thus far, the probabilistic TC forecasting framework has been implemented three days prior to the landfall of Idai. Nevertheless, the forecast's results fluctuate with lead times, consequently influencing the associated evaluations of water levels (Figure 5.10) and flood probabilities (Figure 5.11).

The predicted water levels (tide + surge) vary with lead times (Figure 5.10 - panels A and C). Specifically, at a lead time of five days before landfall, an (unsurprisingly) larger spread between the ensemble members is observed compared to lead times of, for example, one or three days. Moreover, as landfall approaches, the time series converges since increasing ensemble members produce highly similar predictions. For example, notice how individual ensemble members 1 day before landfall show similar storm surges and still water levels (i.e., the concentration of lines which becomes more apparent in Figure 5.10). Moreover, the 5% and 95% exceedance values become less spread out and more peaked around landfall (dashed lines in Figure 5.10). This convergence is more apparent for the storm surge. The CDF of the maximum storm surge levels increases with reducing lead time (Figure 5.10 - panel B). For example, the median storm surge increases from 0.5m five days before landfall to 0.9 and 2.0m for lead times of three days and one day, respectively (notice the increasing median estimate in the CDF plot from 5 to 1 day in Figure 5.10 - panel B). This increase in maximum storm surge shows the increasing certainty that the TC will land near Beira. However, for other locations, the opposite may occur as the landfall shifts away from it. The still water levels are influenced by both tidal motions and the influence of the TC (Figure 5.11 - panel C). This strongly influences the maximum computed still water level (Figure 5.11 - panel D). For instance, the lowest maximum water level for all simulations is around 2 m above MSL, resulting from the maximum tidal range rather than the TC itself. The 95th quantile of the maximum still water level is 3.4 m + MSL five days prior to landfall, which increases to 3.6 and 4.0 m+MSL for lead times of three days and one day, respectively. The best track of Idai is included as a reference and estimated to have a 9% probability of exceedance 1 day before landfall.

A large portion of the Sofala province faces a minor flood risk five days before the actual landfall. The flood probability for the estuary near Beira increases as lead times reduce (Figure 5.11 - panel B). In particular, the average probability of flooding five days before landfall is 15%, increasing to 17 and 24% for lead times of three and one day, respectively. Conversely, for the entire model domain, a probability of greater than 1% flooding declines from 97 to 94 and 64 km2 for lead times of five, three, and one day (Figure 5.10 - panel A). In other words, five days before landfall, less confidence in predictions translates into more spatial variability on flooding probability tied to a larger impact area. Closer to the actual landfall, there is more certainty over which area will be affected.

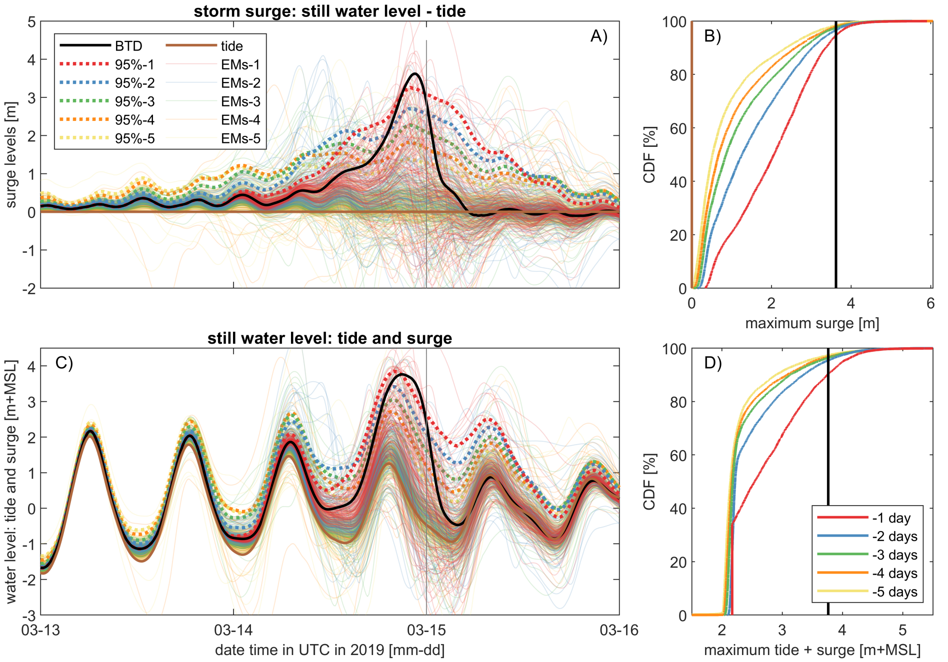

Figure 5.10: Forecasted water levels in Beira for 1-5 day lead times: temporal evaluation and cumulative distribution. Panel A and C: Time series illustrating the forecasted water levels in proximity to Beira with lead times ranging from 1 to 5 days prior to landfall showcasing both individual ensemble members (solid transparent lines; every 100th plotted), tide-only (brown), best-track (black) and quantile estimates (95% dashed lines). Panels A and C use the same colors and line styles. Panel B and D: Cumulative distribution function (CDF) showing the maximum water levels in ascending order for all ensemble members, providing insights into the probability of occurrence for various water level thresholds. Panels B and D use the same colors. Panels A and B show the storm surge levels (computed still water levels minus predicted tidal levels), while Panels C and D present the still water level (tide and surge).

## 5.6. DISCUSSION

This paper describes a new probabilistic method to forecast TC-induced coastal compound flooding by tide, surge, and rainfall using Monte Carlo sampling. Due

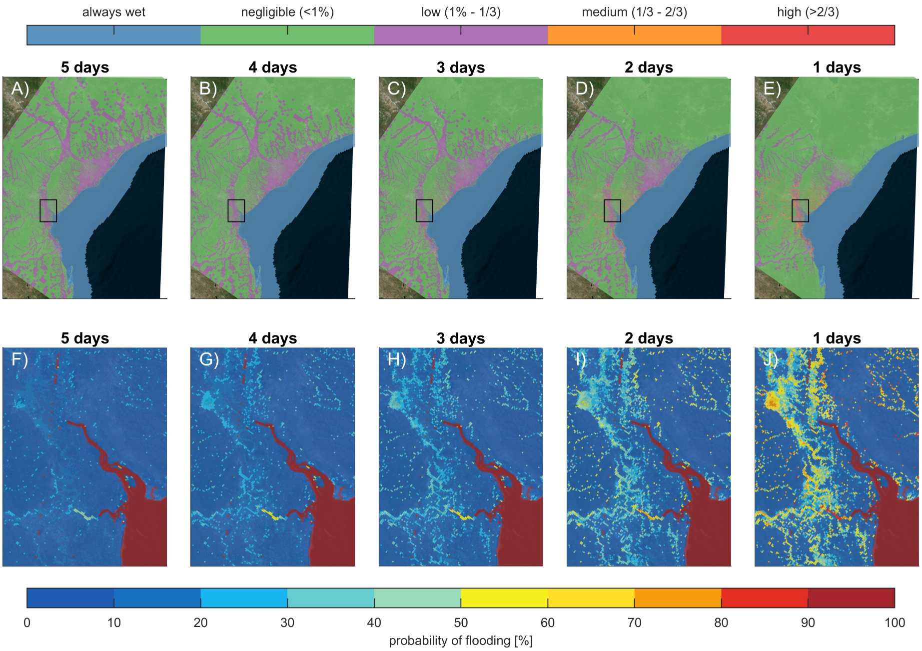

Figure 5.11: Evolution of the flood probability prior to landfall: Panels A-E depict the spatial distribution of flooding probabilities at 5, 4, 3, 2, and 1 day(s) before landfall, respectively. Color gradients represent the varying probability. The top panels focus on the entire area simulated and the bottom panels on the Pungwe and Buzi river deltas. With decreasing lead time, the area that could be affected decreases while there is an increased probability of flooding near Beira. The coordinate system of this figure is WGS 84 / UTM 36 S (EPSG 32736). ©Microsoft.

to the limited number of observations on TC evolution, for short-term operational analyses, an autoregressive technique that imposes potential errors on top of the forecasted track is preferred over those parametric sampling techniques used for long-term strategic risk assessments based on historical records (e.g., Nederhoff et al., 2021a). In addition, for the same scarcity of observation, there is limited knowledge of the underlying joint distribution between TC and ocean characteristics, which makes Monte Carlo sampling preferred compared to sampling techniques that are highly efficient for complex multivariate patterns such as cluster analysis (e.g., Choi et al., 2009a) and MDA methods (e.g., Bakker et al., 2022). However, exploring the possibility of increasing efficiency via the aforementioned methods is important, especially since the error space increases as a function of lead time, and estimating these events requires increasing amounts of ensemble members (Figure 5.9). However, this is a topic that requires an in-depth analysis and is beyond the scope of the present study.

Compared to the implementation of DeMaria et al., 2009 and DeMaria et al., 2013 , the ensemble generation is simplified by removing bias corrections, applying a single normal error distribution calibrated on historical errors (Figure 5.5), and does not account for the uncertainty of the track forecasts on a case-by-case basis via GPCE. While we acknowledge these simplifications, this method does make it possible to account for TC forecasting errors for any ocean basin based on reported average historical errors alone. Nevertheless, the behavior of a specific tropical cyclone (TC) does not necessarily conform to the "average" pattern, and differences between the operational JTWC model were found (Figure 5.6). For Beira, we found minor differences in the comparison of TC-FF and JTWC operational ensembles that do account for the uncertainty of the track forecasts on a case-by-case basis. Thus the case study presented in this paper, suggests that the universal historical error statistics versus a TC-dependent error sampling might be acceptable, however, follow-up work will be needed to test if this findings holds for other TCs. Moreover, the system only accounts for uncertainty in track parameters and does not account for uncertainty in, for example, rainfall or computed storm surge. The implications of these assumptions on the precision and predictive proficiency of our approach for coastal compound flooding remain undetermined. Our implementation has been recently integrated into an operational system tailored for the contiguous United States. Verification of the reliability of this operational system is currently pending. Regardless, TC-FF compares well with the predictions provided by ECMWF of Idai that showed a probability of 50 to 90% of severe flooding four to one day before landfall (Figure 5.10). We hypothesize that track uncertainties dominate several days before landfall while <1-day other sources of uncertainty start to become more important and should ideally be accounted for.

In the introduced methodology, we apply the compound flooding model SFINCS. The validation gave confidence that the hydrodynamic model reproduces the main tidal motions and flooding during Idai. Differences did exist compared to the (limited) validation data (Figure 5.4). Additional data sources to assess the model's spatiotemporal accuracy and reliability in simulating the compound flooding event would be advantageous but were unavailable (when this study was performed). The model skill could be improved by including additional wind radii information in the parametric wind model (e.g. radius of gale-force winds along different quadrants) and more accurately resolving on-land winds, rainfall, and infiltration processes. For example, Done et al., 2020 present a methodology to account for terrain effects by adjusting winds from a parametric wind field model by using a numerical boundary layer model. Here, we applied the IPET empirical relationship that relates pressure drop to rainfall intensity. We chose IPET over other methods since this relatively simple method demonstrated the highest skill at reproducing storm-total precipitation in Brackins and Kalyanapu, 2020. However, deployment showed the necessity to triple the rainfall rate due to severe underestimation of the total rainfall and associated flooding. We hypothesize this does influence model skill from SFINCS but suspect limited influence in results geared towards TC-FF applicability and sensitivity regarding sample size and lead time. Improvement (deterministic or stochastic parametrizations) of TC rainfall could overcome this limitation. For example, we acknowledge that there are other computationally efficient TC rain models in the literature that might perform better (e.g., Lu et al., 2018) and are exploring incorporating these methods in TC-FF. Moreover, SFINCS was run with a constant infiltration rate and does not account for drainage systems, fluvial discharge from the large catchment and flood protection measures besides the frontal levee. It is also unknown how the topo-bathymetry that was collected before Idai influenced results. Lastly, the effects of waves (e.g., setup, runup, overtopping) and morphological change were not considered. All these limitations affect the model skill and could explain some mismatches observed compared to Sentinel-1 data and high-water marks at Beira. However, the computational efficiency of SFINCS allowed us to run thousands of ensemble members on limited computational resources. We accept the loss of some model accuracy with this gain of speed. For future developments, we do envision accounting for these uncertainties in addition to variability in track parameters.

The focus of the development of TC-FF has been geared to the computation of overland flooding. However, TCs pose significant hazards through both water and wind. A study by Rappaport, 2014 indicated that from 1963 to 2012 in the United States, approximately 90% of fatalities associated with tropical cyclones were due to water-related incidents. The wind-related fatalities were about 8%. This does not provide insight into the cause of damage associated with landfalling TCs, nor does it provide insight into how these ratios vary across the globe. Regardless, TC-FF does provide the possibility to estimate extreme wind speeds and link this to potential damage as an additional data product. Including wind damage as part of our framework is something we are planning to work on in the future. Moreover, while this study was written from an operational short-term risk analysis perspective, the same methodology can also be used within strategic long-term risk analysis to explore perturbations to the track and perform 'what if' sensitivity testing to coastal flooding (e.g., Rye and Boyd, 2022).

## 5.7. CONCLUSION

A new method and highly flexible open-source tool was developed to perform probabilistic forecasting of tropical cyclone-induced coastal compound flooding. The Tropical Cyclone Forecasting Framework, TC-FF, computes a set of ensemble members based on a simplified DeMaria et al., 2009 method. In particular, TC-FF uses gridded time- and spatially-varying wind and pressure fields or forecasted tracks and combines this with historical observed error on the along-track, cross-track, and intensity. Subsequently, the tool creates a temporally and spatially varying wind field, including rainfall, to force a computationally efficient compound flood model. This approach allows for the inference of probabilistic wind and flood hazard maps calibrated to any ocean basin in the world with limited computational resources. In contrast to the current practice, TC-FF allows uncertainty analysis using large ensembles produced with physics-based models, narrowing down confidence bands on forecasting coastal compound flooding focused on operational TC risk analyses.

The validation of the quadtree SFINCS model for Mozambique's Sofala province showed reliable skill in terms of tidal propagation in the area of interest (median MAE of 21 cm), including good skill in reproducing the observed flood extent for the case of the flooding caused by Cyclone Idai (2021). The model was able to reproduce the storm surge generation during landfall and flooding near the city of Beira, including the subsequent compound flooding resulting from rainfall runoff in the Pungwe estuary (critical success index of 0.59). Moreover, the model runs efficiently with a wall clock time of 4 minutes for a 7-day event allowing it to be deployed in probabilistic operational assessments when using multiple cores.

TC-FF was calibrated with the average reported errors for the southern hemisphere via the Nelder-Mead method to determine the mean absolute errors and autoregression coefficients. A comparison between TC-FF and JTWC (based on the complete implementation of DeMaria et al., 2009 and DeMaria et al., 2013) revealed minor differences. In particular, for various lead times from 0 to 120 hours, a median Continuous Ranked Probability Score (CRPS) of 0.07, 0.05, 0.10 and median MAE of 37 km, 21 km, and 7 m/s for respectively the along-track, cross-track, and intensity error were found. These findings give confidence that the TC-FF, including the simplified DeMaria et al., 2009 implementation, can be used for more generalized applications in data-scarce environments.

TC-FF provides valuable insights into the uncertainty of wind speeds, water levels, and potential flooding due to Idai, revealing the impacts of track and intensity uncertainties. This is demonstrated in the wide array of possible maximum wind speeds and significant fluctuations in water levels, which are primarily affected by tidal influences and the cyclone. For instance, even just three days prior to landfall, there's a broad spread in the predicted flood areas. This suggests that there is still a significant chance that Idai may not hit the anticipated area or may not generate a substantial storm surge.

The precision of forecasts is directly related to the number of ensemble members used. A mean error in flood probability of less than 1% and <20 cm sampling errors for the 1% exceedance water level at Beira required 200 members. Based on that, we determine that at least 200 ensemble members are needed to get reliable water levels and flood results three days before landfall. A higher number of ensemble members reduces sampling uncertainty and increases the accuracy of water level and flood potential estimates.

The lead time before landfall has a considerable impact on the forecast's precision. As the lead time decreases, the variability of forecasts diminishes, and the forecasts converge to similar predictions. Similarly, the probability of flooding in certain areas, such as the estuary near Beira, increases as the lead time shortens, providing more certainty over the areas that will be affected by the event.

TC-FF offers a significant advancement compared to the current status quo of a single deterministic simulation when forecasting tropical cyclone compound flooding hazards. This approach facilitates a comprehensive understanding of complex interdependencies and uncertainties. By quantifying the likelihood of various outcomes (e.g. by estimating the probability of major flooding in a given neighborhood days before landfall) probabilistic methods enable stakeholders to make more informed decisions, allocate resources better, and enhance preparedness and resilience in the face of these catastrophic natural phenomena.

## APPENDICES ASSOCIATED WITH THIS CHAPTER

### TIDAL CALIBRATION AND VALIDATION

A tidal calibration was performed on the SFINCS computed tidal constituents compared to the tidal constituents at Beira. Constituents with an amplitude of more than 5 cm (M2, S2, N2, K2, and K1) were adjusted in terms of amplitude (multiplication) and phase (addition). Amplitude changes varied between 0.84 and 1.07 while phase difference changed on average by 40○. These calibration steps of adjusting the tidal constituents substantially reduced tidal errors at the Beira from a MAE of 43 to 17 cm. Secondly, model skill in reproducing tidal amplitudes and phases is assessed at 7 tide stations across the area of interest (including the calibration station of Beira). The SFINCS model reproduces tide with a median MAE of 21 cm, median RMSE of 25 cm, and median difference in M2 and S2 amplitude and phase of respectively -10 and -1 cm and -10 to -12○ (median values computed over the different stations). Our hypothesis is that the reduction in tidal error observed at Beira throughout the calibration process might be due to a misalignment in the amplitudes and phases of the TPXO model which were used to generate the tidal boundary conditions (see Section 5.3). Presumably, the bathymetry contributes to the error observed in the validation process.

Table 5.1: Evaluation of model proficiency in replicating tides near the Sofala province. Stations are ordered south to north. Columns one and two present the Mean Absolute Error (MAE) and Root Mean Square Error (RMSE), respectively, as error metrics for the comparison between observed and simulated tidal time series. The final four columns display the discrepancy ($\Delta$) in amplitude (A) and phase difference ($\phi$) for the two most prominent tidal constituents in the area (M2 and S2), where $\Delta$ is calculated as the difference between observed and simulated values

| **Name** | **MAE [m]** | **RMSE [m]** | **ΔM2 A [m]** | **ΔM2 $\phi$ [∘]** | **ΔS2 A [m]** |
|---|---|---|---|---|---|
| **Bazaruto** | 0.13 | 0.15 | -0.1 | -7 | 0.01 |
| **Bartolomeu** | 0.12 | 0.15 | -0.14 | 1 | -0.11 |
| **Chiloane** | 0.3 | 0.41 | 0.2 | -10 | 0.08 |
| **Beira** | 0.17 | 0.2 | 0 | 0 | 0 |
| **Chinde** | 0.21 | 0.25 | -0.08 | -13 | -0.01 |
| **Quelimane** | 0.26 | 0.32 | -0.14 | -15 | -0.09 |
| **Pebane** | 0.21 | 0.25 | -0.14 | -11 | -0.09 |
| **Median** | 0.21 | 0.25 | -0.1 | -10 | -0.01 |

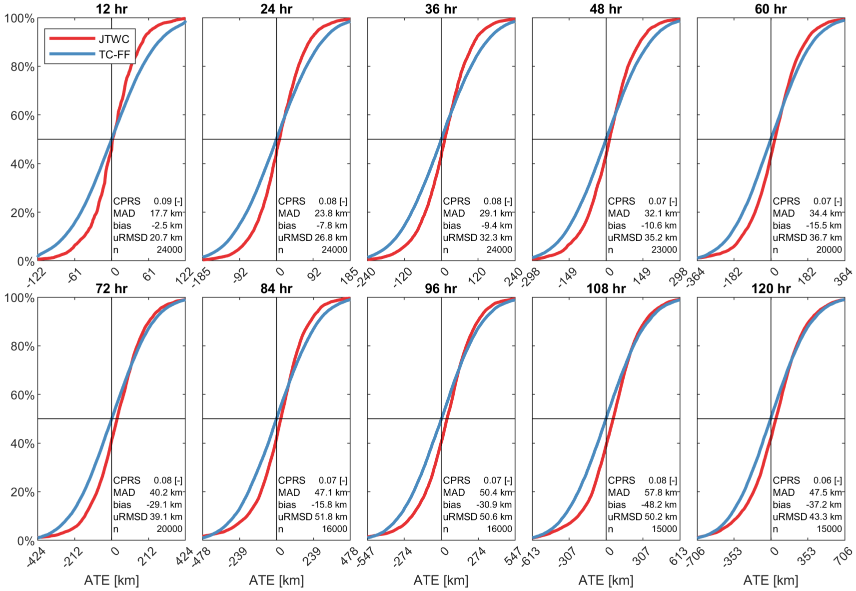

Figure 5.12: Comparison between the cumulative distribution function (CDF) of the along-track-error (ATE) for JTWC (red; reference) and TC-FF (blue; modeled). The different panels represent different lead times.

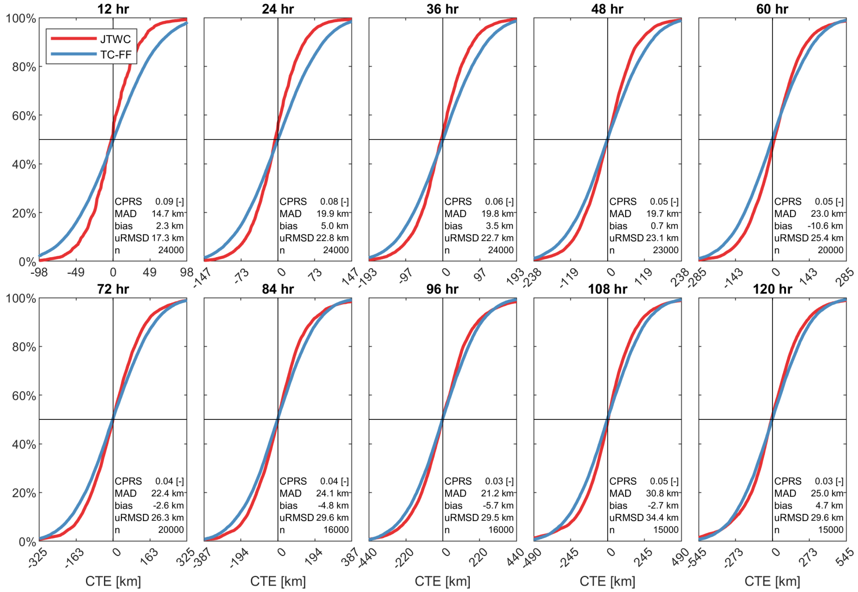

Figure 5.13: Comparison between the cumulative distribution function (CDF) of the cross-track-error (CTE) for JTWC (red; reference) and TC-FF (blue; modeled). The different panels represent different lead times.

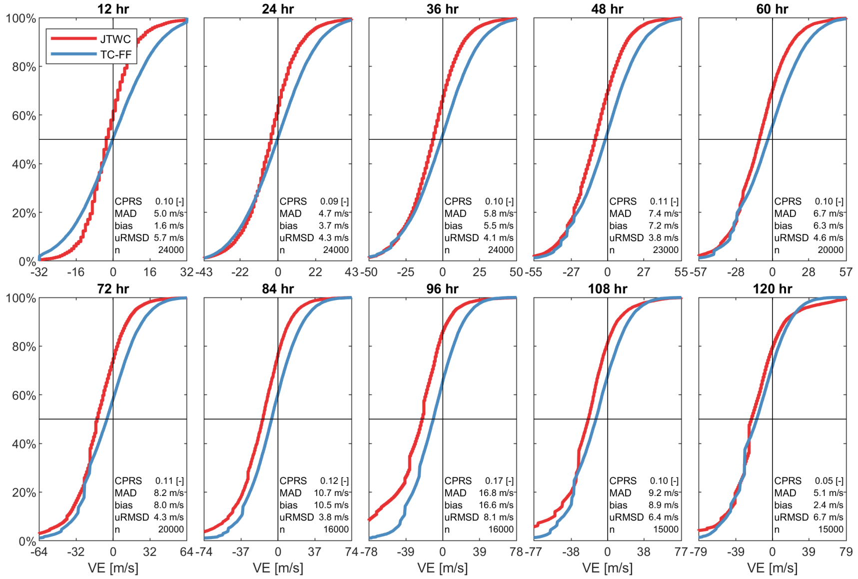

Figure 5.14: Comparison between the cumulative distribution function (CDF) of the intensity error (VE) for JTWC (red; reference) and TC-FF (blue; modeled). The different panels represent different lead times

# 6

# CONCLUSIONS AND WAY FORWARD

This dissertation seeks to determine the extent to which improved tropical cyclone (TC) descriptions of geometry, tracks, and statistical uncertainty can enhance the reliability of forecasts and the accuracy of risk analysis for coastal flood assessments. In this synthesis, the main conclusions and findings are summarized in view of the objective defined in Chapter 1. Additionally, an outlook is given, addressing remaining challenges and future directions of research.

## 6.1. CONCLUSIONS

The main insights are structured as responses to the research questions laid out in Chapter 1. For every research question, an initial brief response (emphasized in italics) is provided, followed by a more detailed description of the findings.

**Research question 1. How to accurately describe TC geometry and winds with parametric relationships?**

*TC geometry can be described accurately when using estimates of the radius of maximum winds (RMW) and the radius of gale force winds (*$\Delta AR35$*). Observed estimates for RMW or* $\Delta AR35$ *or relationships defined in this thesis are accurate sources. When TC geometry can accurately be defined, parametric wind profile models* *can reproduce time and spatially varying winds.*

In Chapter 2, historical data from TCs were used to derive simple but universal equations to estimate TC geometry when the radius of maximum winds and/or radius of gale force winds is unknown. The relationships derived had a higher accuracy with respect to other well-known empirical relationships available from literature (e.g. Vickery and Wadhera, 2008 and Knaff et al., 2007) and relate geometry to wind speed and latitude. Moreover, these relationships include a stochastic description for both the radius of maximum winds (RMW) and the radius of gale force winds ($\Delta AR35$). This allows the quantification of the prediction interval around the median estimates, making the estimation more useful.

The new relationships, in combination with the Holland wind profile model (Holland et al., 2010, can accurately reproduce the (outer) azimuthal wind speeds from the QSCAT-R database (Chavas and Vigh, 2014). This gives confidence that the computed TC wind speeds can be used in computational methods for assessing coastal flooding in both operational and risk assessments. However, when no additional information on wind radii was used to calibrate the wind profile, the surface wind was not well resolved.

**Research question 2. How to reliably account for TCs in coastal flood risk assessments?**

*For reliable coastal flood risk assessments a sufficiently large number of events needs to be included to accurately assess the flood risk. This importance stems from the sensitivity of coastal impacts to the specific characteristics and trajectories of TCs. To capture the full range of potential responses, it's crucial to account for the variability in TC behavior. There are several approaches available in the literature for TCs but the presented Monte Carlo-based approach in which artificially generated paths that TCs might follow (synthetic tracks) is easy to use since each track has the same storm probability and allows for reliable flood risk assessment when used in combination with a computationally efficient method to asses coastal flooding.*

In Chapter 3, an open-source method for the generation of synthetic tracks was introduced called the Tropical Cyclone Wind Statistical Estimation Tool (TCWiSE). TCWiSe is an empirical track model (ETM; Vickery et al., 2000) and is set up as a

Markov model where (historical) meteorological data serve as a source to compute synthetic tracks. In particular, the main variables it keeps track of are location (latitude and longitude), time, maximum sustained wind speeds ($v_{\mathrm{max}}$), forward speed ($c$), and heading ($\theta$).

The validation study showed accurate skill in terms of track initialization and evolution compared to the historical Best Track Data (BTD). For example, an assessment of the goodness of fit showed that normalized errors are generally smaller than 10%. Also, extreme wind speeds showed good agreement.

The main advantage of this approach is that many more (artificially generated) TCs are included in the analysis compared to the limited record length of observed TCs worldwide. Including more estimates of TC conditions will overcome any sampling biases and result in more reliable quantification of coastal hazards (e.g., extreme storm surge levels and waves) and consequent risks and damages resulting from these hazards.

**Research question 3. What is the contribution of TCs in strategic coastal flood risk assessments?**

*The contribution of TCs varies worldwide depending on their frequency and magnitude. For a case study in the Southeast Atlantic Coast of the United States, yearly flood impacts are two times as likely to be driven by extratropical cyclones than TCs. On the other hand, TCs are thirty times more likely to affect people during rarer 100-year events than extratropical cyclones and contribute to more than half of the regional flood risk.*

In Chapter 4, this question was addressed using a large-scale flood hazard and impact assessment across the subtropical Southeast Atlantic Coast of the United States, from Virginia to Florida. The physics-based hydrodynamic modeling used was based on the lower-fidelity model SFINCS (Leijnse et al., 2021) that allowed for the simulation of tens of thousands of emulated tropical cyclones (TCs) and extratropical cyclones (ETCs, or migratory cyclones/storms of middle and high latitudes). The model framework developed could skillfully reproduce coastal water levels with errors for tides of 8.3 cm and storms with 11.9 cm.

In the case study explored, the relative impact of flood hazards from annual storm events was limited to 6.3% of low-lying areas of the U.S. Southeast Atlantic coast at the current sea level. In comparison, 100-year events flooded 27% of the considered area. Extratropical events dominated the annual flood hazards with 56% driven by ETCs versus 43% by TCs. For higher return periods, TCs drove an increasingly larger share of the division. For example, a 2-year event (50% annual probability) was 66% driven by TCs versus 34% for ETCs. This breakdown increased to 96% for TCs and 4% for ETCs for the 100-year event. A similar trend emerged for the flood impact. ETCs resulted in almost twice the amount of negative impact with a yearly frequency. However, for the 100-year event, TC-driven impact is 30x as significant. With rising sea levels, the flooding risk solely attributed to TCs lessens, as areas became susceptible to flooding irrespective of the cause. This evaluation emphasized the importance of both event types and accentuated the need for subsequent studies to account for both flooding drivers.

**Research question 4. How to reliably account for TCs in operational coastal risk analysis?**

*In operational coastal risk analysis it is essential to integrate uncertainties related to forecasting TCs, such as track, speed, and intensity in order to account for them reliably. The Tropical Cyclone Forecasting Framework (TC-FF) offers an innovative approach that relies on a Monte Carlo method and generates hundreds or thousands of realizations. The framework accounts for all relevant drivers of compound flooding while leveraging Gaussian error distributions and auto-regressive techniques to account for the uncertainty regarding the forecast tracks. When utilizing Monte Carlo-based methods, such as TC-FF, enough realizations need to be included to achieve reliable water levels and flood predictions.*

Chapter 4 introduced the open-source Tropical Cyclone Forecasting Framework (TC-FF), a method designed to forecast compound flooding due to TCs that account for uncertainties. TC-FF computes a set of ensemble members based on a simplified implementation of DeMaria et al., 2009. In particular, the tool uses historical observed error on the along-track, cross-track, and intensity and creates a temporally and spatially varying wind field to force the computationally efficient compound flood model SFINCS.

TC-FF can be calibrated with the average reported errors for any oceanic basin via the Nelder-Mead method to determine the mean absolute errors and auto-regression coefficients used in the computation. A comparison between TC-FF and the complete implementation of DeMaria et al., 2009 and DeMaria et al., 2013 revealed minor differences which gives confidence that the TC-FF can be used for more generalized applications in data-scarce environments.

TC-FF was utilized for a case study of Cyclone Idai (2021) in Mozambique's Sofala province. The method gave valuable insights into the uncertainty of wind speeds, water levels, and potential flooding due to Idai, revealing the impacts of track and intensity uncertainties and how this changed as a function of lead time. The precision of the forecasts is influenced by the number of ensemble members used within the tool. Three days before landfall, a mean error in flood probability of less than 1% and <20 cm sampling errors for the 1% exceedance water level at Beira required 200 members to be included. Therefore, we concluded that at least 200 ensemble members are needed to get reliable water levels and flood results with TC-FF. A higher number of ensemble members reduced sampling uncertainty and increased the reliability of water level and flood potential estimates but at greater computational expense.

## 6.2. REMAINING CHALLENGES AND WAYS FORWARD

In this subsection, we move away from addressing the main research question and conclusions and toward reflection focused on practical applications and future research directions.

### 6.2.1. DATA COLLECTION AND MODEL VALIDATION

Observed TC geometry and best-track data underpin the description of TC wind fields (Chapters 2 and 3) used in both strategic (Chapter 4) and operational assessments (Chapter 5). However, the quality and quantity of this information have been increasing due to the rise of observations through satellites. During the course of this work, at least five more years of best-track data were collected. Moreover, more reliable data will allow for a more accurate description of TCs using methods deployed in this thesis or the possibility for other, more data-intensive, methods (e.g. Kumar et al., 2023).

The pivotal role of data collection both in real-time and in measuring the hazard and impact of storm events can also not be overstated. While physics-based models have a good track record and we have a basic understanding of how water moves going back to Navier, 1822 and Stokes, 1845, comprehensive and accurate data still serve as the linchpin that underpins robust analysis. Typically, compound flood models are compared at (permanent) water level stations on open coasts and high water marks on land (e.g. see Chapter 4). However, model skill in, for example, computed area flooded is typically not considered due to the lack of information. Satellite-derived flood extents and duration could serve an essential role in the validation. Precise data not only enhance our understanding of storm characteristics and behaviors but also empower researchers to calibrate and validate models effectively. This is especially relevant for inland hydrological processes such as infiltration which is strongly influenced by soil saturation which is typically unknown.

### 6.2.2. IMPROVING COMPUTATIONAL ASSESSMENTS

Computational methods for assessing coastal flooding are the foundation for our ability to accurately assess coastal flood risk. In this thesis, we have relied on the model SFINCS model (Leijnse et al., 2021). The model accounts for major relevant physical drivers, including tide, surge, and rainfall, and showed good skill in the literature (e.g. Sebastian et al., 2021, Eilander et al., 2022) including several validation cases presented in this thesis. The reduced computational expense compared to traditional computational assessments and increased computational power allow for a more rigorous assessment in strategic (Section 4) and operational risk assessments (Section 5) as presented in this thesis. Conducting more simulations allows for a comprehensive exploration of climate variability, providing a richer and more reliable understanding of conditions instead of basing this on a limited set of simulations that might overlook crucial nuances. For example, the case study of Section 4 explored, the relative impact of tropical cyclones on the U.S. Southeast Atlantic coast. Conducting a similar analysis for other coastal areas would be beneficial to see how these findings translate to other areas.

However, several processes are absent or only partly accounted for in the lower-fidelity SFINCS model that are accounted for in other high-fidelity ones. The non-exhaustive list of physical processes that are absent but relevant for flooding is wave runup, detailed groundwater processes such as infiltration or exfiltration, urban drainage, identification of primary and secondary levees (e.g. elevated roads) and morphological change. It is paramount to continue to explore computationally efficient methods to include these processes to ensure that model predictions are accurate and reliable. The proposed path forward is twofold. First, by an increased understanding of the importance, physics and dynamics of these processes in, for example, high-fidelity models. Secondly, through the exploration of (simplified) methods to describe the relevant drivers of flooding and couple or integrate them in computational assessments in lower-fidelity models. Continuing to explore to what extent multilevel multi-fidelity Monte Carlo methods (MLMF; Clare et al., 2022) could be used as a trade-off is also worth exploring in the context of efficiency and accuracy.

Throughout this thesis, we have largely relied on a parametric wind model developed by Holland et al., 2010, including an estimate of the *averaged* value of gale force winds ($\overline{R35}$ over the four quadrants). However, surface friction in the tropical cyclone boundary layer creates asymmetries in the wind structure over the ocean. This results in stronger winds on the right side in the Northern Hemisphere and on the left in the Southern Hemisphere, due to the combination of the cyclone's translation movement and cyclonic flow. These effects were estimated using the approach of Schwerdt et al., 1979, but were not explicitly validated. Moreover, this estimate does not capture changes in the structure, for example, those occurring during landfall (e.g. see Hlywiak and Nolan, 2022), along with other unaccounted asymmetric effects. The continued development of more accurate parametric wind models that account for cyclone asymmetry, including factors such as estimates for cyclone rainfall, is recommended to further refine computational assessments of hazards.

Climate change is anticipated to affect future TC frequency and intensity, as warmer sea surface temperatures are known to contribute to more intense storms with greater rainfall rates (e.g., Knutson et al., 2010). The synthetic tropical cyclone tracks generated by TCWiSE (as introduced in Chapter 3) can partially account for this shift through a heuristic factor that adjusts the frequency and intensity of TCs to reflect climate change-related alterations. However, TCWiSE's purely data-driven approach does not facilitate the direct incorporation of changes in ocean temperature. Consequently, re-engineering TCWiSE or exploring alternative methods, such as adjusting the KDE, could prove beneficial in the context of climate change.

Another avenue of exploration is more effective usage of the ever-increasing amount of data that is available (in real-time). Operational storm surge forecasting has benefited from data-assimilation techniques, such as Kalman filtering (e.g. Verlaan et al., 2005) and similarly did shoreline modeling with an automatic adjustment of model parameters to best fit any available observed data at the concurrent time step (e.g. Vitousek et al., 2017a. Despite a few novel applications (e.g. Muñoz et al., 2022), data assimilation for compound flood assessment is still a relatively untapped potential. Assimilating data could be explored as part of operational risk assessments (Chapter 5), however, faster computations make it also possible to use data assimilation of historical data for automatic parameter estimation in strategic risk assessments (Chapter 4).

Lastly, throughout this dissertation, we relied on Monte Carlo-based assessments for strategic and operational risk analyses (Chapters 4 and 5). These assessments involved generating a large number of random samples to make probabilistic estimates. It is paramount to move away from the deterministic analysis, however, there are more efficient methods than Monte Carlo for multivariate patterns such as cluster analysis (e.g., Choi et al., 2009b), stratified sampling (e.g. Nadal-Caraballo et al., 2020 and MDA methods (e.g., Bakker et al., 2022). Exploring efficient methods while still capturing the full range of probabilistic outcomes is worth further exploring.

### 6.2.3. HARNESSING DEEP LEARNING

Deep Learning (DL) refers to the use of neural networks to model and process large sets of data. Neural networks are not new, but due to the increased computational power, bigger data sets, and open-source algorithmic advancements, it feels that the Age of Deep Learning has begun (Goodfellow et al., 2017). Despite these developments, DL had a limited impact on the methodologies used in this thesis. This thesis has relied on more traditional statistical methods such as curve fitting, kernel density estimation (KDE), Markov chains, and auto-regression error estimations in combination with physics-based assessments.

However, the ever-increasing amount of data collected through satellites could improve our ability to represent and estimate TCs. DL techniques such as Artificial Neural Networks (ANN) could be used for parameter estimation of wind geometry in Chapter 2 (e.g. Snaiki and Wu, 2019). Another possibility is the use of Convolution Neural Networks (CNN) that were initially developed for computer vision problems for the estimation of spatial TC structure and thus moving away from parametric wind models (e.g. Pradhan et al., 2018) or occurrence locations in Chapter 3 (e.g. Nath et al., 2016). While a TC that makes landfall for a single coastal community is a relatively rare event, worldwide there are about 50 TCs which gives ample data to support these DL techniques.

For flood assessments, data is typically less abundant but DL techniques have shown promising results in hydrology (e.g. Guo et al., 2021, Löwe et al., 2021) and coastal engineering (e.g., Athanasiou et al., 2022, Bentivoglio et al., 2022). The typical approach for more data-poor environments is the emulation of modeled data. In that case, DL techniques are especially interesting for operational forecasting settings where uncertainties in the forcing require the simulations of 100-1000s ensemble members within a limited time window and with limited computational expense. Therefore, the use of ANN could be beneficial in the estimation of storm surge levels or morphological change based on a library of pre-run physics-based assessments. Moreover, the use of CNN can be used to compute spatial flood patterns or provide warning levels for different communities.

A remaining challenge is that DL-based parameterizations should not only be accurate but also credible. Non-credible results, for example, a DL algorithm that computes flooding behind a levee, undermine confidence from the public and thus its usefulness. Hence, the exploration of physics-incorporated DL frameworks (e.g. Yao et al., 2023) should be a path of further research for the coastal science community.

# BIBLIOGRAPHY

Alfieri, L., Burek, P., Dutra, E., Krzeminski, B., Muraro, D., Thielen, J., & Pappenberger, F. (2013). GloFAS-global ensemble streamflow forecasting and flood early warning. *Hydrology and Earth System Sciences*, *17*(3), 1161–1175. https://doi.org/10.5194/hess-17-1161-2013

Antolínez, J. A. A., Murray, A. B., Méndez, F. J., Moore, L. J., Farley, G., & Wood, J. (2018). Downscaling Changing Coastlines in a Changing Climate: The Hybrid Approach. *Journal of Geophysical Research: Earth Surface*, *123*(2), 229–251. https://doi.org/10.1002/2017JF004367

Arthur, W. (2019). A statistical-parametric model of tropical cyclones for hazard assessment. *Natural Hazards and Earth System Sciences*, (October), 1–29. https://doi.org/10.5194/nhess-2019-192

Athanasiou, P., van Dongeren, A., Giardino, A., Vousdoukas, M., Antolinez, J. A. A., & Ranasinghe, R. (2022). Estimating dune erosion at the regional scale using a meta-model based on neural networks. *Natural Hazards and Earth System Sciences*, *22*(12), 3897–3915. https://doi.org/10.5194/nhess-22-3897-2022

Ayyad, M., Orton, P. M., El Safty, H., Chen, Z., & Hajj, M. R. (2022). Ensemble forecast for storm tide and resurgence from Tropical Cyclone Isaias. *Weather and Climate Extremes*, *38*(May), 100504. https://doi.org/10.1016/j.wace.2022.100504

Bader, D. (2019). Including stochastic rainfall distributions in a probabilistic modelling approach for compound flooding due to tropical cyclones. http://resolver.tudelft.nl/uuid:57b9e495-0c90-4cf5-ab22-e169fb908ac1

Bakker, T. M., Antolínez, J. A., Leijnse, T., Pearson, S. G., & Giardino, A. (2022). Estimating tropical cyclone-induced wind, waves, and surge: A general methodology based on representative tracks. *Coastal Engineering*, *176*(August 2021). https://doi.org/10.1016/j.coastaleng.2022.104154

Barnard, P. L., Erikson, L. H., Foxgrover, A. C., Hart, J. A. F., Limber, P., O'Neill, A. C., van Ormondt, M., Vitousek, S., Wood, N., Hayden, M. K., & Jones, J. M. (2019). Dynamic flood modeling essential to assess the coastal impacts of climate change. *Scientific Reports*, *9*(1), 4309. https://doi.org/10.1038/s41598-019-40742-z

Barnard, P. L., van Ormondt, M., Erikson, L. H., Eshleman, J., Hapke, C., Ruggiero, P., Adams, P. N., & Foxgrover, A. C. (2014). Development of the Coastal Storm Modeling System (CoSMoS) for predicting the impact of storms on high-energy, active-margin coasts. *Natural Hazards*, *74*(2), 1095–1125. https://doi.org/10.1007/s11069-014-1236-y

Barnard, P. L., Befus, K. M., Danielson, J. J., Engelstad, A. C., Erikson, L. H., Foxgrover, A. C., Hardy, M. W., Hoover, D. J., Leijnse, T., Massey, C., McCall, R., Nadal-Caraballo, N., **Nederhoff**, **K.**, Ohenhen, L., O'Neill, A., Parker, K. A., Shirzaei, M., Su, X., Thomas, J. A., … Yawn, M. C. (2023a). Future coastal hazards along the U.S. Atlantic coast. *U.S. Geological Survey data release*. https://doi.org/https://doi.org/10.5066/P9BQQTCI

Barnard, P. L., Befus, K. M., Danielson, J. J., Engelstad, A. C., Erikson, L. H., Foxgrover, A. C., Hardy, M. W., Hoover, D. J., Leijnse, T., Massey, C., McCall, R., Nadal-Caraballo, N., **Nederhoff**, **K.**, Ohenhen, L., O'Neill, A., Parker, K. A., Shirzaei, M., Su, X., Thomas, J. A., … Yawn, M. C. (2023b). Future coastal hazards along the U.S. North and South Carolina coasts. *U.S. Geological Survey data release*. https://doi.org/https://doi.org/10.5066/P9W91314

Bates, P. D., Quinn, N., Sampson, C., Smith, A., Wing, O. E., Sosa, J., Savage, J., Olcese, G., Neal, J., Schumann, G., Giustarini, L., Coxon, G., Porter, J. R., Amodeo, M. F., Chu, Z., Lewis-Gruss, S., Freeman, N. B., Houser, T., Delgado, M., … Krajewski, W. F. (2021). Combined Modeling of US Fluvial, Pluvial, and Coastal Flood Hazard Under Current and Future Climates. *Water Resources Research*, *57*(2), 1–29. https://doi.org/10.1029/2020WR028673

Bedient, P. B., Huber, W. C., & Vieux, B. E. (2013). *Hydrology and Floodplain Analysis*.

Bentivoglio, R., Isufi, E., Jonkman, S. N., & Taormina, R. (2022). Deep learning methods for flood mapping: a review of existing applications and future research directions. *Hydrology and Earth System Sciences*, *26*(16), 4345–4378. https://doi.org/10.5194/hess-26-4345-2022

Biesecker, M., & Kastanis, A. (2018). Hurricane Florence breaches manure lagoon, coal ash pit in North Carolina. 2018. Retrieved online https://www.pbs.org/newshour/nation/hurricane-florence-breaches-manure-lagoon-coal-ash-pit-in-north-carolina.

Bilskie, M. V., & Hagen, S. C. (2018). Defining Flood Zone Transitions in Low-Gradient Coastal Regions. *Geophysical Research Letters*, *45*(6), 2761–2770. https://doi.org/10.1002/2018GL077524

Bloemendaal, N., Haigh, I. D., de Moel, H., Muis, S., Haarsma, R. J., & Aerts, J. C. (2020). Generation of a global synthetic tropical cyclone hazard dataset using STORM. *Scientific Data*, *7*(1), 1–19. https://doi.org/10.1038/s41597-020-0381-2

Booij, N., Ris, R., & Holthuijsen, L. H. (1999). A third-generation wave model for coastal regions. I- Model description and validation. *Journal of geophysical research*, *104*, 7649–7666. https://doi.org/10.1029/98jc02622

Booth, J. F., Rieder, H. E., & Kushnir, Y. (2016). Comparing hurricane and extratropical storm surge for the Mid-Atlantic and Northeast Coast of the United States for 1979-2013. *Environmental Research Letters*, *11*(9). https://doi.org/10.1088/1748-9326/11/9/094004

Brackins, J. T., & Kalyanapu, A. J. (2020). Evaluation of parametric precipitation models in reproducing tropical cyclone rainfall patterns. *Journal of Hydrology, 580*. https://doi.org/10.1016/j.jhydrol.2019.124255

Bruun, P. (1954). Coastal erosion and the development of beach profiles. *U.S. Army Corps of Engineers Beach Erosion Board Technical Memo, 44*.

Brzeźniak, Z., & Zastawniak, T. (2000). *Basic Stochastic Processes*. Springer, London.

Caires, S. (2016). A Comparative Simulation Study of the Annual Maxima and the Peaks-Over-Threshold Methods. *Journal of Offshore Mechanics and Arctic Engineering*, *138*(5). https://doi.org/10.1115/1.4033563

Callaghan, J. (2020). Extreme rainfall and flooding from Hurricane Florence. *Tropical Cyclone Research and Review*, *9*(3), 172–177. https://doi.org/10.1016/j.tcrr.2020.07.002

Cangialosi, J. P., Blake, E., Demaria, M., Penny, A., Latto, A., Rappaport, E., & Tallapragada, V. (2020). Recent progress in tropical cyclone intensity forecasting at the national hurricane center. *Weather and Forecasting*, *35*(5), 1913–1922. https://doi.org/10.1175/WAF-D-20-0059.1

Carrasco, C. A., Landsea, C. W., & Lin, Y.-L. (2014). The Influence of Tropical Cyclone Size on Its Intensification. *Weather and Forecasting*, *29*(3), 582–590. https://doi.org/10.1175/WAF-D-13-00092.1

Cashwell, E. D., & Everett, C. J. (1959). A Practical Manual on the Monte Carlo Method for Random Walk Problems. *Los Alamos, NM: Los Alamos Scientific Laboratory of the University of California*. https://www.osti.gov/biblio/4314838

Chang, E. K., Guo, Y., & Xia, X. (2012). CMIP5 multimodel ensemble projection of storm track change under global warming. *Journal of Geophysical Research Atmospheres*, *117*(23). https://doi.org/10.1029/2012JD018578

Chavas, D., Lin, N., Dong, W., & Lin, Y. (2016). Observed tropical cyclone size revisited. *Journal of Climate*, *29*(8), 2923–2939. https://doi.org/10.1175/JCLI-D-15-0731.1

Chavas, D., Lin, N., & Emanuel, K. A. (2015). A Model for the Complete Radial Structure of the Tropical Cyclone Wind Field. Part I: Comparison with Observed Structure*. *Journal of the Atmospheric Sciences*, *72*(9), 3647–3662. https://doi.org/10.1175/JAS-D-15-0014.1

Chavas, D., & Vigh, J. (2014). QSCAT-R : The QuikSCAT Tropical Cyclone Radial Structure Dataset. https://doi.org/http://dx.doi.org/10.5065/D65B00J3

Chen, B. F., Kuo, Y. T., & Huang, T. S. (2023). A deep learning ensemble approach for predicting tropical cyclone rapid intensification. *Atmospheric Science Letters*, *24*(5), 1–11. https://doi.org/10.1002/asl.1151

Choi, K.-S., Kim, B.-J., Choi, C.-Y., & Nam, J.-C. (2009a). Cluster analysis of Tropical Cyclones making landfall on the Korean Peninsula. *Advances in Atmospheric Sciences*, *26*(2), 202–210. https://doi.org/10.1007/s00376-009-0202-1

Choi, K.-S., Kim, B.-J., Choi, C.-Y., & Nam, J.-C. (2009b). Cluster analysis of Tropical Cyclones making landfall on the Korean Peninsula. *Advances in Atmospheric Sciences*, *26*(2), 202–210. https://doi.org/10.1007/s00376-009-0202-1

CIRES. (2014). Cooperative Institute for Research in Environmental Sciences (CIRES) at the University of Colorado, Boulder. 2014: Continuously Updated

Digital Elevation Model (CUDEM). Accessed 6/30/21. https://doi.org/https://doi.org/10.25921/ds9v-ky35

Clare, M. C., Leijnse, T. W., Mccall, R. T., Diermanse, F. L., Cotter, C. J., & Piggott, M. D. (2022). Multilevel multifidelity Monte Carlo methods for assessing uncertainty in coastal flooding. *Natural Hazards and Earth System Sciences*, *22*(8), 2491–2515. https://doi.org/10.5194/nhess-22-2491-2022

Codiga, D. (2011). *Unified Tidal Analysis and Prediction Using the UTide Matlab Functions. Technical Report 2011-01. Graduate School of Oceanography, University of Rhode Island, Narragansett, RI. 59pp* (tech. rep.). ftp://www.po.gso.uri.edu/%20pub/downloads/codiga/pubs/2011Codiga-UTide-Report.pdf

Coles, S. (2001). *An Introduction to Statistical Modeling of Extreme Values*. Springer London. https://doi.org/10.1007/978-1-4471-3675-0

CO-OPS - NOAA Tides and Currents. (2022). Observed water levels retrieved via tidesandcurrents.noaa.gov. Accessed 15 January 2022.

Crosby, S. C., **Nederhoff**, **K.**, VanArendonk, N., & Grossman, E. E. (2023). Efficient modeling of wave generation and propagation in a semi-enclosed estuary. *Ocean Modelling*, 102231. https://doi.org/10.1016/j.ocemod.2023.102231

Czajkowski, J., Engel, V., Martinez, C., Mirchi, A., Watkins, D., Sukop, M. C., & Hughes, J. D. (2018). Economic impacts of urban flooding in South Florida: Potential consequences of managing groundwater to prevent salt water intrusion. *Science of The Total Environment*, *621*, 465–478. https://doi.org/10.1016/j.scitotenv.2017.10.251

Dangendorf, S., Marcos, M., Wöppelmann, G., Conrad, C. P., Frederikse, T., & Riva, R. (2017). Reassessment of 20th century global mean sea level rise. *Proceedings of the National Academy of Sciences of the United States of America*, *114*(23), 5946–5951. https://doi.org/10.1073/pnas.1616007114

Danielson, J. J., Poppenga, S. K., Brock, J. C., Evans, G. A., Tyler, D. J., Gesch, D. B., Thatcher, C. A., & Barras, J. A. (2016). Topobathymetric Elevation Model Development using a New Methodology: Coastal National Elevation Database. *Journal of Coastal Research*, *76*, 75–89. https://doi.org/10.2112/SI76-008

Dean, L., Emanuel, K. A., & Chavas, D. (2009). On the size distribution of Atlantic tropical cyclones. *Geophysical Research Letters*, *36*(14), 1–5. https://doi.org/10.1029/2009GL039051

de Bruijn, K. M. (2005). *Resilience and flood risk management; a systems approach applied to lowland rivers* (Doctoral dissertation). Delft University of Technology. DUP Science.

Deltares. (2017). *Mozambique - Coastal Flooding Hazard Assessment* (tech. rep.). 1230818-000.

Deltares. (2018). Wind Enhance Scheme for cyclone modelling - User Manual, 1–110.

Deltares. (2021). Beira Coastal Protection Preparation study : flood hazard modelling.

DeMaria, M., Knaff, J., Knabb, R., Lauer, C., Sampson, C., & DeMaria, R. T. (2009). A New Method for Estimating Tropical Cyclone Wind Speed Probabilities. *Weather and Forecasting*, *24*(6), 1573–1591. https://doi.org/10.1175/2009WAF2222286.1

DeMaria, M., Knaff, J. A., Brennan, M. J., Brown, D., Knabb, R. D., DeMaria, R. T., Schumacher, A., Lauer, C. A., Roberts, D. P., Sampson, C. R., Santos, P., Sharp, D., & Winters, K. A. (2013). Improvements to the operational tropical cyclone wind speed probability model. *Weather and Forecasting*, *28*(3), 586–602. https://doi.org/10.1175/WAF-D-12-00116.1

de Ridder, M. P., Smit, P. B., Van Dongeren, A., McCall, R. T., **Nederhoff**, **K.**, & Reniers, A. J. (2021). Efficient two-layer non-hydrostatic wave model with accurate dispersive behaviour. *Coastal Engineering*, *164*(February). https://doi.org/10.1016/j.coastaleng.2020.103808

de Vries, H. (2009). Probability Forecasts for Water Levels at the Coast of The Netherlands. *Marine Geodesy*, *32*(2), 100–107. https://doi.org/10.1080/01490410902869185

Dewald, J. R., & Pike, D. A. (2014). Geographical variation in hurricane impacts among sea turtle populations. *Journal of Biogeography*, *41*(2), 307–316. https://doi.org/10.1111/jbi.12197

Done, J. M., Ge, M., J. Holland, G., Dima-West, I., Phibbs, S., R. Saville, G., & Wang, Y. (2020). Modelling global tropical cyclone wind footprints. *Natural Hazards and Earth System Sciences*, *20*(2), 567–580. https://doi.org/10.5194/nhess-20-567-2020

Doran, K., Long, J., Birchler, J., Brenner, O., Hardy, M., Morgan, K., Stockdon, H., & Torres, M. (2017). Lidar-derived beach morphology (dune crest, dune toe, and shoreline) for U.S. sandy coastlines (ver. 4.0, October 2020): U.S. Geological Survey data release. https://doi.org/https://doi.org/10.5066/F7GF0S0Z

Doyle, J., Hodur, R., Chen, S., Jin, Y., Msokaitis, J., Wang, S., Hendricks, E., Jin, J., & Smith, T. (2014). Tropical Cyclone Prediction Using COAMPS-TC. *Oceanography*, *27*(3), 104–115. https://doi.org/10.5670/oceanog.2014.72

Dullaart, J. C. M., Muis, S., Bloemendaal, N., Chertova, M. V., Couasnon, A., & Aerts, J. C. J. H. (2021). Accounting for tropical cyclones more than doubles the global population exposed to low-probability coastal flooding. *Communications Earth & Environment*, *2*(1), 1–11. https://doi.org/10.1038/s43247-021-00204-9

Dullaart, J. C., Muis, S., Bloemendaal, N., & Aerts, J. C. (2020). Advancing global storm surge modelling using the new ERA5 climate reanalysis. *Climate Dynamics*, *54*(1-2), 1007–1021. https://doi.org/10.1007/s00382-019-05044-0

Easterling, D. R., Meehl, G. A., Parmesan, C., Changnon, S. A., Karl, T. R., & Mearns, L. O. (2000). Climate extremes: observations, modeling, and impacts. *Science (New York, N.Y.)*, *289*(5487), 2068–2074. https://doi.org/10.1126/science.289.5487.2068

Egbert, G. D., & Erofeeva, S. Y. (2002). Efficient inverse modeling of barotropic ocean tides. *Journal of Atmospheric and Oceanic Technology*, *19*(2), 183–204. https://doi.org/10.1175/1520-0426(2002)019<0183:EIMOBO>2.0.CO;2

Eilander, D., & Boisgontier, H. (2022). HydroMT. https://doi.org/https://doi.org/10.5281/zenodo.6961871

Eilander, D., Couasnon, A., Sperna Weiland, F. C., Ligtvoet, W., Bouwman, A., Winsemius, H. C., & Ward, P. J. (2022). Modeling compound flood risk and risk reduction using a globally-applicable framework: A case study in the Sofala region. *Natural Hazards and Earth System Sciences Discussions*, (October), 1–31. https://doi.org/10.5194/nhess-2022-248

Elsner, J. B., Elsner, T., & Kara, A. B. (1999). *Hurricanes of the North Atlantic: Climate and Society*. Oxford University Press. https://books.google.com/books?id=Pa-I-7UFMHAC

Emanuel, K. A., Ravela, S., Vivant, E., & Risi, C. (2006). Supplement to A Statistical Deterministic Approach to Hurricane Risk Assessment. *Bulletin of the American Meteorological Society*, *87*(3), S1–S5. https://doi.org/10.1175/bams-87-3-emanuel

Emanuel, K. (2005). Increasing destructiveness of tropical cyclones over the past 30 years. *Nature*, *436*(7051), 686–688. https://doi.org/10.1038/nature03906

Emerton, R., Cloke, H., Ficchi, A., Hawker, L., de Wit, S., Speight, L., Prudhomme, C., Rundell, P., West, R., Neal, J., Cuna, J., Harrigan, S., Titley, H., Magnusson, L., Pappenberger, F., Klingaman, N., & Stephens, E. (2020). Emergency flood bulletins for Cyclones Idai and Kenneth: A critical evaluation of the use of global flood forecasts for international humanitarian preparedness and response. *International Journal of Disaster Risk Reduction*, *50*, 101811. https://doi.org/10.1016/j.ijdrr.2020.101811

Erikson, L., Herdman, L., Flahnerty, C., Engelstad, A., Pusuluri, P., Barnard, P., Storlazzi, C., Beck, M., Reguero, B., & Parker, K. (2022). Ocean wave time-series data simulated with a global-scale numerical wave model under the influence of projected CMIP6 wind and sea ice fields: U.S. Geological Survey data release. https://doi.org/https://doi.org/10.5066/P9KR0RFM

Erikson, L., Barnard, P., O'Neill, A., Wood, N., Jones, J., Finzi Hart, J., Vitousek, S., Limber, P., Hayden, M., Fitzgibbon, M., Lovering, J., & Foxgrover, A. (2018). Projected 21st Century Coastal Flooding in the Southern California Bight. Part 2: Tools for Assessing Climate Change-Driven Coastal Hazards and Socio-Economic Impacts. *Journal of Marine Science and Engineering*, *6*(3), 76. https://doi.org/10.3390/jmse6030076

Esch, T., Heldens, W., Hirner, A., Keil, M., Marconcini, M., Roth, A., Zeidler, J., Dech, S., & Strano, E. (2017). Breaking new ground in mapping human settlements from space – The Global Urban Footprint. *ISPRS Journal of Photogrammetry and Remote Sensing*, *134*, 30–42. https://doi.org/https://doi.org/10.1016/j.isprsjprs.2017.10.012

Evans, C., Wood, K. M., Aberson, S. D., Archambault, H. M., Milrad, S. M., Bosart, L. F., Corbosiero, K. L., Davis, C. A., Dias Pinto, J. R., Doyle, J., Fogarty, C., Galarneau, T. J., Grams, C. M., Griffin, K. S., Gyakum, J., Hart, R. E., Kitabatake, N., Lentink, H. S., McTaggart-Cowan, R., … Zhang, F. (2017). The Extratropical Transition of Tropical Cyclones. Part I: Cyclone Evolution and Direct Impacts. *Monthly Weather Review*, *145*(11), 4317–4344. https://doi.org/10.1175/MWR-D-17-0027.1

Eymold, W. K., Flanary, C., Erikson, L., **Nederhoff**, **K.**, Chartrand, C. C., Jones, C., Kasper, J., & Bull, D. L. (2022). Typological representation of the offshore oceanographic environment along the Alaskan North Slope. *Continental Shelf Research*, *244*, 104795. https://doi.org/10.1016/j.csr.2022.104795

Florczyk, A. J., Corbane, C., Ehrlich, D., Freire, S., Kemper, T., Maffenini, L., Melchiorri, M., Pesaresi, M., Politis, P., Schiavina, M., Sabo, F., & Zanchetta, L. (2019). *GHSL data package 2019* (Vol. JRC117104). https://doi.org/10.2760/290498

Flowerdew, J., Horsburgh, K., Wilson, C., & Mylne, K. (2010). Development and evaluation of an ensemble forecasting system for coastal storm surges. *Quarterly Journal of the Royal Meteorological Society*, *136*(651), 1444–1456. https://doi.org/10.1002/qj.648

Fossell, K. R., Ahijevych, D., Morss, R. E., Snyder, C., & Davis, C. (2017). The practical predictability of storm tide from tropical cyclones in the gulf of Mexico. *Monthly Weather Review*, *145*(12), 5103–5121. https://doi.org/10.1175/MWR-D-17-0051.1

Fujita, T. (1952). Pressure Distribution Within Typhoon. *Geophysical Magazine*, *23*, 437–451.

Giardino, A., Schrijvershof, R., **Nederhoff**, **K.**, de Vroeg, H., Brière, C., Tonnon, P.-K., Caires, S., Walstra, D.-J., Sosa, J., Verseveld, W. V., Schellekens, J., & Slo, C. J. (2018a). A quantitative assessment of human interventions and climate change on the West African sediment budget. *Ocean and Coastal Management*, (February). https://doi.org/10.1016/j.ocecoaman.2017.11.008

Giardino, A., **Nederhoff**, **K.**, & Vousdoukas, M. (2018b). Coastal hazard risk assessment for small islands: assessing the impact of climate change and disaster reduction measures on Ebeye (Marshall Islands). *Regional Environmental Change*, *18*(8), 2237–2248. https://doi.org/10.1007/s10113-018-1353-3

Goerss, J. S. (2007). Prediction of consensus tropical cyclone track forecast error. *Monthly Weather Review*, *135*(5), 1985–1993. https://doi.org/10.1175/MWR3390.1

Gonzalez, T., & Taylor, A. (2018). Development of the NWS ' Probabilistic Tropical Storm Surge Model, 2018.

Goodfellow, I., Bengio, Y., & Courville, A. (2017). *Deep learning*. https://doi.org/9780262035613026203561 8

Gori, A., Lin, N., & Xi, D. (2020). Tropical Cyclone Compound Flood Hazard Assessment: From Investigating Drivers to Quantifying Extreme Water Levels. *Earth's Future*, *8*(12). https://doi.org/10.1029/2020EF001660

Grossman, E. E., Tehranirad, B., **Nederhoff**, **K.**, Crosby, S. C., Stevens, A. W., Van Arendonk, N. R., Nowacki, D. J., Erikson, L. H., & Barnard, P. L. (2023). Modeling Extreme Water Levels in the Salish Sea: The Importance of Including Remote Sea Level Anomalies for Application in Hydrodynamic Simulations. *Water (Switzerland)*, *15*(23). https://doi.org/10.3390/w15234167

Guo, H., John, J. G., Blanton, C., & McHugh, C. (2018). NOAA-GFDL GFDL-CM4 model output prepared for CMIP6 ScenarioMIP ssp585. Download 20190906. Earth System Grid Federation. https://doi.org/https://doi.org/10.22033/ESGF/CMIP6.9268

Guo, Z., Leitão, J. P., Simões, N. E., & Moosavi, V. (2021). Data-driven flood emulation: Speeding up urban flood predictions by deep convolutional neural networks. *Journal of Flood Risk Management*, *14*(1). https://doi.org/10.1111/jfr3.12684

Han, Y., Zhang, M. Z., Xu, Z., & Guo, W. (2022). Assessing the performance of 33 CMIP6 models in simulating the large-scale environmental fields of tropical cyclones. *Climate Dynamics*, *58*(5-6), 1683–1698. https://doi.org/10.1007/s00382-021-05986-4

Harper, B., Kepert, J., & Ginger, J. (2010). Guidelines for converting between various wind averaging periods in tropical cyclone conditions. *World Meteorological Organization*, (October). https://www.wmo.int/pages/prog/www/tcp/documents/WMO_TD_1555_en.pdf

Hasegawa, H., Kohno, N., & Itoh, M. (2015). Development of Storm Surge Model in Japan Meteorological Agency. *14th International Workshop on Wave Hindcasting and Forecasting & 5th Coastal Hazard Symposium*, (May 2010), 1–6.

Hauer, M. E. (2019). Population projections for U.S. counties by age, sex, and race controlled to shared socioeconomic pathway. *Scientific Data*, *6*, 1–15. https://doi.org/10.1038/sdata.2019.5

Hersbach, H., Bell, B., Berrisford, P., Hirahara, S., Horányi, A., Muñoz-Sabater, J., Nicolas, J., Peubey, C., Radu, R., Schepers, D., Simmons, A., Soci, C., Abdalla, S., Abellan, X., Balsamo, G., Bechtold, P., Biavati, G., Bidlot, J., Bonavita, M., … Thépaut, J. N. (2020). The ERA5 global reanalysis. *Quarterly Journal of the Royal Meteorological Society*, (March), 1–51. https://doi.org/10.1002/qj.3803

Hibbert, K., Glenn, E., Smith, T. M., & González-Cruz, J. E. (2023). Changes to Sea Surface Temperatures and Vertical Wind Shear and Their Influence on Tropical Cyclone Activity in the Caribbean and the Main Developing Region. *Atmosphere*, *14*(6), 999. https://doi.org/10.3390/atmos14060999

Hlywiak, J., & Nolan, D. S. (2022). The Evolution of Asymmetries in the Tropical Cyclone Boundary Layer Wind Field during Landfall. *Monthly Weather Review*, *150*(3), 529–549. https://doi.org/10.1175/MWR-D-21-0191.1

Hoek, J. (2017). Tropical Cyclone Wind Statistical Estimation In Regions with Rare Tropical Cyclone Occurrence. https://repository.tudelft.nl/islandora/object/uuid%3A2986959f-53ce-42a6-9299-c24833353616

Hoffman, R. N., & Leidner, S. M. (2005). An Introduction to the Near–Real–Time QuikSCAT Data. *Weather and Forecasting*, *20*(4), 476–493. https://doi.org/10.1175/WAF841.1

Holland, G. J. (1983). Tropical cyclone motion: environmental interaction plus a beta effect. https://doi.org/10.1175/1520-0469(1983)040<0328:TCMEIP>2.0.CO;2

Holland, G. J. (1980). An analytical model of the wind and pressure profiles in hurricanes. https://doi.org/10.1175/1520-0493(1980)108<1212:AAMOTW>2.0.CO;2

Holland, G. J. (2008). A Revised Hurricane Pressure – Wind Model. *Monthly wearther review*, (2), 3432–3445. https://doi.org/10.1175/2008MWR2395.1

Holland, G. J., Belanger, J., & Fritz, A. (2010). A Revised Model for Radial Profiles of Hurricane Winds. *American Meteorological Society*, 4393–4401. https://doi.org/10.1175/2010MWR3317.1

Homer, C., Dewitz, J., Jin, S., Xian, G., Costello, C., Danielson, P., Gass, L., Funk, M., Wickham, J., Stehman, S., Auch, R., & Riitters, K. (2020). Conterminous United States land cover change patterns 2001–2016 from the 2016 National Land Cover Database. *ISPRS Journal of Photogrammetry and Remote Sensing, 162*(February), 184–199. https://doi.org/10.1016/j.isprsjprs.2020.02.019

Hu, K., Chen, Q., & Fitzpatrick, P. (2012). Assessment of a Parametric Hurricane Surface Wind Model for Tropical Cyclones in the Gulf of Mexico. In *Advances in hurricane research - modelling, meteorology, preparedness and impacts*. InTech. https://doi.org/10.5772/51288

Huang, W., Ye, F., Zhang, Y. J., Park, K., Du, J., Moghimi, S., Myers, E., Pe'eri, S., Calzada, J. R., Yu, H., Nunez, K., & Liu, Z. (2021). Compounding factors for extreme flooding around Galveston Bay during Hurricane Harvey. *Ocean Modelling, 158*, 101735. https://doi.org/10.1016/j.ocemod.2020.101735

Huizinga, J., de Moel, H., & Szewczyk, W. (2017). *Global flood depth-damage functions*. https://doi.org/10.2760/16510

IHO, I., & BODC, '. (2003). Centenary Edition of the GEBCO Digital Atlas, published on CD-ROM on behalf of the Intergovernmental Oceanographic Commission and the International Hydrographic Organization as part of the General Bathymetric Chart of the Oceans; British Oceanog.

IPET. (2006). Performance evaluation of the New Orleans and Southeast Louisiana Hurricane Protection System draft final report of the Interagency Performance Evaluation Task Force volume VIII – engineering and operational risk and reliability analysis.

James, M. K., & Mason, L. B. (2005). Synthetic tropical cyclone database. *Journal of Waterway, Port, Coastal and Ocean Engineering, 131*(4), 181–192. https://doi.org/10.1061/(ASCE)0733-950X(2005)131:4(181)

Jelesnianski, C. P., Chen, J., & Shaffer, W. A. (1992). SLOSH : Sea, Lake, and Overland Surges from Hurricanes. *NOAA technical report*, (April).

Johnson, C. L., Chen, Q., Ozdemir, C. E., Xu, K., McCall, R., & **Nederhoff**, **K.** (2021). Morphodynamic modeling of a low-lying barrier subject to hurricane forcing: The role of backbarrier wetlands. *Coastal Engineering, 167*, 103886.

Joint Typhoon Warning Center. (2021). Annual Tropical Cyclone Report: 2020 [PDF file]. Retrieved from https://www.metoc.navy.mil/jtwc/products/atcr/2020atcr.pdf.

Joint Typhoon Warning Center. (2022). Typhoon Idai (2021) Best Track Data [Data File]. Retrieved from https://www.metoc.navy.mil/jtwc/jtwc.html.

Jyoteeshkumar Reddy, P., Sriram, D., Gunthe, S. S., & Balaji, C. (2021). Impact of climate change on intense Bay of Bengal tropical cyclones of the post-monsoon season: a pseudo global warming approach. *Climate Dynamics, 56*(9-10), 2855–2879. https://doi.org/10.1007/s00382-020-05618-3

Kaplan, J., & DeMaria, M. (1995). A Simple Empirical Model for Predicting the Decay of Tropical Cyclone Winds after Landfall. *Journal of Applied Meteorology*, *34*(11), 2499–2512. https://doi.org/10.1175/1520-0450(1995)034<2499:ASEMFP>2.0.CO;2

Kernkamp, H. W. J., Van Dam, A., Stelling, G. S., & de Goede, E. D. (2011). Efficient scheme for the shallow water equations on unstructured grids with application to the Continental Shelf. *Ocean Dynamics*, *61*(8), 1175–1188. https://doi.org/10.1007/s10236-011-0423-6

Kirchhofer, W. (1974). Classification of European 500 mb Patterns. *Arbeitsbericht der Schweiz. Meteorol. Zurich Zentral.*

Klaver, S., **Nederhoff, K.**, Giardino, A., Tissier, M. F. S., Dongeren, A. R., & Spek, A. J. F. (2019). Impact of Coral Reef Mining Pits on Nearshore Hydrodynamics and Wave Runup During Extreme Wave Events. *Journal of Geophysical Research: Oceans*, *124*(4), 2824–2841. https://doi.org/10.1029/2018JC014165

Klotzbach, P. J., Wood, K. M., Schreck, C. J., Bowen, S. G., Patricola, C. M., & Bell, M. M. (2022). Trends in Global Tropical Cyclone Activity: 1990–2021. *Geophysical Research Letters*, *49*(6), 1–11. https://doi.org/10.1029/2021GL095774

Knaff, J., Longmore, S. P., DeMaria, R. T., & Molenar, D. A. (2015). Improved tropical-cyclone flight-level wind estimates using routine infrared satellite reconnaissance. *Journal of Applied Meteorology and Climatology*, *54*(2), 463–478. https://doi.org/10.1175/JAMC-D-14-0112.1

Knaff, J., & Sampson, C. (2015). After a Decade Are Atlantic Tropical Cyclone Gale Force Wind Radii Forecasts Now Skillful? *Weather and Forecasting*, *30*(3), 702–709. https://doi.org/10.1175/WAF-D-14-00149.1

Knaff, J., Sampson, C., DeMaria, M., Marchok, P., Timothy, Gross, J. M., & McAdie, J., Colin. (2007). Statistical Tropical Cyclone Wind Radii Prediction Using Climatology and Persistence. *Weather and Forecasting*, *22*, 781–791. https://doi.org/10.1175/WAF1026.1

Knapp, K. R., Kruk, M. C., Levinson, D. H., Diamond, H. J., & Neumann, C. J. (2010). The international best track archive for climate stewardship (IBTrACS). *Bulletin of the American Meteorological Society*, *91*(3), 363–376. https://doi.org/10.1175/2009BAMS2755.1

Knutson, T. R., McBride, J. L., Chan, J., Emanuel, K. A., Holland, G. J., Landsea, C., Held, I., Kossin, J. P., Srivastava, A., & Sugi, M. (2010). Tropical cyclones and climate change. *Nature Geoscience*, *3*(3), 157–163. https://doi.org/10.1038/ngeo779

Knutson, T. R., Sirutis, J. J., Zhao, M., Tuleya, R. E., Bender, M., Vecchi, G. A., Villarini, G., & Chavas, D. (2015). Global projections of intense tropical cyclone activity for the late twenty-first century from dynamical downscaling of CMIP5/RCP4.5 scenarios. *Journal of Climate*, *28*(18), 7203–7224. https://doi.org/10.1175/JCLI-D-15-0129.1

Kron, W. (2005). Flood Risk = Hazard • Values • Vulnerability. *Water International*, *30*(1), 58–68. https://doi.org/10.1080/02508060508691837

Kumar, S., Dube, A., Ashrit, R., & Mitra, A. K. (2023). A Machine Learning (ML)-Based Approach to Improve Tropical Cyclone Intensity Prediction of NCMRWF Ensemble Prediction System. *Pure and Applied Geophysics*, *180*(1), 261–275. https://doi.org/10.1007/s00024-022-03206-6

Lamers, A., Devi S, S., Sharma, M., Berg, R., Gálvez, J. M., Yu, Z., Kriat, T., Cardos, S., Grant, D., & Moron, L. A. (2023). Forecasting Tropical Cyclone Rainfall and Flooding Hazards and Impacts. *Tropical Cyclone Research and Review*. https://doi.org/10.1016/j.tcrr.2023.06.005

Lasserre, C. G., **Nederhoff**, **K.**, Storlazzi, C. D., Reguero, B. G., & Beck, M. W. (2024). Improved efficient physics-based computational modeling of regional wave-driven coastal flooding for reef-lined coastlines. *Ocean Modelling*, 102358. https://doi.org/10.1016/j.ocemod.2024.102358

Le Bars, D., Drijfhout, S., & De Vries, H. (2017). A high-end sea level rise probabilistic projection including rapid Antarctic ice sheet mass loss. *Environmental Research Letters*, *12*(4). https://doi.org/10.1088/1748-9326/aa6512

Lecacheux, S., Rohmer, J., Paris, F., Pedreros, R., Quetelard, H., & Bonnardot, F. (2021). Toward the probabilistic forecasting of cyclone-induced marine flooding by overtopping at Reunion Island aided by a time-varying random-forest classification approach. *Natural Hazards*, *105*(1), 227–251. https://doi.org/10.1007/s11069-020-04307-y

Lee, C. Y., Tippett, M. K., Sobel, A. H., & Camargo, S. J. (2018). An environmentally forced tropical cyclone hazard model. *Journal of Advances in Modeling Earth Systems*, *10*(1), 223–241. https://doi.org/10.1002/2017MS001186

Leijnse, T., Giardino, A., **Nederhoff**, **K.**, & Caires, S. (2022). Generating reliable estimates of tropical-cyclone-induced coastal hazards along the Bay of Bengal for current and future climates using synthetic tracks. *Natural Hazards and Earth System Sciences*, *22*(6), 1863–1891. https://doi.org/10.5194/nhess-22-1863-2022

Leijnse, T., **Nederhoff**, **K.**, Van Dongeren, A., McCall, R. T., & Van Ormondt, M. (2020). Improving computational efficiency of compound flooding simulations: The SFINCS model with subgrid features. *AGU Fall Meeting Abstracts*, *2020*, NH022–0006.

Leijnse, T., van Ormondt, M., **Nederhoff**, **K.**, & van Dongeren, A. (2021). Modeling compound flooding in coastal systems using a computationally efficient reduced-physics solver: Including fluvial, pluvial, tidal, wind- and wave-driven processes. *Coastal Engineering*, *163*, 103796. https://doi.org/https://doi.org/10.1016/j.coastaleng.2020.103796

Lesser, G. R., Roelvink, D., van Kester, J., & Stelling, G. S. (2004). Development and validation of a three-dimensional morphological model. *Coastal Engineering*, *51*(8-9), 883–915. https://doi.org/10.1016/j.coastaleng.2004.07.014

Li, H., Sheffield, J., & Wood, E. F. (2010). Bias correction of monthly precipitation and temperature fields from Intergovernmental Panel on Climate Change AR4 models using equidistant quantile matching. *Journal of Geophysical Research Atmospheres*, *115*(10). https://doi.org/10.1029/2009JD012882

Liang, Q., Du, G., Hall, J. W., & Borthwick, A. G. (2008). Flood Inundation Modeling with an Adaptive Quadtree Grid Shallow Water Equation Solver. *Journal of Hydraulic Engineering*, *134*(11), 1603–1610. https://doi.org/10.1061/(ASCE)0733-9429(2008)134:11(1603)

Lin, N., & Emanuel, K. (2016). Grey swan tropical cyclones. *Nature Climate Change*, *6*(1), 106–111. https://doi.org/10.1038/nclimate2777

Lin, N., Emanuel, K., Oppenheimer, M., & Vanmarcke, E. (2012). Physically based assessment of hurricane surge threat under climate change. *Nature Climate Change*, *2*(6), 462–467. https://doi.org/10.1038/nclimate1389

Lin, Y., Zhao, M., & Zhang, M. (2015). Tropical cyclone rainfall area controlled by relative sea surface temperature. *Nature Communications*, *6*, 1–7. https://doi.org/10.1038/ncomms7591

Liu, Y. Y., Maidment, D. R., Tarboton, D. G., Zheng, X., & Wang, S. (2018). A CyberGIS Integration and Computation Framework for High-Resolution Continental-Scale Flood Inundation Mapping. *JAWRA Journal of the American Water Resources Association*, *54*(4), 770–784. https://doi.org/https://doi.org/10.1111/1752-1688.12660

Lockwood, J. W., Oppenheimer, M., Lin, N., Kopp, R. E., Vecchi, G. A., & Gori, A. (2022). Correlation Between Sea-Level Rise and Aspects of Future Tropical Cyclone Activity in CMIP6 Models. *Earth's Future*, *10*(4), 1–19. https://doi.org/10.1029/2021EF002462

Loder, N. M., Irish, J. L., Cialone, M. A., & Wamsley, T. V. (2009). Sensitivity of hurricane surge to morphological parameters of coastal wetlands. *Estuarine, Coastal and Shelf Science*, *84*(4), 625–636. https://doi.org/10.1016/j.ecss.2009.07.036

Löwe, R., Böhm, J., Jensen, D. G., Leandro, J., & Rasmussen, S. H. (2021). U-FLOOD – Topographic deep learning for predicting urban pluvial flood water depth. *Journal of Hydrology*, *603*(March). https://doi.org/10.1016/j.jhydrol.2021.126898

Lu, P., Lin, N., Emanuel, K. A., Chavas, D., & Smith, J. (2018). Assessing Hurricane Rainfall Mechanisms Using a Physics-Based Model: Hurricanes Isabel (2003) and Irene (2011). *Journal of the Atmospheric Sciences*, *75*(7), 2337–2358. https://doi.org/10.1175/JAS-D-17-0264.1

Luettich, R. A., Westerink, J. J., & Scheffner, N. W. (1992). ADCIRC: An Advanced Three-Dimensional Circulation Model for Shelves Coasts and Estuaries, Report 1: Theory and Methodology of ADCIRC-2DDI and ADCIRC-3DL, Dredging Research Program Technical Report DRP-92-6. https://erdc-library.erdc.dren.mil/jspui/handle/11681/4618

Matheson, J. E., & Winkler, R. L. (1976). Scoring Rules for Continuous Probability Distributions. *Management Science*, *22*(10), 1087–1096. https://doi.org/10.1287/mnsc.22.10.1087

McAdie, C. J., & Lawrence, M. B. (2000). Improvements in tropical cyclone track forecasting in the Atlantic Basin, 1970-98. *Bulletin of the American Meteorological Society*, *81*(5), 989–997. https://doi.org/10.1175/1520-0477(2000)081<0989:IITCTF>2.3.CO;2

McGranahan, G., Balk, D., & Anderson, B. (2007). The rising tide: assessing the risks of climate change and human settlements in low elevation coastal zones. *Environment and Urbanization*, *19*(1), 17–37. https://doi.org/10.1177/0956247807076960

Merkens, J. L., Reimann, L., Hinkel, J., & Vafeidis, A. T. (2016). Gridded population projections for the coastal zone under the Shared Socioeconomic Pathways. *Global and Planetary Change*, *145*, 57–66. https://doi.org/10.1016/j.gloplacha.2016.08.009

Mori, N., & Shimura, T. (2023). Tropical cyclone-induced coastal sea level projection and the adaptation to a changing climate. *Cambridge Prisms: Coastal Futures*, *1*, e4. https://doi.org/10.1017/cft.2022.6

Mori, N., & Takemi, T. (2016). Impact assessment of coastal hazards due to future changes of tropical cyclones in the North Pacific Ocean. *Weather and Climate Extremes*, *11*, 53–69. https://doi.org/10.1016/j.wace.2015.09.002

Mori, N., Takemi, T., Tachikawa, Y., Tatano, H., Shimura, T., Tanaka, T., Fujimi, T., Osakada, Y., Webb, A., & Nakakita, E. (2021). Recent nationwide climate change impact assessments of natural hazards in Japan and East Asia. *Weather and Climate Extremes*, *32*, 100309. https://doi.org/10.1016/j.wace.2021.100309

Muis, S., Aerts, J. C. J. H., Á. Antolínez, J. A., Dullaart, J. C., Duong, T. M., Erikson, L., Haarsma, R. J., Apecechea, M. I., Mengel, M., Le Bars, D., O'Neill, A., Ranasinghe, R., Roberts, M. J., Verlaan, M., Ward, P. J., & Yan, K. (2023). Global Projections of Storm Surges Using High-Resolution CMIP6 Climate Models. *Earth's Future*, *11*(9). https://doi.org/10.1029/2023EF003479

Muis, S., Verlaan, M., Winsemius, H. C., Aerts, J. C. J. H., & Ward, P. J. (2016). A global reanalysis of storm surges and extreme sea levels. *Nature Communications*, *7*(May), 11969. https://doi.org/10.1038/ncomms11969

Muñoz, D. F., Abbaszadeh, P., Moftakhari, H., & Moradkhani, H. (2022). Accounting for uncertainties in compound flood hazard assessment: The value of data assimilation. *Coastal Engineering*, *171*, 104057. https://doi.org/10.1016/j.coastaleng.2021.104057

Murakami, H., & Sugi, M. (2010). Effect of model resolution on tropical cyclone climate projections. *Scientific Online Letters on the Atmosphere*, *6*(May), 73–76. https://doi.org/10.2151/sola.2010-019

Nadal-Caraballo, N. C., Campbell, M. O., Gonzalez, V. M., Torres, M. J., Melby, J. A., & Taflanidis, A. A. (2020). Coastal Hazards System: A Probabilistic Coastal Hazard Analysis Framework. *Journal of Coastal Research*, *95*(sp1), 1211. https://doi.org/10.2112/SI95-235.1

Nadal-Caraballo, N. C., Yawn, M. C., Aucoin, L. A., Carr, M. L., Taflanidis, A. A., Kyprioti, A. P., Melby, J. A., Ramos-santiago, E., Gonzalez, V. M., Massey, T. C., Cobell, Z., & Cox, A. T. (2022). Coastal Hazards System – Louisiana Coastal and Hydraulics. ERDC/CHL TR 22-16. Vicksburg, MS: US Army Engineer Research and Development Center. (August).

Nakagawa, M. (2009). Outline of the High Resolution Global Model at the Japan Meteorological Agency. *RSMC Tokyo-Typhoon Center Technical Review, 11:25–38, 2009*, 1–13.

NASA GPM. (2019). Global Preciptation Measurement (GPM) of Cyclone Idai via https://gpm.nasa.gov/tropical-storm-idai-measured-gpm. Accessed on 16 March, 2023.

Nath, S., Kotal, S. D., & Kundu, P. K. (2016). Seasonal prediction of tropical cyclone activity over the north Indian Ocean using three artificial neural networks. *Meteorology and Atmospheric Physics*, *128*(6), 751–762. https://doi.org/10.1007/s00703-016-0446-0

National Hurricane Center. (2023). About NHC Graphics. Retrieved June 27, 2023, from https://www.nhc.noaa.gov/aboutnhcgraphics.shtml#WATCHWARN.

Navier, C. (1822). Mémoire sur les lois du mouvement des fluides. *Mémoires de l'Académie Royale des Sciences de l'Institut de France*, *6*, 389–440.

NCEI; NOAA National Centers for Environmental Information. (2022). U.S. Billion-Dollar Weather and Climate Disasters (2022). https://doi.org/https://www.doi.org/10.25921/stkw-7w73

**Nederhoff**, **K.**, Crosby, S. C., Van Arendonk, N. R., Grossman, E. E., Tehranirad, B., Leijnse, T., Klessens, W., & Barnard, P. L. (2024a). Dynamic Modeling of Coastal Compound Flooding Hazards Due to Tides, Extratropical Storms, Waves, and Sea-Level Rise: A Case Study in the Salish Sea, Washington (USA). *Water*, *16*(2), 346. https://doi.org/10.3390/w16020346

**Nederhoff**, **K.**, Erikson, L., Engelstad, A., Bieniek, P., & Kasper, J. (2022). The effect of changing sea ice on wave climate trends along Alaska's central Beaufort Sea coast. *The Cryosphere*, *16*(5), 1609–1629. https://doi.org/10.5194/tc-16-1609-2022

**Nederhoff**, **K.**, Giardino, A., van Ormondt, M., & Vatvani, D. (2019). Estimates of tropical cyclone geometry parameters based on best-track data. *Natural Hazards and Earth System Sciences*, *19*(11), 2359–2370. https://doi.org/10.5194/nhess-19-2359-2019

**Nederhoff**, **K.**, Hoek, J., Leijnse, T., van Ormondt, M., Caires, S., & Giardino, A. (2020). Simulating Synthetic Tropical Cyclone Tracks for Statistically Reliable Wind and Pressure Estimations. *Natural Hazards and Earth System Sciences Discussions*, *2020*, 1–30.

**Nederhoff**, **K.**, Hoek, J., Leijnse, T., van Ormondt, M., Caires, S., & Giardino, A. (2021a). Simulating synthetic tropical cyclone tracks for statistically reliable wind and pressure estimations. *Natural Hazards and Earth System Sciences*, *21*(3), 861–878. https://doi.org/10.5194/nhess-21-861-2021

**Nederhoff**, **K.**, Leijnse, T. W. B., Parker, K., Thomas, J., O'Neill, A., van Ormondt, M., McCall, R., Erikson, L., Barnard, P. L., Foxgrover, A., Klessens, W., Nadal-Caraballo, N. C., & Massey, T. C. (2024b). Tropical or extratropical cyclones: what drives the compound flood hazard, impact, and risk for the United States Southeast Atlantic coast? *Natural Hazards*. https://doi.org/10.1007/s11069-024-06552-x

**Nederhoff**, **K.**, Saleh, R., Tehranirad, B., Herdman, L., Erikson, L., Barnard, P. L., & van der Wegen, M. (2021b). Drivers of extreme water levels in a large, urban, high-energy coastal estuary – A case study of the San Francisco Bay. *Coastal Engineering*, *170*, 103984. https://doi.org/10.1016/j.coastaleng.2021.103984

**Nederhoff**, **K.**, Van Ormondt, M., Veeramony, J., Van Dongeren, A., Antolínez, J. A. Á., Leijnse, T., & Roelvink, D. (2024c). Accounting for Uncertainties in Forecasting Tropical Cyclone-Induced Compound Flooding. *Geoscientific*

*Model Development*, *17*(4), 1789–1811. https://doi.org/10.5194/gmd-17-1789-2024

**Nederhoff**, **K.**, & van Ormondt, M. (2023). Tropical Cyclone Forecasting Framework: TC-FF (v1.0.0-beta). Zenodo. https://doi.org/10.5281/zenodo.10433070

Neumann, B., Vafeidis, A. T., Zimmermann, J., & Nicholls, R. J. (2015). Future coastal population growth and exposure to sea-level rise and coastal flooding - A global assessment. *PLoS ONE*, *10*(3). https://doi.org/10.1371/journal.pone.0118571

Neumann, C. (1991). NOAA Technical Memorandum NWS NHC 38: The National Hurricane Center Risk Analysis Program (HURISK).

Nguyen, D. T., & Chen, S. T. (2020). Real-time probabilistic flood forecasting using multiple machine learning methods. *Water (Switzerland)*, *12*(3), 1–13. https://doi.org/10.3390/w12030787

NHC. (2019). Hurricane Florence. *National Hurricane Center Tropical Cyclone Report: Hurricane Florence*, (September 2018), 1–125.

NOAA. (2018). Costliest U.S. tropical cyclones tables updated. *NOAA Technical Memorandum NWS NHC-6*, 3. https://www.nhc.noaa.gov/pdf/nws-nhc-6.pdf%0Ahttps://www.nhc.noaa.gov/news/UpdatedCostliest.pdf%0Ahttps://www.nhc.noaa.gov/pdf/nws-nhc-6.pdf%0Ahttps://www.nhc.noaa.gov/dcmi.shtml

NOAA. (2021). 'National Water Model data' on https://registry.opendata.aws/nwm-archive. Accessed April 2021.

NOAA. (2022). Climate Change: Global Sea Level on https://www.climate.gov/news-features/understanding-climate/climate-change-global-sea-level.

NOAA. (2023). Frequently Asked Questions webpage. URL https://www.aoml.noaa.gov/hrd-faq/#costliest-tcs. Accessed: 2023-09-30.

NOAA National Geophysical Data Center. (2001). U.S. Coastal Relief Model Vol.3 - Florida and East Gulf of Mexico. Accessed 6/30/21. https://doi.org/10.7289/V5W66HPP

O'Neill, A., Erikson, L. H., Barnard, P. L., Limber, P. W., Vitousek, S., Warrick, J. A., Foxgrover, A. C., Lovering, J., O'Neill, A. C., Erikson, L. H., Barnard, P. L., Limber, P. W., Vitousek, S., Warrick, J. A., Foxgrover, A. C., & Lovering, J. (2018). Projected 21st century coastal flooding in the Southern California Bight. Part 1: Development of the third generation CoSMoS model. *Journal of Marine Science and Engineering*, *6*(2), 59. https://doi.org/10.3390/jmse6020059

Parker, K., Erikson, L., Thomas, J., **Nederhoff**, **K.**, Barnard, P., & Muis, S. (2023). Relative contributions of water level components to extreme water levels along the United States Southeast Atlantic Coast from a regional-scale water level hindcast. *Natural Hazards*, *117*(3), 2219–2248. https://doi.org/10.1007/s11069-023-05939-6

Peduzzi, P., Chatenoux, B., Dao, H., De Bono, A., Herold, C., Kossin, J., Mouton, F., & Nordbeck, O. (2012). Global trends in tropical cyclone risk. *Nature Climate Change*, *2*(4), 289–294. https://doi.org/10.1038/nclimate1410

Powell, M. D., Houston, S. H., Amat, L. R., & Morisseau-Leroy, N. (1998). The HRD real-time hurricane wind analysis system. *Journal of Wind Engineering* *and Industrial Aerodynamics*, *77-78*, 53–64. https://doi.org/10.1016/S0167-6105(98)00131-7

Pradhan, R., Aygun, R. S., Maskey, M., Ramachandran, R., & Cecil, D. J. (2018). Tropical Cyclone Intensity Estimation Using a Deep Convolutional Neural Network. *IEEE Transactions on Image Processing*, *27*(2), 692–702. https://doi.org/10.1109/TIP.2017.2766358

Ranasinghe, R., Callaghan, D., & Stive, M. J. F. (2012). Estimating coastal recession due to sea level rise : beyond the Bruun rule. *Climatic Change*, 561–574. https://doi.org/10.1007/s10584-011-0107-8

Rappaport, E. N. (2014). Fatalities in the united states from atlantic tropical cyclones: New data and interpretation. *Bulletin of the American Meteorological Society*, *95*(3), 341–346. https://doi.org/10.1175/BAMS-D-12-00074.1

Resio, D. T., & Irish, J. L. (2015). Tropical Cyclone Storm Surge Risk. *Current Climate Change Reports*, *1*(2), 74–84. https://doi.org/10.1007/s40641-015-0011-9

Roberts, M. (2019). MOHC HadGEM3-GC31-HM model output prepared for CMIP6 HighResMIP highres-future. Download 20191211. Earth System Grid. https://doi.org/https://doi.org/10.22033/ESGF/CMIP6.5984

Roberts, M. J., Camp, J., Seddon, J., Vidale, P. L., Hodges, K., Vannière, B., Mecking, J., Haarsma, R., Bellucci, A., Scoccimarro, E., Caron, L.-P., Chauvin, F., Terray, L., Valcke, S., Moine, M.-P., Putrasahan, D., Roberts, C. D., Senan, R., Zarzycki, C., … Wu, L. (2020). Projected Future Changes in Tropical Cyclones Using the CMIP6 HighResMIP Multimodel Ensemble. *Geophysical Research Letters*, *47*(14). https://doi.org/10.1029/2020GL088662

Roelvink, D., Mccall, R., Mehvar, S., **Nederhoff**, **K.**, & Dastgheib, A. (2018). Improving predictions of swash dynamics in XBeach : The role of groupiness and incident-band runup. *Coastal Engineering*, (February), 1–21. https://doi.org/10.1016/j.coastaleng.2017.07.004

Roy, C., & Kovordányi, R. (2012). Tropical cyclone track forecasting techniques - A review. *Atmospheric Research*, *104-105*, 40–69. https://doi.org/10.1016/j.atmosres.2011.09.012

Rye, C. J., & Boyd, J. A. (2022). Downward Counterfactual Analysis in Insurance Tropical Cyclone Models: A Miami Case Study, 207–232. https://doi.org/10.1007/978-3-031-08568-0{_}9

Sampson, C., Fukada, E. M., Knaff, J., Strahl, B. R., Brennan, M. J., & Marchok, T. (2017). Tropical Cyclone Gale Wind Radii Estimates for the Western North Pacific. *Weather and Forecasting*, *32*(3), 1029–1040. https://doi.org/10.1175/WAF-D-16-0196.1

Santiago-Collazo, F. L., Bilskie, M. V., & Hagen, S. C. (2019). A comprehensive review of compound inundation models in low-gradient coastal watersheds. *Environmental Modelling & Software*, *119*, 166–181. https://doi.org/https://doi.org/10.1016/j.envsoft.2019.06.002

Schubert, W., & Hack, J. (1982). Inertial Stability and Tropical Cyclone Development. *Journal of the Atmospheric Sciences*, *39*, 1687–1697.

Schwerdt, R. W., Ho, F., & Watkins, R. R. (1979). Meteorological criteria for standard project hurricane and probable maximum hurricane windfields, gulf and east coasts of the United States NOAA Technical Report NWS 23. (September).

Scoccimarro, E., Bellucci, A., & Peano, D. (2017). CMCC CMCC-CM2-VHR4 model output prepared for CMIP6 HighResMIP. Version YYYYMMDD[1].Earth System Grid Federation. https://doi.org/https://doi.org/10.22033/ESGF/CMIP6.1367

Sebastian, A., Bader, D. J., **Nederhoff**, **K.**, Leijnse, T., Bricker, J. D., & Aarninkhof, S. G. J. (2021). Hindcast of pluvial, fluvial and coastal flood damage in Houston, TX during Hurricane Harvey (2017) using SFINCS. *Natural Hazards*, (2017). https://doi.org/10.1007/s11069-021-04922-3

Sehili, A., Lang, G., & Lippert, C. (2014). High-resolution subgrid models: background, grid generation, and implementation. *Ocean Dynamics*, *64*(4), 519–535. https://doi.org/10.1007/s10236-014-0693-x

Snaiki, R., & Wu, T. (2019). Knowledge-enhanced deep learning for simulation of tropical cyclone boundary-layer winds. *Journal of Wind Engineering and Industrial Aerodynamics*, *194*, 103983. https://doi.org/10.1016/j.jweia.2019.103983

Stephens, M. A. (1974). Stephens_EDF Statistics and some comparisons.

Stiles, B., Danielson, R., Poulson, W., & Brennman, M. (2013). Optimized Tropical Cyclone Winds From QuikSCAT: A Neural Network Approach. *IEEE Transactions on Geoscience and Remote Sensing*.

Stockdon, H. F., Holman, R. A., Howd, P. A., & Sallenger, A. H. (2006). Empirical parameterization of setup, swash, and runup. *Coastal Engineering*, *53*(7), 573–588. https://doi.org/10.1016/j.coastaleng.2005.12.005

Stokes, G. (1845). On the Theories of the Internal Friction of Fluids in Motion, and of the Equilibrium and Motion of Elastic Solids. *Transactions of the Cambridge Philosophical Society*, 287–319.

Suh, S. W., Lee, H. Y., Kim, H. J., & Fleming, J. G. (2015). *An efficient early warning system for typhoon storm surge based on time-varying advisories by coupled ADCIRC and SWAN* (Vol. 65). https://doi.org/10.1007/s10236-015-0820-3

Sukop, M. C., Rogers, M., Guannel, G., Infanti, J. M., & Hagemann, K. (2018). High temporal resolution modeling of the impact of rain, tides, and sea level rise on water table flooding in the Arch Creek basin, Miami-Dade County Florida USA. *Science of The Total Environment*, *616-617*, 1668–1688. https://doi.org/10.1016/j.scitotenv.2017.10.170

Sweet, W., Hamlington, B., Kopp, R., Weaver, C., Barnard, P. L., Bekaert, D., Brooks, W., Craghan, M., Dusek, G., Frederikse, T., Garner, G., Genz, A., Krasting, J., Larour, E., Marcy, D., Marra, J., Obeysekera, J., Osler, M., Pendleton, M., … Zuzak, C. (2022). Global and Regional Sea Level Rise Scenarios for the United States. *NOAA Technical Report NOS 01*, 111 pp. https://oceanservice.noaa.gov/hazards/sealevelrise/noaa-nos-

Taherkhani, M., Vitousek, S., Barnard, P. L., Frazer, N., Anderson, T. R., & Fletcher, C. H. (2020). Sea-level rise exponentially increases coastal flood frequency. *Scientific Reports*, *10*(1), 6466. https://doi.org/10.1038/s41598-020-62188-4

Tang, W., & Carey, S. K. (2017). HydRun: A MATLAB toolbox for rainfall–runoff analysis. *Hydrological Processes*, *31*(15), 2670–2682. https://doi.org/https://doi.org/10.1002/hyp.11185

Taylor, A., & Glahn, B. (2008). Probabilistic guidance for hurricane storm surge. *Proc. 88th AMS Annual Meeting*, 8. https://ams.confex.com/ams/pdfpapers/132793.pdf

Taylor-Burns, R., **Nederhoff**, **K.**, Lacy, J., & Barnard, P. (2023). The influence of vegetated marshes on wave transformation in a sheltered estuary. *Coastal Engineering*, *184*(June), 104346. https://doi.org/10.1016/j.coastaleng.2023.104346

Tebaldi, C., & Knutti, R. (2007). The use of the multi-model ensemble in probabilistic climate projections. *Philosophical Transactions of the Royal Society A: Mathematical, Physical and Engineering Sciences*, *365*(1857), 2053–2075. https://doi.org/10.1098/rsta.2007.2076

Tehranirad, B., Herdman, L., **Nederhoff**, **K.**, Erikson, L., Cifelli, R., Pratt, G., Leon, M., & Barnard, P. L. (2020). Effect of fluvial discharges and remote non-tidal residuals on compound flood forecasting in San Francisco Bay. *Water (Switzerland)*, *12*(9), 1–15. https://doi.org/10.3390/w12092481

The City of Charleston. (2015). Sea Level Rise Strategy. (December), 20. https://www.charleston-sc.gov/DocumentCenter/View/10089

Trenberth, K. E., Dai, A., Rasmussen, R. M., & Parsons, D. B. (2003). The Changing Character of Precipitation. *Bulletin of the American Meteorological Society*, *84*(9), 1205–1218. https://doi.org/10.1175/BAMS-84-9-1205

Tuleya, R. E. (1994). Tropical storm development and decay: sensitivity to surface boundary conditions. https://doi.org/10.1175/1520-0493(1994)122<0291:TSDADS>2.0.CO;2

Tyler, D., Cushing, W., Danielson, J., Poppenga, S., Beverly, S., & Shogib, R. (2022). Topobathymetric Model of the Coastal Carolinas, 1851 to 2020: U.S. Geological Survey data release. https://doi.org/https://doi.org/10.5066/P9MPA8K0

UN OCHA. (2019). Business Guide: Cyclone Idai. (April), 1–3. https://media.ifrc.org/ifrc/document/emergency-appeal-mozambique-cyclone-idai/

United States Census Bureau. (2020). 2020 Population and Housing State Data for US Southeast http://censusreporter.org/Accessed 3 August 2022.

United States Department of Agriculture. (1986). Urban Hydrology for Small. *Techincal Release 55*, 164. http://scholar.google.com/scholar?hl=en&btnG=Search&q=intitle:Urban+Hydrology+for+Small+watersheds#1

United States Department of Agriculture. (2009). National Engineering Handbook Chapter 7 Hydrologic Soil Groups.

United States Department of Agriculture. (2020). U.S. General Soil Map (STATSGO2) for Florida, Georgia, South Carolina, North Carolina and Virginia. Available online at https://gdg.sc.egov.usda.gov/ accessed on January 8, 2021.

US Environmental Protection Agency (US EPA). (2019). Storm Water Management Model Reference Manual Errata. *1*(July), 2. https://www.epa.gov/sites/default/files/2018-08/documents/swmm_reference_manual_errata.pdf

U.S. Geological Survey. (2021). Short-Term Network Data Portal, accessed on 2021-12-23, at http://water.usgs.gov/floods/FEV/.

van Ormondt, M., **Nederhoff**, **K.**, & Van Dongeren, A. (2020). Delft Dashboard: a quick setup tool for hydrodynamic models. *Journal of Hydroinformatics*, *22*(3), 510–527. https://doi.org/10.2166/hydro.2020.092

Verlaan, M., Zijderveld, A., de Vries, H., & Kroos, J. (2005). Operational storm surge forecasting in the Netherlands: developments in the last decade. *Philosophical transactions. Series A, Mathematical, physical, and engineering sciences*, *363*(1831), 1441–1453. https://doi.org/10.1098/rsta.2005.1578

Vickery, P. J., Skerlj, P. F., Steckley, A. C., & Twisdale, L. A. (2000). Hurricane Wind Field Model for Use in Hurricane Simulations. *Journal of Structural Engineering*, *126*(10), 1203–1221. https://doi.org/10.1061/(ASCE)0733-9445(2000)126:10(1203)

Vickery, P., & Twisdale, L. A. (1995). Prediction of hurricane wind speeds in the united states. *Journal of Structural Engineering (United States)*, *121*(11), 1691–1699. https://doi.org/10.1061/(ASCE)0733-9445(1995)121:11(1691)

Vickery, P., & Wadhera, D. (2008). Winds of Hurricanes from Flight-Level Pressure and H * Wind Data. *Journal of Applied Meteorology and Climatology*. https://doi.org/10.1175/2008JAMC1837.1

Vickery, P., Wadhera, D., Twisdale, L. A., & Lavelle, F. M. (2009). U.S. Hurricane Wind Speed Risk and Uncertainty. *Journal of Structural Engineering*, *135*(3), 301–320. https://doi.org/10.1061/(ASCE)0733-9445(2009)135:3(301)

Vitousek, S., Barnard, P. L., Limber, P., Erikson, L., & Cole, B. (2017a). A model integrating longshore and cross-shore processes for predicting long-term shoreline response to climate change. *Journal of Geophysical Research: Earth Surface*, *122*(4), 782–806. https://doi.org/10.1002/2016JF004065

Vitousek, S., Barnard, P., Fletcher, C. H., Frazer, N., Erikson, L., & Storlazzi, C. D. (2017b). Doubling of coastal flooding frequency within decades due to sea-level rise. *Scientific Reports*, *7*(1), 1–9. https://doi.org/10.1038/s41598-017-01362-7

Volp, N. D., Van Prooijen, B. C., & Stelling, G. S. (2013). A finite volume approach for shallow water flow accounting for high-resolution bathymetry and roughness data. *Water Resources Research*, *49*(7), 4126–4135. https://doi.org/10.1002/wrcr.20324

Wahl, T., Jain, S., Bender, J., Meyers, S. D., & Luther, M. E. (2015). Increasing risk of compound flooding from storm surge and rainfall for major US cities. *Nature Climate Change*, *5*(12), 1093–1097. https://doi.org/10.1038/nclimate2736

Wand, M. P., & Jones, M. C. (1994). *Kernel Smoothing*. Chapman & Hall. http://oro.open.ac.uk/28198/

Weibull, W. (1939). A statistical theory of strength of materials. *Ing. Vetensk. Akad. Handl.*

Willoughby, H. E., Clos, J. A., & Shoreibah, M. G. (1982). Concentric Eye Walls, Secondary Wind Maxima, and The Evolution of the Hurricane vortex. *Journal of the Atmospheric Sciences*, *39*(2), 395–411. https://doi.org/10.1175/1520-0469(1982)039<0395:CEWSWM>2.0.CO;2

Willoughby, H. E., Darling, R. W. R., & Rahn, M. E. (2006). Parametric Representation of the Primary Hurricane Vortex. Part II: A New Family of Sectionally Continuous Profiles. *Monthly Weather Review*, *134*(4), 1102–1120. https://doi.org/10.1175/MWR3106.1

Willoughby, H. (2012). Distributions and Trends of Death and Destruction from Hurricanes in the United States, 1900–2008. *Natural Hazards Review*, *13*(1), 57–64. https://doi.org/10.1061/(ASCE)NH.1527-6996.0000046

Willoughby, H., & Rahn, M. E. (2004). Parametric Representation of the Primary Hurricane Vortex. Part I: Observations and Evaluation of the Holland (1980) Model. *Monthly Weather Review*, *132*(12), 3033–3048. https://doi.org/10.1175/MWR2831.1

Wing, O. E., Bates, P. D., Sampson, C. C., Smith, A. M., Johnson, K. A., & Erickson, T. A. (2017). Validation of a 30 m resolution flood hazard model of the conterminous United States. *Water Resources Research*, *53*(9), 7968–7986. https://doi.org/10.1002/2017WR020917

Wing, O. E., Bates, P. D., Smith, A. M., Sampson, C. C., Johnson, K. A., Fargione, J., & Morefield, P. (2018). Estimates of present and future flood risk in the conterminous United States. *Environmental Research Letters*, *13*(3). https://doi.org/10.1088/1748-9326/aaac65

Xu, J., & Wang, Y. (2015). A Statistical Analysis on the Dependence of Tropical Cyclone Intensification Rate on the Storm Intensity and Size in the North Atlantic. *Weather and Forecasting Forecasting*, *30*(3), 692–701. https://doi.org/10.1175/WAF-D-14-00141.1

Xu, Z., Han, Y., Tam, C.-Y., Yang, Z.-L., & Fu, C. (2021). Bias-corrected CMIP6 global dataset for dynamical downscaling of the historical and future climate (1979–2100). *Scientific Data*, *8*(1), 293. https://doi.org/10.1038/s41597-021-01079-3

Yamazaki, D., Ikeshima, D., Tawatari, R., Yamaguchi, T., O'Loughlin, F., Neal, J. C., Sampson, C. C., Kanae, S., & Bates, P. D. (2017). A high-accuracy map of global terrain elevations. *Geophysical Research Letters*, *44*(11), 5844–5853. https://doi.org/10.1002/2017GL072874

Yao, Y., Zhong, X., Zheng, Y., & Wang, Z. (2023). A Physics-Incorporated Deep Learning Framework for Parameterization of Atmospheric Radiative Transfer Journal of Advances in Modeling Earth Systems, 1–17. https://doi.org/10.1029/2022MS003445

Ye, F., Huang, W., Zhang, Y. J., Moghimi, S., Myers, E., Pe'eri, S., & Yu, H. C. (2021). A cross-scale study for compound flooding processes during Hurricane Florence. *Natural Hazards and Earth System Sciences*, *21*(6), 1703–1719. https://doi.org/10.5194/nhess-21-1703-2021

Zhang, J. A., & Uhlhorn, E. W. (2012). Hurricane Sea Surface Inflow Angle and an Observation-Based Parametric Model. *Monthly Weather Review*, *140*(11), 3587–3605. https://doi.org/10.1175/mwr-d-11-00339.1

# ACKNOWLEDGEMENTS

This dissertation represents not only the pinnacle of my academic journey but also a remarkable period of personal and professional growth that began at Deltares Netherlands and continued at Deltares USA. As I pen these acknowledgments, I am filled with immense gratitude for completing this challenging yet enriching chapter of my life. So many people have supported me along the way, and to anyone I may have forgotten to mention, please know I appreciate your commitment to my success.

To my supervisory committee, your guidance has been invaluable. Dano Roelvink, your openness to my unconventional PhD approach enabled me to balance this endeavor with my position at Deltares. I always enjoyed our conversations and appreciated your suggestions and advice. Ap van Dongeren, your insights have significantly shaped my growth as a coastal scientist. You have been an exceptional mentor all these years. Jose Antolinez, your critical evaluation of my arguments and statistics has greatly enhanced my work. Jay Veeramony, I deeply appreciate your constructive feedback. I eagerly anticipate our continued collaboration, as this PhD is a milestone, not an endpoint, in our journey. My thanks also go to the evaluating committee members for their diligent assessment of my work and to Allison Penko and Sean Vitousek for providing feedback on the original proposal.

At Deltares Netherlands, my career began with exceptional colleagues, especially in the AMO department. Alessio Giardino, your mentorship and belief in my abilities have been foundational to my confidence and growth. I will always remember your meticulous and constructive feedback on my first journal paper (and first paper in this PhD). Your support in my early years at Deltares continues to propel me forward, even though we do not work closely together anymore. Dirk-Jan Walstra, your leadership and kind encouragement have been transformative, guiding my path within Deltares from my start at AMO in the Netherlands, to my move to Deltares USA, and, lastly, in my pursuit of a PhD. Maarten van Ormondt, your can-do mentality transformed my own attitude toward applied research, and your programming approach established the foundation for every chapter in this PhD. Bob Hoogendoorn, thank you for your willingness to lend an ear and offer thoughtful advice from the Netherlands when needed. I also want to thank Robert McCall for always having a critical eye and our engaging scientific discussions; Stuart Pearson and Lodewijk de Vet for the practical advice regarding doing a PhD; Tim Leijnse for the pleasant collaborations regarding SFINCS and TCWISE; Sofia Caires and Ferdinand Diermanse for their statistical expertise, and last but not least; Deepak

Vatvani for sparking my interest in tropical cyclones almost ten years ago.

In the US, collaborating with the USGS team in Santa Cruz has been a pivotal experience. Thank you, Li Erikson, for your warm welcome and our ongoing collaboration focused on Alaska; Eric Grossman, for your drive and meaningful work in the Pacific Northwest; Patrick Barnard, for our engaging CoSmoS-focused projects; Curt Storlazzi, for your enthusiasm and dedication to research; and Kai Parker, for your kind support and teamwork. My gratitude extends to all of the USGS staff. You all are a talented group of scientists to work with.

At Deltares USA, the collaboration and support of my colleagues, along with memorable team events like our 2022 mountain biking retreat, have been a source of constant motivation and support. Edwin Welles, thank you for facilitating this opportunity for professional growth and the freedom to explore and develop my ideas. While not directly involved in any of the PhD chapters, I also want to extend my gratitude to Rohin Saleh. Your expertise and passion for doing impactful work in the San Francisco Bay are inspiring, and I appreciate being able to work with and learn from you.

Additionally, I would like to thank my friends, particularly H.I.C. Octopus. Schoften for Schoften provided an interactive platform to socialize virtually or in person. Our many conversations while enjoying a beer and weekend get-togethers helped me stay connected and always provided a welcome distraction. Specifically, I want to thank my paranymphs Dr. ir. Lamarmpje and Dr. ir. Omarmpje, because, *goed voorbeeld doet volgen*.

I would also would like to thank my wife, Patrice Lucas. Patrice you are my everything and your laughter makes me smile every time. Your continuous support during personal and professional challenges is invaluable. Our pizza party nights after a Friday of PhD work (or any other day) were the highlight. You are the best and I love you with all my heart.

Finally, I would like to thank my parents. Thank you for your unconditional love and support. From the moment I was kleine Keesje, to my decision to study in Delft, to my move to the US, you have always been encouraging, proud, and happy for me. Throughout my entire life, you have consistently been my greatest source of support, always there to cheer me on. A son cannot wish for more amazing parents than you two.

This journey has been made possible by each one of you (and many others), and for that, I am eternally grateful.

*Cornelis Mattheus (Kees) Nederhoff*
*San Jose, CA, December 24, 2022*

# ABOUT THE AUTHOR

Cornelis Mattheus (Kees) Nederhoff was born in Werkendam on April 3, 1990. He grew up in Wognum, where he graduated from secondary school at Oscar Romero in 2008. Inspired by the Afsluitdijk, he started his academic education at Delft University of Technology. He graduated from the Hydraulic Engineering program in 2014 under the supervision of prof.dr.ir. M.J.F. Stive on an MSc project entitled *Modeling the effects of hard structures on dune erosion and overwash* that was carried out at Deltares.

Kees started his professional career in 2015 as a consultant and researcher at Deltares. In the first few years, he gained broad experience in the application and development of coastal modeling software such as Delft3D, SWAN, XBeach and SFINCS. Moreover, he was a key contributor to numerous coastal research projects across the globe focused on tidal reproduction, storm surges, wave propagation, overland compound flooding, sediment transport, morphological change, tropical cyclones, and risk assessments.

In 2019, Kees was ready for a new challenge and moved to the United States to join Deltares USA as a coastal scientist. In this role, he collaborates part-time with a team at the US Geological Survey (USGS) in Santa Cruz, CA on numerical modeling of coastal processes. In the years that followed, Kees immersed himself in academic writing as his engagement in applied research deepened, and he prioritized making scientific developments accessible, comprehensible, and beneficial to society at large. In 2022, he decided to explore the option of pursuing his PhD part-time. This dissertation is a result of that decision.

When not thinking about coastal modeling and tropical cyclones, Kees can be found recreating outside (ideally on a mountain bike trail), socializing with friends, attending to his herb garden, trying out a new Korean recipe, or binging a TV show while relaxing with his wife (Patrice) and cat (BJ).

# Curriculum Vitæ

**Cornelis Mattheus Nederhoff**

| | |
|---|---|
| April 3, 1990 | Born in Werkendam, the Netherlands. |

## Education

| | |
|---|---|
| 2002–2008 | Secondary School<br>Oscar Romero, Hoorn, the Netherlands |
| 2008–2012 | Bachelor of Science in Civil Engineering<br>Delft University of Technology, Delft, the Netherlands |
| 2012–2014 | Master of Science in Hydraulic Engineering<br>Delft University of Technology, Delft, the Netherlands |
| 2022-2024 | PhD Researcher, *this dissertation*<br>IHE Delft Institute for Water Education, Delft, the Netherlands<br>Delft University of Technology, Delft, the Netherlands |

## Work experience

| | |
|---|---|
| 2015-2019 | Consultant/Researcher<br>Stichting Deltares Netherlands, Delft, the Netherlands |
| 2019-current | Coastal Scientist<br>Deltares USA Inc., San Jose, CA, USA |
| 2019-current | Visiting Scientist<br>United States Geological Survey (USGS), Santa Cruz, CA, USA |

# LIST OF PUBLICATIONS

## PEER-REVIEWED JOURNAL ARTICLES

### FIRST AUTHOR

7. **Nederhoff**, **K.**, Van Ormondt, M., Veeramony, J., Van Dongeren, A., Antolínez, J. A. Á., Leijnse, T., & Roelvink, D. (2024c). Accounting for Uncertainties in Forecasting Tropical Cyclone-Induced Compound Flooding. *Geoscientific Model Development*, *17*(4), 1789–1811. https://doi.org/10.5194/gmd-17-1789-2024

6. **Nederhoff**, **K.**, Leijnse, T. W. B., Parker, K., Thomas, J., O'Neill, A., van Ormondt, M., McCall, R., Erikson, L., Barnard, P. L., Foxgrover, A., Klessens, W., Nadal-Caraballo, N. C., & Massey, T. C. (2024b). Tropical or extratropical cyclones: what drives the compound flood hazard, impact, and risk for the United States Southeast Atlantic coast? *Natural Hazards*. https://doi.org/10.1007/s11069-024-06552-x

5. **Nederhoff**, **K.**, Crosby, S. C., Van Arendonk, N. R., Grossman, E. E., Tehranirad, B., Leijnse, T., Klessens, W., & Barnard, P. L. (2024a). Dynamic Modeling of Coastal Compound Flooding Hazards Due to Tides, Extratropical Storms, Waves, and Sea-Level Rise: A Case Study in the Salish Sea, Washington (USA). *Water*, *16*(2), 346. https://doi.org/10.3390/w16020346

4. **Nederhoff**, **K.**, Erikson, L., Engelstad, A., Bieniek, P., & Kasper, J. (2022). The effect of changing sea ice on wave climate trends along Alaska's central Beaufort Sea coast. *The Cryosphere*, *16*(5), 1609–1629. https://doi.org/10.5194/tc-16-1609-2022

3. **Nederhoff**, **K.**, Saleh, R., Tehranirad, B., Herdman, L., Erikson, L., Barnard, P. L., & van der Wegen, M. (2021b). Drivers of extreme water levels in a large, urban, high-energy coastal estuary – A case study of the San Francisco Bay. *Coastal Engineering*, *170*, 103984. https://doi.org/10.1016/j.coastaleng.2021.103984

2. **Nederhoff**, **K.**, Hoek, J., Leijnse, T., van Ormondt, M., Caires, S., & Giardino, A. (2021a). Simulating synthetic tropical cyclone tracks for statistically reliable wind and pressure estimations. *Natural Hazards and Earth System Sciences*, *21*(3), 861–878. https://doi.org/10.5194/nhess-21-861-2021

1. **Nederhoff**, **K.**, Giardino, A., van Ormondt, M., & Vatvani, D. (2019). Estimates of tropical cyclone geometry parameters based on best-track data. *Natural Hazards and Earth System Sciences*, *19*(11), 2359–2370. https://doi.org/10.5194/nhess-19-2359-2019

## CO-AUTHOR

17. Lasserre, C. G., **Nederhoff**, **K.**, Storlazzi, C. D., Reguero, B. G., & Beck, M. W. (2024). Improved efficient physics-based computational modeling of regional wave-driven coastal flooding for reef-lined coastlines. *Ocean Modelling*, 102358. https://doi.org/10.1016/j.ocemod.2024.102358

16. Grossman, E. E., Tehranirad, B., **Nederhoff**, **K.**, Crosby, S. C., Stevens, A. W., Van Arendonk, N. R., Nowacki, D. J., Erikson, L. H., & Barnard, P. L. (2023). Modeling Extreme Water Levels in the Salish Sea: The Importance of Including Remote Sea Level Anomalies for Application in Hydrodynamic Simulations. *Water (Switzerland)*, *15*(23). https://doi.org/10.3390/w15234167

15. Parker, K., Erikson, L., Thomas, J., **Nederhoff**, **K.**, Barnard, P., & Muis, S. (2023). Relative contributions of water level components to extreme water levels along the United States Southeast Atlantic Coast from a regional-scale water level hindcast. *Natural Hazards*, *117*(3), 2219–2248. https://doi.org/10.1007/s11069-023-05939-6

14. Taylor-Burns, R., **Nederhoff**, **K.**, Lacy, J., & Barnard, P. (2023). The influence of vegetated marshes on wave transformation in a sheltered estuary. *Coastal Engineering*, *184*(June), 104346. https://doi.org/10.1016/j.coastaleng.2023.104346

13. Crosby, S. C., **Nederhoff**, **K.**, VanArendonk, N., & Grossman, E. E. (2023). Efficient modeling of wave generation and propagation in a semi-enclosed estuary. *Ocean Modelling*, 102231. https://doi.org/10.1016/j.ocemod.2023.102231

12. Eymold, W. K., Flanary, C., Erikson, L., **Nederhoff**, **K.**, Chartrand, C. C., Jones, C., Kasper, J., & Bull, D. L. (2022). Typological representation of the offshore oceanographic environment along the Alaskan North Slope. *Continental Shelf Research*, *244*, 104795. https://doi.org/10.1016/j.csr.2022.104795

11. Leijnse, T., Giardino, A., **Nederhoff**, **K.**, & Caires, S. (2022). Generating reliable estimates of tropical-cyclone-induced coastal hazards along the Bay of Bengal for current and future climates using synthetic tracks. *Natural Hazards and Earth System Sciences*, *22*(6), 1863–1891. https://doi.org/10.5194/nhess-22-1863-2022

10. Sebastian, A., Bader, D. J., **Nederhoff**, **K.**, Leijnse, T., Bricker, J. D., & Aarninkhof, S. G. J. (2021). Hindcast of pluvial, fluvial and coastal flood damage in Houston, TX during Hurricane Harvey (2017) using SFINCS. *Natural Hazards*, (2017). https://doi.org/10.1007/s11069-021-04922-3

9. Leijnse, T., van Ormondt, M., **Nederhoff**, **K.**, & van Dongeren, A. (2021). Modeling compound flooding in coastal systems using a computationally efficient reduced-physics solver: Including fluvial, pluvial, tidal, wind- and wave-driven processes. *Coastal Engineering*, *163*, 103796. https://doi.org/https://doi.org/10.1016/j.coastaleng.2020.103796

8. de Ridder, M. P., Smit, P. B., Van Dongeren, A., McCall, R. T., **Nederhoff**, **K.**, & Reniers, A. J. (2021). Efficient two-layer non-hydrostatic wave model with accurate dispersive behaviour. *Coastal Engineering*, *164*(February). https://doi.org/10.1016/j.coastaleng.2020.103808

7. Johnson, C. L., Chen, Q., Ozdemir, C. E., Xu, K., McCall, R., & **Nederhoff**, **K.** (2021). Morphodynamic modeling of a low-lying barrier subject to hurricane forcing: The role of backbarrier wetlands. *Coastal Engineering*, *167*, 103886

6. Tehranirad, B., Herdman, L., **Nederhoff**, **K.**, Erikson, L., Cifelli, R., Pratt, G., Leon, M., & Barnard, P. L. (2020). Effect of fluvial discharges and remote non-tidal residuals on compound flood forecasting in San Francisco Bay. *Water (Switzerland)*, *12*(9), 1–15. https://doi.org/10.3390/w12092481

5. van Ormondt, M., **Nederhoff**, **K.**, & Van Dongeren, A. (2020). Delft Dashboard: a quick setup tool for hydrodynamic models. *Journal of Hydroinformatics*, *22*(3), 510–527. https://doi.org/10.2166/hydro.2020.092

4. Klaver, S., **Nederhoff**, **K.**, Giardino, A., Tissier, M. F. S., Dongeren, A. R., & Spek, A. J. F. (2019). Impact of Coral Reef Mining Pits on Nearshore Hydrodynamics and Wave Runup During Extreme Wave Events. *Journal of Geophysical Research: Oceans*, *124*(4), 2824–2841. https://doi.org/10.1029/2018JC014165

3. Roelvink, D., Mccall, R., Mehvar, S., **Nederhoff**, **K.**, & Dastgheib, A. (2018). Improving predictions of swash dynamics in XBeach : The role of groupiness and incident-band runup. *Coastal Engineering*, (February), 1–21. https://doi.org/10.1016/j.coastaleng.2017.07.004

2. Giardino, A., **Nederhoff**, **K.**, & Vousdoukas, M. (2018b). Coastal hazard risk assessment for small islands: assessing the impact of climate change and disaster reduction measures on Ebeye (Marshall Islands). *Regional Environmental Change*, *18*(8), 2237–2248. https://doi.org/10.1007/s10113-018-1353-3

1. Giardino, A., Schrijvershof, R., **Nederhoff**, **K.**, de Vroeg, H., Brière, C., Tonnon, P.-K., Caires, S., Walstra, D.-J., Sosa, J., Verseveld, W. V., Schellekens, J., & Slo, C. J. (2018a). A quantitative assessment of human interventions and climate change on the West African sediment budget. *Ocean and Coastal Management*, (February). https://doi.org/10.1016/j.ocecoaman.2017.11.008

*Netherlands Research School for the*
*Socio-Economic and Natural Sciences of the Environment*

# DIPLOMA

## *for specialised PhD training*

The Netherlands research school for the
Socio-Economic and Natural Sciences of the Environment
(SENSE) declares that

## *Cornelis Mattheus Nederhoff*

born on the 3rd of April 1990, Werkendam, the Netherlands

has successfully fulfilled all requirements of the
educational PhD programme of SENSE.

Delft, 20 June 2024

Chair of the SENSE board
Prof. dr. Martin Wassen

The SENSE Director
Prof. Philipp Pattberg

*The SENSE Research School has been accredited by the Royal Netherlands Academy of Arts and Sciences (KNAW)*

KONINKLIJKE NEDERLANDSE
AKADEMIE VAN WETENSCHAPPEN

The SENSE Research School declares that **Cornelis Mattheus Nederhoff** has successfully fulfilled all requirements of the educational PhD programme of SENSE with a work load of 40.6 EC, including the following activities:

## SENSE PhD Courses

- Environmental research in context (2022)
- Research in context activity: 'Organising the Deltares USA software courses Online' (2023)

## Other PhD and Advanced MSc Courses

- NCK Summerschool, Netherlands Centre for Coastal Research (2015)

## External training

- XBeach course, Deltares (2019)
- Supervised Machine Learning: Regression and Classification, Coursera (2022)
- Advanced Learning Algorithms, Coursera (2022)
- Unsupervised Learning, Recommenders, Reinforcement Learning, Coursera (2022)
- Neural Networks and Deep Learning, Coursera (2022)
- SFINCS course, Deltares (2023)

## Management and Didactic Skills Training

- Supervising 3 MSc students with thesis (2017-2019)
- Organise software courses, Deltares USA (2019-2022)

## Oral Presentations

- *Impact Assessment of Coastal Hazards due to Typhoons in the Marshall Islands.* American Meteorological Society's 30th Conference on Climate Variability, 27 July 2017, Baltimore, USA
- *Non-Hydrostatic Wave Modelling at West Bay Harbour, UK.* XBeach User Days, 2 November 2017, Delft, The Netherlands
- *Modelling Pluvial, Fluvial and Marine Flooding as a Result of Hurricane Irma for Jacksonville, Florida.* ASBPA, 9 November 2018, Galveston, USA
- *Modelling Hydrodynamics in the Ameland Inlet as a Basis for Studying Sand Transport.* Coastal Sediments, 31 May 2019, Tampa, USA

SENSE coordinator PhD education

Dr. ir. Peter Vermeulen

IHE
DELFT
Institute for
Water Education
under the auspices
of UNESCO

TU Delft
Delft
University of
Technology

This dissertation delves into the dynamics of tropical cyclones (also known as hurricanes or typhoons) focusing on their role in coastal flooding, a phenomenon worsened by climate change and increased human activity. It aims to enhance flood risk analysis and forecasting accuracy by improving the descriptions of cyclones' wind geometry and pathways. The study distinguishes between operational risk analysis, which deals with short-term forecasting surrounding a cyclone event, and strategic risk analysis, which considers long-term climate variability and its impacts over decades.

Significant advancements have been made in several aspects including accurately representing tropical cyclone conditions through the empirical derivation of stochastic relationships for key storm size parameters. Furthermore, the thesis introduces a novel methodology for strategic risk analysis using computer-generated storm pathways (synthetic tracks) to overcome the limitations of historical data scarcity. The research also compares cyclone-induced flooding to other sources for a case study in the United States, revealing the predominant role of tropical cyclones in severe flood hazards despite a higher frequency of flooding that is caused by extratropical cyclones. Moreover, this dissertation presents a new operational risk assessment framework capable of simulating thousands of scenarios to aid in effective storm forecasting, particularly in regions lacking extensive data.

This book is printed on paper
from sustainably managed
forests and controlled sources

9 789073 445611